https://doi.org/10.15388/vu.thesis.982
https://orcid.org/0000-0002-5518-9010

VILNIUS UNIVERSITY
CENTER FOR PHYSICAL SCIENCES AND TECHNOLOGY

Ignas Lukošiūnas

Investigation of Laser Radiation Control via 2D Thin Film Guided Mode Resonance Filters

DOCTORAL DISSERTATION

Natural Sciences
Physics (N 002)
VILNIUS 2026

This dissertation is prepared between 2022 and 2026 at Vilnius University, Laser Research Center. The research was supported by the Research Council of Lithuania.

Academic Supervisor - Prof. Dr. Kęstutis Staliūnas (Vilnius University, Natural Sciences, Physics, N 002).

Dissertation Defense Panel:

Chairman - Prof. Dr. Zigmas Balevičius (Center for Physical Sciences and Technology, Natural Sciences, Physics, N 002)

Members:

Asoc. Prof. Dr. Vygandas Jarutis (Vilnius University, Natural Sciences, Physics, N 002),

Dr. Pavels Onufrijevs (Riga Technical University, Natural Sciences, Physics, N 002),

Prof. Dr. Gintaras Valušis (Vilnius University, Natural Sciences, Physics, N 002),

Asoc. Prof. Dr. Julius Vengelis (Vilnius University, Natural Sciences, Physics, N 002).

This dissertation shall be defended at a public meeting of the Disertation Defence Panel at 2026 m. September 18., 15:00, in Room 306 of the Vilnius University, Faculty of Physics, Laser Research Center. Adress: Sauletekio al. 10, Vilnius, Tel. +3705 236 6050;

https://doi.org/10.15388/vu.thesis.982
https://orcid.org/0000-0002-5518-9010

VILNIAUS UNIVERSITETAS
FIZINIŲ IR TECHNOLOGIJOS MOKSLŲ CENTRAS

Ignas Lukošiūnas

Lazerinės spinduliuotės valdymo, pasitelkus 2D plonasluoksnius šviesolaidinius filtrus, tyrimas

DAKTARO DISERTACIJA

Gamtos mokslai
Fizika (N 002)
VILNIUS 2026

Ši disertacija parengta 2022-2026 m. Vilniaus universiteto lazerinių tyrimų centre. Mokslinius tyrimus rėmė Lietuvos mokslo taryba.

Mokslinis vadovas - prof. dr. Kęstutis Staliūnas (Vilniaus universitetas, gamtos mokslai, fizika, N 002).

Gynimo taryba:

Pirmininkas - prof. dr. Zigmas Balevičius (Fizinių ir technologijų mokslų centras, gamtos mokslai, fizika, N 002)

Nariai

doc. dr. Vygandas Jarutis (Vilniaus universitetas, gamtos mokslai, fizika, N 002),

dr. Pavels Onufrijevs (Rigos technikos universitetas, Latvija gamtos mokslai, fizika, N 002),

prof. dr. Gintaras Valušis (Vilniaus universitetas, gamtos mokslai, fizika, N 002),

doc. dr. Julius Vengelis (Vilniaus universitetas, gamtos mokslai, fizika, N 002).

Disertacija ginama viešame gynynimo tarybos posėdyje 2026 m. rugsėjo 18 d., 15:00, Vilniaus universiteto fizikos fakulteto Lazerinių tyrimų centro 306 auditorijoje. Adresas: Saulėtekio al. 10, Vilnius, Lietuva., tel. +3705 2366050.

Contents

List of abbreviations **7**

Introduction **8**

Aprobation **15**

1 Literature Overview **17**
1.1 Guided Mode Resonance filters and their properties 17
1.1.1 Introduction to 1D guided modes 17
1.1.2 Rayleigh anomaly 19
1.1.3 Guided Mode Resonance 22
1.1.4 Temporal Coupled Mode Theory 24
1.1.5 Resonance quality and Purcell effect 28
1.1.6 Polarization in spherical coordinates 28
1.1.7 Diffraction efficiencies 30
1.1.8 Manufacturing of thin film GMRFs via IBS method . . 31
1.2 Numerical methods for GMRF simulation 33
1.2.1 Maxwell's equations in Frequency Domain 33
1.2.2 2D Finite Difference Frequency Domain 34
1.2.3 Plane wave expansion of Maxwell's equations 44
1.2.4 Implementation of 2D RCWA 47
1.3 Matrix methods for sub-layer connection 49
1.3.1 Implementation of T matrix method 49
1.3.2 Field computation 51
1.3.3 Scattering matrix method 52
1.4 Optimization methods 55
1.4.1 Genetic algorithm 56

2 Broadband reflection and angular filtering based on anomaly **58**
2.1 Trapezium interfaced waveguide concept 58
2.2 Numerical results 60
2.3 Experimental results 62
2.4 Summary 63

3 Investigation of GMR near the 'Edge of Continuum' in conformal thin film gratings **64**
3.1 Analytical model 64
3.2 Numerical results 69
3.3 Experimental results 70
3.4 GMR based broadband reflectance filter comparison 71
3.5 Summary 72

4 Enhanced absorption via Parity-Time symmetry breaking in GMR filters **73**
4.1 Absorption Enhancement with unmodulated substrate 73
4.2 Absorption Enhancement with modulated substrate 78
4.3 Fabrication and spectral characteristics 81
4.4 Summary 82

5 Application of GMRs for enhanced optical gain **84**
5.1 Perovskite thin films 84
5.2 Resonant characteristics of passive GMR filter 88
5.3 Oscillator Chain Model 91
5.4 Summary 95

6 Open-Source User Interface of Frequency based numerical algorithms – "ZenScat" **96**
6.1 Application concept 96
6.2 Benchmark of ZenScat 97
6.2.1 Validation with FDTD 97
6.2.2 Validation with RCWA 100
6.3 Optimization of DFB for enhanced, narrow-band absorption and gain 102
6.4 Application performance 104
6.5 Summary 106

Conclusions and summary of results **107**

Appendix **109**
A1 Maltab 2D RCWA code 109
A2 S matrix method for transmission and reflection regions 119
A3 Dispersion parameters 120
A4 1D eigen-value problem for slab-waveguides 120

Santrauka lietuvių kalba **122**

Acknowledgments **158**

List of abbreviations

C method – Chandezon method
CPU – Central Processing Unit
DE – Diffraction Efficiency
EOC – Edge of Continuum
ERIM – Effective Refractive Index Method
ETM – Enhanced Transmittance Matrix
FDTD – Finite Difference Time Domain
FDFD – Finite Difference Frequency Domain
FP – Fabri Perot
FS – Fused Silica
FWHM – Full Width at Half Maximum
GA – Genetic Algorithm
GMR – Guided Mode Resonance
GPU – Graphics Processing Unit
HfO_2 – Hafnium Dioxide
LIDT – Laser Induced Damage Threshold
LPG – Light Propagation Control
Nb_2O_5 – Niobium Pentoxide
PhC – Photonic Crystal
PML – Perfectly Matched Layer
PWEM – Plane Wave Expansion Method
RCWA – Rigorous Coupled Wave Analysis
RES – Resolution
S matrix – Scattering matrix
SCPML – Stretched Coordinate Perfectly Matched Layer
SiO_2 – Silicon Dioxide
SRC/src – Source
Ta_2O_5 – Tantalum Pentoxide
TCMT – Temporal Coupled Mode Theory
TF/SF region – Total Field/Scattered Field region
TiO_2 – Titanium Dioxide
UPML – Uniaxial Perfectly Matched Layer

Introduction

Periodic nanophotonic and microphotonic structures were first observed in nature and are responsible for vivid color patterns that change with viewing angle. Butterfly wings [1], the tail of common magpie [2, 3], opals [4, 5], and especially chameleons [6] all possess periodically arranged micro-structures that manipulate the back scattering of light. Such periodically arranged materials are defined as photonic crystals. The simplest form of a periodic structure consists of periodically arranged layers of different materials. Such a device is called a Bragg grating. Similar to the way a thin oil film on a puddle produces rainbow colors due to interference, multilayer structures can significantly enhance this effect. These one-dimensional photonic crystals are widely used in many areas of photonics [7]. The enhancement of a back-scattered wave due to constructive interference of multiple reflected waves is known as Bragg reflection, or a photonic bandgap - a frequency range in which electromagnetic waves cannot propagate. More advanced photonic crystals, featuring additional periodic modulation in two or three dimensions, can posses a wider photonic bandgap. This phenomenon is analogous to the electronic bandgap in crystalline solids, where electron states are forbidden within certain energy ranges. Under these conditions, electromagnetic wave propagation can be controlled through deliberate engineering of the material's spatial periodicity and dispersion properties. Such materials are named as band-gap materials, capable of spatial and spectral light propagation control. Besides, 2D and 3D periodically modulated scattering devices can be used for other purposes than reflection, such as wave-guiding [8, 9], angular dispersion control[10–12], optical invisibility cloaking[13], spatial light filtering [14–17], self-collimation, focusing of light [18–20], beam formation [21] and photonic crystal circuits [22, 23]. In other words, the applications are universal and broad in terms of light propagation control in linear photonic cavities.

In the realm of linear optics, the periodically arranged refractive index distribution is in possession of the same effects that are observed in solid-state physics. The beauty of the theory is that the incident light, when scattered (or perturbed), repeats periodic features of the periodically modulated photonic structure, thus mimicking its patterns. Such phenomenon is observed in classical periodic gratings, where diffraction, or angular dispersion, are present.

The diffraction gratings can pertain two-dimensional or one-dimensional surface modulation, which effectively distribute energy of incident wave into forward - diffraction and backward-diffraction orders, whose diffraction and reflection angles and their diffraction order values can be analytically estimated. Meanwhile, slab waveguides are one-dimensional waveguides where light propagation of waveguide modes can be analytically found via application of physical models for symmetrical structures.

When a periodic grating is combined with a slab waveguide, the guided modes enhance mentioned physical effects that belong to classical gratings.

This also results possible waveguide regimes, which controls incident light coupling with diffraction efficiencies. In other words, a resonant cavity is formed in the waveguide region, which is in possession of strong polarization sensitivity [24–27] and its broadband as well as sharp narrow-band resonant features [28–41]. The applications, just like photonic crystals, are vast and each physical effect of interest can be either enhanced or weakened by varying the geometrical and material parameters of the fabricated structures. Such devices are known as Guided Mode Resonance (GMR) filters [42–48].

In addition, precise, strict and practical applications demand high quality photonic crystal or GMR wave-guide designs. It can be achieved by precise control of material properties and geometrical shape. Analytical physical models only allow qualitative and crude estimations of mostly simplified structures. However, even waveguide slabs with one periodically modulated surface acquire numerical treatment of the system's physical properties. For this reason, the necessary algorithms with capabilities of solving Maxwell's equations numerically have been proposed due to the limitations of solving them analytically [49]. Algorithms, suitable for computing the light interaction with linear dielectric media directly, include the Finite Difference Time Domain (FDTD) [50], Finite Difference Frequency Domain (FDFD) [51] as well as Finite Element Method (FEM). They solve Maxwell's equations directly and iteratively in the grid of interest, be it rectangular or oblique. Other known algorithms, such as Plane Wave Expansion Method (PWEM,) [52] Rigorous Coupled Wave Analysis (RCWA) [53] and Chandezon method (C method)[54] are all based on mathematical simplifications, mainly because only periodically arranged devices are analyzed. By these methods, the Maxwell's equations are solved in frequency and Fourier domain, where resolution is controlled in Fourier space, rather than a direct spatial grid. In this case significant speed improvements are achieved, especially for high quality resonant structures, which acquire long simulation times with Finite Difference methods.

By combining the fastest numerical methods, such as RCWA, with global or local optimization algorithms, one can design necessary devices for light propagation control, such as spatial filters, polarization filters, broadband mirrors or highly dispersive devices [55]. The complex design problems of device topology are solved via optimization algorithms, without the need of a manual alterations. Even though the simulation procedures seem simple, implementation of the algorithms becomes problematic, even for mundane tasks, due to the high demands of specialization and knowledge of shifted, oblique grids and eigenvalue decomposition used in theoretical formalism.

In retrospect, the physical interest of GMR filters comes from the shapes and asymmetry of resonances which characterize such structures. Numerical Fourier based methods are capable of simulating them, yet analytical treatment of such resonant systems is lacking. Analytics are ought to provide a system of differential equations, which offer solutions that explain the resonant properties [56]. However, they employ vast simplifications, which are then parsed into the formalism, hence the qualitative agreeableness between analytical and numerical results [57–60]. The most successful cases are presented in the literature

and mainly for high or moderate quality resonance factors [61–64], where the electromagnetic fields in the cavities are located for a long amount of time and possess low decay time coefficients [65–73].

This work is devoted to applying two main frequency-domain numerical algorithms (RCWA and FDFD) to the analysis of 2D resonant interactions between incident light and periodic waveguides. The thesis also encourages open source utilization of such algorithms for public use in scientific community. Furthermore, the thorough analysis of Guided Mode Resonance phenomena is carried via comparisons between numerically simulated spectral characteristics and analytically simulated ones. Such research is performed for optically passive media with and without optical absorption. The theoretical work is also performed likewise for active GMR cavities that involve optical gain, whose designs are calculated by implementing genetic algorithm with the 2D RCWA.

The objective of the Thesis

The aim of this thesis is to develop a framework for 2D photonic device designing with utilization of GMR in periodic dielectric waveguides and improve knowledge of the physical phenomena in such resonant cavities.

The main tasks of the Thesis

To complete the goals, the tasks are acquired to be completed:

1. **Evaluate** the influence of single-layer topology on the GMR properties of periodic optical structures with the use of the developed RCWA solver. Identify spectral and angular resonance characteristics; validate the results through comparison with analytical models, derive explicit analytical solutions for resonant cases including leaky modes and bounded guided modes. Develop fabrication-ready filter designs and verify the approach by comparing measured zeroth-order diffraction efficiencies of manufactured GMR filters with numerically computed results.

2. **Analyze** the GMR properties with an implemented absorber on thin film waveguides. Provide the comparison of the influence of absorber's symmetry and asymmetry on the waveguide's absorption spectra. Calculate a device design for fabrication and verify numerical predictions through comparison with experimental measurements.

3. **Investigate** the diffraction efficiency characteristics of GMR filters based on thin-film structures with optical gain; optimize the device topology to maximize gain-enhanced resonance effects using optimization methods, and compare the numerical and analytical chain model results.

4. **Develop** a numerical solver for periodic optical devices based on 2D RCWA and FDFD methods; validate the solver through comparison with

peer-reviewed results, benchmark it against an industrial implementation, and extend the framework with optimization algorithms and a graphical user interface for efficient data input, processing, and output.

Scientific novelty

This work made a scientific contribution to the field of solid state electrodynamics, computational physics, resonant cavity physics as well as to GMR filter fabrication/autocloning technology:

1. The physics of GMRs near Rayleigh anomaly allows such a design parameter choice that for corrugated thin film structures, a flat-top angular reflection over a broadband wavelength interval can be facilitated.

2. Analytical framework is proposed for GMRFs operating near EOC that maps the optical response of a periodically modulated thin film onto a driven one-dimensional Schrödinger-type equation. This model clarifies the origin of the resonance behavior near the guided-mode threshold and identifies scaling laws and line-shape evolution of the GMRs at the continuum edge, while qualitatively agreeing with numerical simulations.

3. New GMRF design is introduced, enabling unidirectional coupling between external radiation and internal guided modes, allowing incident light to enter the system while suppressing back-coupling to free-space propagating modes. This mechanism demonstrates a new form of light trapping based on asymmetric coupling induced by simultaneous modulation of refractive index and losses, consequently leading to enhanced asymmetrical absorption.

4. Periodically modulated amplifying thin films on passive substrates can operate as active meta-mirrors, where GMRs occur in active media and produce resonant amplification of reflected and transmitted radiation. Also, a simplified analytical description based on coupled-mode/oscillator-chain concepts is developed and validated by rigorous numerical simulations.

5. 2D RCWA User Interface "ZenScat" is proposed, which demonstrates that a carefully engineered and validated 2D RCWA implementation can achieve stable convergence in passive, lossy, and gain-assisted periodic photonic systems while maintaining numerical consistency between T-matrix and S-matrix formulations. Furthermore, through cross-validation with published Lumerical and Fourier Modal studies, "ZenScat" provides an equivalent framework for resonant multilayer structures, yet computationally superior.

Practical value

This work has developed the Open Source User Interface which numerically simulates GMR filter designs for enhanced light to matter interactions, as well as for optical beam filtering in both spectral and spatial domains. Moreover, the analytical framework is developed for clarification and better interpretation of GMR characteristics. Hence the practical value can be divided to:

1. The proposed conformal dielectric GMR based trapezoidal structures enable compact dielectric devices capable of simultaneous broadband spectral selectivity and angular filtering of incident light, making them suitable for integration as broadband spectral filters, polarizers and spatial filters. Its realization using standard thin-film deposition techniques confirms that high-efficiency (>99%) filtering over a 46 nm bandwidth can be achieved.

2. Analytical Schrödinger-type equation model for GMRFs offers physical insight into how structural and coupling parameters influence the resonance behavior. This understanding supports more efficient interpretation of numerical results and guides the parameter selection in the design of resonant photonic structures.

3. The demonstrated unidirectional trapping enhances absorption in thin-film structures compared with symmetric coupling configurations, offering an efficient strategy for increasing light–matter interaction in lossy optical layers. Such non-Hermitian couplers provide a simple system — requiring only a surface grating and an asymmetrically distributed absorber— which improves the performance of devices such as solar cells, photodetectors, and non-reflective optical components.

4. GMR in active media enables controllable amplification of reflected and transmitted light in thin-film nanophotonic structures, offering a route to compact resonant optical amplifiers based on sinusoidal-type of interfaces. Such structures may serve as functional elements in integrated photonic systems, including micro-lasing systems and resonant optical devices, which require narrow spectral/angular amplification and high-Q resonant enhancement.

5. The developed "ZenScat" UI solver delivers approximately twofold computational speed improvement within a MATLAB environment and integrates genetic optimization for rapid device parameter tuning across wavelength and angular domains. By lowering implementation barriers and providing reproducible workflows, it enables efficient design and optimization of guided-mode resonance filters, spatial filtering gratings, and distributed feedback devices in academic and applied research.

Statements of defense

1. A single layer conformal GMR filter tuned to operate near the Rayleigh anomaly can produce broadband zeroth order spectral reflection in a narrow angular range, resulting in spatial filtering.

2. The Edge of Continuum is identified at the point near the Rayleigh region where additional diffraction orders occur. Once GMR is present at EOC, it partakes of a strongly asymmetrical and non-continuous shape in its reflectance spectrum along with narrow resonance width.

3. The non-hermitian system is achieved once a metallic or absorptive material is placed on the periodic thin film waveguide, so that the unit cell's C_2 symmetry is negated, while the asymmetric coupling can lead to absorption enhancement.

4. Amplification in thin-film structure perturbs the resonant frequency of GMR, and both effects simultaneously determine strong resonant enhancement at both normal and oblique incidence for both s and p polarized light.

5. Numerical simulation and analysis of periodic structures in the frequency domain, based on the novel incorporation of S and T matrix methods and compilation in C++ language, can be computationally less expensive than commercially available options, while numerical stability in predicting gain, absorption, and angular selectivity is maintained through a well-conditioned matrix implementation.

Layout of the dissertation

The first chapter consists of the first half of literature overview of the guided mode properties of the 1D slab waveguides, nuances of diffraction gratings and Rayleigh-Woods anomaly. Then the overview shifts towards the mechanism of GMR operating regime, application of Temporal Coupled Mode Theory (TCMT) which is used for fitting. Finally, their characteristics are summarized via diffraction efficiency computations for s and p polarizations.

The second part of the literature overview analyzes Maxwell's numerical equations in frequency domain - their treatments as well as their technical nuances. The first algorithm is FDFD, which computes field distributions first, then calculates DEs later. Then comes the plane wave expansion based RCWA algorithm, which calculates DEs only, but in Fourier Domain. Incorporation of S and T matrix methods into the modal algorihm are hence explained in further sections, along with genetic algorithm, which is used in optimization problems and is combined with RCWA method.

Further sections are devoted to research results. The first section incorporates 2D FDFD and 2D RCWA algorithms and their benchmarks with commercial Lumerical variants and published ones with RCWA. Optimization prop-

erties of cons‘tructed ’ZenScat" UI for DFB systems are explored. Further subsections are devoted to comparison of computation time with commercial Fourier Modal variant (McGrating) and matrix methods. Lastly, performance of RCWA is evaluated via convergence analysis for high DFBs with high refractive index contrast.

The second section focuses on the application of trapezium GMR gratings that pertain double modulation. The Rayleigh anomaly's effects on the broadband reflectance of the structure are analyzed. Subsection is devoted to the manufacturing of such GMR device via IBS method.

Third section focuses on the GMR properties at EOC. The first part is devoted for analytical treatment of Schrodinger's equations for GMR filters at sub-wavelength regime. The second part is devoted to the numerical comparison with the analytical one for low index contrast GMR filter. The third part focuses on the fabrication of GMR filter with double modulation after etching procedure of the trapezium modulated substrate.

Similar GMR devices are further analyzed in the fourth section, but for the asymmetrical shaped ones, which enforces Parity-Time (PT) symmetry breaking. In such a case GMR device pertains asymmetrically placed absorber on top. The whole section is devoted to the comparison between analytics and numerics, then the fabrication and zeroth order DE measurements.

The fifth section is fully devoted to theoretical analysis of GMR applications for enhanced light-to-matter interactions, particularly for dispersive materials with optical gain. This section covers genetic optimization and its use to tune the GMR device parameters for enhancement of zeroth order diffraction efficiencies. Finally, analytical model is compared with the numerical results for sub-wavelength regime.

Statement of contributions

I. Lukošiūnas: full contribution is present for the analysis of literature, numerical simulations, implementation of Rigorous Coupled Wave Analysis and Finite Difference Frequency Domain algorithms in Matlab environment.

Dr. D. Gailevičius: for resources and additional help.

Prof. Dr. K. Staliūnas: The analytical formulas for physical phenomenon interpretation. Academic supervisor.

Doct. Student J. Nikitina and **Dr. L. Grinevičiūtė**: Experimental fabrication of thin film GMR filters and the measurements of their diffraction efficiencies.

Aprobation

Main Publication list

This list ensures the publications that fulfill the plan of the 4 year PhD program.

[**A1**] **I. Lukošiūnas**, L. Grinevičiūtė, J. Nikitina, D. Gailevičius, K. Staliūnas, "Extremely narrow sharply peaked resonances at the edge of the continuum", Phys. Rev. A, **107**, L061501 (2023).

[**A2**] **I. Lukošiūnas**, J. Nikitina, D. Gailevičius, L. Grinevičiūtė, K. Staliūnas, "Guided mode resonances for angular and spectral filtering", Lith. J. Phys, **63**, 4 (2023).

[**A3**] L. Grinevičiūtė, **I. Lukošiūnas**, J. Nikitina, A. Selskis, I. Meškėlaitė, D. Gailevičius, K. Staliūnas "Light Trapping by Non-Hermitian Thin Films", Phys. Rev. Applied, **23**, 054014, (2025).

[**A4**] **I. Lukošiūnas**, K. Staliūnas, "Light Amplification by Active Meta-mirrors", Phys. Rev. A **112**, 033504, (2025).

[**A5**] **I. Lukošiūnas**, D. Gailevičius, K. Staliūnas, "Reducing Complexity in Photonic Simulations: ZenScat's Efficient 2D RCWA Solver", SoftwareX, **33**, 102480 (2026).

Other Publications

This list contains extra works that are not included in the PhD plan.

[**B1**] **I. Lukošiūnas**, D. Gailevičius, and K. Staliūnas "Guided mode resonance optimization for spatial dispersion control", Proceedings SPIE 12991, Nanophotonics X, 1299117 (2024) (Proceedings).

[**B2**] D. Stonytė, V. Jukna, **I. Lukošiūnas**, P. Zakarauskas, H. Huang, T. Katkus, N. Zheng, N. Le, S. Juodkazis, D. Gailevičius and D. Paipulas, "Four-level diffractive photon sieves by deep-UV femtosecond laser ablation". Opt. Express. **32**. 43102-43117, (2024).

[**B3**] A. Zinkevičius, **I. Lukošiūnas**, D. Gailevičius, "ZenBand: a numerical solver of photonic crystals with a graphical user interface", Sci Rep **16**, 7242 (2026).

Conference presentations

Presented by the author:

- **I. Lukošiūnas**, L. Grinevičiūtė, J. Nikitina, D. Gailevičius, K. Staliūnas, "Extremely narrow sharply peaked resonances at the edge of the continuum":

  [**C1**] Open Readings/ Vilnius (Poster session: Laser Physics and Optical Technologies 2023-04-09).

  [**C2**] SPIE Optics and Optoelectronics, Prague (Oral, 2023-04-07, Number: 12568-20).

  [**C3**] International Conference of Young Scientists and Post Graduate Students IEP - 2023, Uzhgorod, Ukraine (Oral session, 2023-05-17).

  [**C4**] CLEO/Europe–EQEC 2023, Munich, Germany (Oral session, 2023-06-27, CK-3.6 17:15 Room 4a ICM).

  [**C5**] Humboldt Kolleg on Synthetic Quantum Matter/Vilnius (Poster session, 2023-07-02).

- **I. Lukošiūnas**, J. Nikitina, D. Gailevičius, L. Grinevičiūtė, K. Staliūnas, "Guided mode resonances for angular and spectral filtering":

  [**C6**] SPIE Photonics Europe: Optics and optoelectronics, France, Strasbourg 12991-113 (Poster, 2024-04-10).

- **I. Lukošiūnas**, K. Staliūnas, "Theoretical investigation of Guided Mode Resonance effect in optical gain cavities":

  [**C7**] Open Readings/ Vilnius (Oral session: Laser Physics and Optical Technologies 2025).

  [**C8**] International Conference of Young Scientists and Post Graduate Students IEP - 2025, Uzhgorod, Ukraine (Oral session, 2025).

  [**C9**] The 29th Central European Workshop on Quantum Optics CEWQO 29 (Poster, 2025)

Chapter 1

Literature Overview

1.1 Guided Mode Resonance filters and their properties

The Bragg reflection was the very first phenomenon which was observed as a consequence of light with periodic matter interaction [74], but there are more unique effects encountered at quasi-periodic materials (periodic in one, usually transverse, dimension, non-periodic in longitudinal direction). Such effects possess special properties which alter the characteristics of light in the angular spectrum, thus enforcing the control of light propagation direction. The main focus here is oriented towards guided modes, GMR filters and their characteristics.

1.1.1 Introduction to 1D guided modes

A slab wave-guide is a dielectric separated by two different media with its refractive indices lower than the slab itself. This 3D device can be represented in 1D by the intersection of materials (superstrate, slab and substrate) and its guided modes in the intersection. Its refractive index distribution provides necessary wave-guiding conditions via total internal reflection. All wave-guiding modes that are excited in the slab possess spatial oscillations, which depend on the thickness and refractive index of the slab. Each guided mode has its effective refractive index, hence its own distinction from another in spatial frequency range. The propagating electric field within the waveguide satisfies Maxwell's equations:

$$\nabla \times \vec{E} = -\mu \frac{\partial \vec{H}}{\partial t}, \tag{1.1a}$$

$$\nabla \cdot \vec{E} = 0, \tag{1.1b}$$

Here, using $\nabla \times \nabla \times \vec{E} \equiv \nabla(\nabla \cdot \vec{E}) - \nabla^2 \vec{E} = -\nabla^2 \vec{E}$, and divergence theorem, the wave propagation equation of a plane wave propagation is derived in frequency domain:

$$\nabla^2 \vec{E} + \omega^2 \mu \varepsilon \vec{E} = 0. \tag{1.2}$$

Here $1/c^2 = \mu\varepsilon$ is the propagation velocity of electric field (i.e. speed of light) and $\mu = \mu_r \mu_0$ is permeability, expressed through relative permeability μ_r and μ_0 is magnetic permeability of free space. The same concept applies to $\varepsilon = \varepsilon_r \varepsilon_0$, where ε_r is relative permittivity and ε_0 is permittivity of free space.

If $\varepsilon_r \neq 1$ and $\mu_r \neq 1$, the product $\omega/c = \omega/c_0 \cdot n \equiv k_0 n$, where $k_0 = \frac{2\pi}{\lambda_0}$ is a wavenumber or wavevector magnitude and n is refractive index, whose value is $\sqrt{\varepsilon_r \mu_r}$. It defines the ratio of the phase velocity between speed of light and the propagating wave in the bulk medium. The model for guide mode propagation in the slab waveguide can be written via Helmholtz equation for the propagating monochromatic wave in the xz plane:

$$\frac{\partial^2 E(z,x)}{\partial z^2} + \frac{\partial^2 E(z,x)}{\partial x^2} + k_0^2 n^2(x) E(z,x) = 0, \tag{1.3}$$

Using the electric field expression $E(z,x) = A(x)\exp(j\beta z - j\omega t)$,

$$\frac{d^2 A(x)}{dx^2} + \left[k_0^2 n^2(x) - \beta^2\right] A(x) = 0. \tag{1.4}$$

Here β is a propagation constant of the wave inside the slab waveguide and $n(x)$ is the refractive index distribution of the waveguide's intersection. The β^2 parameter is the eigenvalue of Eq. (1.4) and defines propagation of the waveguide mode in z direction. Usually, dispersion equation holds $k_x^2 + \beta^2 = k_0^2 n_i^2$ and $k_x = \pm\sqrt{k_0^2 n_i^2 - \beta^2}$, where k_x is transverse wavevector and n_i is refractive index of the homogeneous media outside of the waveguide's core, where there is no variation of geometry. Equation (1.4) has solutions for the propagating modes confined within the waveguide's core:

$$A = \begin{cases} A_{\text{sup}} e^{-\gamma_{\text{sup}}(x-a)} e^{-j\beta z}, & x \geq a, \\ \left[A_{c1} e^{-jk_{c,x}x} + A_{c2} e^{+jk_{c,x}x}\right] e^{-j\beta z}, & 0 \leq x \leq a, \\ A_{\text{sub}} e^{\gamma_{\text{sub}} x} e^{-j\beta z}, & x \leq 0. \end{cases} \tag{1.5}$$

Where parameters in front of the exponents denote amplitudes given superstrate region 'sup', waveguide core 'c' and substrate as 'sub'. The γ_i parameter is used as $\gamma_i = \pm j\sqrt{\beta^2 - k_0^2 n_i^2}$, where index i stands for substrate or superstrate and $j = \sqrt{-1}$ [75].

The fundamental waveguide mode has effective refractive index n_{eff} closest to the refractive index value of the slab's core. The parameter n_{eff} is the ratio of the speed of light in vacuum with the phase velocity of the certain mode. Waveguide modes with higher orders contain lower n_{eff} until they become leaky. This effect is observed for all types (low, high contrast) of 2D and 3D periodic waveguide filters.

For better explanation of the concept of slab waveguides, Fig. 1.1 a) illustrates the cross-section of 1D confinement of slab waveguided modes, where 1D FDFD was used to compute field distributions and effective refractive indexes. The 1D FDFD based method for computing slab modes is presented in appendix.. The lowest order mode will always contain the highest effective refractive index, i.e., the ratio of phase velocity of the guided mode with the phase velocity of light in vacuum. The higher the order of the mode, the lower the effective refractive index, which increases phase velocity of the guided mode. The effective refractive index is a qualitative factor which also specifies

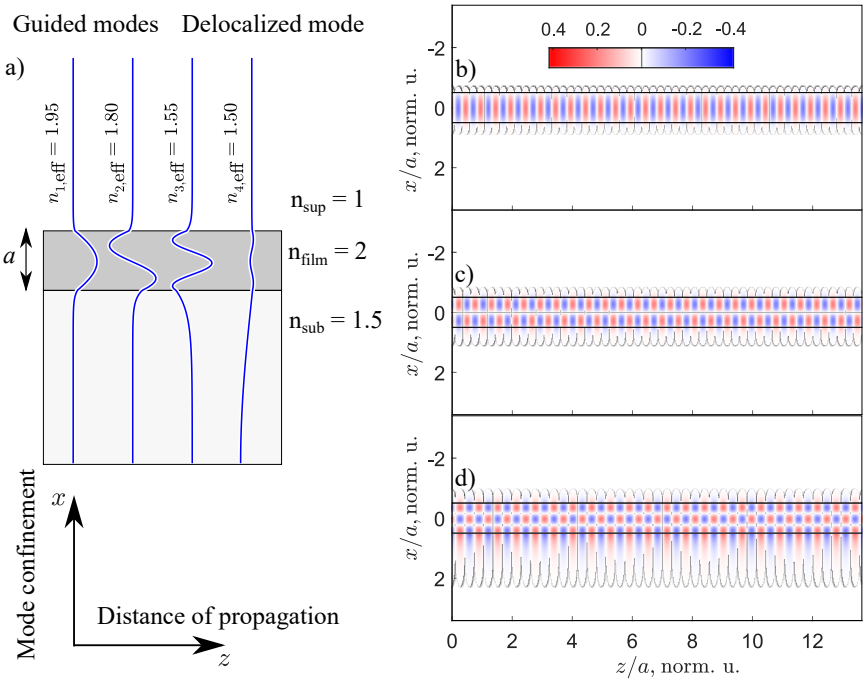


Figure 1.1: Representation of guided slab waveguide modes in 1D confinement. The modes are presented in (a) and their guided parts in (b-d) for TE polarization (H mode). The wavelength is $\lambda_0 = 0.97\mu$m and slab width $a = 1$ μm.

the localization of the mode in the waveguide structure. For instance, fourth order mode is a delocalized mode, which is a solution of Maxwell's eigen-value equation, however, it remains to have the most of its power almost fully localized in the substrate, thus prompting its property $n_{\mathrm{eff}} \to n_{\mathrm{sub}}$. This is true for waveguides that pertain no imaginary refractive index, otherwise the guided modes will correspond to $n_{\mathrm{eff}} = \mathrm{Re}(n_{\mathrm{eff}}) - j\mathrm{Im}(n_{\mathrm{eff}})$, where real part is the phase velocity ratio between the guided mode and speed of light c, and imaginary part corresponds to the exponential absorption loss or exponential gain factor, which depends on what material is used and intersection between it and the amplitude of the guided mode.

1.1.2 Rayleigh anomaly

This phenomenon is observed by Rayleigh and Woods separately, thus the abbreviation. It pinpoints to the strong intensity variations [76] at the oblique angles of incidence upon the diffraction grating. The concept of Rayleigh anomaly is visualized at Fig. 1.2, where the electromagnetic wave is incident upon the grating at the oblique angle. In turn, Rayleigh anomaly refers to the wave fully propagating along the surface of the grating - in this case, the

propagating wave is first diffraction order and is perpendicular to propagation direction y, fully longitudinal to the transverse direction x.

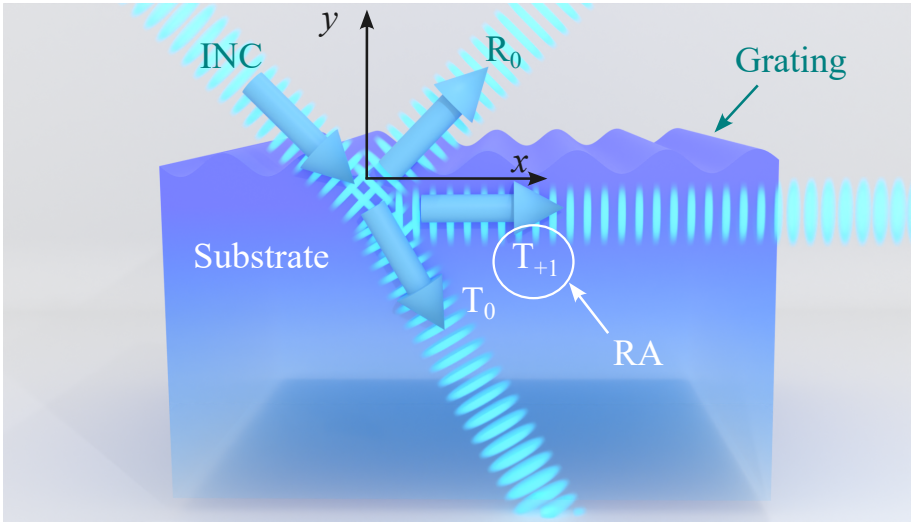


Figure 1.2: The schematic of the Rayleigh anomaly (RA) concept - incident wave (INC) is at an oblique angle, which is then reflected and transmitted via the grating and Rayleigh anomaly corresponds to the longitudinally propagating wave along the surface of the grating. In this case, it is T_{+1} diffraction order.

The essence is that once light is at the oblique angle at the grating, there are sharp features of intensity and diffraction efficiency variations due to the sudden occurrence of new diffraction/reflection orders. This effect also occurs at normal incidence as well. It always starts from the same reference point in spectrum, which entirely depends on the transverse periodicity Λ_x, angle of incidence θ, refractive index of a substrate n_{sub} and superstrate's refractive index n_{inc}. The wavelength dependence on θ can be evaluated through the dispersion relation, given $(k_0 n_j)^2 = k_{x,m}^2 + k_z^2$. Here j is an index which refers to substrate or superstrate refractive indexes. The wavevector k_z then becomes:

$$k_z = \sqrt{(k_0 n_j)^2 - k_{x,m}^2} \tag{1.6}$$

where $k_{x,m} = k_0 n_{\text{sup}} \sin\theta - 2\pi m/\Lambda_x$ and m is diffraction order. It follows that during surface propagating waves $k_z = 0$ and in this case wavelengths at these regions $\lambda_{R,m}$ can be found:

$$\lambda_{R,m} = \frac{\Lambda_x}{m}(n_j \pm n_{\text{sup}} \sin\theta). \tag{1.7}$$

Here n_j is n_{sub} if analysis is performed for forward diffraction and n_j is n_{sup} if analysis is performed for backward diffraction (reflection). The order m denotes

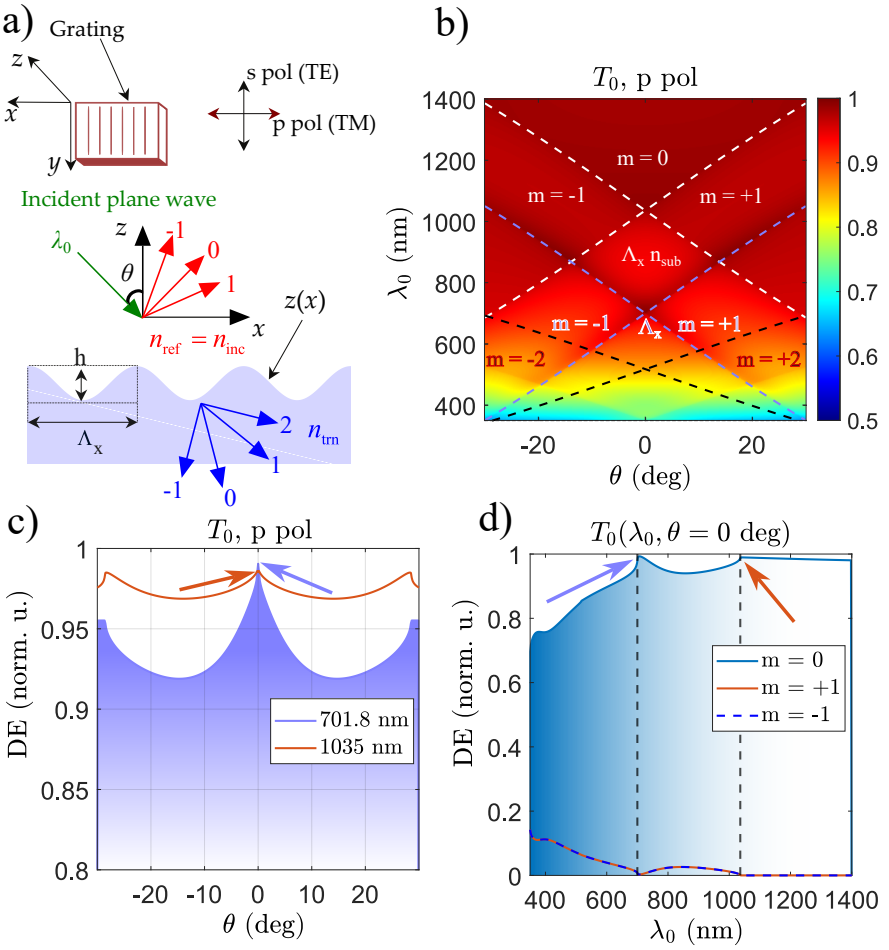


Figure 1.3: Visualization of Rayleigh anomaly given the harmonic grating (a), transmission spectrum for p polarization at (b), angular dependence (c) and transmission dependency at normal incidence (d). The grating parameters are: $n_{\text{sup}} = 1, n_{\text{sub}} = 1.48$, $h = 0.2$ μm, $\Lambda_x = 0.7$ μm. Simulations are performed with 2D RCWA. Light-purple arrows indicate λ_R for which $R_{\pm 1}$ orders appear/disappear, orange arrows indicate sudden diffraction order $T_{\pm 1}$ appearance/disappearance in (c) and (d).

which regime is taken into account. Order $m = 1$ counts as sub-wavelength regime, whereas $|m| > 1$ is dubbed as sup-wavelength regime. Once λ_R wavelength is reached, a new diffraction order is instantly added into the output ports (substrate or superstrate) of the grating. Thus it is observed in diffraction efficiency spectral characteristics as sharp/discontinuous feature for any function of modulation of the gratings. Simulations of a diffraction grating are presented in Fig. 1.3 in order to illustrate the phenomenon. The grating of

interest is harmonic grating. Its interface function $z(x) = h/2 \cdot \sin(2\pi x/\Lambda_x)$ with available diffraction orders and field polarization orientations (see Fig. 1.3 a)). The s polarization here is considered as electric field oscillating longitudinally along the grooves of the grating, whereas p polarization is the one whose electric field oscillates in transverse x direction. The zeroth order transmission spectrum of that grating pertains regions of varying transmittance values with respect to λ_0 and θ. The lines (regions) where the discontinuities are encountered are plotted with Eq. (1.7). White dotted lines separate regions between possible diffraction efficiencies, which are 0 and ± 1. The blue regions separate reflection orders between 0 and ± 1, whereas black ones indicate regions where ± 2 diffraction orders occur. The sharp features at the angular (see Fig. 1.3 c) and spectral (see Fig. 1.3 d) responses indicate Rayleigh wavelengths at normal incidence given the dashed lines in the graph. The first line at $\lambda_R = \Lambda_x n_{\text{sub}} = 1029$ nm indicates the separation between the sup-wavelength and sub-wavelength regimes, where sup-wavelength regime is given by $\lambda_0 < \Lambda_x n_{\text{sub}}$ for normal incidence. Similar characteristics are also observed in gratings via use of Fourier Optics' analytical tools [77].

1.1.3 Guided Mode Resonance

All of the discussed effects are attributes to the Guided Mode Resonance effect. The properties stem from the ability to couple incident light with reflected/diffracted orders via a guided mode.

A guided mode resonance (GMR), is an effect which is encountered when an incident light is coupled with a radiative mode via coupling, which is introduced by a guided mode in a periodically modulated layer [78]. The whole system is thus realized by a corrugated surface. The term 'guided mode' refers to a mode guided along the periodically modulated surface and in this context resonance occurs for specific wavelengths. The outcome is reflection (i.e. backward scattering), which is in possession of both angular and spectral sensitivity, prompting such devices as filters [79]. With this concept in mind, a device can be simulated to control backward scattering by introducing an extra geometrical variability in a slab wave-guide, or an extra degree of freedom.

In order to evaluate angular dispersion (i.e., sensitivity) of a GMR, one would use grating Eq.(1.8), which provides the condition for possibly achieving the resonance once the condition for diffraction is satisfied

$$n_{\text{sup}} \sin \theta_m = n_{\text{sup}} \sin \theta - \frac{m\lambda_0}{\Lambda_x}. \tag{1.8}$$

Where n_{sup} is the refractive index of a top layer (superstrate, reflection region), θ_m is the deterministically predictable angle of diffraction order, which is of the order m, θ is the angle of incidence, Λ_x is a transverse period of a periodically modulated layer. The Eq. (1.8) specifies phase matching conditions of an incident plane wave and a diffracted one, i.e., the "Snell's law" of a diffraction grating. From that the derivation is achieved for the angular sensitivity of a

GMR in Eq. (1.9) (considering $\theta_m = 0$ deg and $\sin\theta \approx \theta$):

$$\frac{\Delta\lambda_0}{\Delta\theta} = \frac{\Lambda_x n_{\text{sup}}}{m}. \tag{1.9}$$

Deviation from normal incidence shifts the resonance in spectral domain, thus altering its background response, which is quite useful for failed designs because it compensates the desired reflection in oblique incidence. For instance, given $\Lambda_x = 625$ nm of periodicity, for $n_{\text{sup}} = 1$, the wavelength shift can be expected for $\Delta\lambda_0 = 625/m$ nm/rad or $\Delta\lambda_0 = 10.9/m$ nm/deg. The main properties of GMR can be illustrated via the use of the inequality (1.10), which suggests that resonances as well as their orders are bound by the effective refractive index of a modulated waveguide part. The inequality is presented in the following:

$$\max[n_{\text{sup}}, n_{\text{sub}}] \leq \underbrace{|n_{\text{sup}} \sin\theta - \frac{m\lambda_0}{\Lambda_x}|}_{n_{eff}} \leq n_g. \tag{1.10}$$

Where $n_g \approx (\sqrt{(\varepsilon_1 + \varepsilon_2)/2})$. Such an inequality in Eq.(1.10) contains n_{eff} as the effective refractive index of a guided mode inside the modulated layer, whose spectral behavior better visualized in Fig.1.4 b) for orders $m = [-3, -2, -1, 1, 2, 3]$.

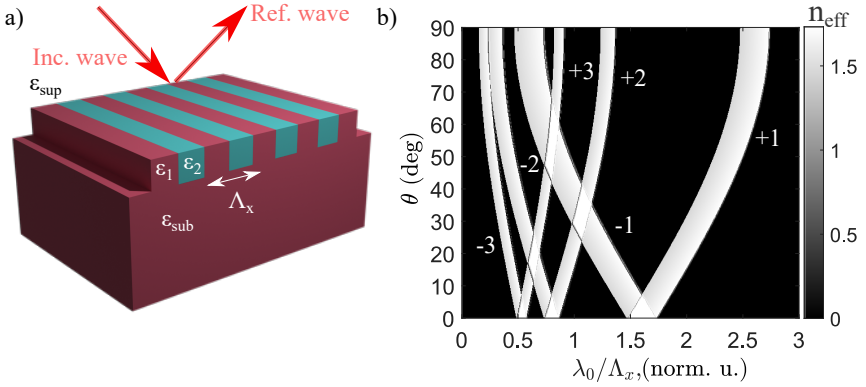


Figure 1.4: The Schematic of GMR and its location in wavelength/angular domain, adapted from [79] in a) and GMR distribution in a harmonic interfaced thin-film waveguide b).

The refractive index $n_{sup} = 1$ and substrate's part is $n_{sub} = 1.5$ and $n_g = 2$. That means that only those guided modes that couple incident light with zeroth order reflection can exist for those effective refractive indexes in the color-bar which satisfy the inequality (1.10). Higher order modes correspond to lower wavelengths, and, compared with lower order modes, pertain lesser angular sensitivity and GMR enables enhanced coupling between incident and reflected

electromagnetic waves. At normal incidence, resonances face a superposition, thus providing a degeneracy to such states. Resonances with order $m = \pm 1$ have a broader intersection at normal incidence and greater angular sensitivity. All in all inequality (1.10) analytical part is satisfactory enough for explaining physical effects qualitatively, but not quantitatively. For instance, diffraction efficiency values cannot be fully predicted for GMR instances from the inequality (1.10). That is why numerical algorithms are needed for such predictions as well as to analyze the field distributions inside such devices in order to quantitatively analyze and categorize these guided modes.

It is noteworthy that numerical solutions to Maxwell's equations scale as long as the geometrical parameters are scaled to the wavelength of incident monochromatic source. This effect is purely universal which means GMRs can be excited for arbitrary wavelengths at a certain angle of incidence as long as the device's geometrical parameters are scaled proportionately to the wavelength of incident light source at material's refractive indexes are not changed, i.e., the material in that spectral range is without optical dispersion.

1.1.4 Temporal Coupled Mode Theory

One crucial method to assess resonance shapes and predictions of their characteristics is via the use of Temporal Coupled Mode Theory (TCMT), whose schematic of port coupling with resonator is present (see Fig. 1.5). The resonator coupled with ports represents a closed cavity system with modes of the amplitude that satisfy the following equation:

$$\frac{\mathrm{d}}{\mathrm{d}t}a = j\Omega a, \tag{1.11a}$$

$$a = \begin{pmatrix} a_1 \\ a_2 \\ \vdots \\ a_n \end{pmatrix}. \tag{1.11b}$$

In Eq. (1.11), the complex mode amplitudes $a = [a_1, a_2, ..., a_n]$ are characterized with frequency matrix Ω that belong to the resonant system and Eq. (1.11a) represents the time evolution of the modes inside the cavity.

Considering a 2 port system, where the resonator couples the incident signal with output signals, via characteristic decay times τ_i. The port-resonator system's coupled equations in time domain are written as [80–82].

$$\frac{d}{dt}a = (j\Omega - \Gamma)a + \kappa^T s^{(+)}, \tag{1.12}$$

$$s^{(-)} = Cs^{(+)} + \kappa a. \tag{1.13}$$

The quantity a represents resonance amplitudes, Ω is the frequency matrix for each resonance, Γ is the decay rate matrix, κ is the coupling matrix, vector

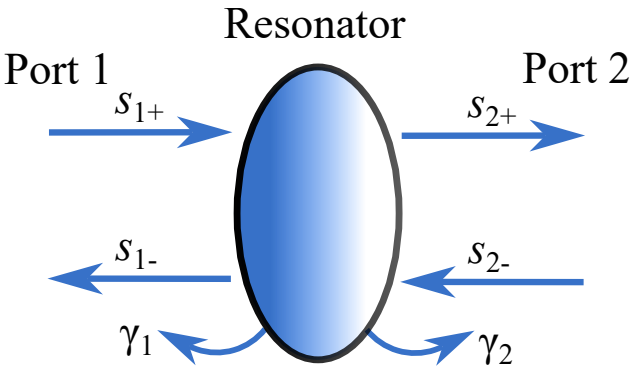


Figure 1.5: TCMT's concept of a resonator with 2 ports with decay coefficients γ_1 and γ_2.

$s^{(+)}$ represents incident waves via input ports, whereas the outgoing waves via the output ports are represented via $s^{(-)}$. Matrix C can be thought of a direct transmission matrix. Such equations are solved for mode vector a in a steady state ($\exp(j\omega t)$ dependence):

$$a = (j(\omega I - \Omega) + \Gamma)^{-1}\kappa^T s^{(+)}. \tag{1.14}$$

Where I is unity matrix. The connection between outgoing and incoming waves can be written in terms of the system's Scattering matrix (S-matrix):

$$s^{(-)} = S(\omega)s^{(+)}, \tag{1.15}$$

Where the scattering matrix is $S(\omega)$. It can be easily found

$$S(\omega) = C + \kappa(j(\omega I - \Omega) + \Gamma)^{-1}\kappa^T. \tag{1.16}$$

Exploring two resonant modes, the matrix forms are

$$\Omega = \begin{pmatrix} \omega_1 & 0 \\ 0 & \omega_2 \end{pmatrix}, \tag{1.17a}$$

$$\Gamma = \begin{pmatrix} \gamma_1 & \gamma_0 \\ \gamma_0^* & \gamma_2 \end{pmatrix}, \tag{1.17b}$$

$$C = \begin{pmatrix} r_d & t_d \\ t_d & r_d \end{pmatrix}, \tag{1.17c}$$

$$\kappa = \begin{pmatrix} \sqrt{\gamma_1}\eta_1 & \sqrt{\gamma_2}\eta_2 \\ p_1\sqrt{\gamma_1}\eta_2 & p_2\sqrt{\gamma_2}\eta_2 \end{pmatrix}. \tag{1.17d}$$

Where $\eta_{1,2}^2 = -(r_d \pm t_d)$ and $p_{1,2} = \pm 1$ denote parity-time operation and $\gamma_i = \frac{2}{\tau_i}$ is normalized relaxation time, given two mode resonance index i = (1,2). The matrix κ is achieved via energy conservation $\kappa^+\kappa = 2\Gamma$ and time reversed

excitation $C\kappa^* = -\kappa$. The end result is $r_d^2 + t_d^2 = 1$ for such a conservative system.

When analyzing two orthogonal resonant modes ($\Omega\Gamma = \Gamma\Omega$), the transmission coefficient is simplified (from off-diagonal elements of $S_{12,21}(\omega)$ and reflectance coefficient from $S_{11,22}$:

$$t(\omega) = t_d \mp \frac{\gamma_1(r_d \pm t_d)}{j\Delta\omega_1 + \gamma_1} \pm \frac{\gamma_2(r_d \mp t_d)}{j\Delta\omega_2 + \gamma_2}, \tag{1.18a}$$

$$r(\omega) = r_d - \frac{\gamma_1(r_d \pm t_d)}{j\Delta\omega_1 + \gamma_1} - \frac{\gamma_2(r_d \mp t_d)}{j\Delta\omega_2 + \gamma_2}. \tag{1.18b}$$

Here $\Delta\omega_i = \omega - \omega_i$, where $i = (1, 2)$ marks the resonance frequencies, and t_d with r_d are direct transmission and reflection coefficients, respectively. The top sign is used when the first mode is even, and the bottom signs are used when the first mode is odd. Such an equation corresponds to the orthogonal modes ($\Omega\Gamma = \Gamma\Omega$) and possess the unique property, which means that if resonant frequencies are further apart from one another, the resonant shape is not altered. In addition, the non-orthogonal modes ($\Omega\Gamma \neq \Gamma\Omega$) posses the transmission and reflectance forms of:

$$t(\omega) = t_d \mp \frac{(r_d \pm t_d)[j\gamma_1\Delta\omega_2 + j\gamma_2\Delta\omega_1]}{(j\Delta\omega_1 + \gamma_1)(j\Delta\omega_2 + \gamma_2) - \gamma_1\gamma_2}, \tag{1.19a}$$

$$r(\omega) = r_d - \frac{(r_d \pm t_d)[j\gamma_1\Delta\omega_2 + j\gamma_2\Delta\omega_1]}{(j\Delta\omega_1 + \gamma_1)(j\Delta\omega_2 + \gamma_2) - \gamma_1\gamma_2}. \tag{1.19b}$$

Where the top signs are used when both modes are even, and the bottom signs are used when both modes are odd. In this case, the denominator is in possession of $\gamma_1\gamma_2$ term, which, no matter the displacement of resonances, affect the overall transmittance shape. The coupling parameters are fitted with optimization algorithm with respect of the data to get the full and correct match. In such a way, the model results can be understood via the applied analytics of the port formalism. A thin layer GMR filter is possession of asymmetrical resonances whose spectral responses (DEs) can be fitted with the TCMT formalism for extraction of the resonator's parameters, mainly $\gamma_{1,2}$, $\omega_{1,2}$ and t_d. The example of fitted resonances is presented in Fig. 1.6 for a doubly modulated thin film without a substrate and with a FS substrate.

It seems that only one curve exists in all cases, however, a single resonance only represents a Lorentzian peak if one of the coupling coefficients γ is zero. Therefore, one curve acquires at least two resonant modes for a qualitative analysis. The fitting parameters for the two modes are presented in Table 1.1 from fitted DEs that are illustrated in Fig. 1.6.

The geometrical parameters of the GMR gratings are presented in the following: modulation depth $h = 0.1$ μm, $n_f = 1.99$ (HfO_2), $n_{\text{sub}} = 1.47$ (SiO_2), $\Lambda_x = 0.6$ μm and thickness $L = 0.3$ μm.

An important matter to consider, that the **bolded frequency** is at sup-wavelength regime, which is the place where other output ports that correspond to diffraction exist. In that case the predictions are not trustworthy and the

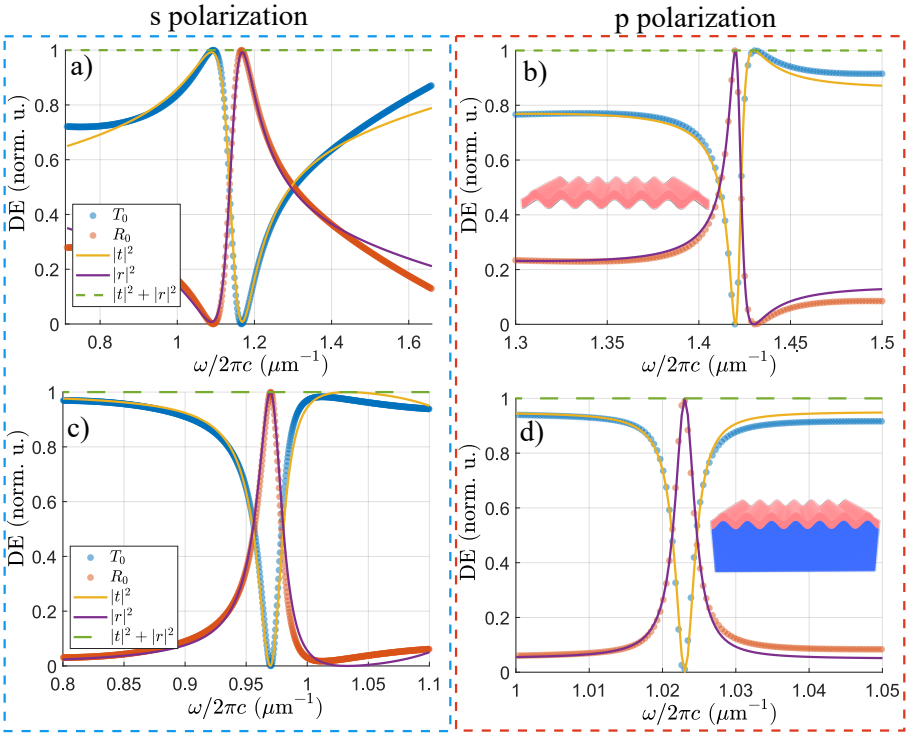


Figure 1.6: Curve fitting representation of the GMRs for a single symmetrical harmonic layer in the air (a,b) and a filter with FS substrate (c,d).

Table 1.1: The fitting parameters of applied TCMT of Fig 1.6.

Case	mode	symmetry	t_d	γ_1	γ_2	ω_1	ω_2
a)	non-ortho	odd	1.0	0.705	0.0568	0	1.1707
b)	ortho	even	1.0	0.6564	0.0038	0.0100	1.4217
c)	ortho	odd	1.0	0.0152	0.0532	0.971	1.2
d)	non-ortho	even	0.975	0.0016	0.01	1.02304	**2**

theory of 2 modes becomes non-usable. Therefore, the extension of output ports must be implemented in order to fully predict the system, however, the equation system becomes too clunky and full of additional fitting parameters, which hinders the simplicity of the formalism.

It is noteworthy that in the non-orthogonal case the denominator has a factor of $\gamma_1\gamma_2$. Therefore, the asymmetry of the resonance's shape is heavily influenced by this factor even if the spectral distance between the peaks is wide enough for them not to overlap.

1.1.5 Resonance quality and Purcell effect

The resonance quality factor Q is considered as a dimensionless quantity and depicts energy storage in the resonant mode. The resonant mode in the cavity radiates energy whose loss is proportional to $1/Q$ and $Q = \lambda_p/\Delta\lambda$, where λ_p and $\Delta\lambda$ are peak wavelength and spectral FWHM, respectively. High quality factor resonances tend to reside in the cavity for a long time compared to emission losses until the power in the cavity is lost and is exchanged to the output port [7].

Furthermore, the mode has an effective volume, or a confinement factor V_{eff} in the resonant cavity, which plays a pivotal role in coupling mechanisms between the cavity and output ports.

Furthermore, resonance quality and mode volume of the resonant cavity, depending on their values, tend to enhance or suppress emission properties once the resonant cavity. This type of interaction is known as Purcell effect and its interaction strength quantity is represented by the Purcell parameter, which is defined as $F_p = \tau_{\text{cav}}/\tau_{fs}$, which is a ratio between the spontaneous emission rates of the resonant cavity τ_{cav} and free space emission τ_{fs}. Purcell parameter is presented in the following [83] for 3D resonators:

$$F_{\text{P}} = \frac{3}{4\pi^2}\left(\frac{\lambda_p}{n_{eff}}\right)^3 \frac{Q^3}{V_{eff}}. \tag{1.20}$$

Where V_{eff} is the effective mode volume, λ_p is the peak wavelength of the resonance and n_{eff} is effective mode index of the waveguide for the "ideal" emitter. The ideal emitter is defined as spectrally matched fluorescence peak wavelength with cavity mode and the cavity mode has its maximum electric (or magnetic) field located in the resonant cavity [83]. The Purcell parameter can also be shown in the following equation for 1D resonant FP cavities [84]:

$$F_{\text{P}} = \frac{1}{\pi}\frac{\lambda_p}{n_{eff}}\frac{Q}{L}. \tag{1.21}$$

Here L is the resonator's cavity's length or thickness value. Another observed quantity is the resonance cavity mode's frequency shift which is influenced by the external driving, which is incident electromagnetic field applied onto the resonant cavity, which might alter the resonance quality factor [84].

1.1.6 Polarization in spherical coordinates

The incident source on the device of interest is generalized in 3D case as a "conical mount". Its analytical formalism is observed in many finite difference and Fourier based algorithms. The physical basis of polarization vector remains the same: it is the direction of electric field vector's oscillation. More importantly, it is the mathematical definition of polarization vectors which is applicable to all 3D numerical models that solve Maxwell's equations for linear media [49, 50, 85]. Here the universal one is presented in spherical coordinate system. It is illustrated in Fig. 1.7.

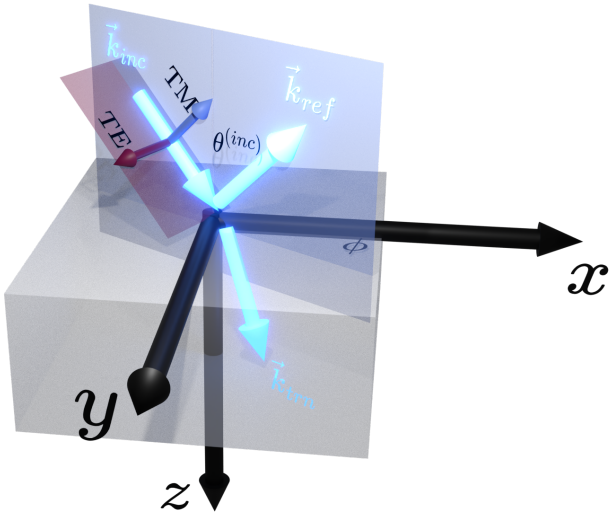


Figure 1.7: Polarization components in spherical coordinate system.

The polarization vector is defined by the plane of incidence. Its orientation along the normal axis $\vec{n_z}$ is defined by the azimuthal angle ϕ. The plane of incidence is where the incident wavevector $\vec{k}_{inc}$ is located, alongside with the transmitted wavevector $\vec{k}_{trn}$ and reflected wave's wavevector $\vec{k}_{ref}$. The main focus here is fixed towards the $\vec{k}_{inc}$, whose components are defined in the following:

$$k_{x,inc} = k_0 \sin\theta \cos\phi, \tag{1.22a}$$
$$k_{y,inc} = k_0 \sin\theta \sin\phi, \tag{1.22b}$$
$$k_{z,inc} = k_0 \cos\theta. \tag{1.22c}$$

Where $\theta = \theta^{(inc)}$ is the angle of incidence. The wavevector magnitude $k_0 = \frac{2\pi}{\lambda_0}$ defines a constant phase accumulation of a plane-wave in vacuum, and λ_0 is the wavelength, i.e., single spatial oscillation distance of a plane wave. The second most important aspect is the polarization of a wave and its 3D representation. Its most consistent formalism is presented in the following: by using the normal vector $\vec{n}_z = (0, 0, 1)$, Transverse Electric (TE) polarization is the unit vector $\vec{a}_{\mathrm{TE}}$, which is a product between $\vec{k}_{inc}$ and $\vec{n}_z$. Transverse Magnetic (TM) polarization vector is a unit vector $\vec{a}_{\mathrm{TM}}$, which is a product between $\vec{k}_{inc}$ and $\vec{a}_{\mathrm{TE}}$ vectors. This process is illustrated in the following:

$$\vec{a}_{\mathrm{TE}} = \frac{\vec{n}_z \times \vec{k}_{inc}}{|\vec{n}_z \times \vec{k}_{inc}|}, \tag{1.23a}$$
$$\vec{a}_{\mathrm{TM}} = \frac{\vec{k}_{inc} \times \vec{a}_{\mathrm{TE}}}{|\vec{k}_{inc} \times \vec{a}_{\mathrm{TE}}|}. \tag{1.23b}$$

The denominator in Eq. (1.23) is the normalization factor. Hence the full polarization vector is defined via a basis of unit polarization vectors $\vec{a}_{\mathrm{TE}}$ and $\vec{a}_{\mathrm{TM}}$ in the following:

$$\vec{P} = p_{\mathrm{TE}} \cdot \vec{a}_{\mathrm{TE}} + p_{\mathrm{TM}} \cdot \vec{a}_{\mathrm{TM}}. \tag{1.24}$$

Here p_{TE} and p_{TM} are power coefficient terms of TE and TM polarization vectors, respectively. They are chosen in such manner so that the magnitude of polarization vector $\vec{P}$ is 1, i.e. $|\vec{P}| = 1$. At an angle $\phi = 0$ deg and at the normal incidence ($\theta = 0$ deg) polarization vector is $\vec{P}$ = (0,1,0) for $p_{\mathrm{TE}} = 1$ and $p_{\mathrm{TM}} = 0$. This hints that main electric field is oscillating along the y direction and only pertains E_y component. For the same angles and for the values of $p_{\mathrm{TE}} = 0$ and $p_{\mathrm{TM}} = 1$, polarization vector is $\vec{P} = (\frac{1}{\sqrt{2}}, 0, \frac{1}{\sqrt{2}})$, thus specifying that E_x and E_z components oscillate along the xz plane. Such formalism is directly applied for 2D RCWA algorithm for the polarizations: TE polarization (s polarization) has components E_y,H_x,H_z whereas TM polarization (p polarization) has the components E_x and E_z of the electric fields and H_y for magnetic field [49].

1.1.7 Diffraction efficiencies

Diffraction efficiencies are defined as fractions of power that diffracted or reflected orders pertain. In literature, it is mainly abbreviated as DE or η and is either measured in normalized units (between 0 and 1), as percentage (i.e., between 0% and 100%) or in decibels (as $10 \lg$ DE, dB) [49, 85, 86]. Diffraction efficiencies are calculated by mainly incorporating material values of transmission and reflection regions, mainly through impedance, and through reflection and transmission wavevectors $\vec{k}_{ref}$ and $\vec{k}_{trn}$. In order to find the efficiencies for reflection and transmission orders, one has to analyze the power flow via Pointing vector's $\vec{\Pi}$ z components. Thus diffraction efficiencies can be defined:

$$R_{\mathrm{DE},m} = \frac{\Pi_{z,m}^{(\mathrm{ref})}}{\Pi_z^{(\mathrm{inc})}} = \frac{1}{2}\,\mathrm{Re}\left[\frac{|\vec{E}_{0,m}^{(\mathrm{ref})}|^2}{\eta_{\mathrm{ref}}}\frac{k_{z,m}^{(\mathrm{ref})}}{|\vec{k}_{\mathrm{ref}}|}\right] \Big/ \frac{1}{2}\,\mathrm{Re}\left[\frac{|\vec{E}_0^{(\mathrm{inc})}|^2}{\eta_{\mathrm{inc}}}\frac{k_z^{(\mathrm{inc})}}{|\vec{k}_{\mathrm{inc}}|}\right], \tag{1.25a}$$

$$T_{\mathrm{DE},m} = \frac{\Pi_{z,m}^{(\mathrm{trn})}}{\Pi_z^{(\mathrm{inc})}} = \frac{1}{2}\,\mathrm{Re}\left[\frac{|\vec{E}_{0,m}^{(\mathrm{trn})}|^2}{\eta_{\mathrm{trn}}}\frac{k_{z,m}^{(\mathrm{trn})}}{|\vec{k}_{\mathrm{trn}}|}\right] \Big/ \frac{1}{2}\,\mathrm{Re}\left[\frac{|\vec{E}_0^{(\mathrm{inc})}|^2}{\eta_{\mathrm{inc}}}\frac{k_z^{(\mathrm{inc})}}{|\vec{k}_{\mathrm{inc}}|}\right]. \tag{1.25b}$$

Here $\vec{H} = \vec{E}/\eta_i$ for homogeneous and infinite regions, and η_i is the impedance of the given region, where $i \to$ ref for reflection region, or superstrate, and $i \to$ trn for transmission region, or substrate, or $i \to$ inc for incidence region. The transmission and reflection regions are considered as infinitely extruded. In the case of simulating DEs for GMR filters, incidence region is reflectance region. The dispersion relation of wavevectors in the reflection and transmission regions are:

$$k_{z,m}^{(\mathrm{ref})} = -\sqrt{(k_0 n_{\mathrm{ref}})^2 - k_{x,m}^2}, \tag{1.26a}$$

$$k_{z,m}^{(\mathrm{trn})} = +\sqrt{(k_0 n_{\mathrm{trn}})^2 - k_{x,m}^2}. \tag{1.26b}$$

Since $|\vec{k}_{\mathrm{inc}}| = |\vec{k}_{\mathrm{ref}}| = k_0 n_{\mathrm{ref}}$, $|\vec{k}_{\mathrm{trn}}| = k_0 n_{\mathrm{trn}}$, $\eta_{\mathrm{ref}} = \sqrt{\frac{\mu_0 \mu_{\mathrm{ref}}}{\varepsilon_0 \varepsilon_{\mathrm{ref}}}}$, $\eta_{\mathrm{ref}} = \sqrt{\frac{\mu_0 \mu_{\mathrm{trn}}}{\varepsilon_0 \varepsilon_{\mathrm{trn}}}}$, $n_{\mathrm{ref}} = \sqrt{\mu_{\mathrm{ref}} \varepsilon_{\mathrm{ref}}}$, $n_{\mathrm{trn}} = \sqrt{\mu_{\mathrm{trn}} \varepsilon_{\mathrm{trn}}}$, the equations reduce following for the DEs without absorption:

$$R_{\mathrm{DE},m} = \mathrm{Re}\left[-\frac{k_{z,m}^{(\mathrm{ref})}}{k_z^{(\mathrm{inc})}}\right] \frac{|\vec{E}_{0,m}^{(\mathrm{ref})}|^2}{|\vec{E}_0^{(\mathrm{inc})}|^2}, \tag{1.27a}$$

$$T_{\mathrm{DE},m} = \mathrm{Re}\left[\frac{\mu_{r,\mathrm{ref}}}{\mu_{r,\mathrm{trn}}} \frac{k_{z,m}^{(\mathrm{trn})}}{k_z^{(\mathrm{inc})}}\right] \frac{|\vec{E}_{0,m}^{(\mathrm{trn})}|^2}{|\vec{E}_0^{(\mathrm{inc})}|^2}. \tag{1.27b}$$

The set of Eqs.(1.27) here contain electric fields, which are solved for electric field, hence the abbreviation as 'E mode' in computational electromagnetics. And the simplified DE calculation from magnetic field strengths is presented in the following:

$$R_{\mathrm{DE}}(m) = \mathrm{Re}\left[-\frac{k_{z,m}^{(\mathrm{ref})}}{k_{z,\mathrm{inc}}}\right] \frac{|\vec{H}_{0,m}^{(\mathrm{ref})}|^2}{|\vec{H}_{0,\mathrm{inc}}|^2}, \tag{1.28a}$$

$$T_{\mathrm{DE}}(m) = \mathrm{Re}\left[\frac{\varepsilon_{r,\mathrm{ref}}}{\varepsilon_{r,\mathrm{trn}}} \frac{k_{z,m}^{(\mathrm{trn})}}{k_z^{(\mathrm{inc})}}\right] \frac{|\vec{H}_{0,m}^{(\mathrm{trn})}|^2}{|\vec{H}_0^{(\mathrm{inc})}|^2}. \tag{1.28b}$$

Here, the diffraction efficiencies in Eq.(1.28) are calculated for the 'H mode'. In 2D RCWA, both Eq.(1.27) and Eq.(1.28) are used for TE and TM polarizations, respectively where wave propagation occurs in xz plane. If xy plane is considered, then y coordinate is the coordinate of propagation, which is generally applied for Finite Difference methods.

The fields for E mode $\vec{E}_{0,m}^{(\mathrm{trn})}$, $\vec{E}_{0,m}^{(\mathrm{ref})}$ and $\vec{E}_0^{(\mathrm{inc})}$ are captured within the grid and are transmitted (total), reflected (scattered) and incident electric field strengths, respectively. Magnetic field strengths $\vec{H}_{0,m}^{(\mathrm{trn})}$, $\vec{H}_{0,m}^{(\mathrm{ref})}$ and $\vec{H}_0^{(\mathrm{inc})}$ are captured within the grid in the same manner as electric fields, but for the H mode. The real part in DE computation neglects evanescent diffraction orders that do not propagate to infinity.

1.1.8 Manufacturing of thin film GMRFs via IBS method

One of the methods known for manufacturing GMR Filters is the autocloning technology [79]. It is the repetition of the surface modulation of a 1D or 2D gratings via an oxide deposition on top of grating the substrate. The top layer is then expected to replicate the surface function of the bottom grating

with great accuracy, however, research shows that smoothing and increased top material's filling ratio of the single unit cell remains problematic and acquires precise knowledge of the deposition technology [79]. The challenge stems from the surface topology of the grating's substrate, the material that is deposited on top of it (can be characterized via its refractive index), and the thickness of the deposited layer.

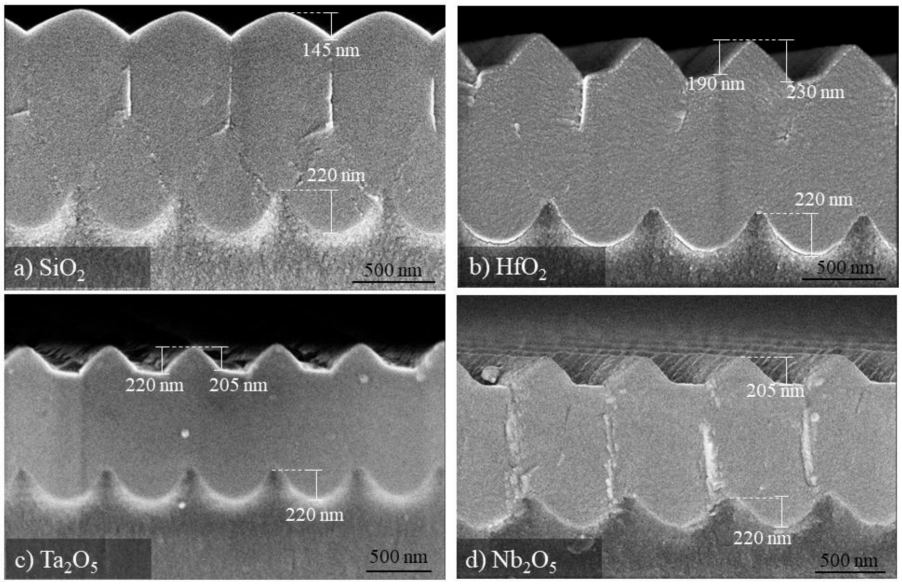


Figure 1.8: The surface replication study by deposition of various oxides via IBS method, adapted from [87]. The top oxide layers with their respective refractive indexes at 970 nm are ordered in the following: SiO_2, $n = 1.48$ a), HfO_2, $n = 1.99$ b), Ta_2O_5, $n = 2.09$ c), Nb_2O_5, $n = 2.25$ d). Scanning Electron Microscope (SEM) is used to visualize fabricated sample slices.

To author's knowledge, the most accurate surface cloning technology used is the Ion Beam Sputtering (IBS) method [87], which is utilized for fabrication of the modulated thin film GMRFs researched in this thesis. It also incorporates grating's surface tuning by active ion etching that either smooth or decrease surface modulation of the grating or the top layer, in order to tune the GMR to its working regime, such as wavelength range, its central wavelength, width, angle of incidence, polarization of incident wave, etc.

As an example, the deposited oxide film layout's SEM pictures are shown in Fig. 1.8 for each material of interest, for $L = 1$ μm of thin film thickness. The loss of modulation depth (first grating's amplitude) is present for SiO_2, given its small refractive index, $n = 1.48$ ($\lambda_0 = 970$ nm). The refractive index increases gradually with each deposited material of interest, such as HfO_2 (see Fig. 1.8 b)), Ta_2O_5, $n = 2.09$ (see Fig. 1.8 c)) and with the greatest refractive index, Nb_2O_5, $n = 2.25$ (see Fig. 1.8 d)). The bottom grating is ORMOCOMP

($n = 1.51$), which is used as the main substrate in the previous thesis work [87]. The Table 1.2 refers to the decrease of the modulation, which is dependent on the material.

Table 1.2: Change of surface modulation given the deposited oxide materials according to [87].

Material	SiO_2	HfO_2	Ta_2O_5	Nb_2O_5
Diff of h, %	35	4.5	3.2	10
n value	1.47	1.99	2.09	2.25

The modulation difference values are gathered from characterization by Atomic Force Microscopy (AFM), which provides surface modulation data. Partial asymmetry is visible at the deposited structures and smoothening of the surface modulation of SiO_2. It is expected that the greater the thickness of the modulated thin film waveguide, the lesser the modulation depth of the device and the greater the filling ratio of the thin film's dielectric permittivity in the unit cell, once deposition of the material is performed.

1.2 Numerical methods for GMRF simulation

Although there are multiple of ways to approximately solve Maxwell's equations for periodic gratings, here two main methods are proposed that are the most efficient and quite simple to understand compared to what other, more cumbersome, methods, such as Chandezon or Finite Element methods. They might be more efficient speed-wise, however, their implementation is too complex, compared to Rigorous Coupled Wave Analysis (RCWA) or Finite Difference Frequency Domain (FDFD) methods. The latter algorithm is capable of calculating stationary light interaction with both periodic and non-periodic materials whose properties are denoted with linear permittivity and permeability. It has the simplest implementation and it is the most useful when calculating field diffraction profiles in scattering media, only for the monochromatic beams. Yet the former (RCWA) algorithm is more speed-wise efficient for computing transmitted and reflected powers from the periodic structures for monochromatic sources. However, this algorithm is analytically processed first in order to work in such manner, thus rendering it more complex than FDFD. This section provides a short introduction and implementation of both methods and their technical nuances.

1.2.1 Maxwell's equations in Frequency Domain

Maxwell's curl equations for wave propagation in uniaxial anisotropical media in frequency domain are presented in the following:

$$\mathrm{rot}\vec{E} = k_0[\mu_r]\vec{\tilde{H}}, \tag{1.29a}$$

$$\mathrm{rot}\vec{\tilde{H}} = k_0[\varepsilon_r]\vec{E}. \tag{1.29b}$$

Here the magnetic field strength is normalized to vacuum impedance $\vec{\tilde{H}} = -j\eta_0\vec{H}$ so that wavevector magnitude $k_0 = 2\pi/\lambda_0$ is multiplied with $\vec{\tilde{H}}$ and $\vec{E}$. Such procedure helps to prepare Maxwell's equations for numerical treatment in programming environment. The relative permittivity $[\varepsilon_r]$ and permeability $[\mu_r]$ tensors of the material are presented in the following:

$$[\varepsilon_r] = \begin{bmatrix} \varepsilon_{xx} & 0 & 0 \\ 0 & \varepsilon_{yy} & 0 \\ 0 & 0 & \varepsilon_{zz} \end{bmatrix} \tag{1.30a}$$

$$[\mu_r] = \begin{bmatrix} \mu_{xx} & 0 & 0 \\ 0 & \mu_{yy} & 0 \\ 0 & 0 & \mu_{zz} \end{bmatrix} \tag{1.30b}$$

Uniaxial material tensors are used so that the Maxwell equations can be treated in 2D simulations. In this case the permittivity and permeability tensors are chosen to have homogeneous device distribution at z coordinate so that the fields also have equivalent homogeneous distribution, hence $\frac{\partial}{\partial z} = 0$. In this case, Maxwell's equations, once grouped, can be decoupled into two polarization modes, given normalized coordinates $x' = k_0 x$ and $y' = k_0 y$:

$$\frac{\partial E_z}{\partial y'} = \mu_{xx}\,\tilde{H}_x, \tag{1.31a}$$

$$-\frac{\partial E_z}{\partial x'} = \mu_{yy}\,\tilde{H}_y, \tag{1.31b}$$

$$\frac{\partial \tilde{H}_y}{\partial x'} - \frac{\partial \tilde{H}_x}{\partial y'} = \varepsilon_{zz}\,E_z, \tag{1.31c}$$

$$\frac{\partial \tilde{H}_z}{\partial y'} = \varepsilon_{xx}\,E_x, \tag{1.31d}$$

$$-\frac{\partial \tilde{H}_z}{\partial x'} = \varepsilon_{yy}\,E_y, \tag{1.31e}$$

$$\frac{\partial E_y}{\partial x'} - \frac{\partial E_x}{\partial y'} = \mu_{zz}\,\tilde{H}_z. \tag{1.31f}$$

The polarization mode is an abbreviation for the Maxwell equations sets. The first mode is called E_z mode, which has electric field strength E_z, $\tilde{H}_x$ and $\tilde{H}_y$ magnetic field strengths. the second mode is termed as H_z mode, which pertains $\tilde{H}_z$, E_x and E_y fields.

1.2.2 2D Finite Difference Frequency Domain

The decoupled polarization modes are then approximated via Finite Difference method, assuming the fields do not exist at the same grid points. The staggered grid, or Yee grid, is a grid where all field components are chosen in the numerical grid so that they do not overlap [88]. At the staggered grid [88], equations for E_z mode are written in the following:

$$\frac{E_{z\,|\,i,j+1} - E_{z\,|\,i,j}}{\Delta y'} = \mu_{xx\,|\,i,j}\,\tilde{H}_{x\,|\,i,j}, \tag{1.32a}$$

$$-\frac{E_{z\,|\,i+1,j} - E_{z\,|\,i,j}}{\Delta x'} = \mu_{yy\,|\,i,j}\,\tilde{H}_{y\,|\,i,j}, \tag{1.32b}$$

$$\frac{\tilde{H}_{y\,|\,i,j} - \tilde{H}_{y\,|\,i-1,j}}{\Delta x'} - \frac{\tilde{H}_{x\,|\,i,j} - \tilde{H}_{x\,|\,i,j-1}}{\Delta y'} = \varepsilon_{zz\,|\,i,j}\,E_{z\,|\,i,j}. \tag{1.32c}$$

All electric and magnetic fields are defined at their respective 2D Yee grid points i, j, together with their permittivity and permeability tensors. The partial derivatives are approximated in the Yee grid for electric fields so that their next grid values are subtracted from the grid current values and such method is applied for all electric fields. The H_z mode's Finite Difference approximation is also defined in the same manner:

$$\frac{\tilde{H}_{z\,|\,i,j} - \tilde{H}_{z\,|\,i,j-1}}{\Delta y'} = \varepsilon_{xx\,|\,i,j}\,E_{x\,|\,i,j}, \tag{1.33a}$$

$$-\frac{\tilde{H}_{z\,|\,i,j} - \tilde{H}_{z\,|\,i-1,j}}{\Delta x'} = \varepsilon_{yy\,|\,i,j}\,E_{y\,|\,i,j}, \tag{1.33b}$$

$$\frac{E_{y\,|\,i+1,j} - E_{y\,|\,i,j}}{\Delta x'} - \frac{E_{x\,|\,i,j+1} - E_{x\,|\,i,j}}{\Delta y'} = \mu_{zz\,|\,i,j}\,\tilde{H}_{z\,|\,i,j}. \tag{1.33c}$$

However, the magnetic field's partial derivative operations are chosen so that current magnetic field strength grid values are subtracted from the previous ones. Hence, a staggered Yee grid approach is applied here as well [88]. The Finite Difference approach, applied for partial derivatives for fields, can be expanded into sparse matrix approach [89]. In such a way, partial derivatives are written as derivative operators, and fields are flattened into 1D field arrays from 2D grid. Thus, derivative operations with periodic boundary conditions at the grid edges are defined as[49, 51, 85, 89]:

$$\underbrace{\frac{1}{\Delta x}\begin{bmatrix} -1 & 1 & 0 & 0 & 0 & 0 & 0 & 0 & 0 \\ 0 & -1 & 1 & 0 & 0 & 0 & 0 & 0 & 0 \\ \Phi_x & 0 & -1 & 0 & 0 & 0 & 0 & 0 & 0 \\ 0 & 0 & 0 & -1 & 1 & 0 & 0 & 0 & 0 \\ 0 & 0 & 0 & 0 & -1 & 1 & 0 & 0 & 0 \\ 0 & 0 & 0 & \Phi_x & 0 & -1 & 0 & 0 & 0 \\ 0 & 0 & 0 & 0 & 0 & 0 & -1 & 1 & 0 \\ 0 & 0 & 0 & 0 & 0 & 0 & 0 & -1 & 1 \\ 0 & 0 & 0 & 0 & 0 & 0 & \Phi_x & 0 & -1 \end{bmatrix}}_{D_x^{(e)}} \begin{bmatrix} E_{z|1,1} \\ E_{z|2,1} \\ E_{z|3,1} \\ E_{z|1,2} \\ E_{z|2,2} \\ E_{z|3,2} \\ E_{z|1,3} \\ E_{z|2,3} \\ E_{z|3,3} \end{bmatrix} = \frac{1}{\Delta x} \begin{bmatrix} E_{z|2,1} - E_{z|1,1} \\ E_{z|3,1} - E_{z|2,1} \\ \Phi_x E_{z|1,1} - E_{z|3,1} \\ E_{z|2,2} - E_{z|1,2} \\ E_{z|3,2} - E_{z|2,2} \\ \Phi_x E_{z|1,2} - E_{z|3,2} \\ E_{z|2,3} - E_{z|1,3} \\ E_{z|3,3} - E_{z|2,3} \\ \Phi_x E_{z|1,3} - E_{z|3,3} \end{bmatrix} \tag{1.34a}$$

$$\underbrace{\frac{1}{\Delta y}\begin{bmatrix} -1 & 0 & 0 & 1 & 0 & 0 & 0 & 0 & 0 \\ 0 & -1 & 0 & 0 & 1 & 0 & 0 & 0 & 0 \\ 0 & 0 & -1 & 0 & 0 & 1 & 0 & 0 & 0 \\ 0 & 0 & 0 & -1 & 0 & 0 & 1 & 0 & 0 \\ 0 & 0 & 0 & 0 & -1 & 0 & 0 & 1 & 0 \\ 0 & 0 & 0 & 0 & 0 & -1 & 0 & 0 & 1 \\ \Phi_y & 0 & 0 & 0 & 0 & 0 & -1 & 0 & 0 \\ 0 & \Phi_y & 0 & 0 & 0 & 0 & 0 & -1 & 0 \\ 0 & 0 & \Phi_y & 0 & 0 & 0 & 0 & 0 & -1 \end{bmatrix}}_{D_y^{(e)}} \begin{bmatrix} E_{z|1,1} \\ E_{z|2,1} \\ E_{z|3,1} \\ E_{z|1,2} \\ E_{z|2,2} \\ E_{z|3,2} \\ E_{z|1,3} \\ E_{z|2,3} \\ E_{z|3,3} \end{bmatrix} = \frac{1}{\Delta y} \begin{bmatrix} E_{z|1,2} - E_{z|1,1} \\ E_{z|2,2} - E_{z|2,1} \\ E_{z|3,2} - E_{z|3,1} \\ E_{z|1,3} - E_{z|1,2} \\ E_{z|2,3} - E_{z|2,2} \\ E_{z|3,3} - E_{z|3,2} \\ \Phi_y E_{z|1,1} - E_{z|1,3} \\ \Phi_y E_{z|2,1} - E_{z|2,3} \\ \Phi_y E_{z|3,1} - E_{z|3,3} \end{bmatrix} \tag{1.34b}$$

These Eqs. (1.34) are the examples of N_xxN_y 3x3 grid resolution, where periodic boundary conditions (PBCs) are enforced for derivative arrays in x and y directions. Here $\Phi_x = \exp(jk_x\Lambda_x)$ and $\Phi_y = \exp(jk_y\Lambda_y)$, which enforce a phase continuity for fields at numerical grid's edges. The quantities D_y^e and D_x^e are for partial derivative matrices for electric fields in y and in x directions, respectively. The derivative operations are chosen in such a manner that the field arrays are flattened as 1D arrays. In this case, every ascending element is an ascending i-th component for the j-th index value. The matrix multiplication ensures that the right hand side obeys Finite Difference method. The 0-th diagonal derivative matrix corresponds to subtraction operation, the first diagonal in D_x^e corresponds to addition. Every final grid point N_x in that diagonal is 0, which enforces Dirichlet boundary boundary conditions (DBCs), which means function values are zero outside of the grid. If PBCs are not used, $\Phi_x = 0$. Furthermore, D_y^e has an off diagonal at N_x. Periodic Boundary Conditions for Φ_y are enforced at $N_x - N_x \cdot N_y$ diagonal. If DBCs are desired in y direction, $\Phi_y = 0$.

Furthermore, magnetic field derivative matrices are related through electric field derivative matrices:

$$\mathrm{D}_x^h = -(\mathrm{D}_x^{(e)})^H, \tag{1.35a}$$
$$\mathrm{D}_y^h = -(\mathrm{D}_y^{(e)})^H. \tag{1.35b}$$

The superscript H is Hermitian transpose operation, applied for derivative arrays in rectangular grid. This relation only applies for the grid whose all points are equally separated by Δx and Δy. In other words, hermitian transpose operation works for homogeneous grids.

The trade-off of the derivative matrices is that other matrix formalism must be applied, since there are too many zeroes in the off diagonals. In this case, such matrices are treated as sparse matrices, which save numerical derivative matrix values and their grid location indices. In order to further employ FDFD method, permittivity and permeability tensors are diagonalized into sparse arrays in the same manner. Then, Maxwell's equations are expanded in their matrix form for the E_z mode:

$$\mathrm{D}_{y'}^{(e)}\, \mathrm{e}_z = \mu_{xx}\, \tilde{\mathrm{h}}_x \tag{1.36a}$$
$$-\mathrm{D}_{x'}^{(e)}\, \mathrm{e}_z = \mu_{yy}\, \tilde{\mathrm{h}}_y, \tag{1.36b}$$
$$\mathrm{D}_{x'}^{(h)}\, \tilde{\mathrm{h}}_y - \mathrm{D}_{y'}^{(h)}\, \tilde{\mathrm{h}}_x = \varepsilon_{zz}\, \mathbf{e}_z. \tag{1.36c}$$

The equations for H_z mode can be expressed as well:

$$\mathrm{D}_{y'}^{(h)}\, \tilde{\mathrm{h}}_z = \varepsilon_{xx}\, \mathrm{e}_x, \tag{1.37a}$$
$$-\mathrm{D}_{x'}^{(h)}\, \tilde{\mathrm{h}}_z = \varepsilon_{yy}\, \mathrm{e}_y, \tag{1.37b}$$
$$\mathrm{D}_{x'}^{(e)}\, \mathrm{e}_y - \mathrm{D}_{y'}^{(e)}\, \mathrm{e}_x = \mu_{zz}\, \tilde{\mathrm{h}}_z. \tag{1.37c}$$

Both Eq. (1.36) and Eq. (1.37) can be further simplified by eliminating x and y field components, hence the operators are derived for each mode:

$$\hat{\mathrm{A}} = \mathrm{D}_{x'}^{(h)} \mu_{yy}^{-1} \mathrm{D}_{x'}^{(e)} + \mathrm{D}_{y'}^{(h)} \mu_{xx}^{-1} \mathrm{D}_{y'}^{(e)} + \varepsilon_{zz},\ E_z \text{ mode}, \tag{1.38a}$$
$$\hat{\mathrm{A}} = \mathrm{D}_{x'}^{(e)} \varepsilon_{yy}^{-1} \mathrm{D}_{x'}^{(h)} + D_E^{(y)} \varepsilon_{xx}^{-1} D_H^{(y)} + \mu_{zz},\ H_z \text{ mode}. \tag{1.38b}$$

Overall, the field operators Eq. (1.38) are derivative arrays normalized and shifted with respect to the diagonalized permittivity and permeability tensor arrays. The numerical and most computationally intense problem to be solved is $f = \hat{\mathrm{A}}^{-1} b$, where b is the wave source in the linear medium.

This is an algorithm which is by far has the simplest implementation and can be used for scattering analysis both for arbitrary periodic and non-periodic material profiles. It is most efficient for calculating field profiles of periodic wave-guides, and an pseudo-algorithm for such computations is presented below in Alg. 1. Its main advantage, compared to FDTD method, is speed and simplicity of implementation and analysis of high quality resonant cavities for Continuous Wave (CW) sources.

Algorithm 1 2D FDFD algorithm for periodic structures, simplified

$\mathrm{d}x = \frac{\lambda_0^{(min)}}{n^{(max)} \cdot N_r}$ ▷ Critical grid pixel width
$\mathrm{d}y = \frac{\lambda_0^{(min)}}{n^{(max)} \cdot N_r}$ ▷ Critical grid pixel length
$\mathrm{d}x_2 = 2\mathrm{d}x$, $N_{2x} = 2N_x$
$\mathrm{d}y_2 = 2\mathrm{d}y$, $N_{2y} = 2N_y$ ▷ 2x grid
Create a device $\varepsilon(x, y)$ and $\mu(x, y)$ from 2x grid
Incorporate PML inside the device
Extract ε_{xx}, ε_{yy}, ε_{zz} and μ_{xx}, μ_{yy}, μ_{zz} and diagonalize them ▷ Yee grid tenzors
Create derivative matrices $\mathrm{D}_{x'}^{(e)}$, $\mathrm{D}_{y'}^{(e)}$, $\mathrm{D}_{x'}^{(h)}$ and $\mathrm{D}_{y'}^{(h)}$,.
if (mode is 'E') **then**
    $\hat{\mathrm{A}} = \mathrm{D}_{x'}^{(h)} \mu_{yy}^{-1} \mathrm{D}_{x'}^{(e)} + \mathrm{D}_{y'}^{(h)} \mu_{xx}^{-1} \mathrm{D}_{y'}^{(e)} + \varepsilon_{zz}$ ▷ 'E_z' mode operator (TM pol.)
else
    $\hat{\mathrm{A}} = \mathrm{D}_{x'}^{(e)} \varepsilon_{yy}^{-1} \mathrm{D}_{x'}^{(h)} + D_E^{(y)} \varepsilon_{xx}^{-1} D_H^{(y)} + \mu_{zz}$ ▷ 'H_z' mode operator (TE pol.)
end if
Calculate Source field $f_{src} = \exp\left(-j(k_x^{(inc)} x + k_y^{(inc)} y)\right)$
Incorporate scattered field masking matrix Q
Q = diag(sparse(Q)), reshape f_{src} to a single column vector
$b = (\mathrm{Q}\hat{\mathrm{A}} - \hat{\mathrm{A}}\mathrm{Q}) f_{src}$ ▷ Source field masking operation
$f = \hat{\mathrm{A}}^{-1} b$ ▷ Solving $\hat{\mathrm{A}} f = b$
Reshape 1D f into a 2D array ▷ sized N_x and N_y
if (Mode is 'E') **then**
    $h_x = \mu_{xx}^{-1} \mathrm{D}_{y'}^{(e)} e_z$ ▷ E_z is f
    $h_y = -\mu_{yy}^{-1} \mathrm{D}_{x'}^{(e)} e_z$
else
    $e_x = \varepsilon_{xx}^{-1} \mathrm{D}_{y'}^{(h)} h_z$ ▷ H_z is f
    $e_y = -\varepsilon_{yy}^{-1} \mathrm{D}_{x'}^{(h)} h_z$
end if
Visualize the fields at the (N_x, N_y) grid
Compute DEs according to Eq. (1.27) and Eq. (1.28)

The main objective of FDFD is to compute a CW solution of Maxwell's equation of the scattering device. The Alg. 1 illustrates the computation of the field profile of a periodic wave-guide directly. Firstly, the grid quantities $\mathrm{d}x$ and $\mathrm{d}y$ are critical pixel width and length, respectively, N_r denotes the

resolution parameter, or a number of grid points per smallest wavelength in the Yee grid. The bigger the resolution size, the greater the convergence of FDFD results, however the longer it takes to complete the computation.

The next step in the FDFD numerical treatment is to incorporate the Uniaxial Perfectly Matched Layer (UPML, pseudo-algorithm is shown in Alg. 2), which is a gradient-like absorption profile with impedance matching. It acts as an absorber on the edges of the grid (in the case of a periodic wave-guide, it is the substrate and superstrate materials) and ensures minimal reflections from the grid boundaries. Periodic Boundary Conditions (PBCs) in x direction acquire the PML to be at the longitudinal direction, which is y coordinate in FDFD's case by default. The absence of UPML will render the simulations of an overall field, which is interfered with itself due to the full reflections from the grid boundaries if Dirichlet Boundary Condition (DBC) is used [85]. The PBCs will equalize the field at the right side of the grid with the previous one with phase matching, thus allowing scattered field propagation right to left in transerse x direction. In such a way, Bloch's theorem is satisfied for the field condition, which incorporates phase distribution $\exp(jk_x\Lambda_x)$ over an entire device period.

Algorithm 2 Incorporation of the 2D UPML into the 2D FDFD algorithm .

Require: ε_{xx}, ε_{yy}, ε_{zz} ▷ Permittivity tensors
Require: μ_{xx}, μ_{yy}, μ_{zz} ▷ Permeability tensors

---

if not periodic in x dir **then**
  $\sigma_y(y) = \sigma_{\max}\sin^2(\frac{\pi y}{2L_x})$ ▷ Artificial conductivity in y direction
  $a_y(y) = 1 + (a_{\max} - 1)(\frac{y}{L_y})^p$ ▷ Scaling factor for $s_y(y)$
  $s_y(y) = a_y(y) \cdot (1 - j\frac{\eta_0\sigma_y(y)}{k_0})$ ▷ Complex conductivity in y direction
else
  $s_y = 1$
end if

$\sigma_x(x) = \sigma_{\max}\sin^2(\frac{\pi x}{2L_x})$ ▷ Artificial conductivity in x direction
$a_x(x) = 1 + (a_{\max} - 1)(\frac{x}{L_x})^p$ ▷ Scaling factor for $s_x(x)$
$s_x(x) = a_x(x) \cdot (1 - j\frac{\eta_0\sigma_x(x)}{k_0})$ ▷ Complex conductivity in x direction

---

$\mu'_{xx} = \frac{s_y}{s_x}\mu_{xx}$, $\mu'_{yy} = \frac{s_x}{s_y}\mu_{yy}$, $\mu'_{zz} = s_x s_y \mu_{zz}$. ▷ Incorporate UPML into μ tenzors
$\varepsilon'_{xx} = \frac{s_x}{s_y}\varepsilon_{xx}$, $\varepsilon'_{yy} = \frac{s_x}{s_y}\varepsilon_{yy}$, $\varepsilon'_{zz} = s_x s_y \varepsilon_{zz}$. ▷ Incorporate UPML into ε tensors
return ε', μ' ▷ Return tensors with PMLs

The PML is conductivity distribution in frequency domain, which has its dependency illustrated in Fig. 1.9. Here, twenty NPML points are used, which are 40 in the 2x grid. Such distribution ensures the wave propagation to be 'smoothly absorbed'. The parameters used are $\sigma_{\max} = 1$, $a_{\max} = 4$, and $p = 3$,

vacuum impedance $\eta_0 \approx 376\ \Omega$ and $k_0 = 2\pi$ a.u.. The PML also has its drawbacks. Firstly, it is not a boundary condition, but an absorber along the boundaries of the grid. Secondly, due it having a gradient-like imaginary refractive index distribution in the grid with, the absorber still reflects the incident/scattered light. Reflections can be minimized by -40 dB up to -70 dB by increasing resolution parameter N_R from 20 units [85]. The reflection coefficient is also sensitive to the angle of incidence. In such a case, it is better to maintain the source's angle of incidence from -60 deg up to 60 deg in reference to the object of interest [49, 51, 85, 89, 90].

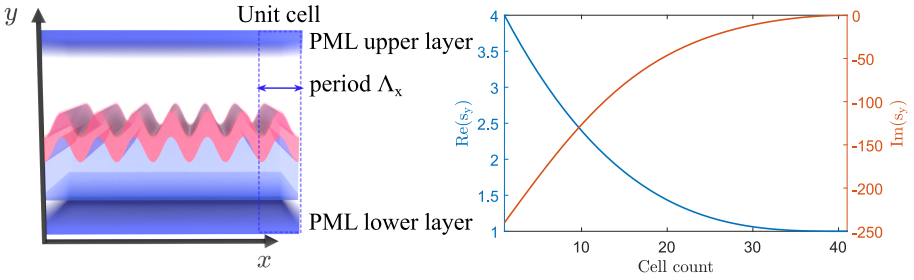


Figure 1.9: PML of a device with PBCs (a) and the unit cell (b) with transverse periodicity.

The second step is to snap a new device into a Yee grid, i.e., creating tenzor elements with an already incorporated PML and flatten them, thus putting them in diagonals in the form of a sparse matrix. The Yee grid in the case of numerical problem solving of Maxwell's equations is a tool proposed by Kane S. Yee himself in 1966 [88]. The idea is heavily focused on the grid in which electric and magnetic field components are computed in time domain method. The same principle is applied in frequency domain method. Interpretation of Yee grid: electric and magnetic fields are considered as functions, however, in order to provide stable numerical solution with precise boundary conditions, the grid in which Maxwell's equations are solved is staggered by a half step at all directions in Cartesian coordinate system (x,y,z). Consequently, the fields are solved in separate locations in the grid without an overlap. The concept of 3D Yee grid is shown in Fig 1.10.

In this way all magnetic and electric field components can be seperated and their curl equations be calculated for each field component. A 2D representation slices the upper and lower parts of a 3D Yee grid's cell, if the propagation in the xy plane is of interest. If a device contains no variability of geometry in z direction, then the 2D representation can be successfully reduced to two polarization modes. The first one is E mode, which is simply E_z field component oscillating in the z direction and has two H_x and H_y magnetic field components oscillating transversely with respect to z and this is why it is called as TM polarization.

The TE polarization corresponds to magnetic field H_z, oscillating in the z direction, alongside with transversely oscillating E_y and E_x field components.

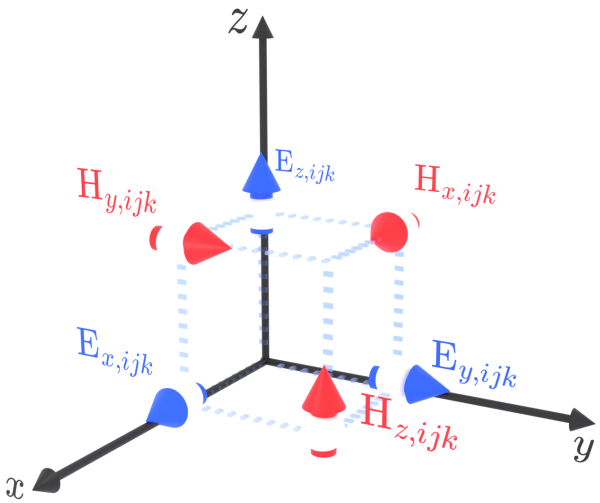


Figure 1.10: A representation of a rectangular 3D cell of the Yee grid.

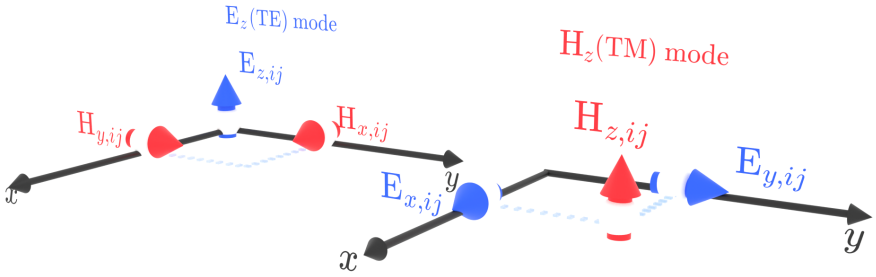


Figure 1.11: A representation of a 2D cells of the Yee grid for TE and TM polarized modes.

Therefore, only two polarizations can be analyzed for 2D numerical analysis of photonic devices for scattering simulations. The main field components which are computed as f are in Alg. 1 are E_z for E mode and H_z for H mode.

Furthermore, numerical boundary conditions can be easily implemented for each boundary cell in the grid, such as Dirichlet (DBC), Periodic (PBC) boundary conditions. The outcome is a stable numerical solution for Maxwell's

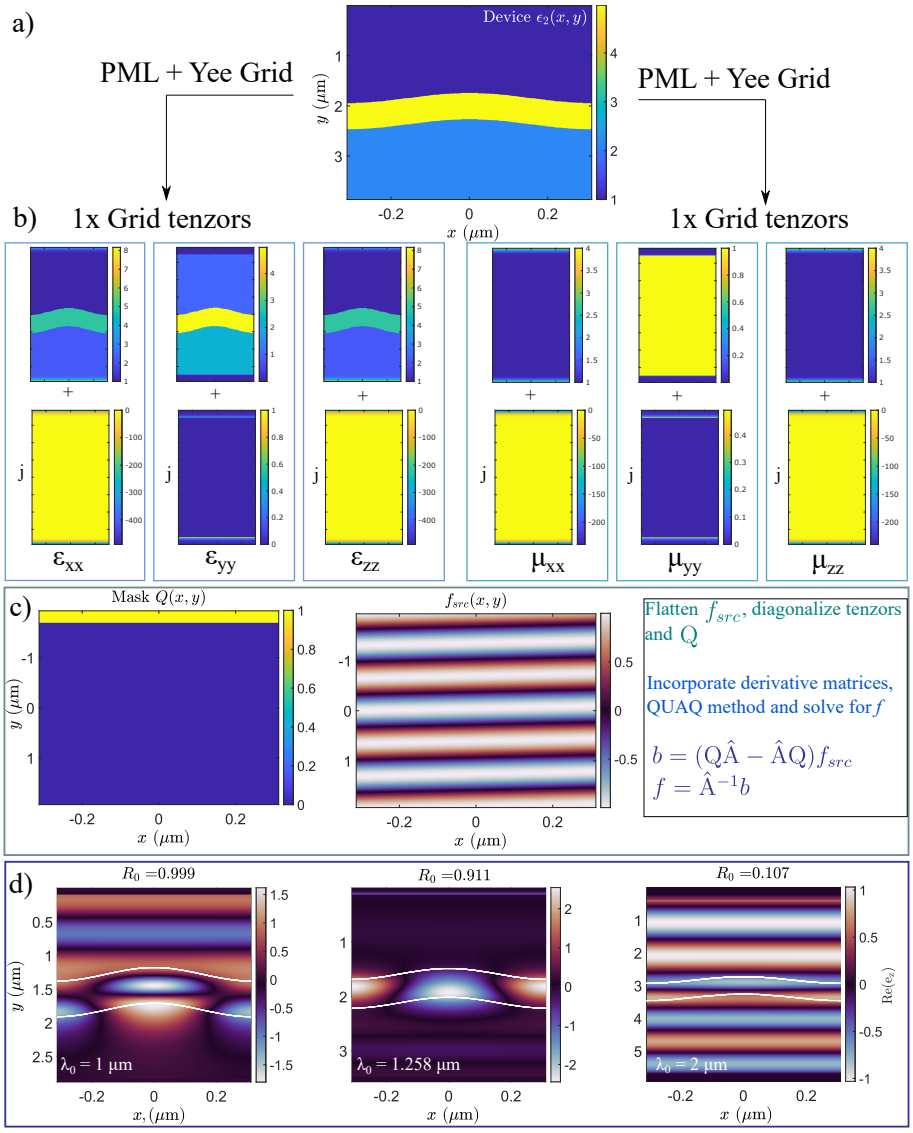


Figure 1.12: 2D FDFD schematic for calculating light scattering by enforcing PBC in transverse (x) and PML in propagation (y) directions.

equations. However, each theoretical concept unfortunately comes with a trade-off. The consideration which is brought here by staggered Yee grid is numerical dispersion, i.e., the grid itself slows the speed of light by a particular factor in reference with angle of incidence and wavelength of the source. That type of dispersion is anisotropic and has directional sensitivity. This problem is mitigated either by increasing grid resolution N_{RES} or by multiplying grid's

permittivity/permeability distributions by a ψ factor, which is a quantity of analytical numerical dispersion. The numerical dispersion is visualized in Fig. 1.13.

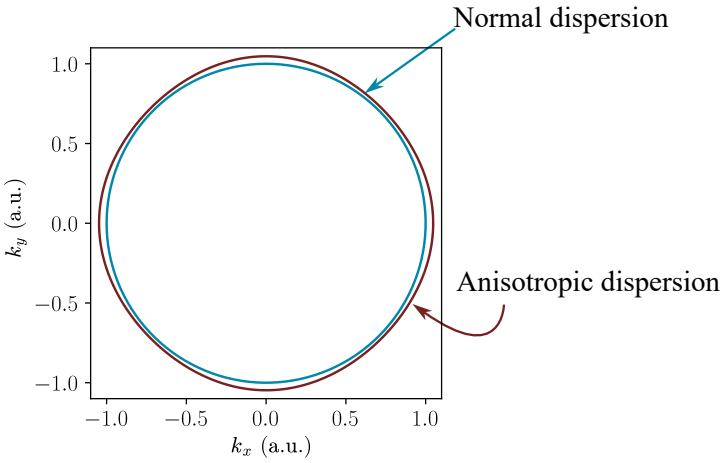


Figure 1.13: Dispersion comparison between the Normal dispersion and the Anisotropic one, given $\Delta x = 1$ and $\Delta y = 1$ a.u. for $\varepsilon_r = \mu_r = 1$.

Henceforth the derivative matrices. The most important step to keep those matrices as sparse matrices, in order to prevent unnecessary memory loading. The next step is then to flatten the tensor arrays and put them in a matrix diagonal and finally incorporate them in the $\hat{A}$ matrix shown in the algorithm 1. The size of such sparse array is $(N_x \cdot N_y, N_x \cdot N_y)$. The last steps is to incorporate a source field (in this case, a plane wave) and incorporate the Q array into the masking operation. The total, affected field is solved via $f = \hat{\mathrm{A}}^{-1}b$ operation. It is a vector, which must be reshaped into the 2D array with (N_x, N_y) dimensions this time. An example of a GMR in one period of a harmonic periodic waveguide is presented in 1.12 (d), alongside with the visualization of the Fig. 1.12 (a-d). The modified field $b = (\mathrm{QA} - \mathrm{AQ})f_{src}$ which is represented in vector form. At the interface between Total Field/Scattered Field (TF/SF) region it will act like a source. Total field in this case is the scattered field interference with the source, scattered field's meaning is self-explanatory.

There is another way to incorporate loss into the system through a method named as Stretched Coordinate Perfectly Matched Layer (SCPML). Such method involves modification of derivative matrices through loss terms. In other words, the coordinates now are "stretched" along the axes of Cartesian coordinate system, but only in complex domain. The tensors of permittivity and permeability remain purely real this time. It is worth mentioning that SCPML is a method which conditions matrix equations to be iteratively solved by Graphics Processing Unit (GPU) for large (bigger than 500x500) arrays. This is particularly useful for large 2D and 3D problems [51, 85, 91].

If the Q matrix has arbitrary form, then the numerical dispersion becomes

evident because of the Yee grid's field displacement by a half step. That dispersion is similar to the anisotropic dispersion. In this case the effect is compensated by dividing permittivity and permeability tensors by ψ factor before applying PML:

$$\psi = \frac{1}{2n^{(src)}k_0}\sqrt{\left(\frac{2}{\Delta_x}\sin\frac{k_x\Delta_x}{2}\right)^2 + \left(\frac{2}{\Delta_y}\sin\frac{k_y\Delta_y}{2}\right)^2} \tag{1.39}$$

Once a field profile $f(x, y)$ is computed, the back-scattered and front-scattered fields are decomposed into Fourier series via Fast Fourier Transform and their quantities are presented in the angular spectrum. The main idea is to apply this procedure near the PML, never inside the area of PML, due it being a lossy medium. Lastly, diffraction efficiencies in those regions are computed via Eq. (1.27) for TM polarization, whereas Eq. (1.28) is for TE polarization.

1.2.3 Plane wave expansion of Maxwell's equations

The 2D expanded Maxwell's equations can be expressed so in xz propagation plane with normalized magnetic field strength, assuming uniform distribution of a device in y direction. Considering the same curl equations in frequency domain like in Eq. (1.29), the following expanded Maxwell's equations become:

$$-\frac{\partial E_y}{\partial z} = k_0\mu\widetilde{H}_x, \tag{1.40a}$$

$$\frac{\partial E_x}{\partial z} - \frac{\partial E_z}{\partial x} = k_0\mu\widetilde{H}_y, \tag{1.40b}$$

$$\frac{\partial E_y}{\partial x} = k_0\mu\widetilde{H}_z, \tag{1.40c}$$

$$-\frac{\partial \widetilde{H}_y}{\partial z} = k_0\varepsilon E_x, \tag{1.40d}$$

$$\frac{\partial \widetilde{H}_x}{\partial z} - \frac{\partial \widetilde{H}_z}{\partial x} = k_0\varepsilon E_y, \tag{1.40e}$$

$$\frac{\partial \widetilde{H}_y}{\partial x} = k_0\varepsilon E_z. \tag{1.40f}$$

Where derivative with respect to the uniform direction $\frac{\partial}{\partial y} = 0$. The magnetic field strength pertains the same normalization factor as in the FDFD method. In order to efficiently simulate diffraction from 1D gratings, GMR filter's diffraction efficiencies, the periodic boundary conditions are enforced in x direction via expanding permittivity and permeability distributions in the plane wave basis:

$$\varepsilon(x) = \sum_m \xi_m \exp\left(j\frac{2\pi m x}{\Lambda_x}\right), \tag{1.41a}$$

$$\mu(x) = \sum_m \Xi_m \exp\left(j\frac{2\pi m x}{\Lambda_x}\right), \tag{1.41b}$$

$$\xi_m = \frac{1}{\Lambda_x}\int_{\frac{-\Lambda_x}{2}}^{\frac{\Lambda_x}{2}} \varepsilon(x)\exp\left(-j\frac{2\pi m x}{\Lambda_x}\right)dx, \tag{1.41c}$$

$$\Xi_m = \frac{1}{\Lambda_x}\int_{\frac{-\Lambda_x}{2}}^{\frac{\Lambda_x}{2}} \mu(x)\exp\left(-j\frac{2\pi m x}{\Lambda_x}\right)dx. \tag{1.41d}$$

The permittivity and permeability are now expanded into the infinite set of plane waves of the order of m, which are dubbed as spatial harmonics. Here ξ_m and Ξ_m are the Fourier coefficients of the relative permittivity and permeability for the m-th spatial harmonic, respectively. Likewise, the field components are also expanded in the Fourier basis, since their amplitudes repeat the same symmetry features of the periodically modulated device. Assuming homogeneous distribution of the device function in z direction, the field expansions are written as:

$$E_i(\vec{r}) = \sum_m s_{i,m}(z)\exp(-jk_{x,m}x), \tag{1.42a}$$

$$\widetilde{H}_i(\vec{r}) = \sum_m u_{i,m}(z)\exp(-jk_{x,m}x). \tag{1.42b}$$

So the fields obey Bloch's theorem, which specifies that the propagating plane wave's amplitude in periodic medium replicates the symmetry of the medium. Quantities s_i and u_i $(i = (x, y, z))$ are Fourier coefficients of the fields that depend on the propagation direction z. Then, substituting the Fourier expanded fields, permittivity and permeability, Maxwell's matrix equations in Fourier space are presented in the straightforward manner:

$$-\frac{d}{dz'}s_y = [\mu_r]u_x, \tag{1.43a}$$

$$\frac{d}{dz'}u_x + j\hat{\mathrm{K}}_{\mathrm{x}}u_z = [\varepsilon_r]s_y, \tag{1.43b}$$

$$-j\hat{\mathrm{K}}_{\mathrm{x}}s_y = [\mu_r]u_z, \tag{1.43c}$$

$$-\frac{d}{dz'}u_y = [\varepsilon_r]s_x, \tag{1.43d}$$

$$\frac{d}{dz'}s_x + j\hat{\mathrm{K}}_{\mathrm{x}}\ s_z = [\mu_r]u_y, \tag{1.43e}$$

$$-j\hat{\mathrm{K}}_{\mathrm{x}}u_y = [\varepsilon_r]s_z. \tag{1.43f}$$

Here only a full derivative matrix is present since the field pertains its propagation in z direction. The relative permittivity and permeability Fourier coefficients are arranged in such a manner that matrix multiplication between $[\varepsilon_r]$ and $[\mu_r]$ with respective field components resemble convolution operation.

The coordinate of wave propagation is normalized to wavevector magnitude $z' = k_0 z$ and $\hat{\mathrm{K}}_\mathrm{x}$ is a diagonal matrix which contains all transverse wavevector $k_{x,m}/k_0$ values for each spatial harmonic m. Solutions of Eq. (1.43) are for E_y mode:

$$\frac{d^2}{dz'^2} s_y - \Omega_s^2 s_y = 0, \tag{1.44a}$$

$$s_y = e^{-\Omega_s z'} s^{(+)}(0) + e^{\Omega_s z'} s^{(-)}(0) \tag{1.44b}$$

As well as for H_y mode:

$$\frac{d^2}{dz'^2} u_y - \Omega_p^2 u_y = 0 \tag{1.45a}$$

$$u_y = e^{-\Omega_p z'} u^{(+)}(0) + e^{\Omega_p z'} u^{(-)}(0) \tag{1.45b}$$

The field amplitudes $s^{(\pm)}(0)$ and $u^{(\pm)}(0)$ are initial conditions for forward and backward propagating waves. The most important quantity is $\Omega_{s,p}$, which withholds information of the spatial harmonics, permittivity and permeability distributions, where indices s and p correspond to s and p polarizations, or TE and TM polarizations, respectively:

$$\Omega_\mathrm{s}^2 = [\mu_\mathrm{r}](\tilde{\mathrm{K}}_\mathrm{x}[\mu_\mathrm{r}]^{-1}\tilde{\mathrm{K}}_\mathrm{x} - [\varepsilon_\mathrm{r}]) \tag{1.46a}$$

$$\Omega_\mathrm{p}^2 = [\varepsilon_\mathrm{r}](\tilde{\mathrm{K}}_\mathrm{x}[\varepsilon_\mathrm{r}]^{-1}\tilde{\mathrm{K}}_\mathrm{x} - [\mu_\mathrm{r}]) \tag{1.46b}$$

The solutions for E_y and H_y modes can then be expanded in the eigen-value/eigen-vector basis [52, 53]:

s pol., E_y mode

$$s_y = \mathrm{W}e^{-\lambda z'} c^{(+)} + \mathrm{W}e^{\lambda z'} c^{(-)}, \tag{1.47a}$$

$$u_x = -\mathrm{V}e^{-\lambda z'} c^{(+)} + \mathrm{V}e^{\lambda z'} c^{(-)},, \tag{1.47b}$$

$$\mathrm{V} = [\mu_\mathrm{r}]^{-1}\mathrm{W}\lambda, \tag{1.47c}$$

p pol., H_y mode

$$u_y = \mathrm{W}e^{-\lambda z'} c^{(+)} + \mathrm{W}e^{\lambda z'} c^{(-)}, \tag{1.47d}$$

$$s_x = -\mathrm{V}e^{-\lambda z'} c^{(+)} + \mathrm{V}e^{\lambda z'} c^{(-)}, \tag{1.47e}$$

$$\mathrm{V} = [\varepsilon_\mathrm{r}]^{-1}\mathrm{W}\lambda. \tag{1.47f}$$

Here W is a Bloch mode matrix that pertains Bloch mode amplitude collection for a wave propagating in a layer with homogeneous distribution of its permittivity and permeability in $-z$ direction. Then, $c_\pm$ are forward and backward propagating power coefficients which are chosen to be equivalent for electric and magnetic field components, i.e., $c^{(\pm)} = \mathrm{V}u^{(\pm)}(0)$ or $c^{(\pm)} = \mathrm{W}s^{(\pm)}(0)$. Another important quantity is the Bloch mode propagation component λ, which is an eigen-value of $\Omega_{s,p}$ matrix. Whatever is left is to find the residual component

of the secondary Fourier fields, preferably u_x and s_x. Then, V matrix formulas are found for them (see Eq. (1.47c) and Eq. (1.47f)). The generalized wave-function of the propagating Bloch modes in the model can be summarized as:

$$\psi(z') = \begin{bmatrix} a \\ b \end{bmatrix} = \begin{bmatrix} \mathrm{W} & \mathrm{W} \\ -\mathrm{V} & \mathrm{V} \end{bmatrix} \begin{bmatrix} e^{-\lambda z'} & 0 \\ 0 & e^{\lambda z'} \end{bmatrix} \begin{bmatrix} c^{(+)} \\ c^{(-)} \end{bmatrix} \tag{1.48}$$

Here a and b are s_y and u_x for s polarization and s_x and u_y for p polarization, respectively. Such generalized parameter is used for boundary conditions of sub-layer connection via transmittance or scattering matrix methods[49, 53, 92].

1.2.4 Implementation of 2D RCWA

Finite Difference Frequency Domain method acquires sparse matrix usage, Yee grid as well as absorption near the boundaries. The numerical parameters then have to be extracted after successfully calculating the field distributions, which is time consuming even when PBCs are applied. The algorithm plane wave expansion of Maxwell's equations solves eigen value problem for periodically modulated sublayers. This formalism exploits resolution in Fourier space, which is spatial harmonic number, and defines the array size.

Algorithm 3 2D RCWA algorithm pseudocode

Require: Grid, device, source params ▷ RCWA parameters
  if Material is only magnetic **then**
    $\Omega_{\mathrm{s}}^2 = \tilde{\mathrm{K}}_{\mathrm{x}}[\mu]_{\mathrm{i}}^{-1}\tilde{\mathrm{K}}_{\mathrm{x}} - \mathrm{I}$ ▷ E mode (s polarization)
    $\Omega_{\mathrm{p}}^2 = \tilde{\mathrm{K}}_{\mathrm{x}}^2 - [\mu]_{\mathrm{i}}$ ▷ H mode (p polarization)
  else if Material is only dielectric **then**
    $\Omega_{\mathrm{s}}^2 = \tilde{\mathrm{K}}_{\mathrm{x}}^2 - [\varepsilon]_{\mathrm{i}}$ ▷ E mode (s polarization)
    $\Omega_{\mathrm{p}}^2 = \tilde{\mathrm{K}}_{\mathrm{x}}[\varepsilon]_{\mathrm{i}}^{-1}\tilde{\mathrm{K}}_{\mathrm{x}} - \mathrm{I}$ ▷ H mode (p polarization)
  else
    $\Omega_{\mathrm{s}}^2 = \tilde{\mathrm{K}}_{\mathrm{x}}[\mu]_{\mathrm{i}}^{-1}\tilde{\mathrm{K}}_{\mathrm{x}} - [\varepsilon]_{\mathrm{i}}$ ▷ E mode (s polarization)
    $\Omega_{\mathrm{p}}^2 = \tilde{\mathrm{K}}_{\mathrm{x}}[\varepsilon]_{\mathrm{i}}^{-1}\tilde{\mathrm{K}}_{\mathrm{x}} - [\mu]_{\mathrm{i}}$ ▷ H mode (p polarization)
  end if
  $[\mathrm{W}_{\mathrm{i}}, \lambda_{\mathrm{i}}^2] = \mathrm{eig}(\Omega_{\mathrm{s,p}}^2)$ ▷ Eigen modes and values for a sub layer
  $\lambda_{\mathrm{i}} = \sqrt{\lambda_{\mathrm{i}}^2}$ ▷ Dimensionless propagation coefficient
  if Mode is 'E' **then**
    $\mathrm{V}_{\mathrm{i}} = [\mu]_{\mathrm{i}}^{-1}\mathrm{W}_{\mathrm{i}}\lambda_{\mathrm{i}}$ ▷ Magnetic field Bloch modes
  else
    $\mathrm{V}_{\mathrm{i}} = [\varepsilon]_{\mathrm{i}}^{-1}\mathrm{W}_{\mathrm{i}}\lambda_{\mathrm{i}}$ ▷ Magnetic field Bloch modes
  end if
  $\mathrm{X}_{\mathrm{i}} = \exp\left(-\lambda_{\mathrm{i}} \cdot k_0 \cdot L_{\mathrm{i}}\right)$ ▷ Propagation exponent

The 2D RCWA algorithm is presented in Alg. 3 involves all linear material cases. All of the quantities are matrices, with $\tilde{K}_x$ being a matrix with each di-

agonal element being the spatial harmonic phase, which is $k_{x,m} = \sin\theta - \frac{2\pi m}{\Lambda_x k_0}$, where the first element is m being the $-N_h$ harmonic, to the last diagonal element being N_h harmonic. Furthermore, $[\mu]_i$ and $[\varepsilon]_i$ are Toeplitz matrices for 2D RCWA case, where the matrix is formed from the Fourier transform of each sub layer i of the sliced device if 1D periodicity is present. Furthermore, quantity I are unitary matrices for unit-valued magnetic permeability or permeability. The exponential of diagonals of Bloch wave propagation phases are taken into account. The meaning of X_i is a propagation phase of a Bloch mode inside a sublayer slice. Consequently, each sublayer has its own unique propagating Bloch vectors back and forth in z direction analytically and are continuous, as well as equivalent, of each sublayer's interface. Such modes acquire matrix treatments, which are presented in the next chapter of "Matrix Methods". They are used to extract diffraction efficiency values as well as for field profile calculations of a dielectric medium with periodic boundaries.

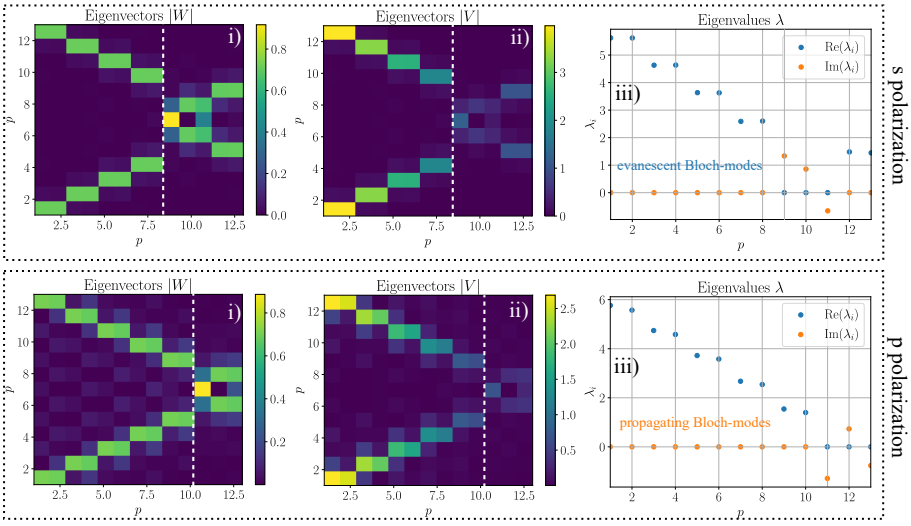


Figure 1.14: 2D RCWA eigen-vector (i,ii) and eigenvalue (iii) visualization of a rectangular grating, whose filling factor $f = 0.5$, $n_{1,2} = [1.47, 1]$, transverse periodicity $\Lambda_x = 0.6$ μm, $\lambda_0 = 0.6$ μm, $\theta = 0$ deg.

The non-sorted eigenvector and eigenvalue arrays' absolute values of rectangular grating are illustrated in Fig. 1.14, which are represented for s and p polarizations. In this manner the real valued eigen-values are evanescent Bloch modes's phases which correspond to each amplitude. The imaginary values correspond to the propagation phases and the greater the λ_0/Λ_x, the lesser the amount of propagating Bloch modes, the greater the amount of the evanescent modes.

1.3 Matrix methods for sub-layer connection

Although the idea of Rigorous Coupled Wave Analysis (RCWA) method was founded in the 80s, the transmission matrix method either is unpopular (mainly one reference of it exists) or its implementation is in the commercial software and no simple info of its implementation is presented, so this chapter is devoted for 2D structures [53]. Although there is a huge variety of formalisms and implementations of various kind of matrix methods, enhanced transmittance T (ETM) and scattering S matrix approaches are the most efficient speed-wise and memory-wise, respectively. Their implementation nuances, hence the pseudocode implementations are presented in the following sections.

1.3.1 Implementation of T matrix method

The implementation of T matrix method is presented in Alg. 4. Here, mul-

Algorithm 4 T matrix algorithm for 2D RCWA, simplified.

Require: $\mathrm{X}, \mathrm{W}, \mathrm{V}, \mathrm{K}_z^{(\mathrm{trn})}, \mathrm{K}_z^{(\mathrm{ref})}$ ▷ RCWA parameters

Init: $\begin{bmatrix} f \\ g \end{bmatrix} = \begin{bmatrix} \mathrm{I} \\ j\mathrm{K}_z^{(\mathrm{trn})} \end{bmatrix}$ and $c^{(\pm)}$ ▷ Starting from substrate

for (i = layer number - 1; i ≤ 1; i−−) **do** ▷ for idx in sub layer count

$\begin{bmatrix} a \\ b \end{bmatrix}_{\mathrm{i}} = \begin{bmatrix} -\mathrm{W_i} & f \\ \mathrm{V_i} & g \end{bmatrix}^{-1} \begin{bmatrix} \mathrm{W_i X_i} \\ \mathrm{V_i X_i} \end{bmatrix}$ ▷ a and b coefficients

$\begin{bmatrix} f \\ g \end{bmatrix} = \begin{bmatrix} \mathrm{W_i}(\mathrm{I} + \mathrm{X_i}a) \\ \mathrm{V_i}(\mathrm{I} - \mathrm{X_i}a) \end{bmatrix}$ ▷ $\begin{bmatrix} f \\ g \end{bmatrix}$ update

end for

$V_R = \begin{bmatrix} \delta_{i0} \\ \delta_{i0} j n_{\mathrm{sup}} \cos\theta \end{bmatrix}$ ▷ Vector stacking for source

$[\mathrm{M_R}] = \begin{bmatrix} -\mathrm{I} & f \\ j\mathrm{K}_z^{(\mathrm{ref})} & g \end{bmatrix}$

$\begin{bmatrix} \tilde{r} \\ c_1^{(+)} \end{bmatrix} = [\mathrm{M_R}]^{-1} V_R$ ▷ reflection coefficient $\tilde{r}$

$c_1^{(-)} = [a_1] c_1^{(+)}$

for (i = 1; i ≤ layer number-1; i++) **do** ▷ for idx in sub layer count

$c_i^{(+)} = [b]_{i-1} c_{i-1}^{(+)}$

$c_i^{(-)} = [a]_{i-1} c_{i-1}^{(+)}$

end for

$\tilde{t} = b_{i-1} c_{i-1}^{(+)}$ ▷ transmission coefficients

tiplication operation corresponds to matrix product operation. Details of the pseudo-code are hence: the conventional RCWA algorithm is run and matrices $\mathrm{X_i}$, $\mathrm{W_i}$, $\mathrm{V_i}$ are respectively eigenvalue exponents and field Bloch matrices (i.e., eigenvector matrices) of the RCWA eigen-matrices, which are calculated

for all sub-layers of the scattering device that are saved in computer's memory. Transmission and reflection region wavevector matrices $\mathrm{K}_z^{(\mathrm{trn})}, \mathrm{K}_z^{(\mathrm{ref})}$ are acquired as well. Then the algorithm for T matrix method is executed via a backpropagation method, which connects the sub-layers together into one matrix.

The most important part of this algorithm is that $\begin{bmatrix} f \\ g \end{bmatrix}$ and $\begin{bmatrix} a \\ b \end{bmatrix}$ are matrices and contain entire information about the scattering properties of each sub-layer within the structure. They are used to obtain $c^{(\pm)}$ propagation (power) vectors for scattered plane waves in each sub layer. They are used for calculating field distributions in the scattering structure as well as for calculating transmission coefficients. It is not a popular method in literature [53] due to memory requirements for a scattering device. The more grid points (i.e., pixels) the scattering device has, the more memory is acquired for storing $\begin{bmatrix} f \\ g \end{bmatrix}$, $\begin{bmatrix} a \\ b \end{bmatrix}$ and $c^{(\pm)}$ matrices for each sub-layer in the calculating regime. It is preferable to calculate reflection coefficients by such algorithm for maximum computational speed efficiency. In such a way additional calculations for transmission coefficients can be skipped.

1.3.2 Field computation

Field computation algorithm in RCWA by far is accomplished via incorporating T matrix method.

Algorithm 5 RCWA T matrix algorithm for field computation

Require: $c^{(+)}, c^{(-)}, \mathrm{W}, \mathrm{V}, \lambda, \tilde{\mathrm{K}}_x$
  Init: $i = 1, \mathrm{X}^{(\pm)}, f_{x,y,z}, F_{x,y,z}, k_x$
  for (i = 1; i ≤ layer number; i++) **do**
    $\mathrm{X}_i^{(+)} = e^{-\lambda k_0 L_i}$ ▷ Forward propagating phase
    $\mathrm{X}_i^{(-)} = e^{\lambda k_0 L_i}$ ▷ Backward propagating phase
    $f_y^{(i)} = \mathrm{W}_i \mathrm{X}_i^{(+)} c_i^{(+)} + \mathrm{W}_i \mathrm{X}_i^{(-)} c_i^{(-)}$ ▷ y Fourier harmonics
    $f_x^{(i)} = -\mathrm{V}_i \mathrm{X}_i^{(+)} c_i^{(+)} + \mathrm{V}_i \mathrm{X}_i^{(-)} c_i^{(-)}$ ▷ x Fourier harmonics
    if Mode is 'E' **then** ▷ s polarization case
      $f_z^{(i)} = -j[\mu]_i^{-1} \tilde{\mathrm{K}}_x f_y^{(i)}$ ▷ z Fourier harmonics
    else ▷ p polarization case
      $f_z^{(i)} = -j[\epsilon]_i^{-1} \tilde{\mathrm{K}}_x f_y^{(i)}$ ▷ z Fourier harmonics
    end if
  end for
  Adjust variables if necessary
  for (i = 1; i ≤ layer number; i++) **do**
    $F_x^{(i)} = \sum_{l=-N}^{l=N} f_x^{(i)} e^{-jk_{x,l}x}$ ▷ Total x field of i-th layer
    $F_y^{(i)} = \sum_{l=-N}^{l=N} f_y^{(i)} e^{-jk_{x,l}x}$ ▷ Total y field of i-th layer
    $F_z^{(i)} = \sum_{l=-N}^{l=N} f_z^{(i)} e^{-jk_{x,l}x}$ ▷ Total z field of i-th layer
  end for

Firstly, an entire T matrix method must be iterated for a device and their eigen matrices alongside with power amplitudes $c^{(\pm)}$ must be extracted. Then, by incorporating an RCWA formalism, its implementation of Fourier field components is executed. Then any dimensionality/periodicity value can be taken for such field computation.

Once algorithm is finished, $F_{x,y,z}$ are field components corresponding to H_x, E_y and H_z if computation is executed for E mode (s polarization), or E_x, H_y and E_z if the code execution is performed for H mode (p polarization). No numerical singularities ("NaNs") are encountered in the Alg. 5 due to $[\epsilon]$ and $[\mu]$ being hermitian Toeplitz matrices for 1D PBC. The small letters f denote field Fourier amplitude components, whereas capital letters F denote their full values, which incorporate spatial harmonics via complex exponents.

1.3.3 Scattering matrix method

Scattering matrix method is used for preserving memory of scattering structures, wave-guides and photonic crystals. Its main strength, compared to ETM method, is reduction of memory requirements via creating a global scattering matrix. However, such methodology acquires extra linear algebra treatment before it can be fully implemented.

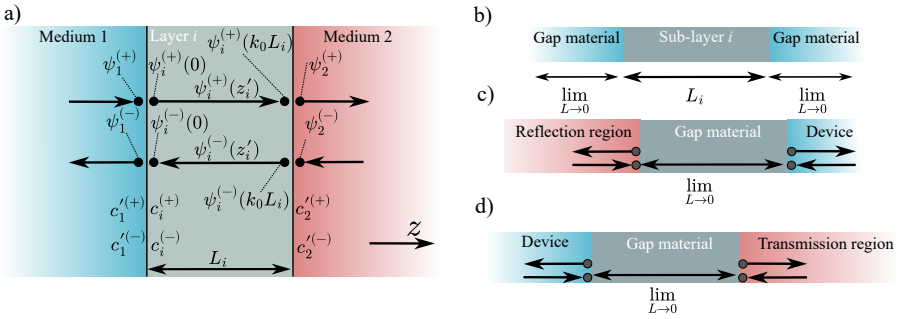


Figure 1.15: Schematics for S matrix method, involving asymmetrical layout of media between intermediate layer i (a), symmetrical layout of vacuum layers between intermediate sub-layer (b), and schematics for computation S matrix of reflection (c) and transmission (d) regions.

$$\mathrm{A}_{ij} = \mathrm{W}_i^{-1}\mathrm{W}_j + \mathrm{V}_i^{-1}\mathrm{V}_j, \tag{1.49a}$$

$$\mathrm{B}_{ij} = \mathrm{W}_i^{-1}\mathrm{W}_j - \mathrm{V}_i^{-1}\mathrm{V}_j, \tag{1.49b}$$

$$\mathrm{X}_i = e^{-\boldsymbol{\lambda}_i k_0 L_i}, \tag{1.49c}$$

$$\mathrm{S}_{11}^{(i)} = \left(\mathrm{A}_{i1} - \mathrm{X}_i\mathrm{B}_{i2}\mathrm{A}_{i2}^{-1}\mathrm{X}_i\mathrm{B}_{i1}\right)^{-1}\left(\mathrm{X}_i\mathrm{B}_{i2}\mathrm{A}_{i2}^{-1}\mathrm{X}_i\mathrm{A}_{i1} - \mathrm{B}_{i1}\right), \tag{1.49d}$$

$$\mathrm{S}_{12}^{(i)} = \left(\mathrm{A}_{i1} - \mathrm{X}_i\mathrm{B}_{i2}\mathrm{A}_{i2}^{-1}\mathrm{X}_i\mathrm{B}_{i1}\right)^{-1}\mathrm{X}_i\left(\mathrm{A}_{i2} - \mathrm{B}_{i2}\mathrm{A}_{i2}^{-1}\mathrm{B}_{i2}\right), \tag{1.49e}$$

$$\mathrm{S}_{21}^{(i)} = \left(\mathrm{A}_{i2} - \mathrm{X}_i\mathrm{B}_{i1}\mathrm{A}_{i1}^{-1}\mathrm{X}_i\mathrm{B}_{i2}\right)^{-1}\mathrm{X}_i\left(\mathrm{A}_{i1} - \mathrm{B}_{i1}\mathrm{A}_{i1}^{-1}\mathrm{B}_{i1}\right), \tag{1.49f}$$

$$\mathrm{S}_{22}^{(i)} = \left(\mathrm{A}_{i2} - \mathrm{X}_i\mathrm{B}_{i1}\mathrm{A}_{i1}^{-1}\mathrm{X}_i\mathrm{B}_{i2}\right)^{-1}\left(\mathrm{X}_i\mathrm{B}_{i1}\mathrm{A}_{i1}^{-1}\mathrm{X}_i\mathrm{A}_{i2} - \mathrm{B}_{i2}\right) \tag{1.49g}$$

The generalized S matrix method presented in Eq. (1.49) incorporates boundary conditions of the field ψ for the i-th medium between the adjacent ones. The expressions in Eq. (1.49) can be simplified by applying mathematical trickery such as "vacuum layers", visualized in Fig. 1.15.

Algorithm 6 RCWA S matrix algorithm for device S matrix computation, simplified.

Require: $\mathrm{K}_z^{(\mathrm{trn})}, \mathrm{K}_z^{(\mathrm{ref})}, \mathrm{K}_x, [\varepsilon_r], \mathrm{L}, k_0$ ▷ RCWA parameters

Init: $\mathrm{W}_0, \mathrm{V}_0, S^{(global)}$

for (i = 1; i ≤ layer number; i++) **do**

Execute RCWA algorithm for i-th sub layer and obtain $\mathrm{X}, \mathrm{W}, \mathrm{V}$

$\mathrm{A} = \mathrm{W}^{-1}\mathrm{W}_0 + \mathrm{V}^{-1}\mathrm{V}_0$

$\mathrm{B} = \mathrm{W}^{-1}\mathrm{W}_0 - \mathrm{V}^{-1}\mathrm{V}_0$

$\mathrm{F} = \mathrm{A} - \mathrm{XBA}^{-1}\mathrm{XB}$

$S_{11} = \mathrm{F}^{-1}(\mathrm{XBA}^{-1}\mathrm{XA} - \mathrm{B})$

$S_{12} = \mathrm{F}^{-1}(\mathrm{A} - \mathrm{BA}^{-1}\mathrm{B})$

$S_{21} = S_{12}$

$S_{22} = S_{11}$

$S_l = \begin{bmatrix} S_{11} & S_{12} \\ S_{21} & S_{22} \end{bmatrix}$

$S^{(global)} = S^{(global)} \bigotimes S^{(l)}$ ▷ Connect layers in z direction

end for

Connect S_G matrix with reflection and transmission regions

$S^{(global)} = S^{(ref)} \bigotimes S^{(global)} \bigotimes S^{(trn)}$

$\tilde{r} = S_{11}\delta_{0,N_h}$ ▷ reflection coefficients

$\tilde{t} = S_{21}\delta_{0,N_h}$ ▷ transmission coefficients

$k_z^{(inc)} = \sqrt{\mu_R \epsilon_R}\cos\theta$

$T = \frac{\mathrm{Re}[\mathrm{K}_z^{(\mathrm{T})}/\mu_T]}{\mathrm{Re}[k_z^{(inc)}/\mu_R]}|\tilde{t}|^2$ ▷ Tranmission orders

$R = \frac{\mathrm{Re}[-\mathrm{K}_z^{(\mathrm{R})}/\mu_R]}{\mathrm{Re}[k_z^{(inc)}/\mu_R]}|\tilde{r}|^2$ ▷ Reflection orders

The first vacuum layer application case is for adjacent layers of the i-th medium. In this scenario, the off-diagonal and on-diagonal elements of S matrix are equal, hence reducing computations only for S_{11} and S_{12} components. The computations are visualized in Alg. 6. Two other cases correspond to the i-the layer being the intermediate one. Their S matrix components are derived separately, including transmission (substrate) and reflection (superstrate) regions. Their respective values are visualized in Alg. 9 and Alg. 10 in Appendix.

The RCWA algorithm is executed inside the S matrix method. Eigen matrices need not to be saved in memory due to their straightforward incorporation into the S matrix formalism inside Alg. 6. Once S matrix components in S_l are saved, they are 'connected' together to form a new S matrix through Redheffer product, which is presented in Alg. 7. The product itself exploits boundary conditions used to connect all of the device sub-layers. Its main property is the update of new matrix elements from S_{11} to S_{12}, then S_{21} and S_{22} in a "zig-zag" fashion. Such procedure is continued until transmission region (substrate) is reached. Then, the new matrix elements are saved, ready to be utilized for further connection with next sublayer's computed S matrix. Unit power source of zeroth harmonic $c_{\mathrm{inc}} = \delta_{0,N_h}$ is incorporated and reflection and transmission

coefficients are extracted through S_{11} and S_{21}, respectively.

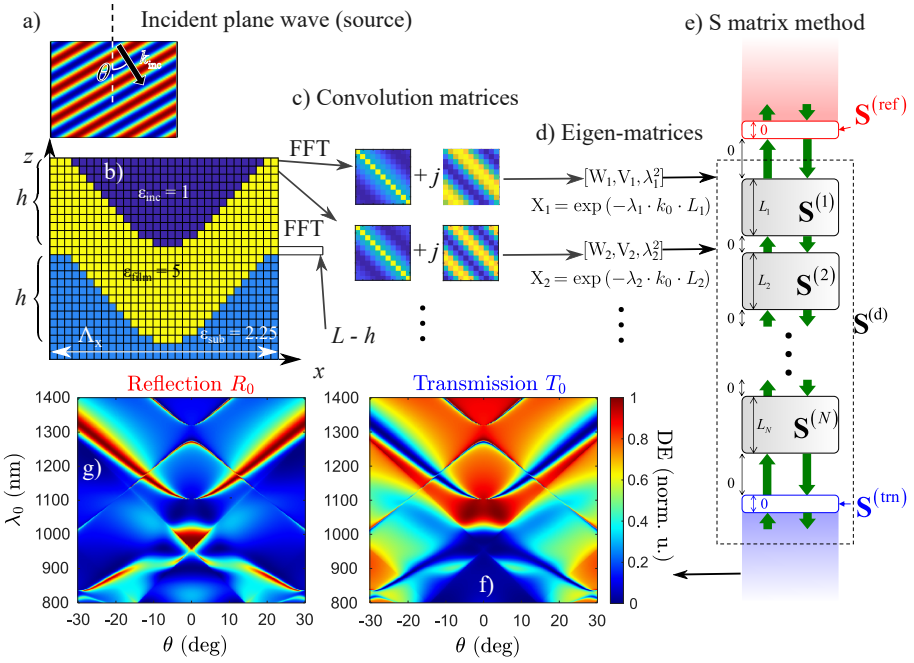


Figure 1.16: A conceptual schematic of RCWA algorithm with memory efficient Scattering matrix method. The step-wise parts are presented in the following: a) incident source field as a plane wave, b) transversely periodic discrete GMR filter/coupler, c) Toeplitz matrices of Fourier transformed sub-layers, d) Eigen-matrices of Ω matrix e) S matrix method schematic (block connection, adapted from [92]) and f) and g) are zeroth order transmission and reflection values of the device b).

The final step is to implement scattering matrix formalism for transmission and reflection regions. Once they are implemented, they are then connected with the Scattering matrix of a device, thus building the global scattering matrix, involving the regions through which DEs are then calculated. An entire DE calculation process can be summarized in the schematic which is illustrated in Fig. 1.16.

The device (shown in Fig. 1.16 a)) pertains the GMR structure with its thickness L greater than grating depth h. In such a case a homogeneous layer persists, a sub-layer with thickness of $L-h$. A full device needs to be simulated by Finite Difference method, however, one slice of homogeneous layer is enough for fast computations in RCWA algorithm, which is the main strength of S and T matrix methods. Each convolution matrix is computed for the sub-layer that are saved in memory. Then, eigen-matrices are computed via Alg. 3 and are incorporated in S matrix method via Alg. 6. Once Redheffer's product is applied S matrices are computed for reflection (superstrate) and transmission

(substrate) regions. The zeroes in 1.16 e) denote vacuum sub-layers with $L = 0$ thicknesses, which is essential for the simplified S matrix

Algorithm 7 RCWA Redheffer product for sub-layer connection.

Require: $\mathrm{S}^{(\mathrm{A})}, \mathrm{S}^{(\mathrm{B})}$

$\mathrm{D} = \mathrm{S}_{12}^{(\mathrm{A})}(\mathrm{I} - \mathrm{S}_{11}^{(\mathrm{B})}\mathrm{S}_{22}^{(\mathrm{A})})^{-1}$

$\mathrm{F} = \mathrm{S}_{21}^{(\mathrm{B})}(\mathrm{I} - \mathrm{S}_{22}^{(\mathrm{B})}\mathrm{S}_{11}^{(\mathrm{A})})^{-1}$

$\mathrm{S}_{11} = \mathrm{S}_{11}^{(\mathrm{A})} + \mathrm{D}\mathrm{S}_{11}^{(\mathrm{B})}\mathrm{S}_{21}^{(\mathrm{A})}$

$\mathrm{S}_{12} = \mathrm{D}\mathrm{S}_{12}^{(\mathrm{B})}$

$\mathrm{S}_{21} = \mathrm{F}\mathrm{S}_{21}^{(\mathrm{A})}$

$\mathrm{S}_{22} = \mathrm{S}_{22}^{(\mathrm{B})} + \mathrm{F}\mathrm{S}_{22}^{(\mathrm{A})}\mathrm{S}_{12}^{(\mathrm{B})}$

$S_{\mathrm{AB}} = \begin{bmatrix} S_{11} & S_{12} \\ S_{21} & S_{22} \end{bmatrix}$ ▷ Save to updated S matrix

Once all of the transmission and reflection components of Fourier modes are calculated, it is time to re-normalize them to transmission T and reflection R orders. The essence of diffraction efficiency calculation is the same as presented in Eq. (1.27) and Eq. (1.28).

1.4 Optimization methods

Optimization algorithms are used to find the parameters $\mathbf{x} = [x_1, x_2, ..., x_N]$ of the minima of a merit function $f(\mathbf{x})$. The most popular ones are a gradient descent and genetic algorithms. The former utilizes initial conditions $\mathbf{x}^{(0)}$ as a guess for N-th number of variables to tune, the latter is used without manually setting initial conditions in phase space and this algorithm utilizes randomness to achieve best-available local minima. The phase space is parameter space, where the algorithm performs a search for a minimum of a function. The requirement for all optimization methods is the use of boundary conditions, which satisfy the boundaries of the physical system and in which the search for best local minimum is numerically applied. In this case, the "best" minimum is lowest possible value being achieved that satisfy given boundaries. This section briefly analyzes the details that are acquired to comprehend genetic algorithm's performance.

1.4.1 Genetic algorithm

Genetic algorithm to this day remains one of the most successful stochastic global optimization algorithms [93, 94]. Global optimization methods do not acquire initial conditions for parameter search of function extrema, whereas local optimization algorithms do. The former characteristic is what brings comfort for device designers and data fitting if there is no prior knowledge of the physical system, hence the comfort of the algorithm. In this work, the genetic optimization problem can be summarized in the pseudo algorithm presented in Alg. 8.

Algorithm 8 Genetic algorithm (pseudo-form)

Require: $f(\mathbf{x})$, UB, LB, var num, hyper params ▷ Initial parameters
  Init: $\mathbf{x}^{(0)}$ and $c = f(\mathbf{x}^{(0)})$ ▷ Random *Position* and its *Cost*
  for (int i = 0; i < max iterations; i++) **do**
    P = $e^{-\beta \cdot c}$ ▷ Selection probability through *Cost* c
    Init: y ▷ offspring population
    for (int j = 0; j < n_C; j++) **do** ▷ Main loop
      $x_{1,2}^{(0)} <-$ RWS (P, population) ▷ Select best parent candidates
      $y_{1,2}^{(c)}$ = uniform crossover($x_{1,2}^{(0)}$,γ) ▷ uniform crossover
    end for
    for (int l = 0; l < n_C; l++) **do** ▷ Perform crossover
      y_l = mutate(x_l, μ, σ) ▷ Population Mutation
      Check for boundaries (UB and LB)
      Evaluate $f(x)$ through $f(y_l)$ ▷ Extract *Cost*
      if (Current *Cost* > Previous *Cost*) **then** ▷ Compare *Costs*
        Best *Cost* = Current *Cost*
      end if
    end for
    Sort population according to *Cost*
    Display iteration and best *Cost* value
  end for

Genetic algorithm acquires boundary conditions for parameter search, variable number (which in the case of the linear optical systems is a parameter vector length len($\mathbf{x}$), where $\mathbf{x}$ incorporates parameter values) as well as its hyper-parameters, which adjust the extrema search procedure alongside with the model.

The very first step is random initiation of the parameter *Position* and calculation of its *Cost*. The former term is is an array of initial conditions all over the parameter space, whereas the latter term is the collection of the merit function values for each random initial condition. The first hyperparameter is the length of *Position* and *Cost* arrays, which is the ***population*** number. The initial conditions are considered as ***parents*** for the upcoming ***populations***, whose cost functions are expected to have lower values. In the case of FDFD or RCWA simulations in frequency domain, the population is considered as

design parameters (mainly geometrical) that satisfy the minimum of a merit function, which is a single number.

The ***iteration number*** is another hyperparameter which is chosen for iterative process count of the genetic algorithm. Furthermore, the probability factor P is calculated via the best cost value and its hyperparameter β, which is a weighing factor in the exponent.

$$y_1 = \alpha \mathrm{x}_1 + (1-\alpha)\mathrm{x}_2, \tag{1.50a}$$
$$y_2 = (1-\alpha)\mathrm{x}_1 + \alpha \mathrm{x}_2. \tag{1.50b}$$

The next step is the population initialization. In the ***offspring*** initialization process, with $x^{(0)}$ in mind, the uniform distribution is applied in the range of given boundaries. The cost is evaluated, and the best cost values are ordered in descending manner. Furthermore, the Rhoulette Wheel Selection (RWS) method is applied. It sums up the fitness of all individuals and asserts the selection probability for each individual, satisfying condition ($r \leq c$), where r is uniformly drawn random value from the population and c is the total cost per all populations.

The cross-over function is done so between two parents x_1 and x_2 with weights α, which is a random number taken from the uniform distribution between $0-\gamma$ and $1+\gamma$. Here the γ ***is another hyperparameter*** which barely "adjusts" the α values in hopes to find a better local minimum.

The cross-over iteration is performed over the times n_C, which is a hyperparameter, specifying the ***cross-over iteration number***. The next step is the population mutation, which is done so with the Normal (Gaussian) distribution for the continuous valued offspring values. The hyperparameter that defines ***which percentage of offspring*** are to be mutated is μ. The hyperparameter σ is the ***dispersion*** (spread) factor of the normal distribution. The cost with populations are sorted out in descending order.

The genetic algorithm's hyper-parameters with their used values can be summarized in the following:

1. Population number n_{pop}, the population array length. Default values are in range $[100, 200]$.
2. Cross-over number $\mathrm{n_C}$, which is mostly 2, but can be increased via parallel programming. Must include high RAM if array size is large.
3. Iteration number n_{it}. Specifies main iteration count in the algorithm.
4. The offset parameter γ. Its values are usually within $[0, 10^{-2}]$.
5. Offspring mutation parameter μ, in range of $[0.1, 0.3]$.
6. Mutation dispersion σ, with default value of 0.1.

Chapter 2

Broadband reflection and angular filtering based on anomaly

Rayleigh anomaly combined with leaky mode regime are known to provide broad-band reflectance in high contrast GMR filters [86] after precisely tuning the geometry of the device. Studies show that wavelength at Rayleigh anomaly λ_R confines broadband reflection in angular spectrum, and such a wavelength also acts as a start of a stop-band, allowing incident light to reflect from the the resonant cavity [95–97]. Such response can be particularly useful for compact lasing systems as a filtering mirror components, where multilayer Bragg gratings are replaced by single layer GMR based thin film gratings, such as vertical-cavity surface-emitting lasers (VCSELs) in order to stabilize their spectral and emission direction [98]. In this work, the same physical mechanism of broadband spectral reflectance is used for trapezium shaped gratings, due to their common abundance in the photonics industry [99, 100]. The main goal of this work is to tune the geometry of the trapezium shaped GMR device, so light filtering properties are realized in both angular and spectral regimes.

The material related to this thesis is published in paper [**A2**] *and conference* [**C6**].

2.1 Trapezium interfaced waveguide concept

The GMR filters of interest possess a trapezium shaped geometry in the transverse period direction. The substrate as well as the thin film in RCWA model pertain the same geometric profiles and the geometry representation of the trapezium filter is shown in Fig. 2.1.

Leaky modes in are guided modes within the thin film that pertain broad evanescent tails to the substrate near the wavelength which corresponds to Rayleigh anomaly. Once it is crossed into the sup-wavelength regime, the leaky mode becomes a propagating diffracted wave with a near-90-degree angle with respect to the normal vector of the grating (in z axis in the RCWA case). The leaky modes can also be added to provide a broadband response - instead of a single guided mode, the reflection response of the device is made of a number of modes that are in superposition and are visible in zeroth-order transmission spectra as sharp dips [95–97]. It is heavily implied that such an addition of guided modes provides continuous reflection in the spectral domain at normal or near-normal incidence. The goal of this work is to achieve a narrow-band reflection in the angular domain by retaining continuous reflection in spectral domain. A trapezium grating is chosen to substantially narrow-pass filtering. The geometrical features so far are chosen to be: $w_{\text{bot}} = 375$ nm, $w_{\text{top}} = 175$ nm, $\Lambda_x = 638$ nm, $h = 238$ nm, $n_{\text{sub}} = 1.5$, $n_{\text{film}} = 2.25$, whereas L, the

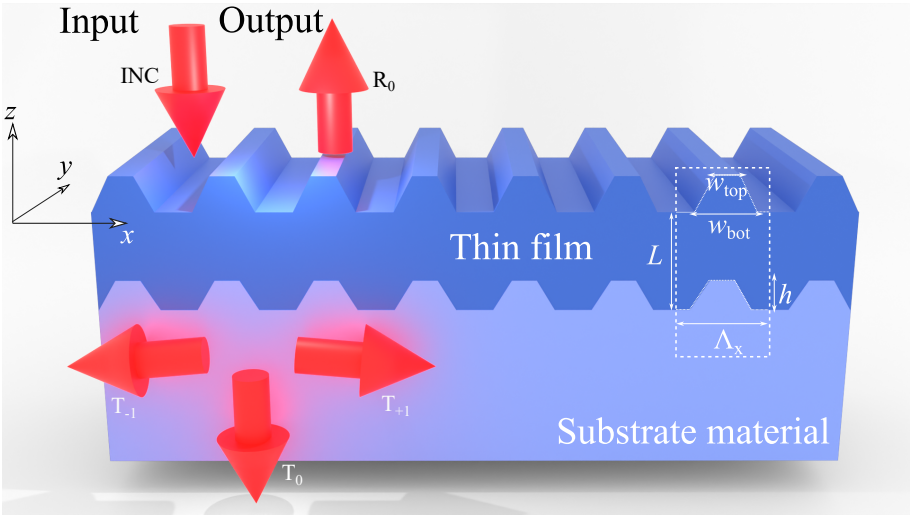


Figure 2.1: The angular filtering device with double periodic thin film modulation via trapezium interface.

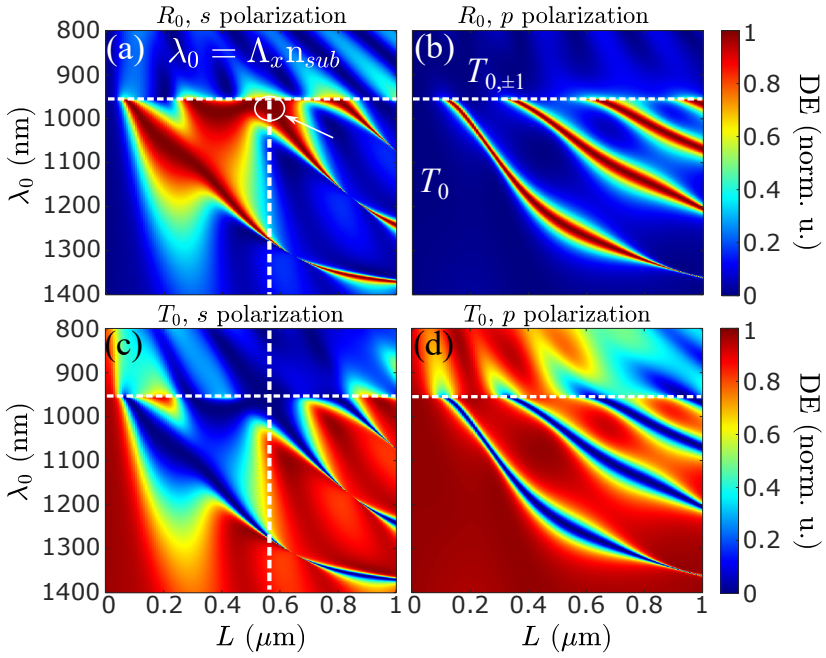


Figure 2.2: Zeroth order reflection profiles for s polarization (a) and p polarization (b) and the transmittance spectra for respective polarizations in (c) and (d). Angle of incidence is $\theta = 0$ deg.

thickness parameter, was found via a parameter sweep of the reflection and transmittance spectra [96]. Such a procedure is illustrated in Fig. 2.2.

The dotted lines in Fig. 2.2 (a-d) correspond to the Rayleigh anomaly, where a smaller wavelength experiences a sudden rise in $T_{\pm 1}$ diffraction orders in the substrate region at normal incidence, which is visible for a sudden loss of T_0 values in Fig. 2.2 (c-d). Near the anomaly, a stop band occurs given $\Delta\lambda_0 =$ 46 nm at $L = 580$ nm. Also, for increased L values, redshift of GMR-based reflectance curves is visible for both s and p polarizations. The s polarization case (see Fig. 2.2 (a)) experiences narrowing of the resonance. Also, the power distribution from the zeroth-order diffraction to first order diffraction is visible in Fig. 2.2 (c) and (d). The s polarized input in this case experiences greater energy redistribution to first order diffraction compared with p polarized incident electromagnetic wave.

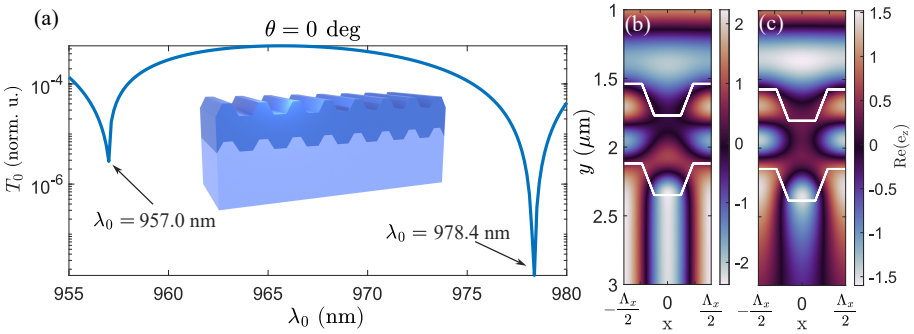


Figure 2.3: Zeroth order transmission with its spectral dips (a) and field distributions given those dips (b,c). The fields (b) and (c) correspond to the transmission dips at $\lambda_0 = 957.0$ nm and $\lambda_0 = 978.4$ nm.

The transmittance T_0 at $L = 580$ nm is shown for s polarized input at a normal angle of incidence in Fig. 2.3 (a), alongside with electric fields e_z at dip wavelengths at $\lambda_0 = 957.0$ nm and $\lambda_0 = 978.4$ nm. The first dip is located directly near the anomaly, and it is the reason why there is much greater leakage of the evanescent field into the substrate. Then, at the second resonance, the field profile resembles very similar perturbation from the grating, but with smaller leakage. Overall, such a stop band is formed out of the superposition of resonances that are identified as dips in transmission on a logarithmic scale. The mode is guided along the interface of the substrate along x the direction with strong field leakage.

2.2 Numerical results

The corresponding zeroth-order reflection profile for s polarized input is presented in Fig. 2.4 (a). It pertains broadband reflectance at normal incidence with its bandwidth at $\Delta\lambda_0 = 46$ nm for near 100% reflection. The triangular

characteristic shape in R_0 spectrum is due to the Rayleigh anomaly, which acts as a cut-off region between sub-diffraction and sup-diffraction regimes.

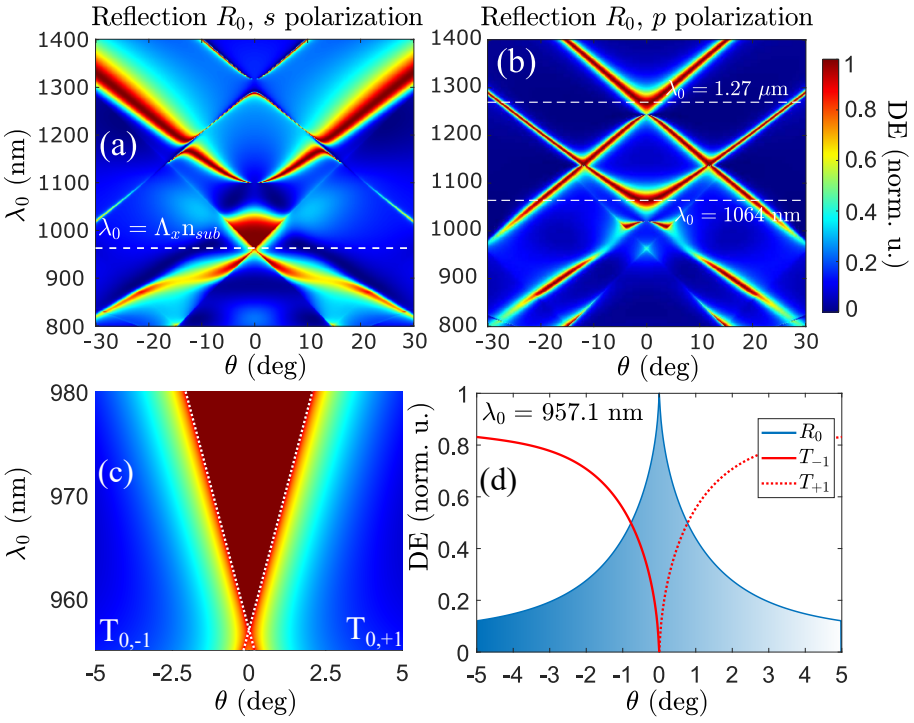


Figure 2.4: Zeroth order reflection of s polarization (a,c) and p polarization (b), alongside with diffraction efficiencies (d) for s polarized input. Dashed lines (and red ones) refer to additional diffraction orders.

If the polarization of input source is p (see Fig.2.4 (b)), GMR will be formed for normal incidence at $\lambda_0 = 1064$ nm as well as at $\lambda_0 = 1.27$ μm. They correspond guided modes that fully couple incident wave with a mirror like reflection. However, broadband reflection profile cannot be achieved for this case, but only for s polarized input. The zoomed-in zeroth order reflection spectrum is shown at Fig. 2.4 (c). Here the broadband reflection [95, 97] pertains its broadband features for normal incidence, and it does so for oblique incidence until cut-off region is reached [101] at Rayleigh anomaly. In this case the exchange of power between the incident wave and additional diffraction orders ($T_{\pm 1}$) for oblique incidence is present. The quantitative numerical result of such an effect is illustrated in Fig. 2.4 (d). The values of $T_{\pm 1}$ increase further away for normal incidence.

In the application sense, this result would be useful to provide losses to high spatial frequency components via first order diffraction (that corresponds to divergence) of noisy incident beam, thus reducing M^2 parameter of highly divergent optical beams. Also, further topology optimization is acquired for

decreasing FWHM of the reflectance, so that only Rayleigh anomaly is able to enforce a more rapid decrease of R_0 value at oblique angle of incidence in angular domain.

2.3 Experimental results

This section covers the fabrication of GMR filter on trapezium shaped FS (Fused Silica) substrate. The deposition of Ta_2O_5 thin film layer is performed with IBS technology. The results are shown in Fig. 2.5.

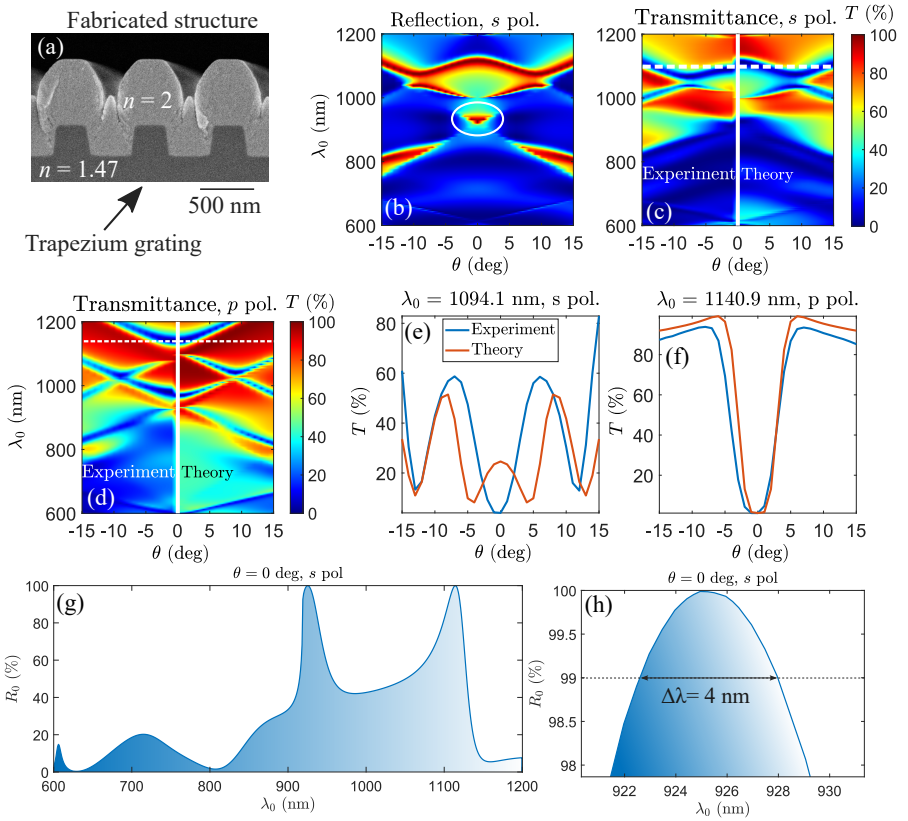


Figure 2.5: Cross-section of the fabricated structure (a), Simulated zeroth order reflection spectrum (b) with triangular reflection, zeroth order transmission comparison between measured and simulated maps of s (c) and p (d) polarizations, as well as their angular profiles in (e) and (f), respectively. The computed reflectance spectrum at normal incidence (g) and its zoom at (h).

The cross-section of fabricated structure (Fig. 2.5 (a)) reveals that thin film repeats only the periodicity, but not the modulation of the structure. The top layer's geometry reveals an expanded dielectric filling along the transverse

direction. Also, grooves pertain additional spurious growths between them. Auto-cloning procedure is performed on the gratings, whose periodicity $\Lambda_x = 625$ nm and grating amplitude $h = 250$ nm. Thin film thickness $L = 460$ nm in this case, and its material's refractive index of 2.09 for 970 nm.

The numerical simulations are accustomed for the same fabricated structure. The measured angular/spectral responses at zeroth order transmission for s and p polarized inputs alongside with numerical results are provided via a comparison in Fig. 2.5 (c,d,e,f). The mirror-like reflection that corresponds perfectly to transmission (Fig. 2.5 (b)) indeed does provide leaky mode regime near the Rayleigh anomaly, even if the modulation function of the top layer is non-repeated, although the flat-top reflection is poorly maintained for $\Delta\lambda_0 = 4$ nm of spectral width, which is shown in Fig. 2.5 (g,h). The agreement between the numerical predictions and the spectral measurements is best for the p polarization case in sub-wavelength regime.

The non-satisfactory results are achieved due to the unexpected behavior of thin film growth on the structure. The trapezium grating pertains sharp edge geometry which led to the increase of dielectric fill factor in a single period during the thin film growth. Therefore, it is mandatory to include additional algorithms that simulate growth topology during autocloning procedure [49]. One candidate is String Method [102], while the other simpler one, Fast Marching Method [103] for prediction of surface topology growth on gratings with sharp geometrical features.

2.4 Summary

This section investigates Rayleigh anomaly's application for broadband resonant reflection which is also confined according to the formula $\lambda_R = \Lambda_x(n_{\text{sub}} \pm \sin\theta)$. The broadband reflectance is due to the interfering GMRs that are at close spectral vicinity to each other and their respective fields pertain evanescent tails straight to the substrate. The device that is suggested for the spectral and angular confinement is trapezium conformal grating with Nb_2O_5 thin film. Due to the spectral and geometry sweep study so far, only s polarization is capable of such broadband spectral response, whereas p polarization pertains partial transmittance in the given wavelength range. The broadband response is observed for $\Delta\lambda = 46$ nm of spectral width. At an oblique angle of incidence, the power of the incident wave is transmitted to the ± 1 diffraction orders once the Rayleigh anomaly is crossed. Normalized geometrical parameters of the trapezium shaped filter are: $L/(\Lambda_x n_{\text{sub}}) = 0.606$ and $h/(\Lambda_x n_{\text{sub}}) = 0.248$ where $\Lambda_x = 638$ nm and $n_{\text{sub}} = 1.5$ and thickness $L = 580$ nm.

Furthermore, the auto-cloning procedure of the thin film filter is performed via IBS method on the trapezium shaped gratings. The topology of the Ta_2O_5 thin film does not repeat the ideal structure and pertains greater filling factor of the material. However, leaky mode based GMR remains near the Rayleigh anomaly and its reflectance is pertained, yet at worse, $\Delta\lambda_0 = 4$ nm of spectral width.

Chapter 3

Investigation of GMR near the 'Edge of Continuum' in conformal thin film gratings

The short theoretical introduction described leaky modes (and its corresponding reflection) as a consequence of the Rayleigh phenomenon which is studied by R. Magnusson [95–97, 101, 104]. In this chapter, the thorough analytical, numerical and experimental analyses are performed on linear waveguide system that possess bounded photonic states at continuum edge.

The material related to this thesis was published in paper[**A1**] *and conferences from* [**C1**] *to* [**C6**].

3.1 Analytical model

The analytical model is borrowed from the fundamentals of quantum mechanics: an asymmetrical finite quantum potential well. Its resonant behavior corresponds to the localization of the incident waves inside the well. By careful tuning the geometrical properties, such as width, depth and potential values of the well, and energy of incident wave, unusual phenomenon occurs at the top edge, which corresponds the separation between the well ant the continuous space in which the wave is capable of traveling. Such a separation is named as the Edge of the Continuum (EOC), and is the driving factor of asymmetrical resonances encountered in zeroth order reflection spectra from excited monolayered thin film wave-guiding devices. Considering the master equation for monochromatic field propagation in the linear media:

$$\nabla \times \left(\nabla \times \vec{E}(\vec{r}) \right) = \frac{\omega^2 \varepsilon(\vec{r})}{c^2} \vec{E}(\vec{r}). \tag{3.1}$$

Here (3.1) can be further reduced to Laplacian propagator, given $\Delta = \nabla^2$, the propagation equation is then written as:

$$\Delta \vec{E}(\vec{r}) = \frac{\omega^2 \varepsilon(\vec{r})}{c^2} \vec{E}(\vec{r}). \tag{3.2}$$

Then, the propagation of the wave can be further simplified given the homogeneous dependence of $\varepsilon(\vec{r})$ on x and z directions, hence the 2D equation for wave propagation:

$$\frac{\partial^2 E_z}{\partial x^2} + \frac{\partial^2 E_z}{\partial z^2} - \frac{\omega^2 \varepsilon(z)}{c^2} E(z) = 0. \tag{3.3}$$

The following ansatz is then substituted into Eq. (3.3).

$$E_1(x, z, t) = A_1(z) e^{j(k_{1,x} x + k_z - \omega t)}. \tag{3.4}$$

Here $k_{1,x} = k_{0,x} \pm q_x$ and $q_x = 2\pi/\Lambda_x$, where only one spatial harmonic of diffraction is included. Here, $k_{0,x}^2 + k_{0,z}^2 = k_0^2$ satisfies dispersion relation, given $k_0^2 = \omega^2/c^2$.

From this point, the model can be constructed to include the ansatz Eq. (3.4) into the propagator Eq. (3.2). Then, for guided modes in thin films, the propagator is written in the following:

$$\frac{\mathrm{d}^2 A_1(z)}{\mathrm{d}z^2} + \left(\frac{\omega^2 \varepsilon(z)}{c^2} - (k_{0,x} + q_x)^2 \right) A_1(z) = 0 \tag{3.5}$$

Equation (3.5) rigorous for the case of s-polarized waves and is similar to the Schrödinger's equation for a quantum particle with the energy $E = k_0^2 - (k_{0,x} + q_x)^2$ in the potential well with the potential profile $V(z) = (1 - \varepsilon(z))k_0^2$. The mentioned potential V supports the states bounded within the well. Such resonances correspond to the guided modes within the thin film. The coupling between the bounded resonances $A_1(z)$ and a considered Fabri-Perrot (FP) radiation $A_0(z)$ results in Fano-type resonance with asymmetrical features in the energy spectrum. A Fano resonance in this case is the asymmetrical spectral line shape that arises from the interference between a discrete guided mode and a FP radiation mode within the periodically modulated thin-film structure. A more useful manner is to rewrite the propagator Eq. (3.5) which incorporates coupling between guided modes and the FP radiation via external driving component (source injection):

$$\underbrace{\frac{\partial^2 A_1(z)}{\partial z^2} + (E - V(z))A_1(z)}_{\text{Schrödinger's equation}} - \underbrace{j\gamma(z)e^{jk_{0,z}z}A_0(z)}_{\text{external driving}} = 0 \tag{3.6}$$

Here $E = k_0^2 - (k_{0,x} + q_x)^2$ and coupling coefficient is $\gamma(z)$. The (3.6) includes a plane wave component, which is:

$$E_0(x, z, t) = A_0(z)e^{j(k_{0,z}z + k_{0,x}x - \omega t)}. \tag{3.7}$$

The asymmetrical potential well system is presented in Fig. 3.1 (a) and EOC is at the potential value V_S. Deeper within the potential well, the reflection profile is visible, which has an asymmetry, but continuous features. In this case, the field is confined within the thin film (see Fig. 3.1 e)). However, at the EOC, the resonant field, corresponding to the sharp asymmetrical reflection, pertains evanescent tail (see Fig. 3.1 f)).

In order to achieve the resonance response of Eq.(3.6), the ansatz is then applied:

$$A_{1,s}(z) = \underbrace{a_{0,s}e^{jk_{0,s}z}}_{\text{FP mode}} + \underbrace{a_{+,s}e^{jk_{z,s}z} + a_{-,s}e^{-jk_{z,s}z}}_{\text{guided modes}} \tag{3.8}$$

Where $k_{z,s}^2 = E - V_s$ is a wavevector at a potential section s and $a_{0,s} = \frac{j\gamma_s A_{0,s}}{E - V_s - k_0^2}$. Here, the solution is provided through matching wave-functions at the sections of a driven potential well as well as their derivatives. To calculate

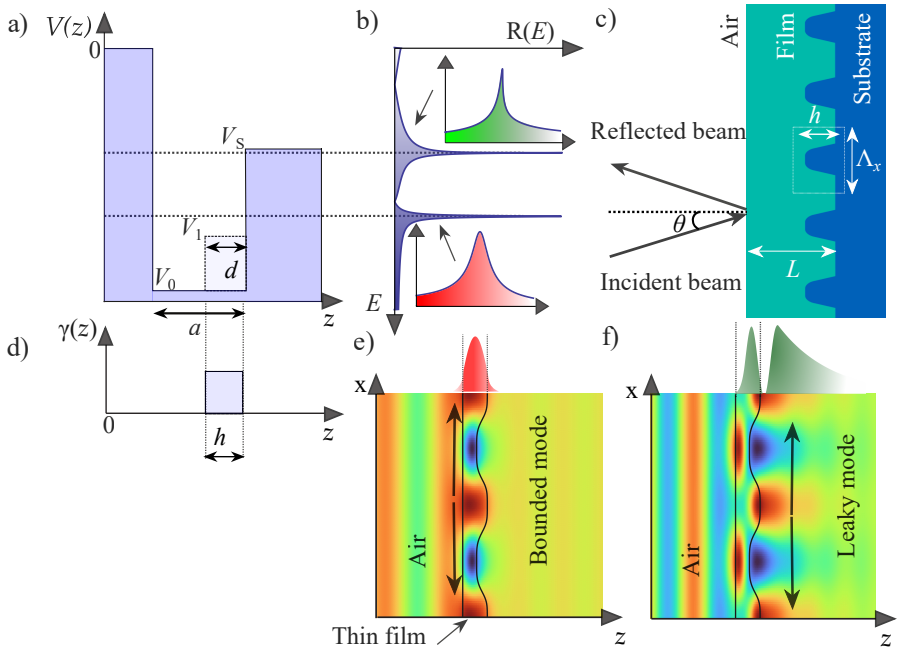


Figure 3.1: Potential well (a,b) is equivalent to the film of high refraction index with periodically modulated interfaces (d). The interface modulation couples the FP mode into the waveguided modes (e) or leaky surface modes (f), resulting in usual Lorenz or sharp-peaked resonances, respectively (c). The modification of the refraction index in the coupling area is shown by the line in (a).

the transmission and reflection coefficients, it is convenient to introduce the response function of the FP mode

$$g_0 = \frac{j}{A_0} \int \gamma(z) A_1(z) e^{jk_{0,s}z} \mathrm{d}z \tag{3.9}$$

The i-th roundtrip formula for the FP mode's amplitude in the film with respect to the incident amplitude $A^{(\mathrm{inc})}$ is considered as with introduced response/gain factor g_0:

$$A_0^{(i+1)} = A_0^{(i)}(1+g_0)r^2 e^{j\phi} + A^{(\mathrm{inc})} \tag{3.10}$$

At the normal incidence, the transmittance coefficient $t = \frac{\sqrt{2n}}{n+1}$ and $r^2 + t^2 = 1$. The phase accumulation $\phi = 2nak_{0,z}$ is around one trip i in a potential well with its width a. The optical path length in this case is $2na$ for $i = 1$. In this model coupling is chosen $\gamma = \frac{\gamma_0}{a}$, where a is the width of the potential well. For the shallow modulation $h << \lambda_0$, the $\gamma_0 \approx h\frac{n-1}{\lambda_0}$. Given the condition that $A_0^{(i+1)} = A_0^{(i)}$, it follows:

$$\frac{A_0^{(i)}}{A_0^{(\mathrm{inc})}} = \frac{t}{1-(r^2+g_0)e^{j\phi}}. \tag{3.11}$$

In this case the g_0 can be used as a parameter for the calculation of the reflection coefficient R_{FP}. By choosing $\phi = 0$, the simplification occurs and the formula for the reflection can be derived:

$$R_{FP} = \frac{|1-\frac{g_0}{t^2}|^2 - 1}{|1-\frac{g_0}{t^2}|^2} \tag{3.12}$$

The principles are applied for the system, comprised of the potential well with external driving. The potential well is defined in the following. For $z = [-\infty, 0]$, the potential $V(z) = \infty$. Then, for $z = [0, L]$, $V(z) = -V_0$. At $z > L$, $V = 0$. In other words, the potential well is divided into the 2 regions where the wave amplitudes are non-zero, therefore

$$A_1(z) = \alpha_1 \cos(k_1 z) + \beta_1 \sin(k_1 z) + \delta_1 e^{jk_0 z}, \text{region I}, \tag{3.13a}$$

$$A_2(z) = \alpha_2 e^{jk_2 z}, \text{region II}. \tag{3.13b}$$

Where wavevectors correspond to $k_1 = \sqrt{E - V_0}$, $k_2 = \sqrt{E}$ and

$$\delta_1 = \frac{j\gamma A_0}{E - V_0 - k_0^2}. \tag{3.14}$$

The constants $\alpha_{1,2}$ and β_1 can be found by introducing boundary conditions $A_1(a) = A_2(a)$ and $\frac{\mathrm{d}}{\mathrm{d}z}A_1(a) = \frac{\mathrm{d}}{\mathrm{d}z}A_2(a)$. The goal is to find g_0, which is done so via (3.9). Assuming narrow potential well $ak_0 << 1$:

$$g_0 = \frac{\gamma_0^2}{a^2(E-V_0)k_1} \cdot \frac{2k_2 - (2k_2 + jak_1^2)\cos(ak_1) - k_1(ak_2 - j)\sin(ak_1)}{k_1\cos(ak_1) - jk_2\sin(ak_1)}. \tag{3.15}$$

The near resonance approximation can be applied for the response function (3.12), where g_0 approaches infinity, due to zeroing of the denominator. Then, introducing $\phi = \arctan(jk_2/k_1)$, the generalized response is reduced to

$$g_0 = \frac{\gamma_0^2}{a^2}\frac{j\sqrt{V_0}}{k_1^3 k_2} \cdot \frac{2k_2^2 + (k_1^2 - 2k_2^2)\cos(ak_1)}{\cos(ak_1 + \phi)} \tag{3.16}$$

The analytical solutions are presented in two cases, whose corresponding gain factors are provided in (3.17) and (3.18) for asymptotic behavior:

$$g_0^{(bot)} = \frac{2j\gamma_0^2}{a^2}\frac{1}{\sqrt{a^2 - \pi^2/V_0}}\frac{1}{\Delta E} \tag{3.17}$$

$$g_0^{(top)} = \frac{-8\gamma_0^2}{\pi a^2}\frac{1}{\sqrt{\Delta E}} \tag{3.18}$$

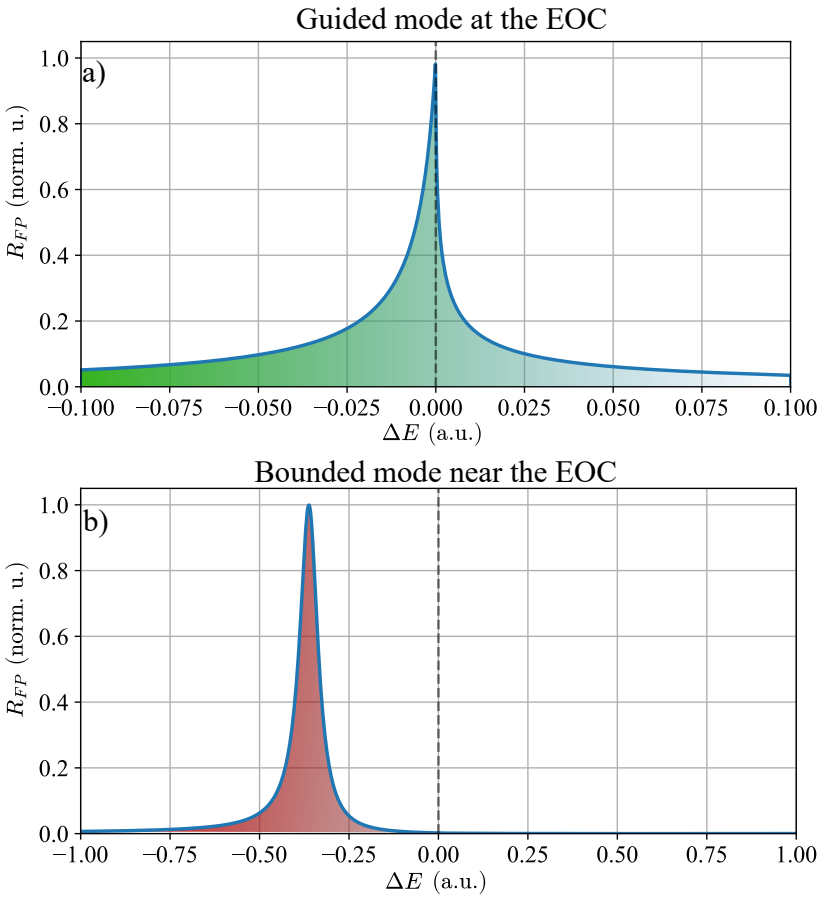


Figure 3.2: Two resonance types encountered in FP potential well model - An asymmetrical resonant reflection at the EOC (a), derived from Eq. (3.17) and bounded mode near the EOC (b), achieved from Eq. (3.16). The parameters chosen here are as follows: $a = \pi/2$, $t = 0.6$, $\gamma_0 = 0.16$, $V = 2$.

Where the coupling coefficient $\gamma_0 = h\Delta n/\lambda_0$ and ΔE is the is the energy shift of the resonance with respect to the EOC. The lowest energy bound state's response function $g_0^{(bot)}$ is found for the potential well with E, $V_0 \to -\infty$. Then $|k_1| \ll |k_2|$, phase shift $\phi \to -\pi/2$ at the resonance. In this case, the denominator $\cos(ak_1 + \phi) \to 0$, then $ak_1 \to \pi$. Overall, bounded state pertains $\pi/2$ phase at the resonance given phase delay response between 0 and π.

The lowest energy bound state for $g_0^{(top)}$ is achieved with such assumptions: if $z > a$, $E = 0$. Then $|k_2| \ll |k_1|, \phi \to 0$ and $\cos(ak_1) \to 0$, thus providing $ak_1 \to \pi/2$.

The equation (3.18) is the main result of the analytical study, which corresponds to the leaky modes in resonance with the potential drive at the con-

tinuum boundary, while (3.17) remains resonant guided modes deep within the potential well and correspond to the lowest mode energies. Coefficient of leaky modes have a $\sqrt{1/\Delta E}$ dependence, whereas $1/\Delta E$ dependence. The concept as well as analytical results for the bounded and near-continuum modes is illustrated in Fig. 3.1.

As an example, the corresponding reflection shapes are predicted from using Eq. (3.12) and (3.16). The narrow asymmetrical resonance is visualized in Fig. 3.2 a), whereas b) represents the bounded mode deep within the potential well. The most noticeable feature is the narrowness of the asymmetrically shaped reflectance.

3.2 Numerical results

The validity of analytic solutions is observed in the results which are simulated by 2D RCWA program and are visualized in Fig. 3.3. The simulations were performed for a 2D wave-guide which has a harmonic interface of the substrate and a flat top shaped thin film (see Fig. 3.1), for which the analytical model is derived.

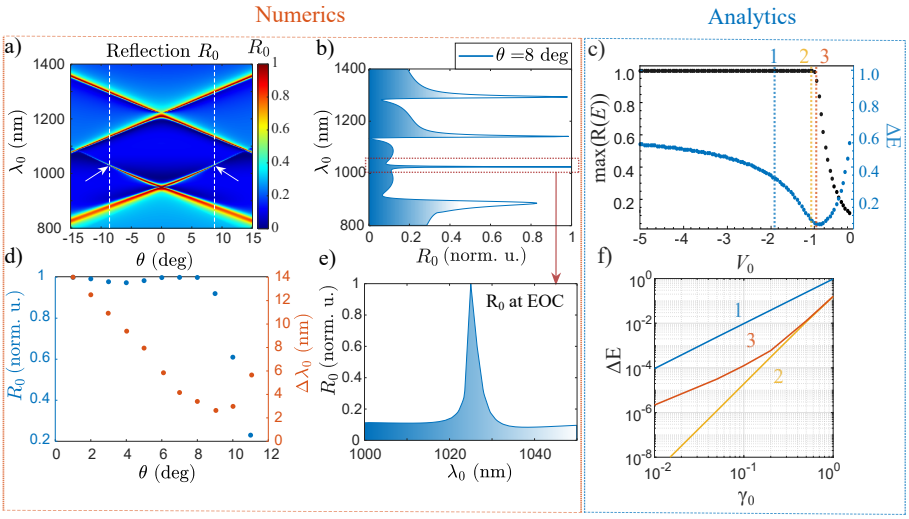


Figure 3.3: Reflection angular spectrum (a), and its cross-section at an oblique angle of incidence (b). The arrows indicate the points corresponding to the resonance at the EOC. The peak reflectance and its spectral width dependence vs potential well's depth V_0 analytical model. The peak reflectance and its spectral FWHM dependence on angle of incidence from RCWA model (d) and the zoomed in resonant reflection at e). The width dependence of the resonance from analytical study is present at f).

The geometrical parameters of the waveguide are presented in the following: $h = 200$ nm, $n_{\mathrm{f}} = 2.25$, $L = 460$ nm, $\Lambda_x = 625$ nm, $n_{\mathrm{sub}} = 1.5$. The

parameters of the analytical model: $\gamma_0 = 0.75$ and $a = \pi/10$ for qualitative analysis. The resonance characteristic at EOC can be extracted by examining reflection spectrum at an oblique angle of incidence (see Fig. 3.3 a)). At the cross-section, the multitude of resonances are present (see Fig. 3.3 b)). The resonances splitting are due to the GMR effect and at an angle of incidence at the EOC the reflection profile becomes asymmetrical. If the angle is tilted, the guided mode then couples the incident beam with a diffraction order. Given the asymmetrical distribution of the resonance, the half-width analysis is performed via analytics as well as via RCWA model (see Fig. 3.3 c) and d)). In analytical part, the analysis of resonance width is performed for $V_0 = -1.05$ (EOC location), $V_0 = -1.00$ and $V_0 = -2.00$. It is clear that once the EOC in analytics is reached and the reflection is tuned, the FWHM of the asymmetrical reflection scales with respect to γ_0 at the factor of 4 and Fano resonances (bounded modes) scale at the factor of 2, given $V_0 = -2.00$. Such dependence is illustrated in Fig. 3.3 f).

3.3 Experimental results

The fabrication is performed for the periodic structure with both corrugated interfaces and for a different type of a modulation function, which is super Gaussian.

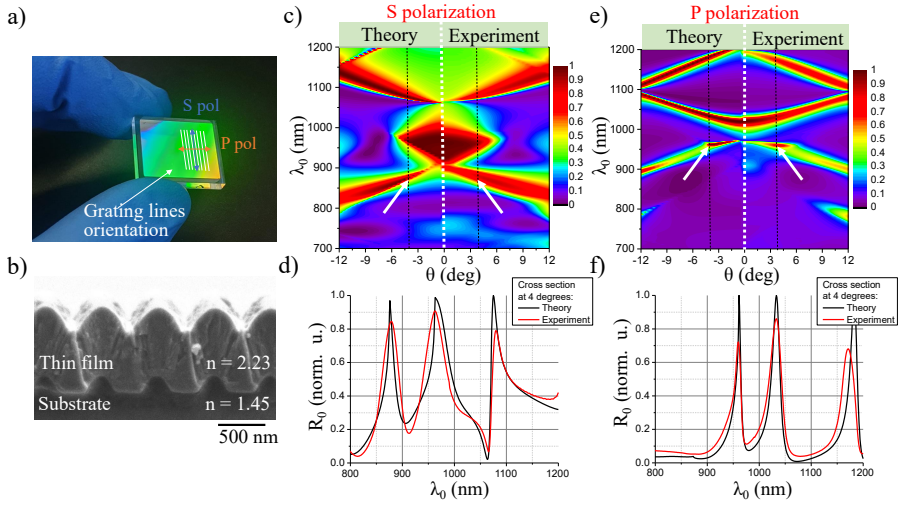


Figure 3.4: Photo of fabricated GMR filter (arrows indicate polarization directions (a), and the SEM image of specimen sample cross-section (b). Numerical/measured spectra of the reflection in the plane of angle-wavelength for (c,d) S polarization and (e,f) P polarization, with their cross-sections at 4 degrees of light incidence angle. The arrows indicate guided modes crossing the EOC.

Such a structure is achieved from trapezium shaped grating, which was

before auto-cloning procedure is applied. This procedure was done so that the edges of a grating are smoothened in order to improve deposition of the thin waveguide film.

The geometrical parameters are presented in the following: $h = 220$ nm, $L = 530$ nm, $\Lambda_x = 625$ nm, $n_{\text{sub}} = 1.45$ (SiO_2 substrate) and $n_{\text{film}} = 2.23$ (Nb_2O_5 thin layer film). All refractive index numbers are presented for 970 nm source. The surface of the thin film (i.e., width of corrugations), has expanded, yet reflection properties remain for both s and p polarizations, which means that such properties have low sensitivity due to deposition errors (mainly the non sharp geometrical shape and form of a periodically modulated thin film). Due to higher film thickness this periodic wave-guide is capable of exciting 3 GMRs, where two of them are guided modes and the highest energy resonance is a delocalized mode, which is slightly above the EOC but is chosen to be represented at 4 deg angle of incidence due to it being a distinct resonance at EOC.

Also, a much clearer stop band is present for the reflectance of s polarization (see Fig. 3.4 c)). At normal incidence, the $\Delta\lambda_0 = 43.25$ nm bandwidth is achieved, which is a significant improvement, compared with thin film deposition on trapezium shaped substrate. Hence the broadband reflectance properties are maintained in spectral regime, however, in the angular regime, the drop of reflectance value is more continuous compared with trapezium conformal grating's case.

3.4 GMR based broadband reflectance filter comparison

The comparison is carried out between trapezium and supergaussian interfaces to ascertain which topologies grant lower $\Delta\theta$ given broadband spectral reflectance. The comparison is illustrated in the following figure:

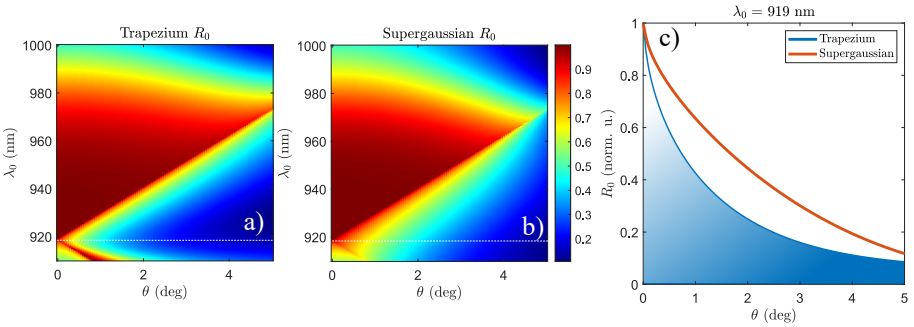


Figure 3.5: Computed zeroth order reflection spectra for trapezium (a) and supergaussian (b) thin film broadband filters, which and the reflectance slice at $\lambda_0 = 919$ nm (c), which is marked by a plotted white line in (a) and (b).

The supergaussian thin film filter pertains the same geometrical and material parameters and trapezium shaped filter differs from the previous design by modulation depth $h = 220$ nm, $\Lambda_x = 625$ nm , $w_{bot} = 375$ nm, $w_{top} = 195$ nm and with thicknes $L = 540$ nm. The Rayleigh anomaly's confined broadband reflectance of trapezium thin film filter is shown in Fig. 3.5 (a) and for supergaussian interface situation at 3.5 (b). The comparison between them is carried out for $\lambda_0 = 919$ nm and is visualized in 3.5 (c). Here the $\Delta\theta = 1.65$ deg at FWHM for supergaussian modulated filter, whereas $\Delta\theta = 0.8$ deg for trapezium shaped filter, which means that the latter geometry is better for low-pass filtering.

3.5 Summary

This work investigates the characteristics of single GMR near the Rayleigh zone, which is considered as the EOC in Schrodinger's adapted model for FP filters. The analytical model adds external driving into the differential equation and additional FP mode in the ansatz of the equation. The main objective is computation of g_0 factor, which represents FP response function and is involved in reflectance computations. Two extreme cases of g_0 are derived: Lorentzian distribution of resonant reflection for deep bounded photonic states, proportional to ΔE^{-1}. The second extreme state is the one occurring at the EOC, which pertains strong asymmetry and discontinuity at the EOC. Its response function is proportional to $\left(\sqrt{\Delta E}\right)^{-1}$. The scaling of such resonance's width at half maximum is proportional to the coupling constant γ_0^4, whereas for the bounded modes is γ_0^2 in the analytical model.

Fabrication of thin film conformal GMR based gratings is done on the smoothed trapezium gratings that pertain super-gaussian shape of order of 2 and ats FWHM at 306 nm, with modulation depth $h = 220$ nm. The autocloning is performed with Nb_2O_5 material at a thickness of $L = 530$ nm. Top layer's interface, according to the SEM imagery, is broadened in transverse direction. However, the increased filling factor of the material did not heavily influence the broadband reflection near the Rayleigh region for s polarized input. At that regime, the asymmetrical resonances are present at oblique angle of incidence for $\theta = 4$ deg, hinting the GMRs at the EOC. The normalized design parameters of GMRF are: $L/(\Lambda_x n_{\text{sub}}) = 0.5768$ and $h/(\Lambda_x n_{\text{sub}}) = 0.2395$, given $n_{\text{sub}} = 1.47$ (FS) and $\Lambda_x = 625$ nm.

Chapter 4

Enhanced absorption via Parity-Time symmetry breaking in GMR filters

The material related to this thesis was published in paper[**A3**].

The non-symmetrical response of the GMR filters is vastly studied for two reasons: interest of physics, optical (angular based) switching, enhanced absorption and for sensing applications [105–110]. To author's knowledge, the first works of such structures are traced back to 2004 where numerical simulations present non-symmetrical response in transmission regime. Although the subject is quite old, the field itself has something new to offer - asymmetrical placement of absorbing material on the waveguide which provides non-hermitian optical effects even without the use of amplifying media [111]. Here we explore briefly the passive non-symmetrical filter case, as well as the enhancement of optical absorption via lossy material's asymmetrical placement on the filter.

This chapter analyzes how the cancellation of Parity-Time (PT) symmetry influences the absorption of the GMR filter. The modulation of the complex refractive index along side with asymmetrically placed absorber can be expressed in the following:

$$\Delta n \approx \Delta n_{\mathrm{Re}} \cos kx + j\Delta n_{\mathrm{Im}} \sin kx \tag{4.1}$$

From Eq.(4.1), the modulation comprises of the real part of refractive index modulation Δn_{Re}, imaginary part Δn_{Im}, as well as via wavevector part k in the harmonic functions. Such functions can be expanded via complex exponents and, assuming $\Delta n_{\mathrm{Re}} = \Delta n_{\mathrm{Im}}$, the refractive index modulation pertains only the $+k$ component:

$$\Delta n = \Delta n_{\mathrm{Re}} e^{jkx} \tag{4.2}$$

Usually, the guided mode propagates in the lossless thin film along the x direction with both $\pm k$ wavevectors, however, due to the asymmetrical modulation of the absorptive layer on top, the guided mode is ideally expected to pertain only a single wavevector component. Thus, unidirectional mode propagation would be achieved in such a manner.

4.1 Absorption Enhancement with unmodulated substrate

The geometry of the substrate is super-gaussian modulation of GMR filters with an absorber on top of the TiO_2 thin film, illustrated in Fig. 4.1 a). The resulting occurrence is the unidirectional propagation of the guided mode in the GMR cavity, which pertains strong metallic asymmetrically placed absorber. The absorber is metallic Nickel (Ni). At oblique angle of incidence ($\theta = -17.5$) deg, the thin film modulated structure exhibits properties of broken symmetry

which is then repeated by the guided mode, resulting in both unidirectional propagation of the guided mode and decrease of the radiation in zeroth orders via asymmetrical absorption.

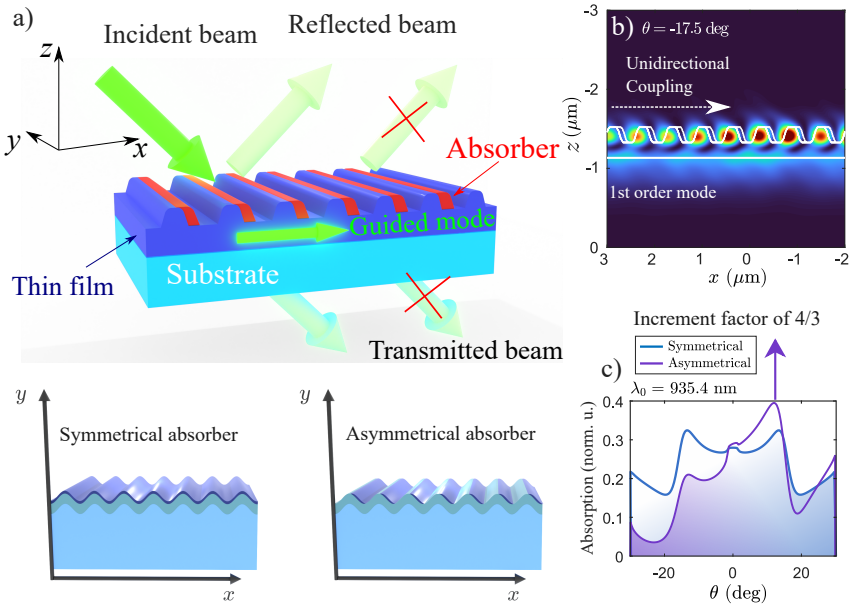


Figure 4.1: Absorption enchancement concept (a), first order GMR mode (b) and comparison between symmetrical and asymmetrical absorptions (c), resulting in increment of absorption.

The main focus is the comparison analysis between absorption profiles, which consist of two structures: the first one belongs to the symmetrical one, whereas the other one - non-symmetrical one. In numerical models, the absorber's pixel amount was kept the same for both absorbers in the unit cell to provide quantitative numerical comparisons. The purpose of such a comparison is enhancement of absorption via introduced non-symmetry. Analysis, provided in Fig. 4.1 (c), suggests non-symmetrical case provides 1.33 times greater absorption than the symmetrical one. To quantitatively analyze this enhancement, an analytical treatment is employed to compare the absorption enhancement between the two proposed symmetries. Firstly, a fully confined guided mode inside the resonant absorbent cavity can react:

$$\frac{\mathrm{d}A}{\mathrm{d}t} = (j\omega_A - \alpha)A. \tag{4.3}$$

Thus, yielding solution of $A = A_0 \exp(j\omega t) \exp(-\alpha t)$, where A is the amplitude of the guided cavity mode. Over time, given high resonance quality, a fully confined guided mode is completely absorbed in the absorber, given absorption coefficient α and mode's oscillation frequency ω_A. Secondly, the simplest model

can be proposed - simplified cavity equation of the FP mode:

$$\frac{\mathrm{d}B}{\mathrm{d}t} = \left(j\omega_B - \frac{1}{\tau}\right) B + \frac{f}{\tau} B_0, \tag{4.4a}$$

$$B = \frac{fB_0}{1 - j\omega_0\tau} \left(1 - \exp\left(j\omega_B t - \frac{t}{\tau}\right)\right). \tag{4.4b}$$

Here B is FP mode amplitude and terms f and τ denote finesse and decay rate of the FP mode, respectively. The parameter B_0 is External driving amplitude of FP mode. The solution to the FP mode equation in Eq. (4.4a) is Eq. (4.4b) with initial condition of $B(0) = 0$, giving the stationary solution $B(t \to \infty) = fB_0/(1 - j\omega_B\tau)$. Here ω_B is the FP resonance frequency. Further analysis is based on Temporal Coupled Mode (TCM) equations, which describe the interaction between the Fabry–Pérot cavity's amplitude B and a GMR amplitude A in modulated thin films. The description is provided in Coupled Mode Eq. (4.5) by introducing additional coupling parameters:

$$\frac{\mathrm{d}A}{\mathrm{d}t} = j\Delta\omega_A A + j\kappa_+ B - \alpha A, \tag{4.5a}$$

$$\frac{\mathrm{d}B}{\mathrm{d}t} = \frac{B_0\sqrt{f} - B}{\tau} - \alpha B + j\Delta\omega_B B + j\kappa_- A. \tag{4.5b}$$

Where A and B are guided mode and FP mode amplitudes, respectively, coupling parameters $\kappa_\pm = (\Delta\varepsilon_{Re} + j\Delta\varepsilon_{Im}e^{\pm j\phi})\frac{\omega_0}{8}$ and absorption coefficient $\alpha = \frac{\Delta\varepsilon_{Im}\omega_0}{4}$. The de-tuning angular frequencies are $\Delta\omega_{A,B} = \omega_0 - \omega_{A,B}$, where $\kappa_\pm$ are coupling coefficients, and "+" denotes an in-coupling from the FP mode to the waveguide mode of the the film, "-" denotes the out-coupling. In this case, the coupling coefficients are not necessarily hermitian with reference to one another.

The stationary solutions ($\frac{\mathrm{d}}{\mathrm{d}t}A = 0$, $\frac{\mathrm{d}}{\mathrm{d}t}B = 0$) to the temporal equations provide amplitudes A and B, hence

$$B_{\mathrm{st}} = \frac{B_0\sqrt{f} + j\kappa_-\tau A_{\mathrm{st}}}{1 + \alpha\tau - j\Delta\omega_B\tau}, \tag{4.6a}$$

$$A_{\mathrm{st}} = \frac{j\kappa_+\sqrt{f}B_0}{(\alpha - j\Delta\omega_A)(1 + \alpha\tau - j\Delta\omega_B\tau) + \kappa_+\kappa_-\tau} \tag{4.6b}$$

From the analytics, the total intensity absorption is expressed in the following as $\gamma = 2\alpha(|A|^2 + |B|^2)$, assuming that there is no detuning of the FP resonant mode ($\Delta\omega_B = 0$):

$$\gamma = \frac{2\alpha f(|\kappa_+|^2 + |\alpha - j\Delta\omega_A|^2)}{|(\alpha - j\Delta\omega_A)(1 + \alpha\tau) + \kappa_+\kappa_-\tau|^2} \tag{4.7}$$

At the resonance ($\Delta\omega_A = 0$) and given the decay rate with low absorption ($1 << \alpha\tau$), the maximum intensity absorption would become

$$\gamma = \frac{2\alpha f(|\kappa_+|^2 + |\alpha|^2)}{|\alpha + \kappa_+\kappa_-\tau|^2} \tag{4.8}$$

With no out-coupling and with ideal unidirectional coupling (permittivity values $\Delta\varepsilon_{\mathrm{Re}} = \Delta\varepsilon_{\mathrm{Im}}, \kappa_- = 0, \kappa_+ = \alpha$), the peak possible intensity absorption is $\gamma_{max} = 4\alpha f$, whereas given the uniform case ($\Delta\varepsilon_{\mathrm{Im}} = 0, \kappa_+ = j\kappa_- = \frac{\alpha}{2}$), then $\gamma_{uni} = \frac{5}{2}\alpha f$. Given such parameters, the total intensity absorption of an asymmetrical structure can be increased by a factor of

$$\frac{\gamma_{max}}{\gamma_{uni}} = \frac{8}{5} \tag{4.9}$$

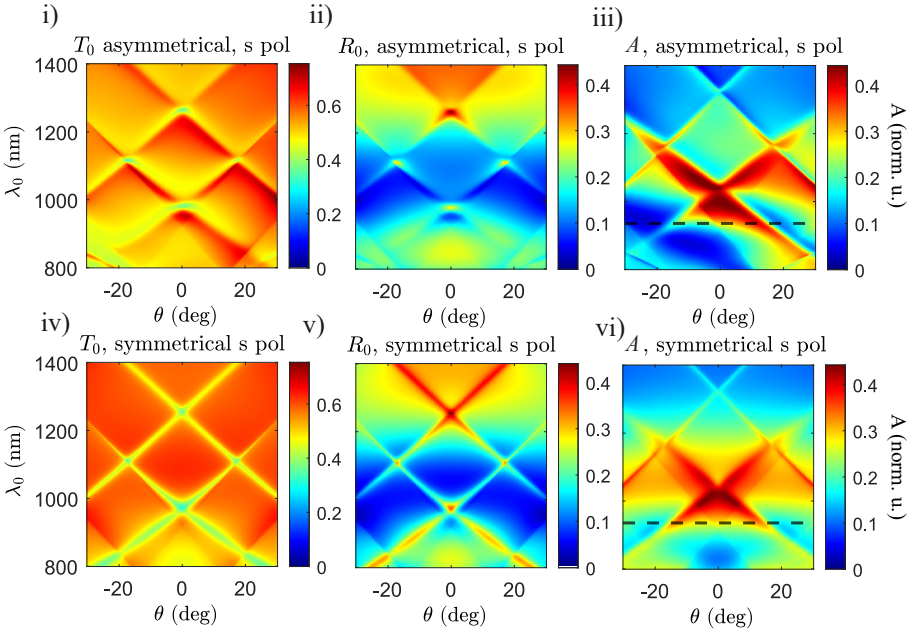


Figure 4.2: The calculated spectra for asymmetrical (i - iii) and symmetrical (iv-vi) device's zeroth order transmission, reflection and absorbance (given flat interface function). The dashed lines ar at 935.4 nm, used for absorbtion comparison, which is visualized in Fig. 4.1 c).

Compared with the Fig. 4.1 (c), whose maximum increment factor at an oblique angle of incidence is $\frac{4}{3}$, the offset is at 17%. It is due to the assumption weak damping $\alpha\tau \ll 1$ and due to full coupling between the waveguide mode and the absorber. Also, the analysis itself is performed for the leaky modes (taken from data, presented in Fig. 4.2 iii) and vi)), where reflection occurs. At leaky mode regime, the reflection coefficient possesses lowest resonance quality factors, i.e., the leaky wave is rapidly dissipating energy and increases its resonance width, compared with resonances that may possess high quality factors [112].

A thorough investigation and comparison between thin film's with symmetrically placed absorber and asymmetrically placed absorber is carried out for the zeroth order DEs, which are shwon in Fig. 4.2 for s polarization. Absorption is computed through $A = 1 - R - T$, where R is total reflection and T is total transmission. Symmetrically placed absorber partially decreases reflectance where GMRs should occur, resulting in partially increased zeroth order transmission. On the other hand, asymmetrically placed absorber substantially increases transmittance along the lines where GMRs should exist (see Fig. 4.2 i) and iv)). Zeroth order reflection case pertains symmetry for asymmetrical and symmetrical placements of the absorber (see Fig. 4.2 ii) and v)). Then, the absorption A is slightly increased along GMR line at $\lambda_0 = 1000$ nm for asymmetrical layer, and comparison is performed at $\lambda_0 = 935.4$ nm, where the enhancement of absorption is visible and whose angular response is visualized in Fig. 4.1 c). The parameters of the grating: $\Lambda_x = 625$ nm, $L = 500$ nm, $w_{FWHM} = 305$ nm, super-gaussian order $m = 2$, $h = 200$ nm. The complex refractive index of Ni $n_{\mathrm{Ni}} = 2.4 - 2.3j$.

Other details worth of interest is how do the guided modes behave inside the thin film whenever the modulation depth is varied. The comparison then is extended by adding the asymmetrical absorber on the side. The details and calculated spectra along field distributions are illustrated in Fig. 4.3.

Low modulation depth provides greater field confinement (see Fig. 4.3 (a,d,g)) for guided modes. The decreased FWHM of the resonance consequently increases the quality factor, thus greater the field confinement within of the fields within the thin film. Such characteristic is indicated in the peak colorbar values of the real field amplitude. Increased modulation depth case (see Fig. 4.3 (b, e, h)) provides lower quality factors due to the increased resonance widths at half-maxima, thus the smaller field confinement. The field confinement within thin film worsens overall when asymmetry is introduced on top of thin film (see Fig. 4.3(c,f,i)) and the guided modes themselves are distorted due to the metallic absorber's presence. In such a way portion of the field is transmitted at normal incidence.

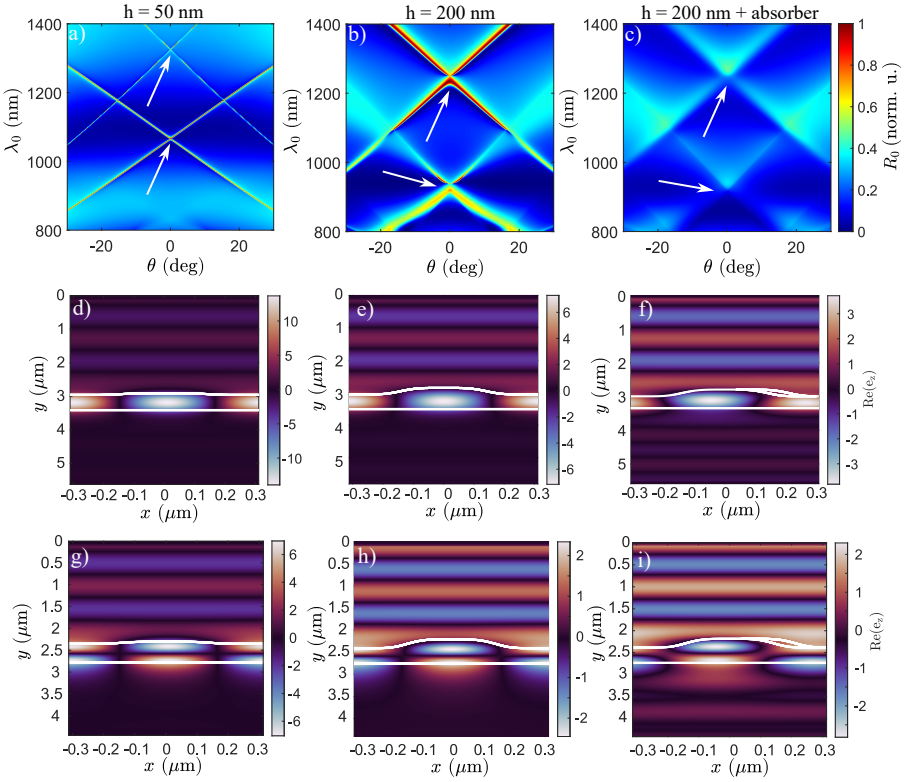


Figure 4.3: Numerically calculated reflectance map for s polarization of TiO2 layer on silica substrate. Small amplitude periodic perturbation is represented in (a) with its first (d) and second (g) order guided modes. The strong periodic perturbation (b) and respective field configurations (e,h) as well as with the absorber (c) with the respective field configurations (f,i),

4.2 Absorption Enhancement with modulated substrate

Further investigation is carried out for doubly modulated structures. The substrate's modulated interface provides enhanced effects for transmittance and reflectance, illustrated in Fig. 4.4 a) b), d) and e), as well as absorption spectra, which are illustrated in Fig. 4.4 c) and f).

The thickness of such structure $L = 300$ nm and modulation depth, with other parameters, remain unchanged. The absorber's function is also super-gaussian, with 50 nm offset from the center. The device design is made solely for fabrication via IBS method. The numerical simulations of the non lossy filter are performed as well, whose spectral features agree with experimentally measured ones (see Fig. 4.5). The sharp features persist, especially for p

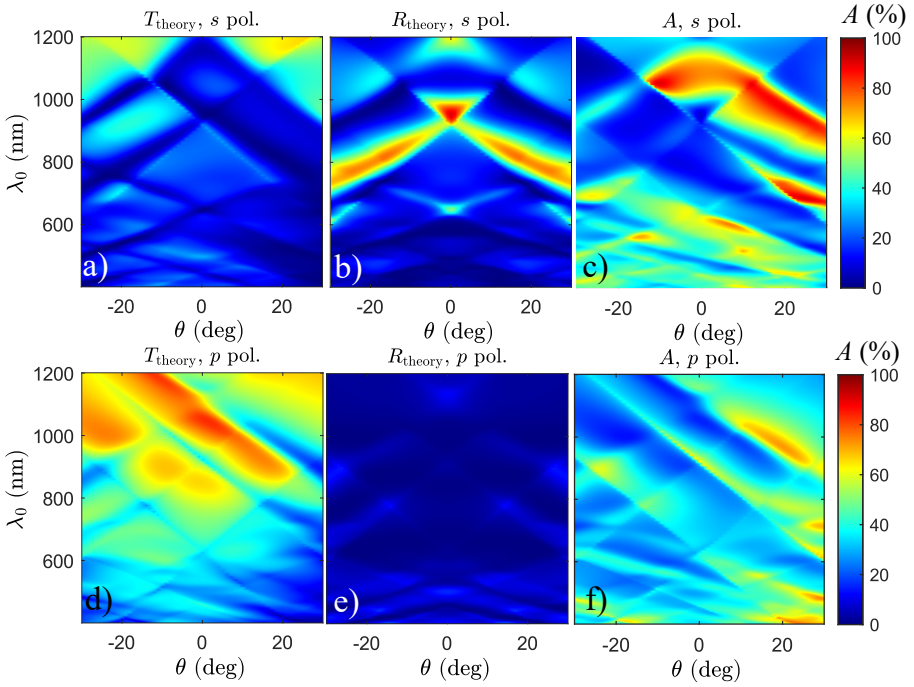


Figure 4.4: Doubly modulated GMR structure with the asymmetrical absorber. The transmission and reflection spectra for s polarization (a,b), absorption profile for s polarization (c), transmission and reflection spectra for p polarization (d,e) respectively and the absorbance for p polarization (f).

polarized input in zeroth order transmittance spectrum (see Fig. 4.5 b)). Then, the zoomed in transmittance and reflectance spectra of the same spectral maps, visualized in Fig. 4.4, are shown in Fig. 4.5 c), e), d) and f), for comparison with measured zeroth order diffraction spectra in the next section.

The disappearance of T_0 for s polarization at sup-diffraction regime (dark blue spots in the colormap) suggests that majority of incident power, if not reflected or absorbed, is transferred through $T_{\pm 1}$, $T_{\pm 2}$ and $R_{\pm 1}$ orders. Comparing the reflection spectra between s and p polarizations, s polarization pertains leaky mode reflection (see Fig. 4.4 d)), restricted by Rayleigh phenomenon, whereas the peak reflection spectrum for p polarization is close to 20% (see Fig. 4.4 e)). The absorption for s polarization is the strongest for the first order GMR guided mode at sub-wavelength regime and for the guided modes at sup-wavelength regime. Consequently, Rayleigh anomaly acts as a cutoff between GMR based absorption and diffraction (see Fig. 4.4 c)). The absorption angular spectrum for p polarization does not pertain a strong absorption response, and the absorption line peaks for s polarization also occur at the Rayleigh zones, where phase and group velocities of propagating light may decrease due to the propagation wavevector of the diffracted wave being longitudinal to the

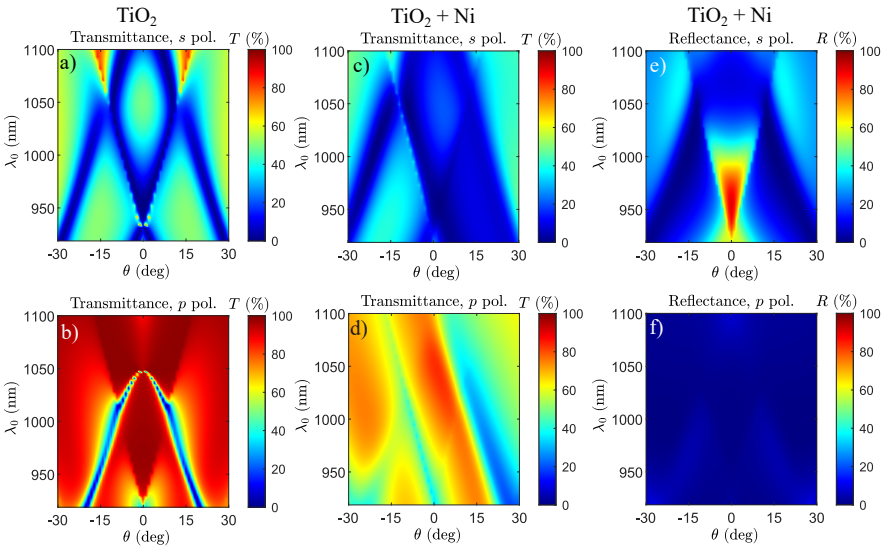


Figure 4.5: Numerically simulated zeroth order transmission spectrum of s and p polarization for $L = 300$ nm GMR TiO_2 thin film filter without absorber (a,b). The zeroth order diffraction efficiency maps for asymmetrically placed absorber is present for s (transmittance c) and reflectance e)) and p polarizations (transmittance d) and reflectance f)).

grating's grooves [113, 114]. Furthermore, absorption for p polarization case, compared with absorption of the grating for s polarized input, does not hold any significant enhancement, with valleys having peak absorption close to 65% for positive oblique incidence.

4.3 Fabrication and spectral characteristics

The fabrication of thin film asymmetrical absorber was performed via IBS deposition method. Thin film GMR based filter is fabricated with the same $L = 300$ nm thickness of TiO_2 layer. The spectral measurements of zeroth

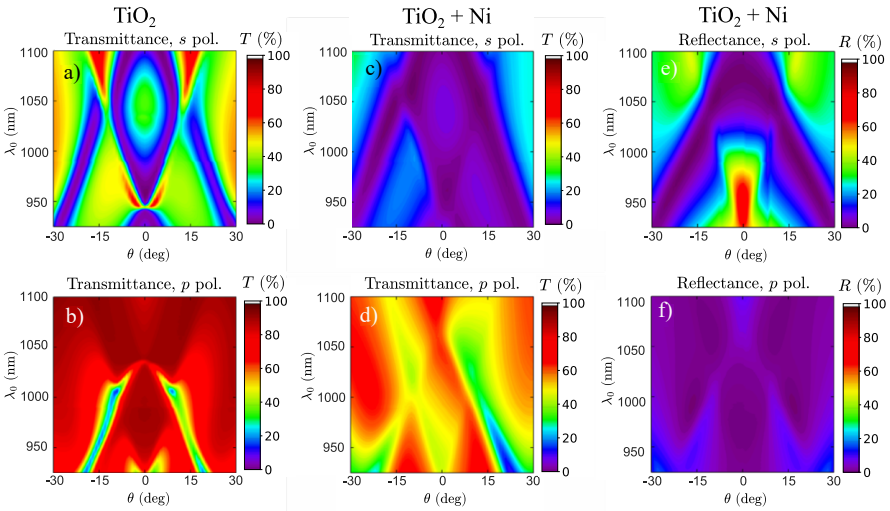


Figure 4.6: Experimentally measured zeroth order transmission spectrum of s and p polarization for $L = 300$ nm GMR TiO_2 thin film filter without absorber (a,b). The zeroth order diffraction efficiency measurements for asymmetrically placed absorber is present for s (transmittance c) and reflectance e)) and p polarizations (transmittance d) and reflectance f)).

order diffraction efficencies are presented in Fig. 4.6 a) and b) for the non absorbent device.

The absorbent device with deposited Ni layer pertains asymmetry in its zeroth order transmittance spectra, yet symmetry remains in measured reflection spectra. The spectral "blurring" is persistent due to the limitations of the spectrometer resolution, therefore the measured resonant features do not possess sharp features and discontinuities.

The device's morphology is captured via SEM microscope (Fig. 4.7 a)). The difference between the absorbance measured and simulated data is also present due to the spectrometer's limited resolution, hence the broadening of the absorption regions. The calculation of absorption was performed via the following formula:

$$A = 1 - R_0 - \left(\sum_{i=-1}^{+1} T_i \right) \tag{4.10}$$

Since $T_{\pm 1}$ orders are immeasurable in the substrate, they were included from the model. The T_0 and R_0 are included from the measured data, visualized in

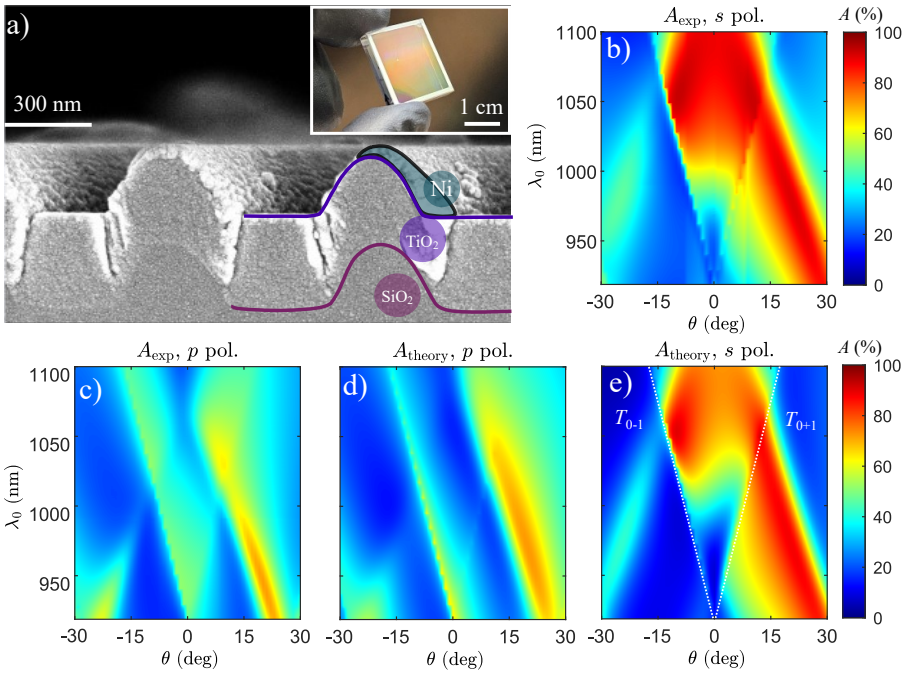


Figure 4.7: Experimental fabrication of doubly periodic GMR filter with an asymmetrical absorber (SEM picture) (a), indirect measurement of absorption for s polarized input (b) and p polarized input (c). Simulated spectra are presented in (d,e) [115].

Fig. 4.6 (c,d,e,f).

4.4 Summary

This section investigates PT symmetry breaking by asymmetrically placing metallic absorber on top of the thin film of the GMR filter. Parity-Time symmetry is broken due to the modulation of refractive index having a single wavevector component, given the fact that real part of the index is equivalent to the imaginary one. Therefore, unidirectional mode propagation is expected, or at least the opposite propagation of the guided mode in thin film layer is weakened due to this effect.

The coupled mode equations are used to predict the increment of intensity absorption by such asymmetrically placed absorber on the photonic device, when compared with symmetrically placed one. The increment factor is 8/5, whereas numerical simulations confirm it to be 4/3 for layers with single periodic modulation, due to the fact that coupling depends on all of the geometrical parameters and topology of the filter. The absorbent structures possess symmetrical zeroth order reflectance for both s and p polarizations.

The design for fabrication is presented, with thin film of TiO_2 with thickness of $L = 300$ nm on top of the super-gaussian interface of FS substrate with modulation depth $h = 200$ nm, preserving surface modulation of thin film. These parameters, normalized to Rayleigh wavelength (normal incidence), are $L/(\Lambda_x n_{\text{sub}}) = 0.326$ and $h/\Lambda_x n_{\text{sub}} = 0.217$. The FWHM of the super-gaussian groove is 306 nm and the order $m = 2$. Asymmetrical placement of the Ni metal on top is roughly at 50 nm at an angle of the GMR filter. Both simulations and indirect measurements of absorption spectra confirm that absorption is enhanced, and is cut-off via Rayleigh zone. Its peaks are found near those Rayleigh zones at oblique angle of incidence. This means that Rayleigh anomaly acts as a cut-off region and enhances linear optical absorption.

All in all, this works presents simple strategy for controlling light–matter interaction in planar photonic devices. Practical applications can be thought of: energy harvesting, sensing, and advanced optical components requiring efficient absorption and minimal reflection.

Chapter 5

Application of GMRs for enhanced optical gain

The gain materials, incorporated in the GMR resonant cavities, is the next concept to be studied in this chapter. Various works have been published with the gain materials in mind, illustrating the increased luminosity and fluorescence in periodic resonant cavities due to the coupling of incident light via periodic boundary conditions and waveguiding effects [116–126]. However, the scarcity of such structures is very limited and such field is more open for scientific exploration. The gain materials that are used possess very high gain coefficients whose order match for dye materials with great optical gain coefficients ($\gamma \sim 10^3 \text{cm}^{-1}$) and are abbreviated as perovskites [127–131]. This type of materials is the focus of this section.

The material related to this thesis was published in paper [**A4**] *and conferences* from [**C7**] to [**C9**]. *This section has results similar to the paper, but the difference is, that enhanced gain in the paper is achieved via implementation of active substrate. This section is devoted to the study, whose physical mechanism is equivalent to the mentioned publication. The main difference is - active material is a thin film.*

5.1 Perovskite thin films

In this section the perovskite-type of metamaterial is considered to be amplifying the propagating guided mode with gain coefficient of $\gamma = 500$ cm^{-1} [116]. Here the gain coefficient must have a relation with complex refractive index, where imaginary part corresponds to exponential gain rather than exponential loss. The guided mode distortion, which is observed in previous chapter, is not present here due to the low enough gain coefficient, when compared to absorption loss of $n_{\text{Ni}} = 2.4 - 2.3j$, which was used for asymmetrical absorption on GMR filters in previous section. Therefore, high quality GMR can be excited within the thin film's cavity. The gain can be achieved from extinction κ coefficient for the propagating plane wave in the following manner: $E(z) = E_0 \exp(jk_0(n + j\kappa)z) = E_0 \exp(jk_0 nz) \exp(-k_0\kappa z)$, where E_0 is source amplitude. Here κ plays role of exponential decay for its positive values and is linked with absorption coefficient α in the following relationship: $\alpha = 2k_0\kappa = 4\pi\kappa/\lambda_0$. From here, $\kappa = \alpha\lambda_0/(4\pi)$. Loss can be turned into gain by assuming negative absorption $\alpha < 0$, so $\kappa = -\gamma\lambda_0/(4\pi)$, where gain coefficient γ replaces absorption coefficient α. The peak complex value is then $\kappa_{\text{peak}} = -2.74 \cdot 10^{-3}$ for $\gamma = 500$ cm^{-1} gain coefficient at $\lambda_0 = 690$ nm.

The perovskite thin film (see Fig. 5.1 a)) refractive index is adopted from the parameters of this paper [116] with enlarged resonance width. The refrac-

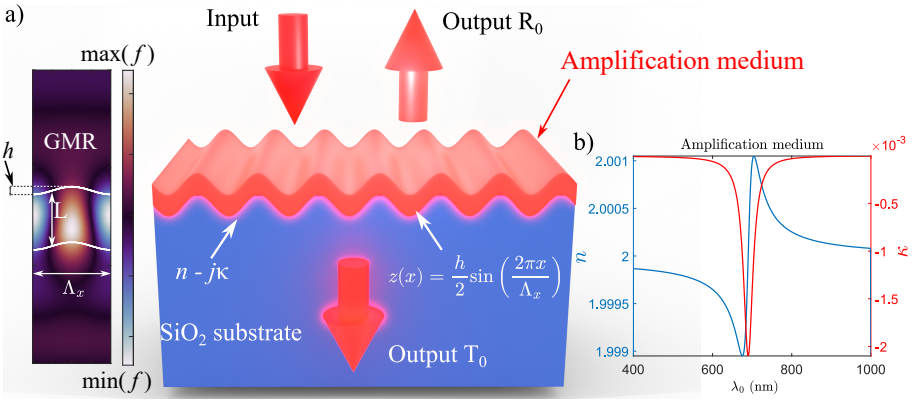


Figure 5.1: The concept of a GMR filter with active thin film a), enhancing diffraction efficiencies. Anomalous dispersion cases of b) amplification, used in this section.

tive index dispersion is shown in the updated Lorentz' anti-resonance formula in the following model:

$$\varepsilon_r = \varepsilon_1 + \frac{f}{\lambda_0^2 - \lambda_c^2 + j\Gamma}, \tag{5.1a}$$

$$\Gamma = \frac{\Delta\lambda n_1}{2}, \tag{5.1b}$$

$$f = 2n_1\Gamma\kappa_{\max} \tag{5.1c}$$

$$n = \sqrt{\varepsilon_r} = n_1 - j\kappa. \tag{5.1d}$$

The anti-resonance is a term used to simulate materials with gain as media where propagating wave experiences exponential negative loss, which is concerned as amplification. From quantum mechanical systems, the anti-resonance represents negative oscillator strength of the dispersive system of atoms, which means most, if not all of them, occupy an excited state, which refers to population inversion. The oscillator strength is a measure of transition probability and should always be positive for absorption processes, although it can be negative for emission [132–134]. Such characteristic is also common and extended for 3 level systems as well [135].

In the Lorentzian model (see Eq. (5.1)), ε_r is the initial relative permittivity value, f is the oscillator strength, λ_c is the peak wavelength and Γ is the line-width parameter. The parameters are: $n_1 = 2$, $f = 1.68 \cdot 10^{-4}$ μm^2, $\Delta\lambda = 20$ nm, $\Gamma = 0.015$ μm for $\kappa_{\max} = 2.7 \cdot 10^{-3}$, in order to match the specific fluorescence of the perovskite material $CsPbI_3$ used in work [116]. The influence of absorption of the GMR cavity is not analyzed due to absorbance of the perovskite being at 400 nm [116], and lasing at 690 nm. The formula

exhibits Lorentz resonance shape (see Fig. 5.1 b) and c)). Here amplification medium has the inverse resonance, where, if the wavelength is red-shifted its value decreases close to the resonance. The GMR field in the resonant cavity is ought to be amplified due to its prolonged propagation in the cavity until all of the power is radiated in zeroth order DEs. In order to tune geometrical

Table 5.1: Lower and upper boundary values for genetic algorithm optimization, applied for 2D RCWA model.

	L, (μm)	h, (μm)	Λ_x, (μm)	Merit function
Lower bounds	0.00	0.02	0.30	$-R_0$
Upper bounds	0.50	0.15	1.00	$-R_0$

parameters of the thin film GMR filter, optimization problem of enhanced amplification via genetic algorithm is incorporated, and the merit function is $M = -R_0(h, \Lambda_x, L, \theta = 0, \lambda_c = 0.69\mu\text{m})$ for normal incidence at the peak of the Lorentzian gain. Genetic optimization is performed for the geometrical boundaries of sinusoidal modulation that are presented in Table 5.1.

The achieved geometrical parameters are presented in Table 5.2 and satisfy the reached local minima after successful genetic optimization run.

Table 5.2: Achieved optimization parameters via genetic algorithm.

Polarization	L, (μm)	h, (μm)	Λ_x, (μm)	Value
S (TE)	0.4237	0.1384	0.7299	$-2.278 \cdot 10^4$
P (TM)	0.2641	0.0387	0.3989	$-7.790 \cdot 10^4$

Rayleigh wavelength for s polarization is $\lambda_R = \Lambda_x n_{\text{sub}} = 1.070$ μm at normal incidence, hence the amplification is peak at the sup-wavelength regime. The sub-wavelength working regime is achieved for p polarized input, due to the product of $\Lambda_x n_{\text{sub}} = 590$ nm, so zeroth order DEs persist.

When analyzing s polarization's optimization case at sup-wavelength regime, the GMR exhibits enhanced reflectance and transmittance at the resonance crossing and partially in oblique incidence. Reflectance is the strongest at the crossing only. Diffraction at first orders in transmission and reflection regions accordingly, and are present at oblique incidence as well, adding additional complexity to the resonance shape.

The corresponding field of peak reflectance is illustrated for Fig. 5.3 (c), where high order GMR is present. Due first order diffraction, for wavelengths $\lambda_0 < 689$ nm, transparency remains enhanced due to the reflectance holding its values up to -20 dB. Due to the sup-wavelength regime, no GMR is present for the p polarization, so the device is capable of amplifying only the s polarized input.

In p polarization's optimization case, enhanced amplification is present for both s and p polarized inputs, due to the sub-wavelength work regime of the optimized filter's topology. The resonance is in possession of shifting when

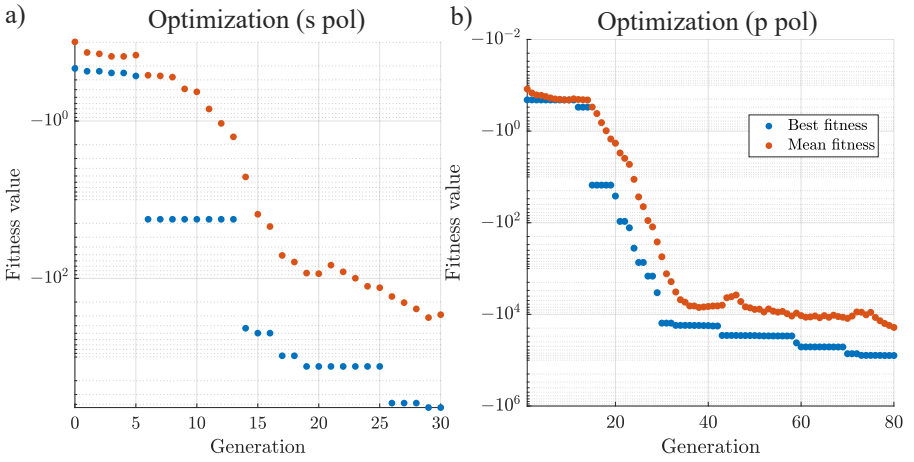


Figure 5.2: The genetic algorithm's optimization procedure for s polarization a) and for p polarization b).

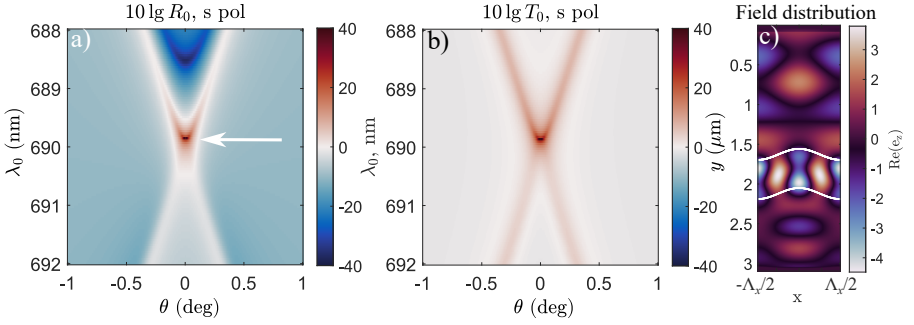


Figure 5.3: Reflection (a,d) and transmission (b,e) spectra with the respective guided resonant modes (c,f) of sup-wavelength operating regime. The arrow indicates field the spectral location for field distribution.

the polarization is being changed, as visualized between Fig. 5.4 (a,d), where transmittance of the grating follows the similar pattern. First order guided modes are visible for such devices, shown in Fig. 5.4 (c,f). The peak value for p polarization at normal incidence is chosen to be 40 dB.

Unlike the sup-wavelength regime, the sub-wavelength regime offers resonance tuning at oblique angle of incidence if the device fabrication is not ideal. In this case, both transmittance and reflectance will pertain enhanced gain where the GMR exists for s and p polarizations. The decreased width of GMR allows to enhance amplification for even lower values of complex refractive index, which is $\mathrm{Im}(n) = 2.5 \cdot 10^{-4}$ for $\lambda_0 = 725$ nm (see Fig. 5.4 d) and e)).

The GMR's features can be summarized for amplifying materials in the following: both resonances experience asymmetric shapes for normal incidence

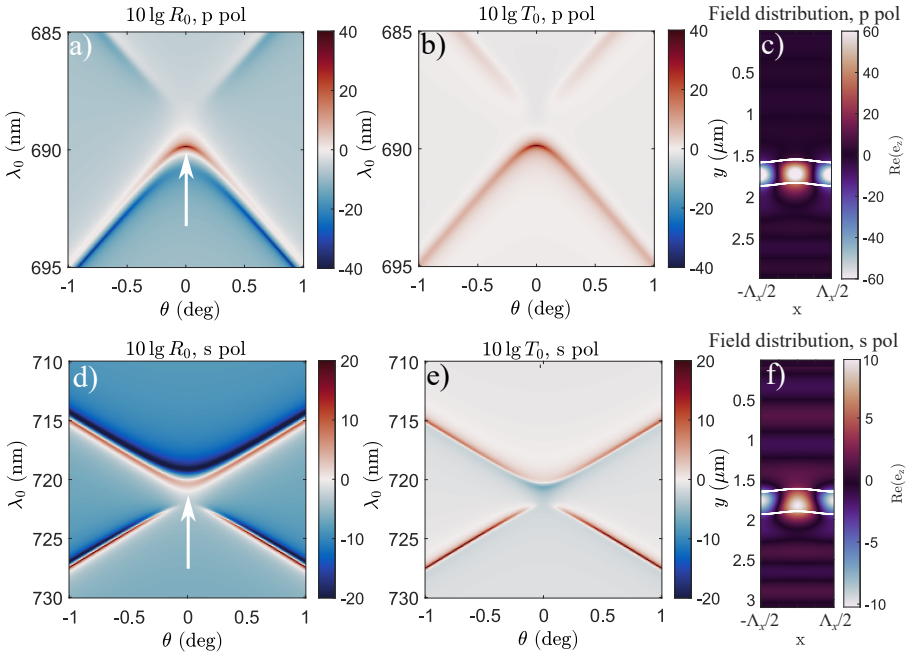


Figure 5.4: The enlarged reflection (a,d) and transmission (b,e) spectra with the respective guided resonant modes (c,f) of sub-wavelength operating regime.

(see Fig. 5.5 a) and c)). The main difference is that the p polarization case reflectance omits a minimum redshift away from the resonance peak, while s polarization case has a blue-shift of the reflection minimum. Also, the resonance exhibits strong narrow spatial amplification (as in low-pass filtering) for p and s polarization cases, which makes such structures operate as amplifiers and as low-pass beam filters accordingly.

Since the small change of the permittivity is able to shift the resonance, amplified reflection starts at the imaginary index of $8 \cdot 10^{-4}$ a.u. and descends from $3.3 \cdot 10^{-3}$ a.u. for s polarization. Transmittance amplification at zeroth order, no matter if the gain is varied, is pertained.

5.2 Resonant characteristics of passive GMR filter

The gain is chosen to be 0 the GMR filters in order to properly evaluate resonance quality for the passive filter. The zeroth order DEs are illustrated in Fig. 5.7.

Here, small FWHM widths and peak wavelengths are found, which are used to evaluate quality factors $Q = \lambda_p/\Delta\lambda_0$, where λ_p is wavelength of the resonance peak, and $\Delta\lambda_0$ is its FWHM. The quality factors are computed

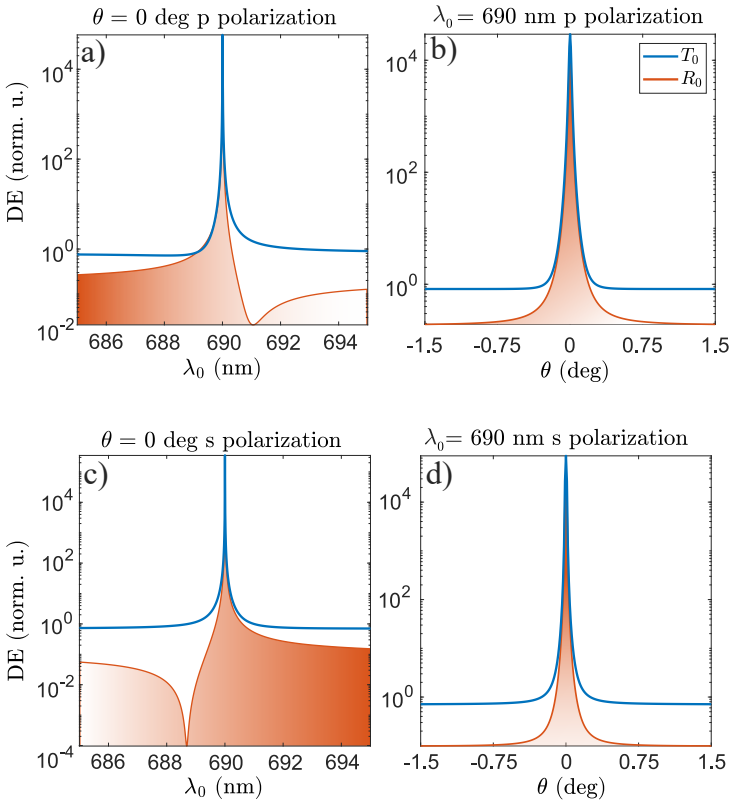


Figure 5.5: The zeroth order diffraction efficiencies at normal incidence (a,c) for p and s polarizations, as well as their angular dependence at peak gain (b,d).

only for the sub wavelength case due to single radiation channels (R_0 and T_0 DEs), whereas sup-wavelength regime pertains multitude of diffraction and reflection orders of ± 1 for the optimized geometry, hence its Q factor cannot be properly evaluated computed diffraction efficiency data. Resonance Q factors are summarized within Table 5.3 for sub wavelength case.

Table 5.3: Quality factors for GMR for sub-wavelength regime, extracted from data, which is visualized in Fig. 5.7 b) and 5.7 d). Words 'red' and 'blue' denote arrows at resonance peaks.

	Q, $\theta = 0$ deg	Q, $\theta = 1$ deg (red)	Q, $\theta = 1$ deg (blue)
p pol	378.57	568.75	746.24
s pol	378.90	807.67	714.00

Guided Mode Resonance in R_0 spectra, both for s and p polarized inputs,

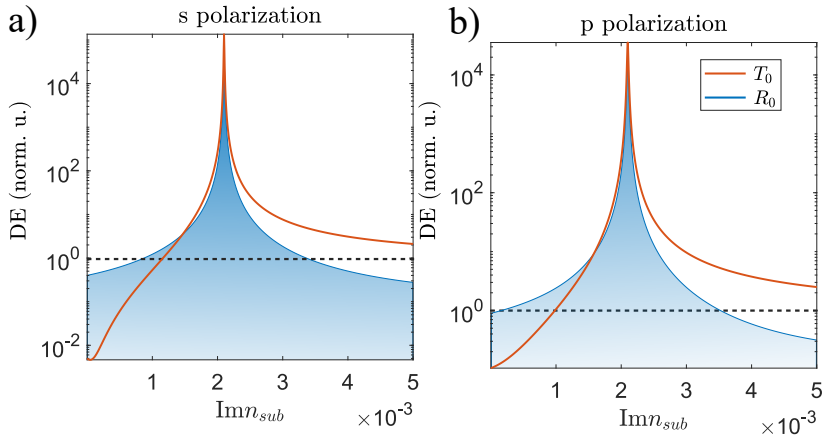


Figure 5.6: The dependence of zeroth order diffraction efficiencies from imaginary part of the refractive index of thin film for s polarization a) and p polarization b) at normal incidence.

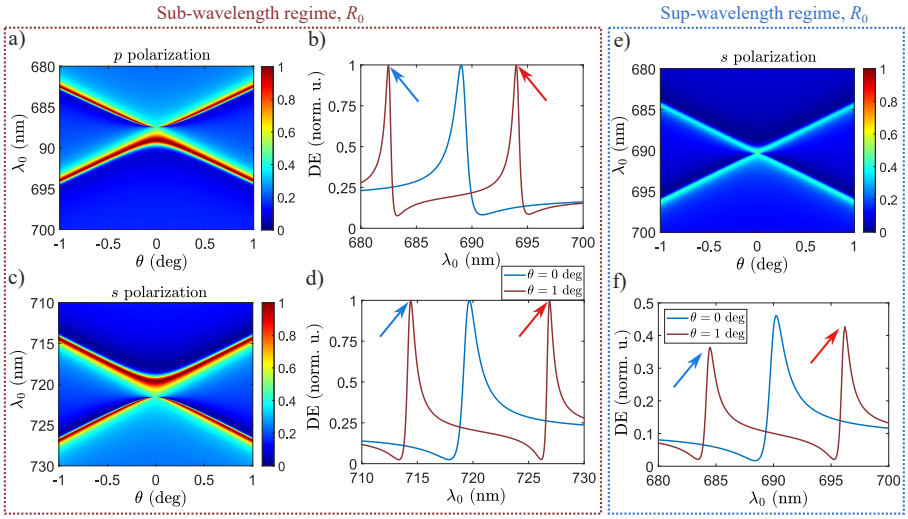


Figure 5.7: Zeroth order reflection spectra for the passive thin film GMR filter. Reflection is provided for p polarized input in a) and its resonances at $\theta = 0$ deg and $\theta = 1$ deg angle of incidence at b). Reflection is provided for s polarized input in c) and its resonances at $\theta = 0$ deg and $\theta = 1$ deg angle of incidence at d). Sup-wavelength regime of R_0 is provided for s polarized input in e) and its slices at $\theta = 0$ deg and $\theta = 1$ deg angle of incidence at f).

pertains to its features; however, given a different value of $n_f = 2.0$, there is a 1 nm blue-shift of GMR, which is visible in Fig. 5.7 a) and Fig. 5.7 b). At normal incidence, the resonance is characterized by $Q = 378.57$ with a FWHM

of 1.82 nm, which is sufficient for enhanced amplification. The Purcell factor can be estimated using Eq. (1.21). Using $n_{eff} = \sin\theta + m\lambda_0/\Lambda_x$, $n_{eff} = 1.729$ and $F_p \approx 182$ for normal incidence.

Oblique AOC detunes the resonance to the point where FWHM becomes narrower, thus providing around 1.20 nm FWHM, at which Q factor increases. Hence, blueshifted resonance has $Q = 568.75$ and redshifted one has $Q = 746.24$ with FWHM of 0.93 nm.

Furthermore, R_0 for s polarized input is in possession of similar order quality factors due to the redshift of GMR and are capable enough of enhanced selective amplification even if $\mathrm{Im}(n_f) = 8 \cdot 10^{-5}$, for oblique incidence. It is due to increased resonance quality $Q = 807.67$. The more narrower the resonance, the greater the quality, hence the longer the field remains in the resonant cavity. It can also be achieved with smaller refractive index difference between thin film, substrate and superstrate [70]. Furthermore, at sup-wavelength regime, GMR does not pertain 100% reflectance. It does, however, amplify incident wave given Lorentzian dispersion.

5.3 Oscillator Chain Model

The analytical model is a connected chain of oscillators [136], whose system is illustrated in Fig. 5.8. Here, the chain serves as the periodic medium through which oscillators can exchange energy. The classical chain system is specifically chosen to represent the GMR phenomenon in the thin film. The optical problem involves interaction between a continuum of radiative states and a discrete guided mode supported by the structure, and this interaction is represented via coupled oscillators. The mathematical description of the oscillator chain is borrowed from classical mechanics and is presented in Eq. (5.2).

$$\frac{\partial^2 A_n}{\partial t^2} = \omega_A^2 (A_{n-1} + A_{n+1} - 2A_n). \tag{5.2}$$

This chain model's characteristic equation compliments the propagating wave excitation:

$$A_n = A^{(+)}(k) e^{j(kn-\omega t)} + A^{(-)}(k) e^{j(-kn-\omega t)}. \tag{5.3}$$

Here the + sign promotes right side wave propagation along the oscillating chain, whereas the - sign notes the left wave propagation. In this model the quantity ω is the frequency, whereas k is a wave-number. The other quantity is order of the propagating wave n, which is the mode number. The quantity ω_A has a meaning of the phase velocity of the wave in terms of propagation through lattice sites per time unit. Between such parameters, the dispersion relation is:

$$\omega^2 = 2\omega_A^2 (1 - \cos k). \tag{5.4}$$

Overall, the system of coupled oscillators acts as a medium through which a wave with continuous angular frequency ω can propagate. In the case of amplifying or lossy medium, the chain can be coupled with it, thus the following

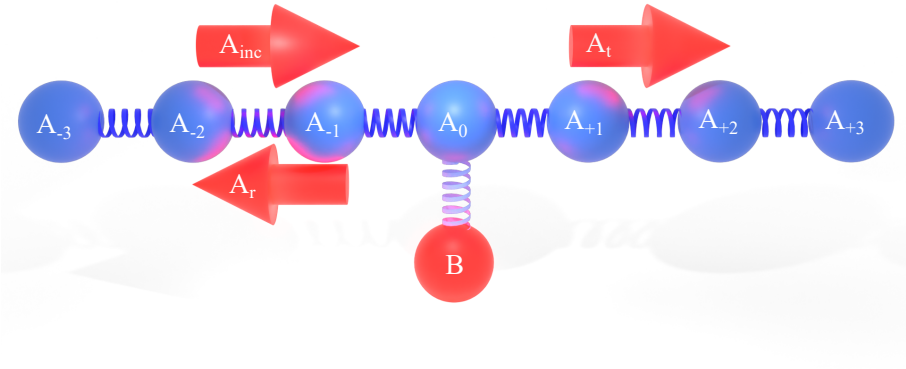


Figure 5.8: The model's concept of an oscillator chain, marking $\mathrm{A_{inc}}$ as incident wave and its reflected A_r and transmitted A_t waves. Additional central and side-coupled component (B to A_0) is added as a perturbation, and such oscillator part represents the Fabry–Perot and guided-mode resonance of the thin-film structure.

equations for the $A = [A_{-1}, A_0, A_{+1}]$ amplitudes. With the coupling coefficients $\kappa = [\kappa_{AB}, \kappa_{BA}]$, loss factors $\gamma = [\gamma_A, \gamma_B]$ in mind, the coupled temporal evolution equations for the oscillator chain model is empirically suggested for central oscillator part A_0 with a perturbation oscillator B:

$$\frac{\partial^2 A_0}{\partial t^2} = \omega_A^2 \underbrace{(A_{-1} + A_1 - 2A_0)}_{\text{Oscillator Laplacian}} - \underbrace{2\gamma_A \frac{\partial A_0}{\partial t}}_{\text{Losses from } A} + \underbrace{\kappa_{AB}\omega_B(B - A_0)}_{\text{Coupling } A\text{-}B}, \tag{5.5a}$$

$$\frac{\partial^2 B}{\partial t^2} = -\omega_B^2 B - \underbrace{2\gamma_B \frac{\partial B}{\partial t}}_{\text{Losses from } B} + \underbrace{\kappa_{BA}\omega_B(A_0 - B)}_{\text{Coupling } B\text{-}A}. \tag{5.5b}$$

The oscillator B serves as an additional mode which can be excited via its resonance frequency ω_B by the propagating wave A_n. That mode represents the guided mode resonance, whereas A_0 represents a FP scattering region. The loss coefficients $\gamma_{A,B}$ are involved for A_0 and B quantities and can be turned into gain if the $\gamma_{A,B} < 0$, hence the negative sign. The ansatz A_n is substituted into Eq. (5.5), which is presented in the following by including ± 1 and 0 order

modes:

$$A_n = e^{j(kn-\omega t)} + re^{j(-kn-\omega t)}, n < 0, \tag{5.6a}$$

$$A_n = te^{j(kn-\omega t)}, n > 0, \tag{5.6b}$$

$$A_0 = A_c e^{-j\omega t}, n = 0, \tag{5.6c}$$

$$B = B_0 e^{-j\omega_B t}. \tag{5.6d}$$

In the analytical model, $n < 0$ refers the incident wave with unitary amplitude, and reflection coefficient r. The $n > 0$ region refers to transmitted wave with complex transmission coefficient t. The ansatz is substituted into the Eq. (5.5), the response function $S(\omega)$ of the coupling region between A_C and B_0 oscillators is related through:

$$B_0 = \frac{\kappa_{BA}\omega_B}{\omega^2 - \omega_B^2 + 2j\gamma_B\omega + \kappa_{BA}\omega_B} A_C = S(\omega)A_C \tag{5.7}$$

The simplified reflection and transmission coefficients are then derived, given $k \ll 1$:

$$r(\omega) = -\frac{j\kappa_{AB}\omega_B(S(\omega) - 1) + 2\gamma_A\omega}{j\kappa_{AB}\omega_B(S(\omega) - 1) + 2\gamma_A\omega + 2\omega\nu}, \tag{5.8a}$$

$$t(\omega) = \frac{2\omega\nu}{j\kappa_{AB}\omega_B(S(\omega) - 1) + 2\gamma_A\omega + 2\omega\nu}, \tag{5.8b}$$

$$S(\omega) = \frac{\kappa_{BA}\omega_B}{\omega^2 - \omega_B^2 + 2j\gamma_B\omega + \kappa_{BA}\omega_B}. \tag{5.8c}$$

The dimensionless ν quantity defines dispersion slope instead of ω_A. Such equations decrease the significance of k which potentially alters the phase shift between resonances. Therefore, with one less parameter , the analysis becomes simpler. The next step is to compare the results with the ones achieved after the application of global optimization, mainly for p polarization, since the amplification is present there for the sub-wavelength regime.

The parameter fitting is best done via the use of optimization method. Hence the genetic algorithm can also be used here. The parameters for numerical fitting are expressed in the following: $[\gamma_A, \gamma_B, \kappa_{AB}, \kappa_{BA}, \nu, \omega_B]$. Since the p polarization contains only zeroth diffraction efficiencies, the optimization procedure is performed for this case. The results are summarized in the following Table 5.4 and Fig. 5.9. Asymmetrical coupling $\kappa_{AB} \neq \kappa_{BA}$ is needed to match analytically calculated and computed DEs.

Table 5.4: Achieved optimization parameters via genetic algorithm (normalized) for analytics.

Polarization	γ_A, a.u.	γ_B, a.u.	κ_{AB}, a.u.	κ_{BA}, a.u.	ν, a.u.	ω_B, a.u.
P (TM)	0	-0.0337	0.6340	0.1955	0.8364	4.0861

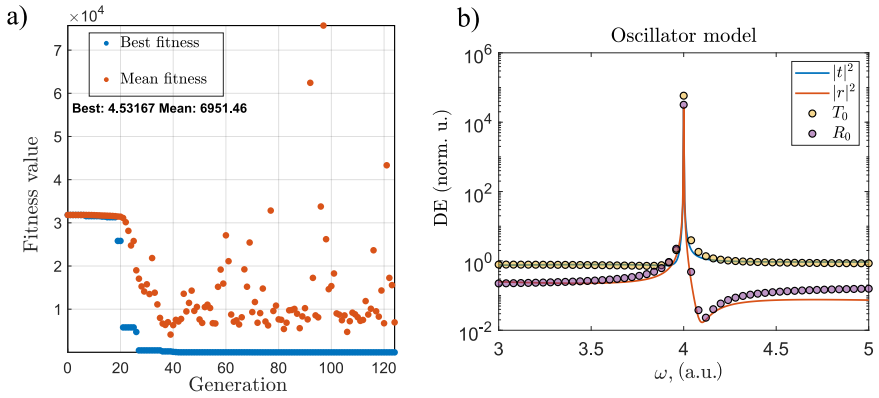


Figure 5.9: Optimization results (a) for the presented parameters in Table 5.4. The oscillator analytical model's comparison with the model's results, illustrated in Fig. 5.5 (a). The dots in the graph (b) represent numerically computed zeroth order diffraction efficiencies, whereas the lines represent resonance fitting.

The peak reflectance value is stationed at $\omega_R = 4 \neq \omega_B$. The resonance shift in this case occurs due to the presence of coupling and gain coefficients, mainly to the influence of γ_B and κ_{BA} coefficients, which are present in Eq. (5.8c) and oscillator chain pertains no absorption nor gain due to $\gamma_A = 0$.

The resonant frequency shift in the model can be analyzed firstly for the perturbed oscillator chain in the following manner: assuming the near resonance approximation $|\omega - \omega_B| \ll \omega$ with weak gain/loss limit $|\gamma_{A,B}| \ll \omega$:

$$g(\omega) = \frac{\kappa_{BA}}{2(\omega - \omega_B) + 2j\gamma_B + \kappa_{BA}}, \tag{5.9a}$$

$$A_c = \frac{2\nu}{j\kappa_{AB}\big(g(\omega) - 1\big) + 2\gamma_A + 2\nu}. \tag{5.9b}$$

Then, assuming $\kappa_{AB} = \kappa_{BA} = \kappa$ and $\gamma_A = \gamma_B = 0$.

$$t = \frac{2(\omega - \omega_B) + \kappa}{\kappa + \left(2 - \frac{j\kappa}{\nu}\right)(\omega - \omega_B)}. \tag{5.10}$$

Reflectance values are zero when $\omega = \omega_B$ and transmittance is zero when $\omega = \omega_B - \kappa/2$ and width between those zeroes is $\Delta\omega = \kappa/2$. The best fitting is found at $\gamma_A = 0$ for non-simplified chain model, which is illustrated in Fig. 5.9 b), hence γ_B gain parameter can be substituted in the Eq. (5.10) via $\omega_B \to \omega_B + j\omega_{\mathrm{Im}}$. When gain $-\gamma_B$ is incorporated in Eq. (5.9), the denominator is in possession of the poles where the resonant frequencies are equal to zero. In this manner the resonance frequency experiences a shift which depends on both coupling and gain an additional imaginary part:

$$\omega_R = \underbrace{\omega_B - \frac{2\kappa/\nu}{4+\kappa^2/\nu^2}}_{\omega_{\mathrm{Re}}} + j\underbrace{\left(-\gamma_B - \frac{\kappa^2/\nu}{4+\kappa^2/\nu^2}\right)}_{\omega_{\mathrm{Im}}} \tag{5.11}$$

Consequently, even the simplest system with no gain or loss has a frequency shift of its real part $\mathrm{Re}(\omega_{\mathrm{R}})$ which depends on the coupling between the A_0 and B oscillators.

5.4 Summary

This work expands on the enhanced light to matter interaction via high quality GMRs that are applied for the enhancement of optical gain. Such procedure is accomplished via implementation of an active thin film layer on top of the passive sinusoidally modulated substrate. Genetic algorithm is used to fully tune geometrical parameters of the thin film layer and the substrate's modulation in order to match a GMR into the spectral peak of the optical gain/fluorescence region, which is chosen as a negative Lorentz resonance. The tuning of geometry leads to sub wavelength operation if the optimization procedure is applied for p polarization, whereas the operation at sup-wavelength regime is gained when optimization is done for s polarized input. In sub wavelength case, resonant reflection with enhanced gain is encountered both for s and p polarizations, with greatest resonance peaks at oblique angle of incidence. However, sup-wavelength regime enhances gain only for s polarization, hence the selectivity. Also, the resonant phenomena depend on the angle of incidence and wavelength as well, and enhanced gain is present for R_0 and T_0 diffraction efficiencies.

Analytical oscillator chain model is introduced with small coupling between the periodic chain and loss/gain factor. The fitting is performed for p polarization case (normal angle of incidence), and agreement is observed only for asymmetrical coupling, where the coupling coefficients κ_{AB} and κ_{BA} are not equal. Interestingly, the resonance frequency ω_R in the numerical fitting and in the simplified analytical models are shifted due to the interaction between the perturbation oscillator B and oscillator A_0.

Chapter 6

Open-Source User Interface of Frequency based numerical algorithms – "ZenScat"

The applications, user interfaces and open source libraries are crucial to scientific development, data analysis, data acquisition, and, importantly, data generation. Open source computational tools allow engineers and researchers to develop their own algorithms, such as introducing non-linear terms in linear solvers (such as MEEP computational toolbox for instance, which specializes in FDTD [137], or TDYNO [138]), use optimization for inverse design problems and parameter retrieval. Furthermore, open source packages enhance bridging between theory and experiment, which is of great importance for general scientific development. With the use of capable hardware, GPU acceleration and parallel computing, the designed libraries and software perform computations at a much faster rate, thus enabling rapid data generation. The open source, user friendly software ZenScat is hereby presented as an ***addition*** to the vast diversity of open source algorithms and software that solve problems numerically in the field of linear optics [139–146].

The material related to this thesis was published in paper [**A5**].

6.1 Application concept

The "ZenScat" application is divided into 2 categories: the main 2D RCWA app and 2D FDFD field app. The former contains fixed dielectric interface functions, interface import and optimization regimes, whereas the latter is used primarily for field distribution computations of the resonant gratings in frequency domain. The concept ZenScat UI with application layout is illustrated in Fig. 6.1. The application is made with the goal of computing diffraction efficiencies for arbitrary structures for TE (s) and TM (p) polarizations. The "casual" application is focused primarily on multilayer thicknesses and each layer's material is abbreviated by the refractive index value. It is done so for the embedded geometries, such as harmonic, supergaussian or trapezium interface functions. Other functions can be added in the Github repository as well. The "import" application calculates convolution matrix from each sub layer of imported refractive index geometrical distribution in a single period. It serves the same purpose as "casual" application, which is the calculation of diffraction efficiencies in superstrate and substrate. The optimization app part is used for maximizing diffraction efficiency values, absorption or gain with genetic algorithm. It contains import function for arbitrary geometries, as well as for same embedded geometries. Field app is based on the 2D FDFD algorithm and is chosen for better computation speed (via controlled grid resolution) of the field profiles for E_z and H_z modes.

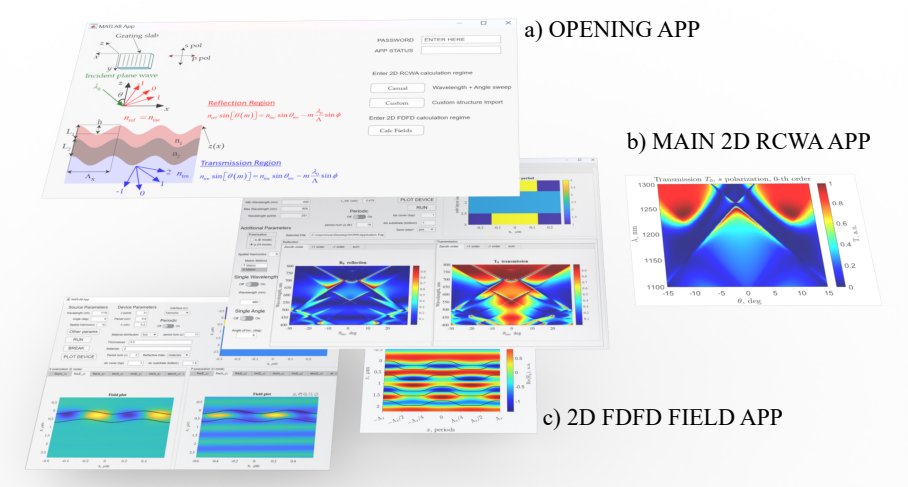


Figure 6.1: User interface concept of 2D RCWA + 2D FDFD software and its components: (a) opening app, (b) main 2D RCWA app, (c) 2D FDFD Field app.

6.2 Benchmark of ZenScat

The cross-validation of the diffraction efficiency computations across literature is handful for determining if the implemented algorithm works correctly with no errors or loss of accuracy. Here the analysis of diffraction efficiencies has been performed for rectangular and harmonic interfaces for the GMR filters, as well as for the dispersive Bragg coupler with rectangular grating on top.

6.2.1 Validation with FDTD

The results calculated by Lumerical commercial FDTD software is the first step for the carried validation. The grating of interest is selected for biosensing of biological analytes [147]. The idea presented in this work is to create a single-wavelength sensory device without the requirement of spectrometer, but is sensitive enough to the ambient refractive index change that a monochromatic detector is capable of registering a GMR shift. What is notable is that a conical mount is considered in this model as a full 3D simulation in commercial Lumerical software. However, the system can be presented for 2D cases, and be modeled as well, but without incident beam with circular or elliptical polarizations.

The grating results are simulated via FDTD (Ansys Lumerical Inc.) software and presented in [147]. The geometrical and material parameters of the GMRF in the publication are: $n_{sup} = 1$, $n_{sub} = 1.47$, $h = 120$ nm, $L = 80$ nm,

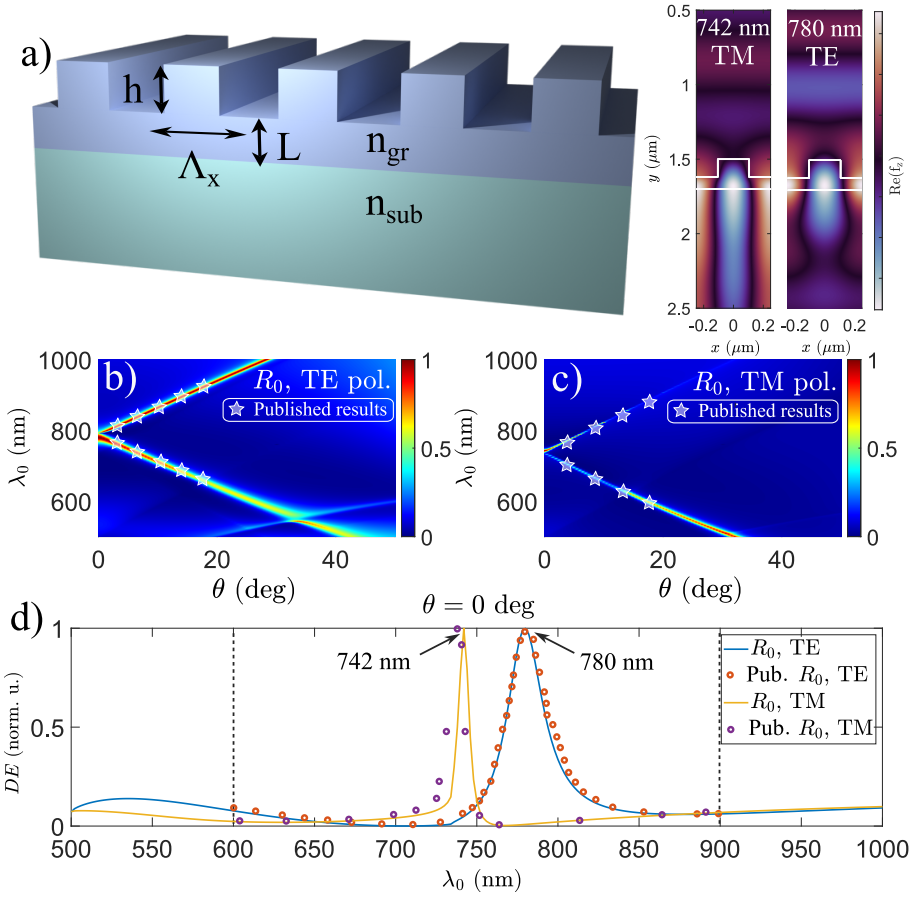


Figure 6.2: Guided mode resonance reflection spectra of SiN_4 grating via the RCWA approach. Accordingly, (a) for TE (b) and TM (c) polarizations, as well as diffraction efficiencies for both polarizations at normal incidence (d). The structure is derived from [147]. The dotted line in d)

$\Lambda_x = 500$ nm, $w_{gr} = 250$ nm. The offset of resonance peaks in the wavelength spectrum for TE polarization is 2 nm, whereas, for TM polarization, it is 4 nm once compared with 2D RCWA results. These correspond to resonance peaks of 780 nm and 742 nm calculated by RCWA, and offsets of 0.26% and 0.54%, respectively. One explanation would be that the initial study features a smaller mesh grid resolution to decrease calculation time as a full 3D model was used, which accounts for the resonance peak shift, thus the non-convergence of the results. The $\lambda_c = \Lambda_x n_{\text{sub}} = 735$ nm, which indicates that GMR is present in sub-wavelength regime.

The other structure of interest is the GMR harmonic grating, which pertains two layered interfaces. The geometry parameters are precisely tuned that the

reflectance peaks remain at the same wavelength, which is at $\lambda_{0,\text{peak}} = 510.6$ nm, as reported in the paper [148]. The problem presented in the paper is the

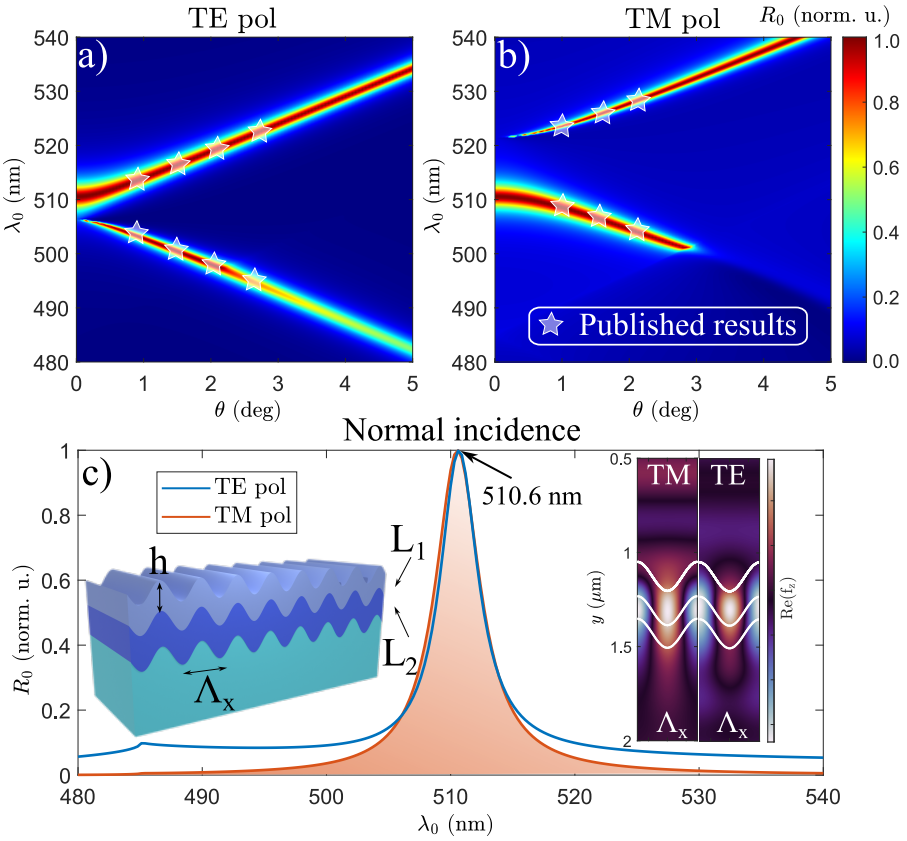


Figure 6.3: RCWA derived reflection spectra distributions of TE polarization (a), TM polarization (b) and their intersection at normal incidence (c) for double layered harmonic gratings first reported in [148].

ability to pertain GMR at both TE and TM polarizations via two layers at normal incidence, since there is an offset between GMR based reflections once linear polarization of the incident wave is varied. So thickness values of two layers are varied to match GMR at $\lambda_{0,\text{peak}} = 511$ nm. The offset corresponds to 0.0783%.

The parameters of the device are presented in the following: upper layer thickness $L_1 = 0.182$ μm, lower layer thickness $L_2 = 120$ nm, transverse periodicity $\Lambda_x = 320$ nm, modulation depth $h = 154$ nm, substrate refractive index $n_{sub} = 1.516$. Layer material parameters involve $n_1 = 1.781$ and $n_2 = 1.650$ for upper and lower layers, respectively. In ZenScat UI, 11 spatial harmonics were used in the simulation. The field profiles indicate that at resonance peaks two distinct guided modes appear for normal incidence for that particular

wavelength.

6.2.2 Validation with RCWA

The validation is further carried out for R. Magnusson's work. The concept of spatial optical beam filtering via thin films. The idea is to use GMR of modulated thin films at ***sup-wavelength regime***, which is due to observable narrow reflection (0.1 deg = 1.75 mrad) features. The main results are illustrated in Fig.6.4 (a-d).

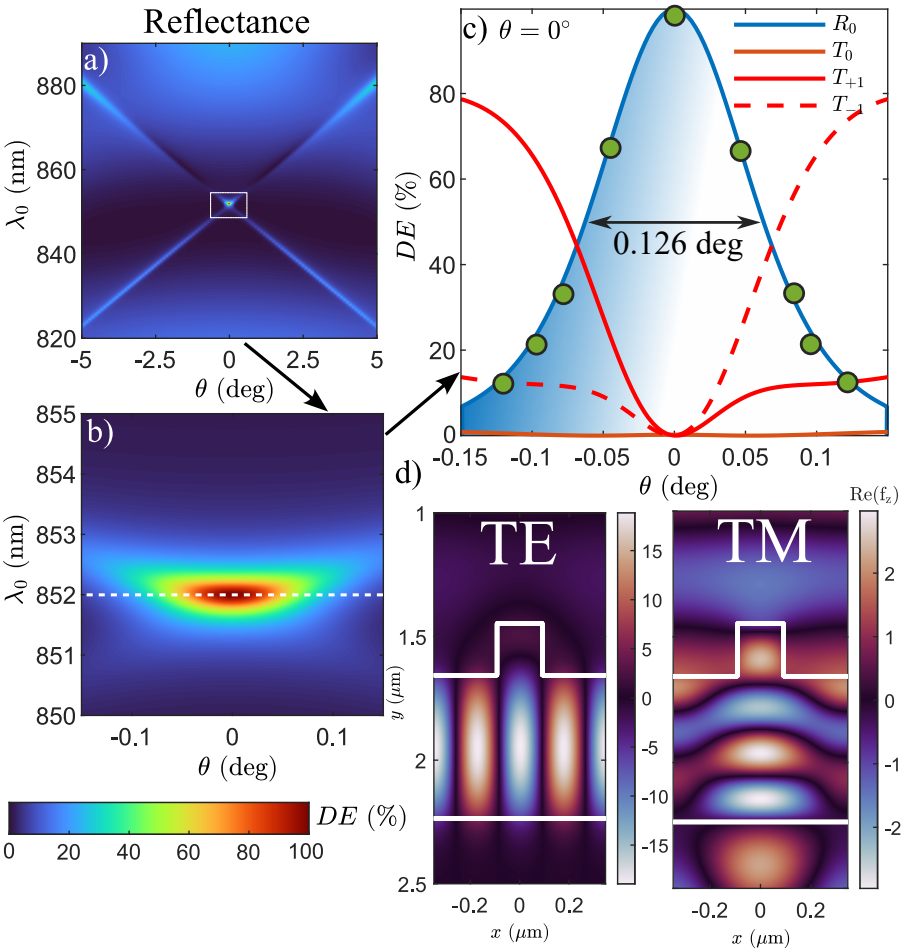


Figure 6.4: Magnusson's spatial filtering results first reported in [86] and reproduced here with "ZenScat". The zeroth order reflection is denoted at a) zoomed at b), the diffraction efficiency is present at with benchmark data represented with green dots c) for the thin film GMR sup-wavelength grating, shown at d).

The parameters of the GMR device used: $n_g = 2.52$ TiO_2 film, $n_{sub} = 1.54$,

$n_{sup} = 1$, $\Lambda_x = 696$ nm, film thickness $L = 578$ nm, grating amplitude $h = 210$ nm. The filling factor of the rectangle grating $f = 0.33$. The GMRs are encountered in sub wavelength regime, however, the filtering is proposed for the sup-wavelength regime region, where high order GMR is present (see Fig 6.4 a) and b)). The GMR is present for $\Delta\lambda_0 = 0.6$ nm at its FWHM, and for the $\Delta\theta = 0.126$ deg. Both first order diffraction efficinecies occur at oblique angle of incidence for that case (see Fig. 6.4 c)). Furthermore, FDFD method outputs the field distribution where the 2nd order GMR is present for TE polarization, whereas TM polarization does not, due to the resonance being polarization sensitive (see Fig. 6.4 d)).

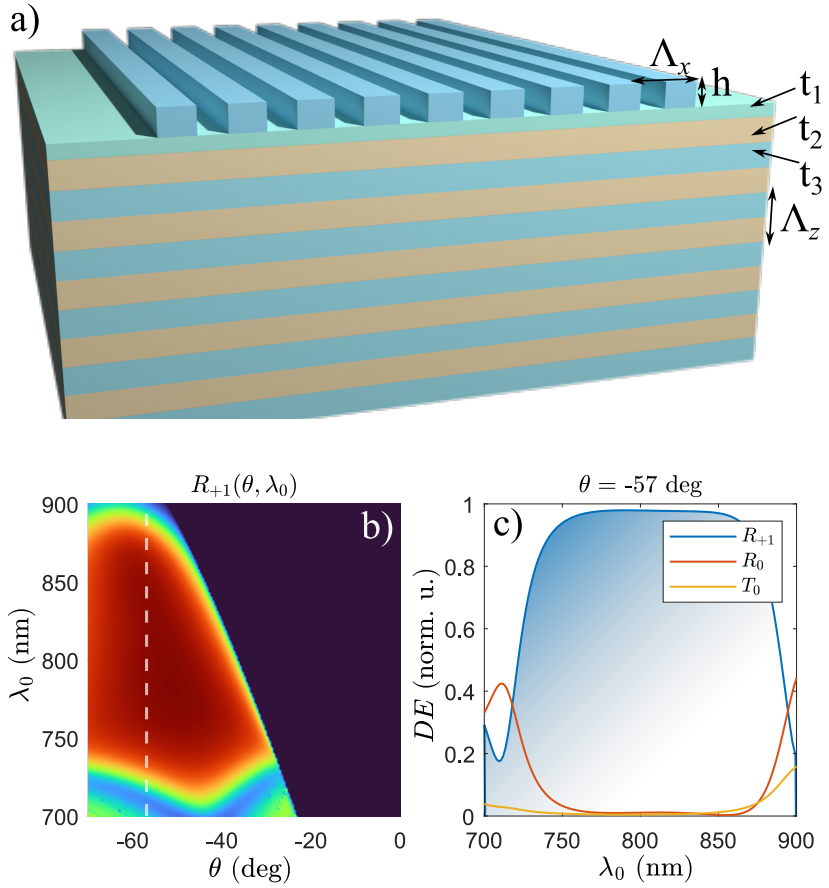


Figure 6.5: Flat top dispersive reflector spectrum [55]. a) denotes a device of interest with its geometrical parameters, b) its first-order reflection coefficient and c) diffraction order distribution.

Also, with the enhancement of the angular dispersion, Laser Induced Damage Threshold (LIDT) can be improved with such devices as well, due to their diffractive operative regimes. In this work [55], the rectangular HfO_2 grating

is placed on top of the SiO_2 match layer on top of 1D photonic crystal, whose layers alternate between Ta_2O_5 and SiO_2. The photonic crystal acts like a reflector at quarter-reference wavelength for high and low refractive index distributed layers, and a grating is a coupler between incident beam and R_{+1} reflection order. Device parameters, such as periodicity, grating depth, its fill factor in a single transverse period, match-layer thickness are all parameters that are fine tuned in order to provide continuous, broad-band reflectance at R_{+1}, given oblique angle of incidence and sup-wavelength regime. In such a way, the field's amplitude is reduced from the grating, in order to minimize electric field's peak amplitude. The flat top for the first-order reflection coefficient is present here, which signifies the operating regime for 100 nm from 750 nm to 850 nm. The parameters are hence grating amplitude $h = 185$ nm, periodicity $\Lambda_x = 502$ nm, thicknesses $t_1 = 40$ nm, $t_2 = 136$ nm, $t_3 = 109$ nm, refractive indexes $n_1 = 1.47$ (FS), $n_2 = 2.17$ (Ta_2O_5), $n_3 = 1.47$ (FS). The parameters are shown in Fig. 6.5 a), the spectra in 6.5 b) and c). Even though authors present spectral data for single angle of incidence $\theta = -57$ deg, spectral and angular response provides 0.9 to 0.95 flat top reflectance, which means that such a device is able to operate broader range of oblique angle of incidence, such as 57 ± 10 deg.

6.3 Optimization of DFB for enhanced, narrow-band absorption and gain

Furthermore, the ZenScat user interface provides an optimization app specifically for fine tuning device's geometrical parameters to satisfy a lowest possible minimum of a diffraction efficiency, gain or absorption loss. As a demonstration of the application's capabilities, the Distributed Feedback (DFB) system is selected (see Fig. 6.6 a)), which consists of the rectangular grating layer, homoegenous layer which is connected with the grating and absorption/gain layers. The device is classically engulfed with superstrate ($n_{\text{sup}} = 1$) and with substrate (n_{sub}) = 1.5. The main idea is to use propagating GMR modes inside the grating that are coupled with the bottom active/absorbent layers in order to enhance absorption loss or optical gain. For this reason, the s polarized source of $\lambda_0 = 700$ nm at normal incidence is chosen for three cases of the homogeneous third layer (marked green in Fig. 6.6 a)): gain medium (perovskite material), metallic absorber (silver) and weak absorber (Silicon) for that specific wavelength. The boundary conditions for the algorithm are shown in Table 6.1.

Table 6.1: DFB boundary conditions for genetic optimization, given $n_{sub} = 1.5$.

Boundary value	Λ_x, μm	L_1, μm	L_2, μm	L_3, μm
LB	0.3	0.0	0.0	0.0
UB	0.8	1.0	1.0	1.0

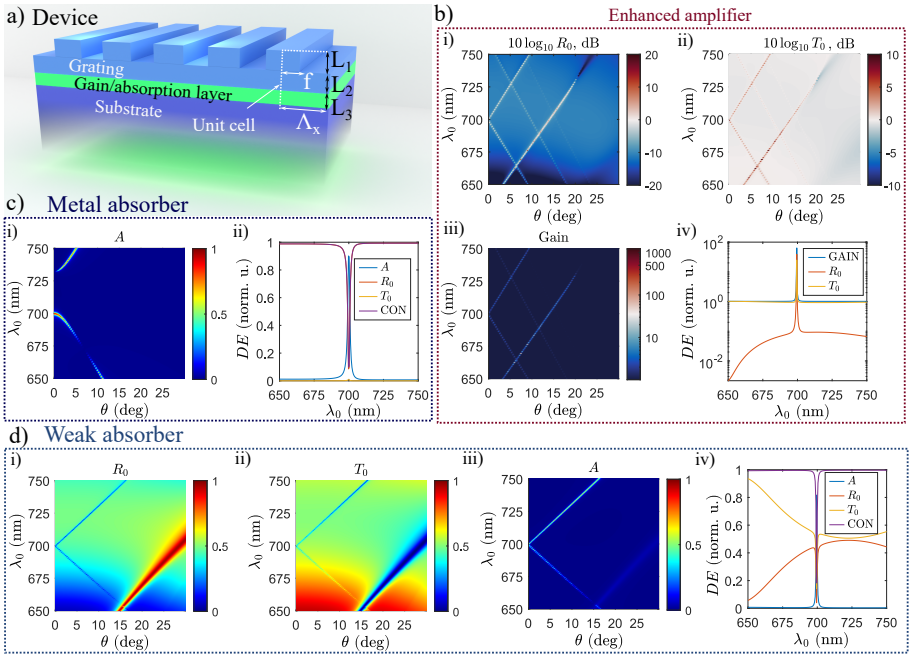


Figure 6.6: DFB system which utilizes GMR-based coupling from the grating with gain/absorption layer (a). The enhanced gain spectrum is shown in b), given the Diffraction Efficiencies (DE) R_0 and T_0, as well as values for normal incidence (shown in b, iv). The absorption A profiles of the metallic absorber are shown in c). The weak absorber's DE characteristics are provided in d).

After the genetic optimization procedure, the parameters that satisfy the best minima are achieved (and presented in Table 6.2) and presented in the Table 6.2. Enhanced amplifier case pertains up to 20 dB of gain in reflectance and up to 10 dB in transmittance spectra. Total gain is up to 20.42 dB at the resonant lines pinpointed in Fig. 6.6 b) iii), providing only the narrow resonances which enhance gain in zeroth diffraction orders. Metallic absorber only pertains pure reflectance until the GMR is reached, so only absorption angular spectrum is shown (see Fig. 6.6 c) i)). Oblique angle of incidence is what offsets the resonant absorption lines. At the point where energy conservation drops, at normal incidence (see Fig. 6.6 c) ii)) only one resonant absorption is obtainable.

Table 6.2: DFB parameters achieved of genetic optimization, given $n_{sub} = 1.5$.

Λ_x, μm	L_1, μm	L_2, μm	L_3, μm	n_{gr}	n_c
0.5336	0.1098	0.1006	0.1	2.0	$0.04 - 4.80j$
0.343	0.1606	0.1858	0.2845	2.0	$3.4 - 10^{-3}j$
0.4027	0.1578	0.01767	0.8117	1.5	$2.04 + 10^{-3}j$

Other system of interest is GMR based DFB, where silicon is placed as the last layer. It is termed as weak absorber and has its imaginary part $\mathrm{Im}(n) = 10^{-3}$. The narrow-band absorption is achieved at normal incidence and pertains its linear shift in spectral domain vs oblique angle of incidence. Absorption is achieved due to the GMR being narrow band, resulting in strong light confinement within the DFB device. A minute absorption is also visible within the second resonance at oblique angle of incidence, however, it is too broad to enhance light-to-matter interaction.

6.4 Application performance

The goal of this work is to evaluate the performance between S and T matrix methods that are implemented in Matlab, as well as their compiled versions via Matlab Coder app as well as with the variants provided by accessible commercial software [149]. Compared with the Scattering matrix method, the ETM approach can increase the RCWA algorithm's speed performance. However, accuracy needs to be evaluated for GMR filters and photonic crystals. For a specific example, we chose the sinusoidal holographic layer type structure [150–153]. The selectivity of such structures for polarisation states is well known [154] and can be used as a benchmark. Figure 6.7 summarises the relevant results.

The ETM approach is abbreviated as the T-matrix method [53], whereas the scattering matrix method is abbreviated as the S—matrix method [92]. The device is constructed in the algorithm before launching 2D RCWA calculations for wavelength sweep at normal incidence (**dispersionless** case). For a single wavelength ($\lambda_0 = 1.0$ μm), the results are presented in (a) and (b). The compiled version provides a thorough 2 times speed improvement via the "MATLAB" coder app. The unusual feature is presented in Fig. 6.7 (b), where the calculation procedure is much longer for spatial harmonic counts lower than 11. The compiled version allows to overcome that for both S and T matrix methods. Results presented in Fig. 6.7 (c,d) evaluate relative accuracy performance for the same structure. The calculation is simply performed by $\Delta\eta_T = |T_0^{(\mathrm{Tmatrix})} - T_0^{(\mathrm{Smatrix})}|$ as well as $\Delta\eta_R = |R_0^{(\mathrm{Tmatrix})} - R_0^{(\mathrm{Smatrix})}|$.

Furthermore, convergence study is performed for rectangular gratings, mainly zeroth order DE's dependence of both the GMR resonance of the first Lumerical's filter (Fig. 6.2) and optimized DFB metallic absorber (Fig. 6.6 c)). The former, and the latter variants' convergence are visualized in Fig. 6.7. Both resonant cases acquire 6 spatial harmonics (13 total from -6 to +6) for fully converged resonances, be it sub-wavelength regime (see Fig. 6.7 e)) and sup-wavelength regime (see Fig. 6.7 f)).

Calculation speed was compared with the modal method used in "MC grating" software [149]. It is summarized in the Table 6.3.

The computation was performed on the old hardware, Intel(R) Core(TM) i5-33320M @ CPU 2.6 GHz to achieve this comparison. The calculation was performed on the trapezium-shaped interface parameter sweep for the given

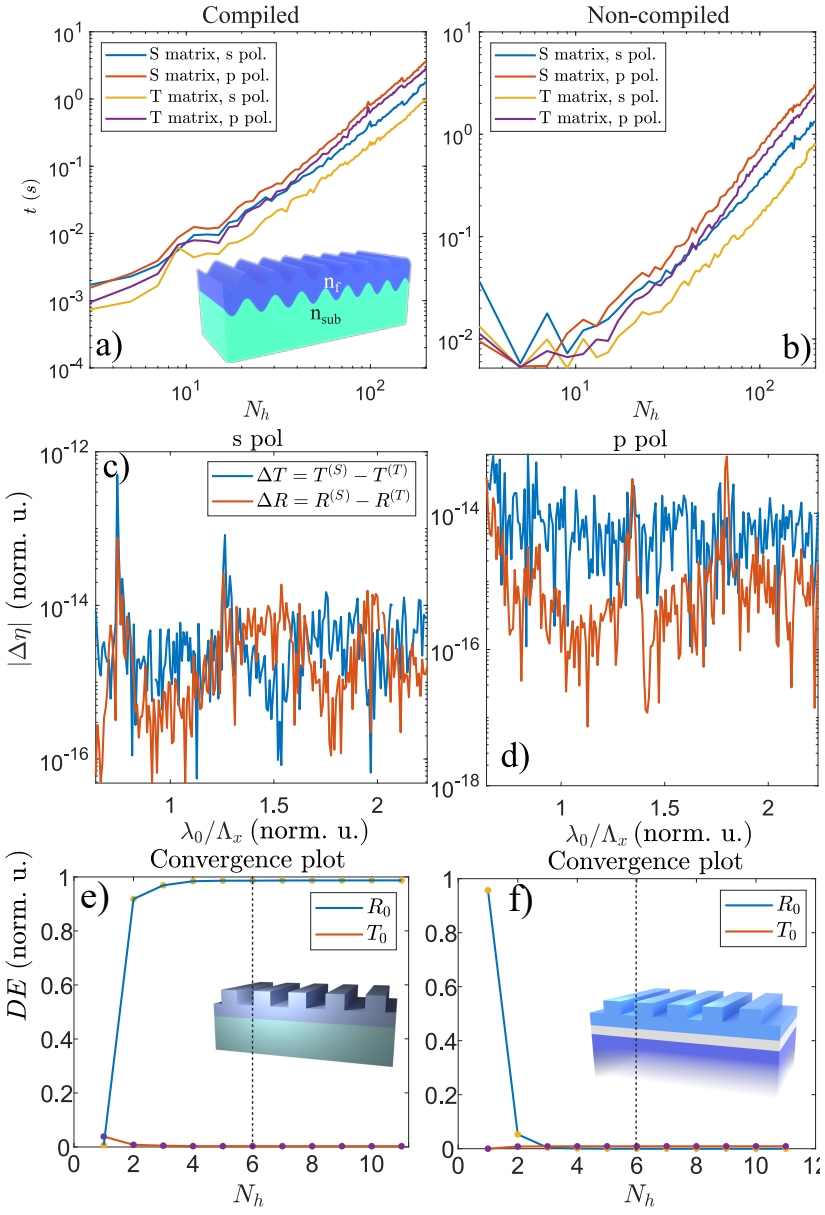


Figure 6.7: Algorithm performance with compiled (a) and non-compiled (b) matrix methods. The diffraction efficiency errors for monolayered GMR filter for s and p polarizations (c,d) for $\theta = 15$ deg angle of incidence. The convergence results are for rectangular GMR filter [147] e) and metallic DFB device from optimization case (f).

Table 6.3: Computation speed comparison (in time).

Polarization state	S Matrix, s	T matrix, s	MCGrating, s
TE (s pol)	34.77	20.48	≈ 50
TM (p pol)	39.15	27.46	≈ 60

parameters: $N_z = 11$, $N_x = 1028$, $N_h = 11$, $n_\lambda = 101$, $n_\theta = 101$, all corresponding to discrete layers along z and x directions, spatial harmonics, wavelength and angle of incidence. Note that such results are attained only for compiled C++ files (denoted as 'mex') in Matlab (version 2023b, MathWorks, Inc., using the "MATLAB Compiler$^{\text{TM}}$").

Reflection and transmission calculations were performed for T matrix method separately, thus reducing the amount of matrix operations in the function and achieving computational speeds twice as fast **as** the MCgrating commercial software.

6.5 Summary

This section introduces frequency based 2D RCWA and FDFD Open Source UI "ZenScat" for numerical simulation applications of the Guided Mode Resonance gratings, which are primarily used for sensing, spectral, polarization selectivity, spatial filtering by conformal harmonic/rectangular gratings and for enhanced angular dispersion via rectangular grating on top of Bragg filters. Benchmark procedure is applied for mentioned devices whose spectral characteristics are computed by commercial Lumerical method and are published in scientific literature. The spectral reflectance peak offset errors are highest for rectangular grating case (0.54%), and lowest for harmonic conformal grating case (0.08%). Furthermore, compared with other RCWA variants, numerical simulations of concurrent narrow band rectangular spatial filter case, there is no observed offset of error.

The User Interface embeds S and T matrix methods into the RCWA algorithm, which are hence compiled into C++ files via "MATLAB Compiler$^{\text{TM}}$ and gains tenfold computational speed advantage up to of 9 spatial harmonics and twofold speed advantage for greater resolution. Also, compared with commercial MCgrating's Fourier Modal Method, "ZenScat" exceeds the computational speed 1.5-2 times with the use of 11 spatial harmonics resolution in the model. Moreover, convergence study is performed for the rectangular GMR grating from benchmark study in sub wavelength regime ($\lambda_0 > \Lambda_x n_{\text{sub}}$) and for the DFB with metallic homogeneous layer in sup wavelength regime ($\lambda_0 < \Lambda_x n_{\text{sub}}$) with additional ± 1 diffraction in substrate region. Both study cases confirm that 6 spatial harmonics are enough for convergence of narrowband GMR based reflection and absorption.

Also, optimization of GMR based absorption and gain is performed for DFB based photonic structures with rectangular conformal gratings. The geometry parameters of the device are then tuned to maximize enhanced optical gain, and

improve narrow band absorption for weak absorber (Si) and strong absorber (Ag). Zeroth order diffraction efficiencies' spectral characteristics reveal that enhanced linear light to matter interactions are present for narrowband GMRs in the DFB case with periodically modulated grating on top.

Conclusions and summary of results

1. The trapezium interface enforces leaky mode-type reflection with varying FWHM widths in the angular regime and continuous uniform distribution up to $\Delta\lambda = 46$ nm of bandwidth in the spectral regime. This is due to the topology of the filter and multiresonant phenomena, which are confined within the Rayleigh region. The experimental fabrication presents non-repetitiveness of Ta_2O_5 thin film's interface function; however, the leaky mode-based reflection is still pertained near the $\Lambda_x n_{\text{sub}}$ wavelength at normal incidence for reduced bandwidth of $\Delta\lambda = 4$ nm.

2. The analytical model, in order to characterize GMR, exploits Schrödinger's equations with field injection to solve the bounded eigen-mode problem for s polarization, specifically for GMR filters that pertain to a single transverse modulation function. At the EOC, the $\sqrt{1/\Delta E}$ dependence illustrates the asymmetrical and non-continuous features of the leaky modes. At this point, the analytical expressions predict the scaling at the order of 4, while deep bounded modes scale at the order of 2 and FP response function pertains $1/\Delta E$ dependence. Fabricated GMRF is with non-preserved modulation function of the Nb_2O_5 thin film, but pertains broadband reflectance, which is confined by the Rayleigh phenomenon and EOC for GMR is identified at oblique angle of incidence of $\theta = 4$ deg.

3. The asymmetrical distribution of an absorber provides greater absorption than the symmetrical one with the same volume of the metallic material due to the enhanced coupling between the FP mode and the GMR. According to the coupled mode theory, absorption is enhanced by the factor of 8/5. The single interfaced GMR filter only does so via the factor of 4/3 according to RCWA. The GMR structure with normalized thickness $L/(\Lambda_x n_{\text{sub}}) = 0.326$ is proposed because of its strong operation at leaky mode regime at s polarized input. In this case Rayleigh anomaly is capable of enhancing a cut-off wavelength, which is predictable at $\lambda_R = \Lambda_x(n_{\text{sub}} \pm \sin\theta)$, given the first order diffraction. This signifies the cut-off of the enhanced absorption of the surface wave traveling perpendicular to the grooves of modulation.

4. Enhanced zeroth order diffraction efficiencies is present only for GMRs with high quality factors, i.e., at small enough FWHM where the highest localization of the field is possible. At the width of $\Delta\lambda_0 \approx 30$ nm, the amplification is present for all zeroth-order DEs for the first-order GMRs.

With this property in mind, the geometry of the GMR filter can be tuned to properly enhance gain with obligation to the mode confinement within the active thin film, where the presence of gain is able to shift the resonance at the scale of nanometer. Due to the use of GA, the zeroth-order DEs amplification is experienced for all linear polarizations at the subwavelength regime ($\Lambda_x n_{\text{sub}} < \lambda_0$), given their sensitivity to the angle of incidence of the source. Single polarization amplification is only experienced at the sup-wavelength regime ($\Lambda_x n_{\text{sub}} > \lambda_0$) for s polarization, where $T_{\pm 1,0}$ and $R_{\pm 1,0}$ diffraction efficiencies are present.

5. Comparison with Lumerical's 3D FDTD simulations, RCWA's algorithm, implemented in ZenScat, offsets at 0.54% for TM polarized GMRs. Compared with FDTD, in the harmonic interface case, computed spectral maxima differ only by 0.08% in the subwavelength regime. Comparison with another RCWA variant, such as a concurrent rectangular GMR-based spatial filter, operating in the sup-wavelength regime, leads to non-differing results. The MATLAB compilation of T and S matrix methods allows faster calculations at low spatial harmonics (up to 9) at a factor of 10, whereas after 11 spatial harmonics, the computational speed is 1.5-2 times as fast, which is preferable for faster numerical evaluations of GMRs and scattering effects, as well as for optimization-based problems.

Appendix

A1 Maltab 2D RCWA code

This section contains Maltab code for 2D RCWA involving scattering matrix method. The source parameters such as wavelength Lam0 and Theta are defined withing the script. Params() is a struct containing necessary values of the system being analyzed. Zeroth order DEs are T0 and R0. The function 'Device' is called to construct the permittivity array, which is incorporated in the eigenvalue computations in S matrix method. Finally, forward 'TRN' and backward 'REF' DEs are computed ans stored into memory. Other available functions, such as T matrix method and interface parameters, are in the GITHUB repository: `https://github.com/ElectroMagneticAddict/ZenScat-UI`.

Main play-script of the 2D RCWA

```
clear all
close all
clc
%% Parameters
NH = 6;              % Spatial harmonic num: N = 2*NH + 1
interface  = 'sin'; % Interface str - see 'Device'

% Additional interface params
interface_params = Int_Params;
%% ------------------------------------------------

% Layer stacking (thickness + refr idx)
% Params -> L1, L2, L3, n1, n2, n3
Params       = [0.182 0.120 1.781 1.650];
is_S_matrix  = 0;  % 0 if T matrix used

% Arbitrary distribution - 'all', periodic - 'two'
distribution = 'all';

if strcmp(distribution, 'all')
    % 1 refr index for 1 layer
    layer_num = ceil(length(Params)/2);
else
    % 2 refr indexes for all layers
    layer_num = length(Params) - 2;
    if layer_num == 0
        layer_num = 1;
    end
end
% Extract source and resolution parameters in [P]
[P] = Parameters(layer_num, distribution);
```

```
%% -------- Regular RCWA algorithm ------------------
for Mode =  ['E', 'H'] % run for TE and TM pols
    % Assert main params
    P.Params = Params;
    % Build grid struct
    grid   = Grid(Params, interface, P);
    % Extract sub_L and ERC in device struct
    device = Device(NH,grid,...
        interface, interface_params);
    %% ---------------------------------------------

    if is_S_matrix
        % compile to mex afterwards
        [TRN, REF] = Launch_RCWA_S(NH, grid,...
        device, Mode);
    else
        % compile to mex afterwards
        [TRN, REF] = Launch_RCWA_T(NH, grid,...
        device, Mode);
    end
    % Function for plotting diffraction efficiencies
    Plot_TRN_REF(TRN,REF,grid,Mode,Params,interface)
end
```

Parameter function for 2D RCWA

```
function [P] = Parameters(layer_num, distribution)
%% Define geometrical parameters for the optimization procedure
P.layer_num    = layer_num;
P.distribution = distribution;
%% ------- Periodic distribution -------
P.is_periodic = 0 ;
P.period_num = 33;
%% ------- Layer dims distribution for optimization -------
if layer_num == 1 || layer_num == 2
    % default layer lengths - this can be changed
    P.Lengths = [0.580];
    % refractive indexes - this can be changed
    P.idx = [2] .* ones(1,layer_num);
    % total parameters - don't change this as well
    P.Params = [P.Lengths, P.idx];
else
    P.Lengths = ones(1,layer_num); % default layer length in um
    switch distribution
        case 'all'
            P.idx = [2] .* ones(1, layer_num);
        case 'two'
            P.idx = [2 3]; % periodic refr. idx distribution
    end
```

```
    P.Params = [P.Lengths P.idx];
end
P.n_sup = 1;
P.n_sub = 1.516; %
%% Modulation depth & transverse period
P.h  = 0.154;   % modulation depth
P.Lx = 0.32;  % transverse period
%% Define wavelength, discretization (Nz)
lam_num   = 201;
theta_num = 4;
rad       = pi/180; % transformation from degrees to radians
P.Lam0    = 1e-9 * linspace(480, 540, lam_num);
% P.Theta   = rad * linspace(0, 15, theta_num);
P.Theta   = 0 * rad;
P.Nx      = 1028;
P.Nz      = 15; % window size for 1 interface (25)
P.layer_num = layer_num;
end
```

Device function for 2D RCWA

```
function device = Device(NH,grid,interface, interface_params, ...
is_flat)
% This function builds sub_layer thicknesses and convolution matrix
% for each sub_layer
% It extracts:
% Array  /--------- Meaning -------/ Dimensions
% ER    -> relative permettivity -> (x, sub_layer)
% ERC   -> convolutional matrix  -> (NH,NH,sub_layer)
% sub_L -> sub_layer thicknesses -> (sub_layer)

layer_num = grid.layer_num;
Length    = grid.Length;

% Choose if substrate is flat
if nargin == 4
    is_flat = 0;
else
    is_flat = 1;
end
%% Various structures
    %% cases for different interfaces
    if strcmp(interface, 'sin') == 1
        % Ideal harmonic interface
        z = grid.h/2 * sin(grid.qx * grid.x - pi/2);
    elseif strcmp(interface, 'DE1') == 1
        % Ideal trapezium interface
        z = trapezium(grid.x, grid, ...
        interface_params) - grid.h/2;
```

```
    z = [z(:,floor(grid.Nx/2+1):end) ...
    flip(z(:,floor(grid.Nx/2+1):end),2)];
elseif strcmp(interface, 'DE4') == 1
    % Supergaussian interface
    z = Trapezium_Softened(grid.x, grid, ...
    interface_params) - grid.h/2;
elseif strcmp(interface, 'tri') == 1
    % Triangular interface
    z = Triangle(grid.x, grid, interface_params);
else
    z = grid.h/2 * sin(grid.qx * grid.x - pi/2);
end
% Define d matrix - locations of interfaces + substrate
d = zeros(1+length(Length),length(z));
%% ----------- Main interface conversion to array  ---------
d(1,:) = z;
for i = 1:length(Length)
    if Length(i) > grid.h % Field
        Length(i) = grid.h/(grid.Nz) + grid.h;
    end
    d(i+1,:) = z(:) - sum(Length(1:i));
end
% air vs n_high
Area  = grid.erR * ones(grid.Nx,grid.Nz+grid.delta);
%% ----------- Main interface conversion to array  --------
idx = 1; % idx for all arbitrary profiles
for i = 1:length(Length) + 1
    if i == length(Length) + 1
       idx = length(Length);
    end
    d_0 = d(i,:);
    for nx = 1:grid.Nx
        nz  = round((d_0(nx) + grid.Lz/2)/grid.dz);
        % fill epsilon(z,x)
        Area(nx,1:nz+grid.delta) = grid.erIdx(idx);
    end
    idx = idx + 1;
end
%% Substrate part
if is_flat
    d_0 = z(:) * 0 - sum(Length) + 1*grid.h/2; % flat surface
else
    d_0 = d(end,:);
end

for nx = 1:grid.Nx
    nz  = round((d_0(nx) + grid.Lz/2)/grid.dz);
    Area(nx,1:nz+grid.delta) = grid.erSub;
end
```

```
    %% Post processing part
    ER = rot90(Area);

    ER(ER<=0) = 1;
    D         = size(ER);
    %% find indices where epsilon of substrate is the same
    Ind_Substr = zeros(1,D(1));
    for i = 1:D(1)
        Ind_Substr(i) = sum(ER(i,:))/length(ER(i,:)) - grid.erSub;
    end
    idx_substr   = abs(Ind_Substr) < 1e-6;
    INT_substr   = diff(idx_substr);
    Substr_Index = find(INT_substr==1); % Find where is substrate
    ER(Substr_Index + 4:end,:) = [];    % Eliminate bad layers
    D = size(ER);
    %% Insert bigger thicknesses there when L_i > h
    indices = zeros(length(Length),D(1));
    for j = 1:length(Length)
        for i = 1:D(1)
            indices(j,i) = sum(ER(i,:))/length(ER(i,:)) ...
            - grid.erIdx(j);
        end
    end
    idx   = abs(indices) < 1e-6;           % returns 1s for L > h
    sub_L = GeometrySub_Lengths(grid,idx); % returns L distribution
    %% Convolution for smoothing the edges if n(x,z) is not smooth
    B = exp(-((grid.x-mean(grid.x))/grid.Lx*100).^8);
    SS = size(Area);

    if interface_params.smooth
        for j = 1:layer_num
            for i = SS(2):length(ER(:,1,1))
                ER0 = fft(ER(i,:,j)).*fft(B)/sum(B(:));
                ER0 = ifftshift((ifft(ER0)));
                ER(i,:,j) = ER0;
            end
        end
    end
    %% Fourier transform along z and calculate convolution matrix
    E = convmat1D(ER,NH);
    %% Save all the data inside the structure
    device.ER    = ER;
    device.ERC   = E;
    % conversion to nm (Used for X = expm(- sub_L * k0 * eigen_val)
    device.sub_L = sub_L * 1e-6;
end
```

Wavevector function

```
function [Kx,KzT,KzR] = calcK(grid,lam0,theta,NH)
%% Calculate K_x, K_z^{(trn)} and K_z^{(ref)} diagonal matrices.
    ninc = sqrt(grid.erR * grid.urR);%n_inc
    N    = 2*NH + 1;
    k0   = 2*pi / lam0;
    %----------------------------------------
    kinc_x = k0*ninc * sin(theta); %kx^(inc)
    M      = -((1:N)-NH-1); % harmonic orders
    N      = length(M); %Size of matrices
    k_x    = complex(zeros(1,N));
    for i = 1:N
        k_x(i) = kinc_x  - 2*pi*M(i)/(grid.Lx*1e-6);
    end
    k_x(k_x==0) = 1e-6; % replace zeroes
    Kx  = diag(k_x(:)/k0);
    KzT = conj(sqrt(complex(grid.erT.*grid.urT.*eye(N) - Kx.^2)));
    KzR = -1*conj(sqrt(complex(grid.erR*grid.urR*eye(N) - Kx.^2)));
end
```

Wavevector functions

```
function [TRN,REF] = Launch_RCWA_S(NH,grid,device,Mode)
%% Define variables
N = 2*NH + 1;
SG.S11 = complex(zeros(N,N));
SG.S12 = complex(eye(N));
SG.S21 = complex(eye(N));
SG.S22 = complex(zeros(N));
S = cell(1,4*grid.layer_num + 2);
S = coder.nullcopy(S);
for i = 1:length(S)
    S{i} = SG;
end
src = zeros(N,1);
src(floor(N/2)+1) = 1;
Zeros = zeros(length(grid.Lam0), length(grid.Theta));
% Transmission profiles
TRN.minus_1 = Zeros;
TRN.plus_1  = Zeros;
TRN.TRN0    = Zeros;
TRN.sum     = Zeros;
% Reflection profiles
REF.minus_1 = Zeros;
REF.plus_1  = Zeros;
REF.REF0    = Zeros;
REF.sum     = Zeros;
for mode = Mode
    for i = 1:length(grid.Lam0)
```

```
        lam0 = grid.Lam0(i);
        for j = 1:length(grid.Theta)
            theta = grid.Theta(j);
            %% Kx, Kz and eigen-modes of outer regions
            [Kx, KzT, KzR] = calcK(grid,lam0,theta,NH);
            [SG, W0, V0] = calcFreeSpace(Kx,N);
            [Wref, Sref] = calcReflectionSide(Kx,KzR,N,W0,V0,...
            grid,mode);
            [Wtrn, Strn] = calcTransmissionSide(Kx,KzT,N,W0,V0,...
            Wgrid,mode);
            %% S matrices for a device
            for layer = 1:grid.layer_num
                for sub_layer = 1:length(device.sub_L)
                    [Si] = calcLayer(Kx,lam0,N,W0,V0,...
                    device,sub_layer,mode);
                    SG   = star(SG,Si);
                end
            end
            SG = star(Sref,SG);
            SG = star(SG,Strn);
            %% Calculate Source Mode Coefficients
            csrc = Wref \ src;
            %% REFLECTED FIELDS
            ry = Wref * SG.S11 * csrc;
            R  = abs(ry).^2;
            kzInc = cos(theta)*sqrt(grid.erR * grid.urR);
            R = real(-KzR / kzInc) * R;
            REF.minus_1(i,j) = R(floor(length(R)/2));
            REF.plus_1(i,j) = R(floor(length(R)/2)+2);
            REF.REF0(i,j) = R(floor(length(R)/2)+1);
            REF.sum(i,j) = norm(sum(sum(R))); % all reflection orders
            %% TRANSMITTED FIELDS
            ty = Wtrn * SG.S21 * csrc;
            T  = abs(ty).^2;
            theta_i = asin((1/grid.erSub).^2 * sin(theta));
            if mode == 'E'
                T = real((grid.urR / grid.urT) * KzT/kzInc) * T;
            elseif mode == 'H'
                T = real(KzT * sqrt(grid.erR) ...
                /(grid.erT * cos(theta))) * T;
            end
            TRN.minus_1(i,j) = T(floor(length(T)/2));
            TRN.plus_1(i,j)  = T(floor(length(T)/2)+2);
            TRN.TRN0(i,j)    = T(floor(length(T)/2)+1);
            TRN.sum(i,j)     = norm(sum(sum(T))); % all DEs
        end
    end
end
```

S matrix functions

```
%% ----------------------------------------------------------------------
function [SG, W0, V0] = calcFreeSpace(Kx,N)
%% Free space propagation
Kz = conj(sqrt(complex(eye(N) - Kx.^2)));
Omega2 = Kx.^2 - eye(N);
W0  =  eye(N);
LAM =  1i*Kz;
V0 =  Omega2/LAM;
SG.S11 = complex(zeros(N,N));
SG.S12 = complex(eye(N));
SG.S21 = complex(eye(N));
SG.S22 = complex(zeros(N));
end
%% ----------------------------------------------------------------------
function [Wref, Sref] = calcReflectionSide(Kx,KzR,N,W0,V0,grid,mode)
%% Reflected modes from the surface of the device
Wref = eye(N);
Vref = complex(zeros(N));
if mode == 'E'
    Q    = (Kx.^2) - eye(N) * grid.erR * grid.urR;
    lam  = -1i*KzR;
    Vref =  grid.urR \ Q / lam;
elseif mode == 'H'
    Q    = (Kx.^2) - eye(N) * grid.urR * grid.erR ;
    lam  = -1i*KzR;
    Vref =  grid.erR \ Q / lam;
end
A = W0\Wref + V0\Vref;
B = W0\Wref - V0\Vref;
Sref.S11 = -A\B;
Sref.S12 = 2*inv(A);
Sref.S21 = 0.5*(A - B/A*B);
Sref.S22 = B/A;
end
%% ----------------------------------------------------------------------
function [Wtrn, Strn] = calcTransmissionSide(Kx,KzT,N,W0,V0,...
grid,mode)
%% Transmitted modes throught the device
Wtrn = eye(N);
Vtrn = complex(zeros(N));
if mode == 'E'
    Q    = (Kx.^2)/grid.urT - eye(N) * grid.erT;
    lam  = 1i*KzT;
    Vtrn = Q/lam;
elseif mode == 'H'
%     Q = (Kx.^2)/grid.erT - eye(N) * grid.urT;
    lam  = 1i*KzT;
    Vtrn = (grid.erT\Wtrn*lam); % according to Moharam et al, 1995.
```

```
end
A = W0\Wtrn + V0\Vtrn;
B = W0\Wtrn - V0\Vtrn;
Strn.S11 = B/A;
Strn.S12 = 0.5*(A - B/A*B);
Strn.S21 = 2*inv(A);
Strn.S22 = -A\B;
end
```

Additional interface functions in Device function

```
% --------------------------------------------------------------------
function trap = trapezium(x, grid, interface_stuff)
%% Parameters
    Lx    = grid.Lx; % period
    h     = grid.h; % modulation depth
    w_top = interface_stuff.trapz_w_top; % trench w_top
    wx1   = (Lx -  w_top)/2;
    w_bot = interface_stuff.trapz_w_bot;
    wx2   = (w_top - w_bot)/2;
%% line params
    alpha = h/ wx2;
    b     = alpha * ( wx1 +  wx2 - Lx/2);
    z     = zeros(1,length(x));
    for i = 1:length(z)
        if  x(i) <= -Lx/2 +  wx1
            z(i) = h;
        elseif x(i) >= -Lx/2 +  wx1
            z(i) = -alpha * x(i) + b;
        end
        if x(i) > -Lx/2 +  wx1 +  wx2
                z(i) = 1e-6;
        end
        if x(i) > -Lx/2 +  wx1 +  wx2 +  w_bot
            z(i) = alpha * x(i) + b;
        end
        if x(i) > -Lx/2 +  wx1 + 2* wx2 +  w_bot
            z(i) = h;
        end
    end
    trap = z;
end
% --------------------------------------------------------------------

function z = Triangle(x, grid, interface_stuff)
    h  = grid.h;
    w1 = interface_stuff.triangle_w1 * grid.Lx;
    w2 = interface_stuff.triangle_w2 * grid.Lx;
    w3 = interface_stuff.triangle_w3 * grid.Lx;
```

```
    gamma = min(x) + w1; delta = min(x) + w1 + w2;
    sigma = delta + w3;
    a1 = h/(delta - gamma); b1 = -gamma*a1;
    a2 = h/(sigma - delta); b2 = sigma * a2;
    for i = 1:length(x)
        if min(x) <= x(i) <= min(x) + w1
            y(i) = 0;
        end
        if and(min(x) + w1 <= x(i), x(i) <= min(x) + w1 + w2 )
            y(i) = a1 * x(i) + b1;
        end
        if min(x) + w1 + w2 <= x(i)
           y(i) = -a2 * x(i) + b2;
        end
        if x(i) >= min(x) + w1 + w2 + w3
            y(i) = 0;
        end
    end
    % plot(y)
    z = y;
end

% ------------------------------------------------------------------

function [out] = Trapezium_Softened(x, grid,interface_stuff)
    sigma     = interface_stuff.supergauss_sigma;
    n         = 2*interface_stuff.supergauss_m;
    Amplitude = grid.h;
    out       = Amplitude * exp(-0.5 * ((x./(sigma)).^n)) ;
end
```

A2 S matrix method for transmission and reflection regions

Separate S matrix components are calculated for transmission and reflection regions, then saved into memory. The transmittance matrix method's pseudoalgorithm is shown in Alg. 9.

Algorithm 9 RCWA S matrix algorithm for S matrix computation of transmission region.

Require: W_g, $\mathrm{W_T}$, V_g, $\mathrm{V_T}$

$\mathrm{A_T} = \mathrm{W}_g^{-1}\mathrm{W_T} + \mathrm{V}_g^{-1}\mathrm{V_T}$

$\mathrm{B_T} = \mathrm{W}_g^{-1}\mathrm{W_T} - \mathrm{V}_g^{-1}\mathrm{V_T}$

$\mathrm{S}_{11}^{(\mathrm{trn})} = \mathrm{B_T}\mathrm{A}_\mathrm{T}^{-1}$

$\mathrm{S}_{12}^{(\mathrm{trn})} = 0.5\left(\mathrm{A_T} - \mathrm{B_T}\mathrm{A}_\mathrm{T}^{-1}\mathrm{B_T}\right)$

$\mathrm{S}_{21}^{(\mathrm{trn})} = 2\mathrm{A}_\mathrm{T}^{-1}$

$\mathrm{S}_{22}^{(\mathrm{trn})} = -\mathrm{A_T}\mathrm{B_T}$

$S_T = \begin{bmatrix} S_{11}^{(\mathrm{trn})} & S_{12}^{(\mathrm{trn})} \\ S_{21}^{(\mathrm{trn})} & S_{22}^{(\mathrm{trn})} \end{bmatrix}$ ▷ Save to transmission S_T matrix

The S matrix method for reflection region is visualized in Alg. 10. It is noted that the intermediate layer is a vacuum gap material for both transmission and reflection regions, with zeroth thickness. Left hand side and right hand side regions are considered as infinite in the formalism.

Algorithm 10 RCWA S matrix algorithm for S matrix computation of reflection region.

Require: W_g, $\mathrm{W_R}$, V_g, $\mathrm{V_R}$

$\mathrm{A_R} = \mathrm{W}_g^{-1}\mathrm{W_R} + \mathrm{V}_g^{-1}\mathrm{V_R}$

$\mathrm{B_R} = \mathrm{W}_g^{-1}\mathrm{W_R} - \mathrm{V}_g^{-1}\mathrm{V_R}$

$\mathrm{S}_{11}^{(\mathrm{ref})} = -\mathrm{A}_\mathrm{R}^{-1}\mathrm{B_R}$

$\mathrm{S}_{12}^{(\mathrm{ref})} = 2\mathrm{A}_\mathrm{R}^{-1}$

$\mathrm{S}_{21}^{(\mathrm{ref})} = 0.5\left(\mathrm{A_R} - \mathrm{B_R}\mathrm{A}_\mathrm{R}^{-1}\mathrm{B_R}\right)$

$\mathrm{S}_{22}^{(\mathrm{ref})} = \mathrm{B_R}\mathrm{A}_\mathrm{R}^{-1}$

$S_R = \begin{bmatrix} S_{11}^{(\mathrm{ref})} & S_{12}^{(\mathrm{ref})} \\ S_{21}^{(\mathrm{ref})} & S_{22}^{(\mathrm{ref})} \end{bmatrix}$ ▷ Save to reflection S_R matrix

To conclude, both S_T and S_R are computed, saved into memory, and are included in the global scattering matrix via use of Redheffer product.

A3 Dispersion parameters

The measured refractive index distributions have been fitted by the Sellmeier formula, and the coefficients are shown in the table below

Table 6.4: Fitted parameters to Sellmeier formula of measured refractive index dispersion.

Material	A_1	A_2	A_3	λ_{r1}	λ_{r2}	λ_{r3}
HfO_2	1.047	0.10062	1.7627	0.025858	7.9443e-06	0.014883
Nb_2O_5	0.76701	3.1242	0.0022551	0.089628	0.021107	29.1694
SiO_2	1.1716	0.0062783	0.10664	0.010968	41.5007	42.4266
Ta_2O_5	2.1818	1.0909	7.0513e-06	8.7187e-05	0.066202	10.9028
TiO_2	1.094	2.8404e-05	3.1709	0.1094	22.3133	0.0076468

The formula that was used is provided (6.1)

$$n = \sqrt{1 + \sum_{i=1}^{3} \frac{A_i \lambda_0}{\lambda_0^2 - \lambda_{ri}^2}} \tag{6.1}$$

The amplitude A_i is the resonance strength μm^{-1} and λ_{ri} is the resonance wavelength.

A4 1D eigen-value problem for slab-waveguides

The equation for TE polarization of guided modes in 1D FDFD and the solution with its constituents [49, 85] of the form of

$$\underbrace{-(\mathrm{D}_{x'}^{(h)} \mu_{zz}^{-1} \mathrm{D}_{x'}^{(e)} + \epsilon_{yy})}_{A} \underbrace{e_y}_{x} = \widetilde{\gamma}_m^2 \underbrace{\mu_{xx}^{-1}}_{B} \underbrace{e_y}_{x}, \tag{6.2a}$$

$$E_y^{(m)}(x', z') = e_y^{(m)}(x') \cdot e^{-\gamma_m z'/k_0}, \tag{6.2b}$$

$$\gamma_m = k_0 \sqrt{\widetilde{\gamma}_m^2}, \tag{6.2c}$$

$$n_{\text{eff}}^{(m)} = \frac{\gamma_m}{j k_0}. \tag{6.2d}$$

Here the main Eq is of the form of generalized eigen-value problem $Ax = \lambda Bx$, where λ is an eigen-value, which is $\widetilde{\gamma}^2$. The e_y is the eigen-vector (m-th order mode), which is the electric field's amplitude. The material parameters are expressed in relative permittivity ϵ_{xx} and permeability μ_{xx}, μ_{zz} tensors. Relative permeability tensors in transparent dielectrics $\mu_r \approx 1$, which brings the master equation as an ordinary eigen-value problem. The derivative FD matrices are $\mathrm{D}_{x'}^{(h)}$ and $\mathrm{D}_{x'}^{(e)}$, which are used for magnetic and electric fields in Yee grid, respectively. The transformed coordinates $x', z' \to k_0 x, k_0 z$, where $k_0 = \frac{2\pi}{\lambda_0}$ is the wavevector magnitude and λ_0 is wavelength of the mode in

vacuum, not to be confused with eigenvalue λ. According to Eq. (6.2b), the solution is of the form of the amplitude and its phase accumulation, which is desirable for such models, hence the master Eq. (6.2a), which can be used to solve for any linear 1D slab waveguide of interest.

Santrauka lietuvių kalba

Įvadas

Periodiškai moduliuotos terpės yra dažnai gamtoje aptinkamos struktūros, pasižyminčios erdvinėmis ir spektrinėmis charakteristikomis, kurios priklauso nuo šių struktūrų geometrijos, lūžio rodiklių kontrasto ir nuo stebėjimo kampo. Tokios terpės vadinamos fotoniniais kristalais, kurie pasižymi plačios juostos atspindžiu, kuri kieto kūno fizikoje vadinama draustiniu fotoninės juostos tarpu. Fotoninius kristalus gamtoje galima aptikti drugelio sparnuose ar paukščių, tokių kaip paprastųjų šarkų, sparnuose [1–5]. Kiti fotoniniai kristalai yra randami opaluose ir t.t., kurių išskirtinis bruožas - ryškus mėlynos šviesos atspindys -atsiranda kristalų simetrijos ir periodiškumo dėka. Vienas įdomiausių reiškinių - nuo posūkio kampo priklausantis šviesos atspindys, kuriam taip pat įtakos turi fotoninių kristalų geometrija. Šie elementai gaminami tiek industrijoje, tiek mokslinėse bendruomenėse naudojantis litografijos metodais arba nusodinimo technologijomis [7]. Pavyzdžiui, paprasčiausias fotoninis kristalas yra 1D Brego gardelė, kuri pasižymi periodiniu skaidrių sluoksnių išdėstymu pagal lazerinės spinduliuotės sklidimo kryptį. Lazerio spinduliuotė ties tam tikru kritimo kampu yra atspindėta, jeigu jo dažnio spektras atitinka fotoninio elemento draustinį juostos plotį. Kiti elementai yra sudėtingesnės formos, tokios kaip 2D korėtos gardelės arba litografijos metodu gaminamos 3D gardelės, kurių draustinis plotis užtikrina šviesolaidinį efektą fotoninių kristalų defektuose. Tokie elementai naudojami naujos kartos šviesolaidinėse grandinėse [8, 9, 22, 23].

Šių struktūrų esminė savybė yra geometrijos mastelio invariantiškumas, kurio esmė - visi kristalų erdvinės dispersijos efektai yra nekintantys, išlaikant vienodą santykį tarp krentančios šviesos dažnio ir fotoninio elemento geometrijos, atsižvelgiant į tai, kad medžiaga yra nesugerianti ir pasižymi labai menka lūžio rodiklio dispersija. Todėl fotoninių kristalų taikymai yra lankstūs ir pasižymi plačia įvairove. Be draustinės fotoninės juostos plotį, kiti taikymai naudojami arti draustinės fotoninės juostos krašto, kurio erdvinę dispersiją galima pritaikyti šviesos sklidimo valdymui. Populiariausi pavyzdžiai yra fotoninių kristalų kolimatoriai [18–20], lazerio pluoštų transformatoriai, metalęšiai ir šviesos nematomumo optiniai elementai [10–13].

Šiems taikymams reikalingas didelis gardelių skaičius, todėl elementų matmenys, palyginus su šviesos bangos ilgiu, išlieka gan dideli, daugiau nei 10 bangos ilgių, priklausomai nuo lūžio rodiklio kontrasto. Erdvinės ir spektrinės šviesos charakteristikų valdymui galima pasitelkti šviesolaidinius arba bangolaidinius rezonatorius, kurie pasižymi periodine lūžio rodiklio moduliacija tik viena, skersine, kryptimi, o lazerinės spinduliuotės sklidimo kryptimi yra plonas okdsido sluoksnis, kurio matmenys mažesni už spinduliuotės bangos ilgį. Šie įtaisai gali imituoti fotoninių kristalų fiziką ir pasižymi aukštos kokybės rezonansais, kurie, indukuojami krentančios lazerinės spinduliuotės, ir yra švieso-

laidinės modos, kadangi moduliuotas sluoksnis pasižymi didesniu lūžio rodikliu nei jos aplinka. Tokie prietaisai naudojami lazerinės spinduliuotės erdviniams ir spektriniams filtravimams [14–17, 42, 86], kampinės dispersijos valdymui ir kaip poliarizuojantys filtrai. Jų gamyba įgyvendinama joninių pluoštų purškimo metodu (angl. Ion Beam Sputtering, trumpinys - IBS), kai ant difrakcinės sub - bangos gardelės nusodinamas aukšto lūžio rodiklio oksido sluoksnis, kurių paviršiaus geometrija turi atitikti padėklo moduliaciją.

Visi minėti elementai yra gaminami pagal dizainus, kurie yra gaunami sprendžiant Maksvelio lygtis skaitmeniškai [49]. Lygtys yra sprendžiamos kompiuteryje tiesiogiai, t.y., pritaikius baigtinio skirtumo metodą su laikiniu žingsniavimu (angl. Finite Difference Time Domain, FDTD) [50], siekiant apskaičiuoti lazerio pluoštų ir impulsų sąveiką su fotoninių įtaisų geometrija. Toks algoritmas yra pilnai iteracinis ir yra populiariausias bei plačiai naudojamas. Tačiau laikinis žingsniavimas algoritme reikalauja daug iteracijų modeliuojant nesugeriančias terpes ir aukštos kokybės rezonatorius. Lygiaverčiai Maksvelio lygčių sprendiniai yra randami greičiau pritaikius baigtinio skirtumo metodą dažninėje erdvėje (angl. Finite Difference Frequency Domain, FDFD) [51, 89, 91], o tai atitinka nuolatinės veikos lazerio pluošto sąveiką su šviesolaidiniais filtrais. Siekiant apskaičiuoti gardelių, kristalų ar periodiškai moduliuotų fotoninių įtaisų difrakcinius efektyvumus, Maksvelio lygtis galima išspręsti dar greičiau pritaikius Furjė [52] ir sklaidos matricos metodus periodiškai moduliuotoms terpėms. Šią procedūrą atlieka RCWA algoritmas (Rigorous Coupled Wave Analysis) [53]. Skaičiavimo greitis yra išlošiamas transformavus lygtis plokščių bangų bazėje ir laukai yra skaičiuojami Furjė erdvėje, tad algoritmas yra analitiškai sudėtingesnis nei baigtinio skirtumo metodas, kadangi lygtys reikalauja papildomo matematinio, analitinio apdorojimo. Taip pat yra ir Chandezon metodas, kuris pritaiko tą patį principą, tačiau per koordinačių transformaciją, kas apsunkina tiek analitinį formalizmą, tiek jo implementaciją į programinę terpę. Pagrindiniai gardelių parametrai, kuriuos visi 4 algoritmai gali apskaičiuoti, yra difrakciniai efektyvumai, tačiau RCWA metodas lieka geriausiu dėl jo implementacijos lengvumo, palyginus su C metodu [54]. Tuo tarpu FDFD algoritmas efektyviausias apskaičiuojant elektromagnetinių laukų skirstinius ties aukštos kokybės rezonansais. Todėl šiame darbe modeliuojant šviesolaidinius filtrus, jų difrakcijos efektyvumus ir laukų skirstinius yra pasitelkti RCWA ir FDFD algoritmai.

Skaitinio modeliavimo rezultatai yra toliau lyginami su analitiniais modeliais, kuriais siekiama apibūdinti šviesolaidinių modų rezonansus ir jų spektrines charakteristikas, kai fotoniniai įtaisai pasižymi optine sugertimi ar stiprinimu. Šių rezonansų formos yra unikalios, t.y., ne Lorentz'o formos ir pasižyminčios asimetrija, kurią galima apibūdinti ir analitiškai. Toliau, šie elementai yra gaminami IBS metodu [115] ir jų difrakciniai efektyvumai (nulinės eilės pralaidumo ir atspindžio koeficientai) yra išmatuojami ir palyginami su skaitinio modeliavimo rezultatais.

Disertacijos išdėstymas

Ši disertacija susideda iš literatūros apžvalgos skyrių ir tyrimų rezultatų. Literatūros apžvalgoje aptariama 1D šviesolaidžių veikimo principai, difrakcinių gardelių ir Reilėjaus efekto niuansai. Vėlesniuose skyriuose aptariama šviesolaidinių rezonansų fizikinė prasmė remiantis ankstesnėmis dviejomis teorijomis. Taip pat pateikiami skyreliai, šiems rezonansams apibūdinti, tokie kaip susietų modų laikinis modelis (angl. Temporal Coupled Mode Theory) bei difrakcinių eilių skaičiavimas s ir p poliarizacijoms. Galiausiai, aptariami plonasluoksnių filtrų geometrijos ypatumai pasitelkus jonino pluošto nusodinimo metodą.

Literatūros apžvalgos antroje dalyje, nuo 1.2 skyriaus, išdėstyti skaitiniai algoritmai, naudojami Maksvelio lygtims su monochromatiniais šviesos šaltiniais spręsti programinėje terpėje. Šioje dalyje taip pat aprašoma tyrimo metodika, naudojama skaitiniam fotoninių struktūrų modeliavimui, įskaitant ir tiesinius šviesos su medžiagos sąveikos tyrimus. Pirmasis aptariamas algoritmas - baigtinio skirtumo metodas (angl. Finite Difference Frequency Domain). Antrasis yra susietų bangų algoritmas (Rigorous Coupled Wave Analysis), skirtas spręsti sklaidos uždavinius fotoninėms struktūroms, pasižyminčioms periodinėmis kraštinėmis sąlygomis. Aptariami sklaidos ir pralaidumo matricos metodai ir optimizavimo uždavinys pasitelkus genetinį algoritmą.

Vėlesniuose skyriuose aprašomi tyrimai, atlikti naudojantis minėtais algoritmais. Antrame skyriuje aptariamas trapecinių gardelių pritaikymas plačiajuosčiams veidrodžiams ir erdviniam kampiniam filtravimui per Reilėjaus anomaliją. Šių filtrų gamybos IBS metodu ypatumai aptariami skyrelio pabaigoje.

Trečias skyrius susitelkia ties šviesolaidinių rezonatorių tyrimu arti potencinės duobės krašto. Šiame skyrelyje aptariami analitinio potencinės duobės metodo ypatumai. Jo analitinių sprendinių rezultatų ypatumai yra palyginami kartu su RCWA metodu apskaičiuotais difrakciniais efektyvumais. Vėliau šių šviesolaidinių filtrų gamyba realizuojama IBS metodu. Galiausiai, pagamintos struktūros, RCWA metodu modeliuotos ir išmatuotos spektrinės charakteristikos, yra palyginamos.

Ketvirtas skyrius nagrinėja PT asimetrines struktūras, daugiausia šviesolaidinius filtrus su nesimetriškai išdėstytu metaliniu sugėrikliu. Palyginamas analitinis modelis su RCWA algoritmu ir vėliau - pagamintos struktūros bei RCWA algoritmu modeliuotos ir išmatuotos spektrinės charakteristikos.

Penktame skyriuje nagrinėjamos optiškai aktyvios šviesolaidinės terpės, kurios pasižymi Lorenco pavidalo lūžio rodiklio dispersija. Šiame skyriuje panaudotas genetinis algoritmas RCWA modelyje, siekiant padidinti gardelės nulinės eilės difrakcinių efektyvumų stiprinimą pasitelkus aukštos kokybės rezonansus. Paskutinėje tyrimo dalyje palyginamas analitinis metodas ir skaitiniai rezultatai.

Šeštas skyrius yra RCWA ir FDFD modeliais paremtos atviros prieigos vartotojo sąsajos "Zenscat" palyginimas su Lumerical komercinių programų versijomis. Iš esmės - publikuotų straipsnių rezultatų atkartojamumas bei

skaičiavimų spartos palyginimas su komerciniu Furjė modaliniu metodu, įterptu komercinėje "MCgrating" programoje. Vėliau išbandomas šviesolaidinių, grįžtamojo ryšio sistemų geometrijos optimizavimas sugeriančioms ir aktyvioms optinėms terpėms bei atliekamas kiekybinis šių struktūrų raiškos tyrimas RCWA modelio konvergavimui.

Darbo tikslas

Šios disertacijos tikslas yra ištirti šviesolaidinių rezonansų fizikines savybes tiesinėse terpėse, jų pasyvių ir aktyvių rezonatorių veiką gardeliniuose rezonatoriuose pasitelkus skaitinius metodus.

Pagrindinės užduotys

Iškeltas tikslas yra sprendžiamas atliekant šiuos uždavinius:

1. Įvertinti vieno sluoksnio gardelinio rezonatoraus topologijos poveikį šviesolaidinių rezonansų spektrinėms charakteristikoms. Išvesti analitinius modelius, kuriais galima paaiškinti šių rezonansų fizikinį veikimą. Palyginti skaitinio modeliavimo skaičiuotus difrakcinius efektyvumus su analitiniu modeliu. Taipogi, pateikti filtrų dizainus gamybai bei palyginti išmatuotas spektrines charakteristikas su skaitmeniškai apskaičiuotais duomenimis.

2. Išanalizuoti šviesolaidinių rezonansų spektrines charakteristikas, kuomet rezonatoriai pasižymi nesimetriškai išdėstyta, šviesą sugeriančia terpe. Palyginti tokio rezonatoriaus difrakcinius efektyvumus su išmatuotais duomenimis bei įtaiso topologinės asimetrijos įtaką šviesos sugerties nuostoliams.

3. Išnagrinėti šviesolaidinių rezonatorių difrakcinių efektyvumų spektrines charakteristikas, kuomet šviesolaidžio sluoksnis yra aktyvi optinė terpė. Naudojantis genetinio optimizavimo algoritmu, rasti įtaiso geometrinius parametrus, kurie tenkina didžiausią difrakcinių efektyvumų stiprinimą ir identifikuoti šviesolaidinių modų rezonatoriaus veikimo režimus.

4. Implementuoti skaitinius 2D RCWA ir 2D FDFD algoritmus programinėje MATLAB terpėje ir sukompiliuoti vartotojo sąsają. Palyginti sąsajos skaičiavimų rezultatų patikimumą su publikacijose pateiktais duomenimis bei gauti greitesnę skaičiavimo spartą už komercinių programų modalinius variantus.

Mokslinis naujumas

Šis darbas suteikė daugiau žinių kieto kūno elektrodinamikos, kompiuterinės fizikos, fotonikos srityse ir fotoninių struktūrų gamybos, klonavimo technologi-

joje:

1. Šviesolaidiniai rezonansai, kurie pasireiškia prie Reilėjaus anomalijos, leidžia suderintos geometrijos plonasluoksniams filtrams pasižymėti plačiajuosčiu atpsindžio spektru ir siaurajuosčiu kampiniu atsaku.

2. Šviesolaidiniams rezonansams gardeliniuose filtruose paaiškinti pasiremta potencinės 1D duobės modeliu, kuris išskiria du rezonansų režimus: surištų fotoninių būsenų egzistavimą giliai duobėje ir fotoninių būsenų atsiradimą arti duobės krašto. Su šiuo analitiniu modeliu galima išsiaiškinti, kaip priklauso fotoninių būsenų atspindžio charakteristikos nuo mastelio parametrų - sieties koeficiento ir energijos skirtumo.

3. Pasiūlytas neermitinės plonasluoksnių filtrų struktūros dizainas, kuris pasižymi vienkrypte sietimi tarp kritusios šviesos šaltinio, vienkryptės šviesolaidinės modos ir difrakcijos, kuri slopinama nesimetrinės sugeriančios terpės dėka.

4. Periodiškai moduliuotos plonasluoksnės aktyvios terpės, esančios ant pasyvaus padėklo, pasižymi šviesolaidiniais rezonansais, gebančiais stiprinti nulinės eilės difrakcinius efektyvumus. Taipogi, papildytas surištų modų analitinis grandinės modelis, detalizuojantis šių rezonansų veikimą per asimetrinę sietį tarp pasyvios ir stiprinančios terpių.

5. Atviros prieigos vartotojo sąsaja "ZenScat" yra sukurta MATLAB terpėje, kuri skaitmeniškai modeliuoja šviesos ir medžiagos tiesines bangines sąveikas periodiškai išdėsytoms terpėms. Pademonstruota, kad programa puikiai konverguoja modeliuojant tiek skaidrias, tiek sugeriančias terpes, išlaikant vienodus sprendinius tarp sklaidos ir pralaidumo matricų metodų. Programa "ZenScat" validuota pagal Lumerical skaičiavimus, kurie pristatyti mokslinėje literatūroje.

Praktinė darbo vertė

Rengiant šią disertaciją, sukurta atviros prieigos vartojo sąsaja "ZenScat", kurioje implementuoti 2D RCWA ir 2D FDFD algoritmai. Pasitelkus šia programą, buvo skaitiškai modeliuojamos šviesolaidinės struktūros, tokios kaip grįžtamojo ryšiai įtaisai, plačiajuosčiai filtrai, šviesos sugertį bei fluorescenciją stiprinančios terpės, kurios pasižymi trapecine, supergausine ir sinusoidine gardelių geometrija:

1. Pasiūlytas trapecinių šviesolaidinių gardelių dizainas užtikrina pastovų plačiajuostį selektyvumą iki 99% per 46 nm spektrinį plotį s poliarizacijai bei erdvinio filtravimo režimą, apribotą Reilėjaus zona. Analogiškas veikimas realizuotas ir supergausinės formos dvigubos moduliacijos šviesolaidinėmis gardelėmis.

2. Pirmą kartą Šriodingerio pavidalo potencinės duobės analitinis modelis yra pasiūlytas šviesolaidinių filtrų sistemoms. Šiuo formalizmu galima nagrinėti šviesolaidinių rezonansų charakteristikas priklausomai nuo potencinės duobės parametrų, kurie yra susieti su šviesolaidžio geometrija. Ties potencinės duobės kraštu įmanoma indukuoti siaurus šviesolaidinius rezonansus, kuriuos galima panaudoti kaip naujus šviesos monochromatorių ir poliarizatorių elementus.

3. Vienkryptis modų sklidimas šviesolaidiniuose filtruose, kuris įgyvendinamas asimetriškai ant filtro uždėjus optinį sugėriklį, užtikrina didesnę sugertį nei simetrinės periodinės terpės. Šiuos įtaisus galima pritaikyti Saulės elementuose.

4. Šviesolaidiniai rezonansai aktyviose periodiškai moduliuotose terpėse, jei rezonanso kokybė aukšta, padidinus šviesos-medžiagos sąveiką, sustiprina florescenciją arba padidina stiprinimo koeficientą nulinės eilės difrakciniams efektyvumams, priklausomai nuo šviesos spinduliuotės kritimo kampo. Taigi, šie įtaisai gali būti panaudojami kaip funkciniai filtravimo/stiprinimo elementai mikrolazerių sistemose, arba šviesos kryptingos fluorescencijos tyrimuose.

5. Atviros prieigos vartotojo sąsaja "ZenScat" dvigubai sparčiau skaičiuoja difrakcinių gardelių, šviesolaidinių filtrų, fotoninių kristalų difrakcinius efektyvumus palyginus su komercine MCgrating programa. Tuo tarpu vartotojo sąsaja yra suderinta su genetiniu algoritmu, kuris panaudojamas daugiasluoksnių fotoninių struktūrų topologijos optimizavimui. Tai galima panaudoti tiek akademiniams, tiek industriniams uždaviniams spręsti. Pavyzdžiui, plačiajuosčių veidrodžių, spektrinių filtrų, erdvinių filtrų, poliarizatorių ir difrakcinių elementų taikymams.

Ginamieji teiginiai

1. Vienasluoksnis šviesolaidinis filtras gali būti parinktas veikti arti Reilėjaus anomalijos - tokiu būdu padidinant plačiajuostį atspindį, o kampinį atsaką - siaurame diapazone.

2. Potencinės duobės kontinuumo kraštas yra sritis, kuomet fotoninės būsenos nebeegzistuoja šviesolaidiniame rezonatoriuje ir yra randamos prie Reilėjaus anomalijos. Ties šia sritimi, šviesolaidinio rezonanso spektrinė forma įgija aštrią asimetrinę smailę su siaurėjančiu pločiu ties puse maksimumo.

3. Neermitinė PT asimetrinė sistema yra realizuojama, kai metalinė ar sugerianti medžiaga yra asimetriškai išdėstyta ant periodinio šviesolaidinio filtro taip, kad C_2 simetrija panaikinama. Toks elementarus narvelis gali padidinti šviesos sugertį.

4. Šviesą stiprinančios plonasluoksnės struktūros keičia šviesolaidinio rezonanso dažnį ir abu reiškiniai padidina šviesos stiprinimą statmenai ir kampu krentančiai šviesos s ir p poliarizuotai spinduliuotei.

5. Periodiškai moduliuotų terpių skaitinis modeliavimas ir jų analizė, pasitelkus dažninės erdvės skaitinius metodus, kompiliuotuos C++ kalba, yra greitesnis ir išlaiko konvergavimą tiek pasyviems, tiek aktyviems 2D fotoniniams elementams, palyginus su komercinėmis programomis.

Skaitmeniniai algoritmai, panaudoti tyrimo metodikoje

Šiame darbe naudojamas 2D RCWA algoritmas, kuris yra suderintas su genetiniu algoritmu siekiant skaitmeniškai modeliuoti šviesolaidinių filtrų difrakcinius efektyvumus ir spręsti filtrų geometrijos optimizavimo uždavinius. Tuo tarpu 2D FDFD algoritmas yra naudojamas šviesolaidinių rezonansų laukų skirstiniams apskaičiuoti. Difrakcinis efektyvumas yra elektromagnetinės galios dalis, tenkanti difrakcinei eilei tiek pralaidumo srityje, tiek atspindžio srityje. Nulinės eilės difrakciniai efektyvumai yra išmatuojami eksperimentiškai, todėl tik tos dalys iš skaitmeninių skaičiavimų yra pateikiamos šiame darbe.

Furjė modalinis metodas (angl. FMM) yra RCWA atitikmuo ir šio algoritmo fizikinė esmė yra periodiškai pasiskirsčiusių dielektrinės ir magnetinės skvarbų funkcijų skleidimas Furjė eilutėmis. Kadangi elektrinis ir magnetinis laukai atkartoja gardelės periodiškumą ir pasižymi poslinkio simetrija - tai atitinka Blocho teoremą. Todėl RCWA algoritmas veikia pagal kieto kūno fizikos principus. Šio algoritmo koncepcija yra pavaizduota 3 pseudoalgoritme, kur skaičiuojamos elektrinio ir magnetinio laukų Furjė komponenčių amplitudės, taip vadinamos Blocho modomis kiekvienai erdvinei harmonikai. Erdvinė harmonika šiuo atveju yra skleidimo į Furjė eilutę eilė, t.y., sveikas skaičius, padaugintas iš atvirkštinio gardelės periodo $\frac{2\pi}{\Lambda_x}$. Tai traktuojama kaip periodinių kraštinių sąlygų pasekmė. Sėkmingai radus Blocho modų skirstinius elektriniui ir magnetiniam laukams bei Blocho modų sklidimų koeficientų narius vienam diskrečiam sluoksniui, jie įtraukiami į pralaidumo (angl. transmittance) arba sklaidos (angl. scattering) matricų formalizmus, kurie naudojami norint sujungti diskrečius sluoksnius, ir tokiu būdu apskaičiuoti difrakcinius efektyvumus fotoninio elemento padėkle (angl. substrate) ir viršaus (angl. superstrate). Šios terpės traktuojamos kaip begalinės RCWA ir FDFD modeliuose.

Baigtinio skirtumo dažninėje erdvėje (FDFD) metodika yra matricinė, kaip RCWA, tačiau matricos (arba masyvai) yra *išretintos* (angl., sparse matrices), o palyginus RCWA metode masyvai yra pilni. Dauguma elementų iš išretintų masyvų turi "0" vietoje baigtinių reikšmių, todėl masyvuose yra išsaugojamos tik baigtinių reikšmių vertės ir jų indeksai. Baigtinio skirtumo metodo algoritmas yra pavaizduotas 1 pseudoalgoritme. Visi nariai kairėje pusėje yra 2D masyvai, kuomet dešinėje - 1D masyvas. Dielektrinių ir magnetinių skvarbų masyvai yra suformuojami diagonalinės išretintos matricos pavidalu, tuo tarpu

dalinių išvestinių masyvai turi nediagonalinius elementus, kurie daro įtaką diferencialinio masyvo $\hat{\mathrm{A}}$ simetrijai. Pagrindinė lygtis, kuri sprendžiama, yra $f = \hat{\mathrm{A}}^{-1}b$ pavidalo, kur b yra lauko šaltinis, o $\hat{\mathrm{A}}$ yra gradiento operatoriaus masyvas, kurio dalinių išvestinių elementai normuoti į dielektrinės ir magnetinės skvarbų tenzorius. Periodinės kraštinės sąlygos sudarytos skersine kryptimi ir tobulas elektromagnetinių bangų sugėriklis yra įterptas pagal lazerio pluošto sklidimo kryptį padėkle ir prietaiso viršuje, difrakciniai efektyvumai atspindžiui fiksuojami sklaidyto lauko zonoje, o pralaidumo srityje - pilno signalo, t.y., sklaidyto ir krentančio laukų superpozicijoje.

Šviesolaidinių modų rezonanso ypatumai

Šviesolaidinių modų rezonansų veikimas susideda iš dviejų fizikinių reiškinių - šviesolaidyje sklindančių modų mechanizmo ir iš šviesos sklaidos nuo periodiškai moduliuotų paviršių (difrakcinių gardelių).

Šviesolaidžių veikimas paremtas visiškojo vidaus atspindžio principu, kuomet šviesolaidžio šerdyje sklindanti šviesa pagal šviesolaidžio geometriją ir visiško vidaus atspindžio sąlygas sudaro diskrečias sklindančių modų būsenas, kurias kiekybiškai apibūdina jų laukų skirstiniai ir efektinis lūžio rodiklis. Efektinis lūžio rodiklis yra šviesos greičio santykis su šviesolaidinės modos faziniu greičiu. Žemiausios eilės moda yra labiausiai koncentruota ties šviesolaidžio šerdimi, todėl jos efektinis lūžio rodiklis yra artimiausias šerdies lūžio rodikliui. Pats paprasčiausias šviesolaidis yra vienmatė šerdies plokštė, apribota padėklu ir viršutine terpe. Šerdies geometrija tokiu atveju riboja modų sklidimą tik viena, statmena, kryptimi. Todėl ties ja ir turės 1D amplitudžių skirstinius ir jie apskaičiuojami 1D FDFD metodu.

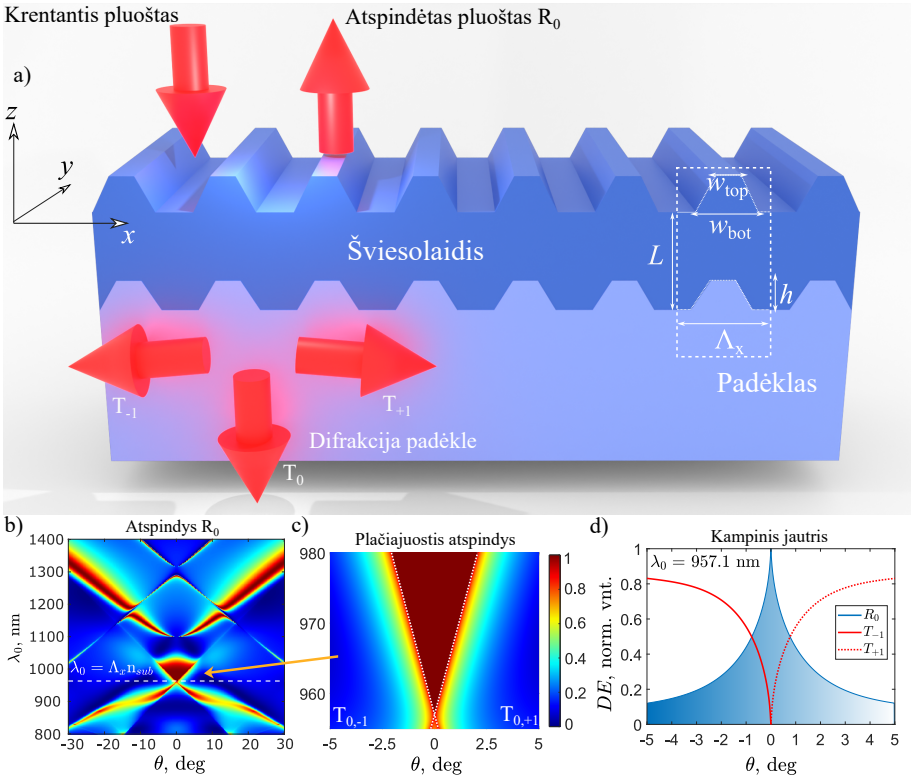
Difrakcinių gardelių veikimo principas subtilus, kadangi užtenka periodinių kraštinių sąlygų, t.y., žinoti struktūros skersinio periodo vertę, difrakcijos eilę, gardelės, padėklo ir viršutinės terpės lūžio rodiklių vertes bei lazerio pluošto kritimo kampą, kad nuspėti, kokiais kampais pasireiškia kritusios bangos difrakcija. Tai paprastai apibūdinama gardelės lygtimi (1.8). Tačiau yra neaišku, kaip apskaičiuoti difrakcinius gardelės efektyvumus šviesolaidžiams, kurie turi bent vieną periodiškai moduliuotą paviršių. Tokiu atveju pasitelkiama RCWA ir FDFD skaitmeniniais metodais, kurie sprendžia Maksvelio lygtis dažninėje erdvėje, ir šie algoritmai pritaikomi tokioms struktūroms.

Svarbu pastebėti, kad pereinant iš vieno difrakcinio režimo į kitą, atspindžio ir pralaidumo koeficientų spektriniai ir kampiniai skirstiniai patiria trūkius ir pasižymi aštriais, netolydžiais bruožais. Tie trūkiai įvardijami kaip Reilėjaus anomalijos, o jų priežastis - papildomų difrakcinių eilių staigūs atsiradimai ir išnykimai, keičiant šviesos dažnį ir bangos kritimo kampą į gardelę. Reilėjaus anomalija nepriklauso nuo krintančios poliarizacijos, o priklauso nuo elektromagnetinės bangos kritimo kampo, gardelės skersinio periodo padėklo ir viršutinės terpės lūžio rodiklių. Nuo krintančios šviesos poliarizacijos priklauso tik fotoninių įtaisų difrakcinio efektyvumo vertės. Jos yra svarbios šio darbo tyrimų šviesolaidinių rezonansų būsenoms apibūdinti.

Šviesolaidiniai rezonansai pasireiškia, kai 1D šviesolaidžio plokštės bent vienas paviršiaus lūžio rodiklis yra periodiškai moduliuotas. To pasekmė yra padidinta sietis tarp krentančios bangos ir difrakcinės eilės per gardele sklindančią šviesolaidinę modą. Kokybiškai efektinio lūžio rodiklio priklausomybę nuo lazerio pluošto kritimo kampo ir bangos ilgio galima aprašyti ir analitiškai (1.9). Tai difrakcijos lygtis, apribota padėklo ir viršutinės terpės lūžio rodikliais. Su šia nelygybe galima nuspėti sritis, kuriose pasireikštų tokie rezonansai, pilnai siejantys kritusią bangą su nulinės eilės atspindėta banga. Rezonansų būsenos ties stačiu lazerio pluošto kritimo kampu yra išsigimusios, t.y., skirtingos būsenos, atitinkančios tuos pačius rezonansų dažnius. Išsigimimas eliminuojamas keičiant lazerio pluošto kritimo kampą. Taip pat šviesolaidinio rezonanso reiškinys pasižymi savo kampiniu ir spektriniu jautriais, pilnu veidrodiškuoju atspindžiu, siaurajuosčiu pralaidumu bei jų asimetrinėmis spektro formomis. Centrinis rezonanso bangos ilgis, spektrinis plotis, atspindžio rezonanso asimetrija ir rezonansų (sklindančių modų) kiekis priklauso nuo šviesolaidžio geometrijos, periodiškumo, krentančios lazerio pluošto poliarizacijos, gardelės lūžio rodiklių kontrasto ir nuo padėklo ir viršutinės terpės lūžio rodiklių verčių. Šie įtaisai pasižymi tiek aukšta, tiek žema rezonansų kokybėmis, spektriniu ir kampiniu jautriais, yra taikomi erdviniams, spektriniams filtravimams bei gali būti naudojami kaip plačiajuosčiai veidrodžiai bei poliarizuojantys filtrai. Pagrindinis privalumas yra tas, kad šiems taikymams užtenka vieno sluoksnio šviesolaidinėms būsenoms sukelti, o difrakciniai efektyvumai ties šiais rezonansais gali pasižymėti plačios arba siauros juostų spektriniais pločiais.

Plačiuojasčio atspindžio riba ties Reilėjaus anomalija - antras skyrius

Šiame darbe nagrinėjamas plačiajuostis atspindys, kurio kampinis jautris yra apribojamas Reilėjaus anomalija. Siekiant pagaminti stačiakampės formos gardeles, gamybos baigtinėje stadijoje neišlaikoma tobula forma ir gardelės amplitudė turi tam tikrą nuolydį ties kraštais, o pati gardelės forma viename periode - trapecinė. Pastebima, jog trapecinės formos šviesolaidinėms gardelėms Reilėjaus anomalija išlaiko plačios juostos atspindį (99 proc.) nuo $\lambda_R = \Lambda_x n_{\text{sub}}$ bangos ilgio statmenai krentančiai bangai. Tokia vieno sluoksnio sistema gali pakeisti mikro-lazeriuose naudojamus daugiasluoksnius Brego veidrodžius. Šis bangos ilgis nusako sub-banginę difrakcijos ribą, kur mažesniems bangos ilgiams - staigiai atsiranda papildoma difrakcijos eilė ties stačiu šviesos kritimo kampu. Kampinis jautris, apribotas Reilėjaus anomalija, pasižymi tokia charakteristika: $\lambda_R = \Lambda_x(n_{\text{sub}} \pm \sin\theta)$, kur θ yra šviesos kritimo kampas, o n_{sub} yra padėklo, lūžio rodiklis. Ties šiais bangos ilgiais atspindžio koeficientas apribojamas visame kampiniame diapozone s poliarizacijai (TE pol.), kuomet šviesolaidis p poliarizaicijai (TM pol.) pasižymi pilnu pralaidumu ir šviesolaidiniais rezonansais. Trapecinės formos filtras yra pavaizduotas 6.8 pav. a), atspindžio nulinės eilės spektras 6.8 pav. b), Reilėjaus anomalijos apribotas plačiaju-



6.8 pav. Trapecijos formos šviesolaidinis filtras (a), filtruojantis kritusią šviesą per difrakciją, o filtruotas pluoštas yra atspindėtas. Šios struktūros atspindžio skirstinys iliustruojamas (b) grafike, kuriame matyti plačiajuostis atspindys (priartintas, c). Jo difrakciniai efektyvumai nurodyti (c) grafike, kur raudonos kreivės atitinka ± 1 difrakcines eiles.

ostis atspindys 6.8 pav. c), o difrakcinių efektyvumų kampinė priklausomybė (jautris) -6.8 pav. d).

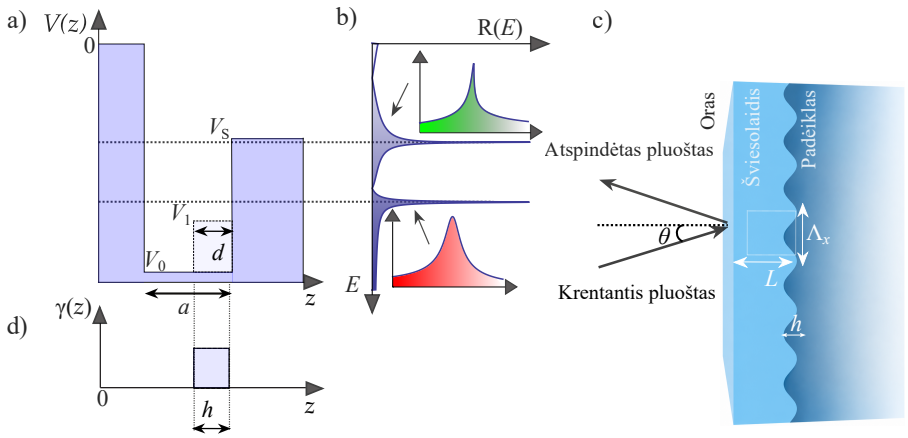
Trapecinis filtras pasižymi tokiais parametrais: viršutinis plotis $w_{\text{bot}} = 375$ nm, apatinis gardelės $w_{\text{top}} = 175$ nm, skersinis periodas $\Lambda_x = 638$ nm, gardelės gylis $h = 238$ nm, padėklo lūžio rodiklis $n_{\text{sub}} = 1.5$ ir Nb_2O_5 sluoksnis $n_{\text{film}} = 2.25$, o šviesolaidžio storis $L = 580$ nm. Filtras pasižymi dviguba periodine moduliacija. Gautas plačiajuostis atspindys yra realizuotas ties 46 nm pločiu, kuomet atspindžio koeficientas yra didesnis už 99%, o tokios vertės pastovus atspindys yra pilnai apribotas reilėjaus bangos ilgio λ_R Skaitinio modeliavimo rezultatai taip pat parodo, jog šis plačiajuostis atspindys pasižymi bent dviejais rezonansų minimumais pralaidumo spektre, todėl šis reiškinys yra realizuojamas šviesolaidinių rezonansų superpozicijos dėka. Taigi užtenka bent dviejų persiklojančių šviesolaidinių rezonansų arti Reilėjaus anomalijos, kad

būtų pasiektas plačiajuostis atspindys.

Filtro gamyba yra įgyvendinama naudojantis joninio pluošto dulkinimo (angl. Ion Beam Sputtering) metodu. Viršutinis nusodintas sluoksnis yra Ta_2O_5 sluoksnis ($n = 2.04$) ant trapecinės gardelės, kurios parametrai: $\Lambda_x = 625$ nm, gardelės gylis $h = 250$ nm, padėklo lūžio rodiklis $n_{\text{sub}} = 1.47$. Joninio pluošto dulkinimo metodu užaugintos dangos forma neatkartoja trapecinės gardelės padėklo moduliacijos ir pasižymi padidėjusia dielektrine užpilda ties vienu periodu. Palyginus apskaičiuotus ir išmatuotus filtro pralaidumus, gauta, jog atspindys prie Reilėjaus anomalijos išlieka, tačiau jo veikimas gautas ties 4 nm spektriniu pločiu, kuris atitinka 99% pastovų atspindį.

Rezonansų spektrinės charakteristikos arti kontinuumo krašto - trečias skyrius

Šis darbas sudarytas iš trijų dalių - analitinio formalizmo, skaitmeninio modeliavimo palyginimo su analitikos gautais rezultatais ir galiausiai - pagamintos šviesolaidinės sistemos išmatuotų atspindžio spektrų palyginimas su RCWA modelio rezultatais. Nagrinėjama problema yra nesimetrinės formos rezonansas atspindyje, kuris pasižymi netolydumu ties Reilėjaus anomalija. Šiuo atveju sklindančio lauko amplitudė yra koncentruota ties moduliuoto padėklo paviršiumi.



6.9 pav. Potencinės duobės schema (a) su surištų būsenų rezonansais (b). Ši schema atitinka šviesolaidinių modų filtro struktūrą (c). Moduliacijos gylis h atitinka sietį tarp kritusio šviesos pluošto, šviesolaidinės modos ir atspindėto lazerio pluošto, kuris pavaizduotas d).

Analitinė tyrimo dalis nagrinėja Šriodingerio lygties sujungimą su išoriniu šaltiniu, o lygčiai yra priskirtas potencinės duobės modelis, kurio koncepcija

pateikta 6.9 pav.. Lygčiai išspręsti yra priskirtos dvi spėjinių dalys: superpozicija tarp šviesolaidinės surištos būsenos ir Fabri-Perot modos. Tokiu atveju, kai išorinis laukas su tolydžiu spektru sąveikauja su diskrečiomis potencinės duobės būsenomis, rezonaninis atspindžio koeficientas praranda simetrijos formą, bet spektrinės kreivės išlieka tolydžios. Tokie rezonansai vadinami Fano rezonansais. Svarbu paminėti, kad potencinės duobės modelis yra Fabri Perot sistema, kuri nusako, jog tokios būsenos negali potencinėje duobėje egzistuoti be galo daug laiko, taigi jos pasižymi nuostoliais pralaidume ir atspindyje. Suradus šios sistemos bendrą atsako funkciją, galima įvertinti potencinės duobės atspindžio koeficientą. To pasekoje yra sukurtas bendras analitinis modelis siekiant ištirti surištų fotoninių būsenų priklausomybę nuo potencinės duobės parametrų. Šviesolaidinis filtras, kuris atitinka šią sistemą, yra parinktas tik su pirmu nemoduliuotu paviršiumi, pagal kurį analitinis formalizmas yra išvestas. Tokia sistema pasižymi dviejais nesimetrinės formos rezonansais, kurie atitinka surištas būsenas potencinės duobės viduje. Pirma yra surišta būsena, kuri yra giliai duobėje. Tokio rezonanso atspindžio smailė yra tolydi ir gali pasižymėti Lorentz'o rezonanso forma, jeigu jos būsena egzistuoja labai giliai duobėje. Jos atsako funkcija kinta proporcingai nuo energijos ΔE^{-1}. Kita dalis priklauso būsenai arti duobės krašto (angl. Edge of Continuum), kuomet atspindžio smailė nėra tolydi. Jos atsako funkcija kinta pagal $\Delta E^{-1/2}$ priklausomybę. Čia ΔE yra energijos nuokrypis nuo potencinės duobės krašto, kuris parodo ribą tarp surištų diskrečių būsenų ir laisvai sklindančios bangos, kurios spektras yra kontinuumas, o potencinės duobės kraštas atitinka Reilėjaus anomaliją.

Nesimetrinės formos atspindys taip pat randamas skaitinio modeliavimo dėka iš atspindžio spektrinio/kampinio skirstinio ties 8° kritimo kampu. Keičiant elektromagnetinės bangos kritimo kampą, spektro plotis ir atspindžio smailės koeficientas sumažėja, kaip ir analitikoje ir tokiu būdu identifikuojamas rezonansas, kuris atitinka surištą būseną ties potencinės duobės kraštu. Vadovaujantis analitiniais skaičiavimais, tokio rezonanso plotis ties pusė maksimumo sumažėja per 4 eiles keičiant potencinės duobės sieties koeficientą $\gamma_0 \approx h\frac{n-1}{\lambda_0}$, kuris nusako kreivės plotį. Čia n yra moduliuotos šviesolaidžio dangos lūžio rodiklis, h yra gardelės moduliacijos gylis, o λ_0 yra vakuumo bangos ilgis.

Šviesolaidinių filtrų gamyba yra realizuota IBS metodu. Paviršiaus ėsdinimas aktyviais jonais yra pritaikytas trapecinei gardelei siekiant suglotninti paviršiaus moduliaciją bei sumažinti moduliacijos gylį. Padėklo moduliacijos gylis sumažintas iki 220 nm ir gardelės forma išlieka supergausinė, su pločiu ties pusė aukščiu 306 nm, o funkcijos eilė $m = 2$. Šiuo atveju Nb_2O_5 yra panaudotas šviesolaidžio sluoksnio augimui, sluoksnio storis po dangos nusodinimo yra 530 nm. Užgarinto sluoksnio morfologija pakitusi - dangos užpildas vienąme periode skersine kryptimi yra padidėjęs, tačiau atspindžių charakteristikos prilygsta modeliuotam nulinės eilės atspindžiui. Kita vertus, Reilėjau anomalijos apribotas plačiajuostis atspindys irgi sėkmingai gautas su $\Delta\lambda = 43.25$ nm pastovaus atspindžio pločiu. Kampinio atsako plotis irgi padidėjęs dėl šviesolaidinio sluoksnio morfologijos, palyginus su trapecinės gardelės atspindžiu. Ties 4 laipsnių bangos kritimo kampu randamas nesimetrinės formos rezonansinis atspindys tiek s, tiek p poliarizacijoms ir jų forma atitinka potencinės duobės

modeliu paskaičiuotas kreives.

PT asimetrijos įtaka ŠMR charakteristikoms - ketvirtas skyrius

Šiame skyriuje nagrinėjama kompleksinio lūžio rodiklio įtaka šviesolaidinių modų rezonansams, difrakcinių efektyvumų skirstiniams, kuomet surišti laukai šviesolaidžio viduje gali būti susieti su sugeriančiu sluoksniu. Tam palyginami simetriškai ir asimetriškai išdėstyti sugėrikliai ant periodiškai moduliuoto šviesolaidžio.

Šiame darbe pasitelkiama nesimetrine sugertimi, kadangi tokiu būdu sukeliama kompleksinio lūžio rodiklio moduliacija, kuri moduliuoja ir šviesolaidinę modą. Periodinė lūžio rodiklio moduliacija pasireiškia taip

$$\Delta n \approx \Delta n_{\mathrm{Re}} \cos kx + j\Delta n_{\mathrm{Im}} \sin kx. \tag{6.3}$$

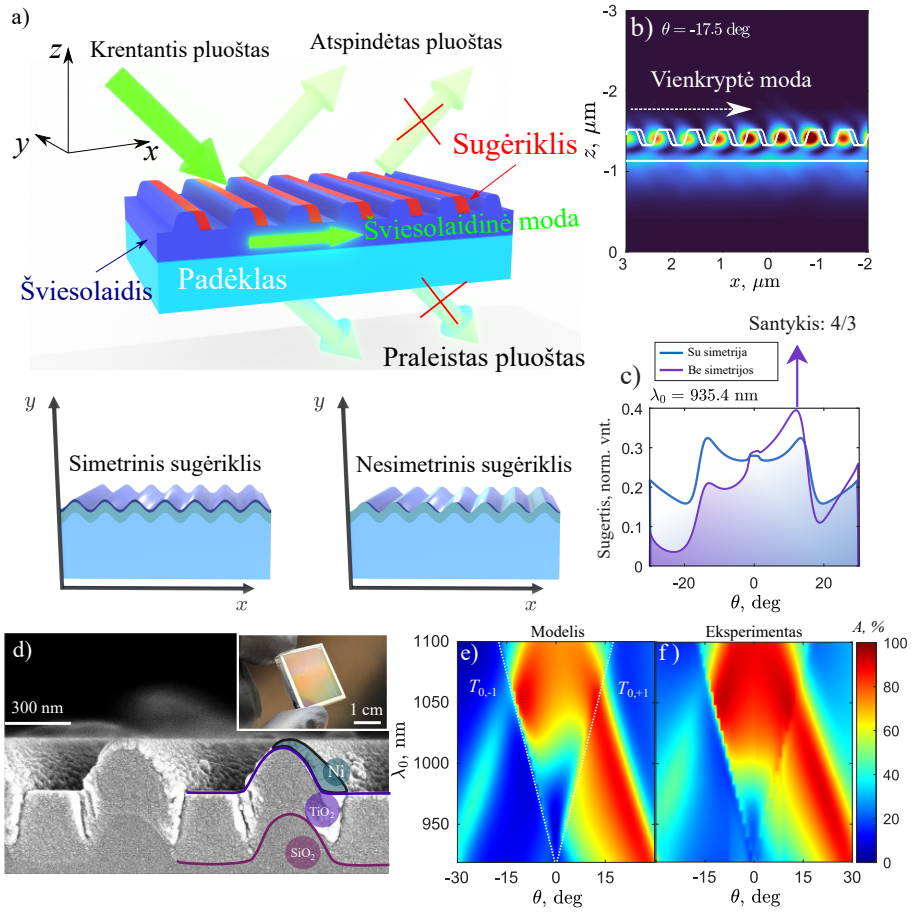
Išskleidus harmonines f-jas į jų kompleksines eksponentes ir, įterpus $\Delta n_{\mathrm{Re}} = \Delta n_{\mathrm{Im}}$, tokiu atveju atvirkštinėje erdvėje moduliuosis tik viena šviesolaidinės modos banginio vektoriaus komponentė (+k), o tuo tarpu kita erdvinė komponentė (-k) pasišalins:

$$\Delta n = \Delta n_{\mathrm{Re}} e^{jkx} \tag{6.4}$$

Taip ir realizuojama PT (angl. Parity Time) asimetrija, kuomet signalo dažninės komponentės nebetenkina veidrodinės simetrijos ir sklindanti šviesolaidinė moda šviesolaidyje tampa vienkryptė.

Šiame darbe nagrinėjama asimetriškai išdėstytas sugėriklis ant skaidrios moduliuotos rezonansinės dielektrinės dangos. Jų dėka galima susieti krentantį elektromagnetinį lauką su sugėrikliu, tačiau, jeigu sugertis pakankamai didelė (metalo atveju), rezonansai gali nepasižymėti siauromis spektrinėmis juostomis - sumažėtų jų kokybė ir pasikeistų rezonanso dažnis ties smaile. Remiantis analitiniu surištų bangų modeliu, nesimetrija gali padidinti šviesos sugertį su nesimetriniu sugėriklio išdėstymu, palyginus su simetriniu. Šiam palyginimui įgyvendinti pasitelkta šviesolaidiniu rezonatorium su lygaus paviršiaus padėklu, o dangos paviršius pasižymi supergausine moduliacija, kaip ir praeitame skyriuje, tik moduliacijos gylis $h = 200$ nm, o storis $L = 460$ nm. Plonasluoksnė šviesolaidinė terpė yra TiO_2, $n = 2.35$, o nikelis yra sugerianti terpė, kurios lūžio rodiklis atitinka $n_{\mathrm{Ni}} = 2.4 - 2.3j$. RCWA metodu paskaičiuotas sugerties spektrinis skirstinys tiek asimetriniui, tiek simetriniui, rezonatoriams. Rezonatorių struktūros ir šviesolaidinės modos vienpusio sklidimo koncepcija yra iliustruojamos 6.10 pav. a) ir b). Palyginus simetriškai ir asimetriškai išdėstytus sugėriklius ant gardelinio šviesolaidžio, asimetrinis išdėstymas padidina sugerties koeficientą 4/3 karto nei simetriškai išdėstyta struktūra esant nemoduliuotam padėklui. Šis parametras vaizduojamas 6.10 pav. c).

Analitinis surištų modų formalizmas yra pasiūlytas siekiant palyginti, kiek daugiau sugerties galima gauti su tokia rezonatorių konfigūracija. Fabri-Perot terpė yra susieta kartu su sugeriančioje terpėje gęstančia šviesolaidine moda.



6.10 pav. Viena kryptimi sklindančios šviesolaidinės modos koncepcija (a ir b), kur dėl nesimetriškai išdėstyto sugėriklio padidėja sugertis (c). Dviguba moduliacija pasižymintis supergausinis filtras (d) ir jo atitinkamai paskaičiuoti (e) ir išmatuoti (f) sugerties spektrai.

Sieties koeficientai yra kompleksiniai ir yra išreikšti per realią ir menamą dielektrines konstantas $\Delta\varepsilon_{\mathrm{Re}}$ ir $\Delta\varepsilon_{\mathrm{Im}}$, atitinkamai. Šis modelis laikosi prielaidos, jog šviesolaidinės terpės (dangos) sugertis α yra maža palyginus su FP modos gyvavimo trukme τ, t.y., $\alpha\tau \ll 1$. Suradus intensyvumo sugerties koeficientą, analitiniu modeliu spėjama, jog parinkus žemos sugerties rezonanso sistemą, sugertis gali būti padidinta iki 8/5 kartų daugiau su nesimetriniu sugėrikliu.

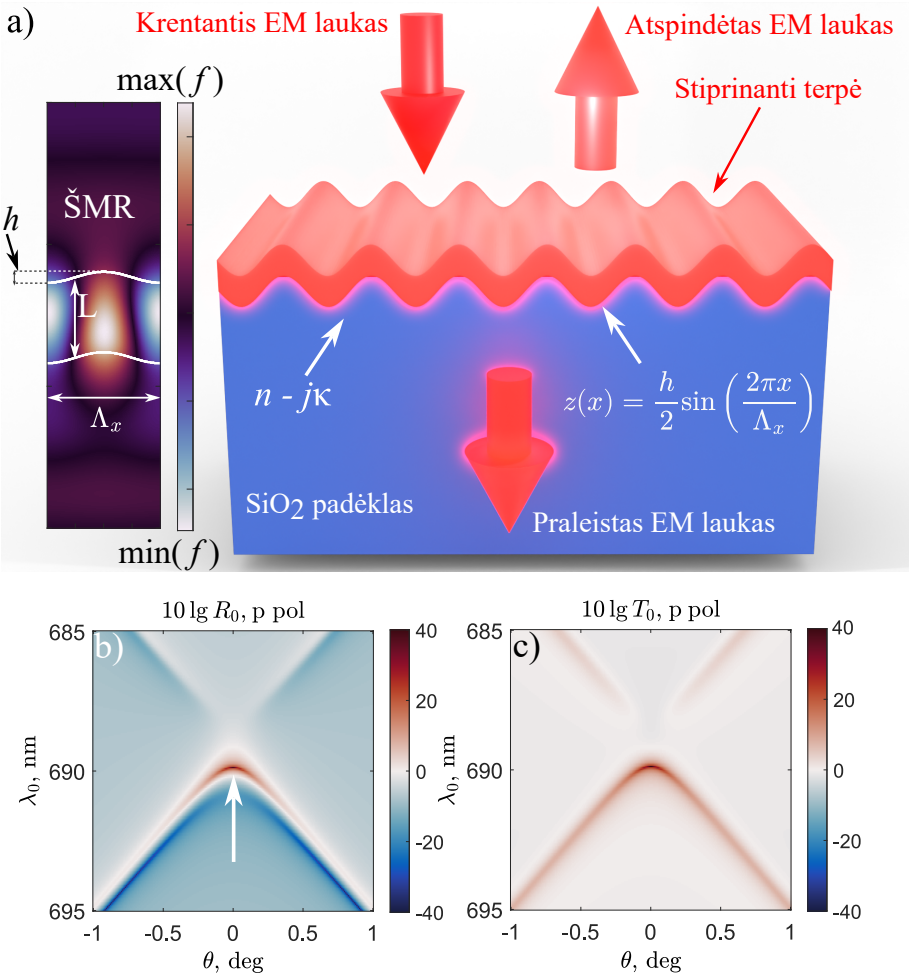
Siekiant šį reiškinį įgyvendinti, pasitelkta TiO_2 ir Ni nusodinimai ant supergauso moduliacijos gardelės, kurio SEM nuotrauka pateikta 6.10 pav. d). Nikelis nusodintas ant šviesolaidžio 50 nm storiu, užtikrinant asimetriją ir tokiu būdu pagaminamas dviejų moduliuotų paviršių šviesolaidinis filtras. Dėl dvigu-

bos moduliacijos pasireiškia stipri sugertis ties Reilėjaus zona (teigiamas bangos kritimo kampas) ir aiškiai matosi sugerties trūkiai ties jomis, kas iliustruojama 6.10 pav. e) ir f) grafikuose.. Ties Reilėjaus zonomis yra sugerties padidėjimas teigiamiems šviesos kritimo kampams, o ties neigiamu kampu - staigus sugerties spektro kritimas krentančiai šviesai su s poliarizacija. Tokie prietaisai su gali būti palankūs kaip fotodetektoriai arba kaip naujos kartos Saulės elementai.

ŠMR panaudojimas šviesos stiprinimui - penktas skyrius

Stipri šviesos lokalizacija periodiškai moduliuotame šviesolaidyje pasižymi aukštos kokybės ir siauro spektrinio pločio rezonansais, kurių kokybės faktoriai kinta nuo 300 iki 1000 lūžio rodiklio kontrastui $\Delta n \approx 0.5$, sumažinus šviesolaidinio filtro moduliacijos gylį h. Siauras spektrinis plotis užtikrina ilgą rezonanso išlikimą pačiame šviesolaidyje ir, jeigu šviesolaidinė terpė yra aktyvi, ji tuo tarpu sustiprins ir rezonansinę modą būtent dėl aukštos rezonanso kokybės, kas būdinga ir Purcel'io efektui - spontaninės emisijos padidėjimui palyginus su nerezonansine terpe [83, 84]. Šviesolaidžio dizainas yra iliustruojamas 6.11 pav. a) su atitinkama aukštos kokybės šviesolaidine moda. Stiprinanti terpė šiame darbe yra parinkta perovskito medžiaga su Lorenco formos stiprinimo kreive, kur kompleksinio lūžio rodiklio vertė ties smaile yra $n = 2.04 - 2.7 \cdot 10^{-3} j$, kur $j = \sqrt{-1}$. Kadangi atspindžio rezonansai siauri ir šiame darbe spektrinių pločių ties pusė maksimalaus rezonanso pločio siekia 1.0 nm statmenai krentančiai elektromagnetinei bangai ir 0.8 nm krentančiai bangai iki 1 laipsnio kritimo kampo, kokybės faktorius yra nuo 10^2 iki 10^3 eilės ir gali selektyviai stiprinti krentančią elektromagnetinę spinduliuotę, esant mažai spektrinei rezonanso modifikacijai. Tokios aktyvios sistemos gali būti panaudotos šviesos ir medžiagos sąveikos stiprinimui ir kaip aktyvūs filtrai mikrolazerių sistemose.

Šiame darbe pasitelkta genetiniu algoritmu siekiant rasti šviesolaidinio filtro geometrinius parametrus, kurie padidina difrakcinių efektyvumų vertes daugiau už 0 dB - padidinti stiprinimą atspindžio R_0 ir pralaidumo T_0 vertėms stačiai krentančiai elektromagnetinei spinduliuotei. Pati plonasluoksnė šviesolaidžio struktūra ant SiO_2 padėklo yra aprašoma kaip Lorentz'o antirezonansinė terpė su $\Delta\lambda \approx 30$ nm stiprinimo juosta, o stiprinimo koeficientas ties 690 nm smaile yra 500 cm^{-1}. Optimizavimas atliktas s ir p poliarizacijoms atskirai ir atitinkamai pasižymi sup-difrakciniu ir sub-difrakciniu veikimo režimais. Pirmasis režimas sustiprina tik vienos poliarizacijos krentančią bangą ties 0 laipsnių kritimo kampu tiek pralaidumo, tiek atspindžio srityse iki 40 dB ties 690 nm ir pasižymi siaurais kampiniais jautriais. Tuo tarpu p poliarizacijos optimizuotam įtaisui sub difrakciniam režime veikiantis elementas pasižymi padidintu stiprinimu ir s, ir p poliarizacijoms. o difrakcinių eilių vertės siekia 40 dB ties nuliniu kritimo kampu p poliarizacijai, kas iliustruojama 6.11 pav. b) ir c). Abu režimai pasižymi kampiniais jautriais iki 0.2 laipsnio. Pakeitus kritimo poliarizaciją šviesolaidinis rezonansas patiria raudoną poslinkį ir išlaiko stiprinimą, kuomet



6.11 pav. Aktyvios šviesolaidinės terpės su harmonine moduliacija dizainas (a) bei atspindžio (b) ir pralaidumo (c) spektrai p poliarizacijai.

kompleksinė lūžio rodiklio dalis sumažėja iki 10 kartų vien dėl padidėjusios rezonanso kokybės, o tai atsiranda dėl sumažėjusio $\Delta\lambda = 0.8$ nm spektrinio pločio.

Genetinis algoritmas padėjo suderinti rezonansą aktyviai terpei. Jeigu terpė yra pasyvi, t.y., pasižymi pastoviu lūžio rodikliu be sugerties nuostolių ar stiprinimo, rezonanso kreivės pasislenka į mėlyną sritį. Rezonanso smailių poslinkiai yra iki 1 nm - vadinasi stiprinanti terpė (dispersija) modifikuoja patį rezonansą, todėl geometrijos derinimas optimizacijos metodu yra būtinas, siekiant suderinti šviesolaidinį rezonansą kartu su šviesolaidžio kompleksiniu lūžio rodiklio maksimumu.

Siekiant analiziškai aprašyti tokią šviesolaidinių modų rezonanso sąveiką su stiprinančia terpe, pasitelkta periodiškai surištų harmoninių osciliatorių modeliu, kur kiekvienas osciliatorius tarpusavyje yra periodiškai surištas. Ši sistema yra naudojama kaip terpė, per kurią sklinda periodiškai moduliuota banga. Šis modelis modifikuojamas prijungiant prie osciliatorių grandinės papildomą osciliatorių kaip perturbaciją, kuris pasižymi tiek sugerties nuostoliais, tiek stiprinimu. Tokia sistema pasižymi sietimi tarp dviejų dalių, kur klasikinė periodinė osciliatoriaus dalis pažymėta "A", o apatinis osciliatorius "B", o sietis - κ_{AB} bei κ_{BA} ir išplėsta lygčių sistema yra nurodyta (6.5) lygtyje:

$$\frac{\partial^2 A_0}{\partial t^2} = \underbrace{\omega_A^2(A_{-1} + A_1 - 2A_0)}_{\text{Osciliatoriaus laplasianas}} - \underbrace{2\gamma_A \frac{\partial A_0}{\partial t}}_{\text{Nuostoliai nuo } A} + \underbrace{\kappa_{AB}\omega(B - A_0)}_{\text{Sietis tarp } A\text{-}B}, \tag{6.5a}$$

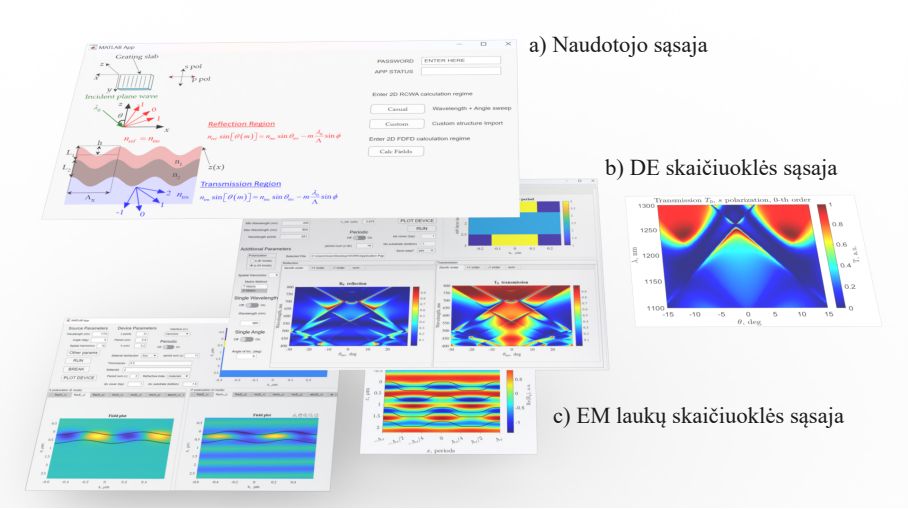
$$\frac{\partial^2 B}{\partial t^2} = -\omega_0^2 B - \underbrace{2\gamma_B \frac{\partial B}{\partial t}}_{\text{Nuostoliai nuo } B} + \underbrace{\kappa_{BA}\omega(A_0 - B)}_{\text{Sietis tarp } B\text{-}A}. \tag{6.5b}$$

Čia terminai „osciliatoriaus laplasianas" ir „nuostoliai nuo A" nurodo periodinės grandinės charakteristikas, kuomet nėra perturbacijos B. Su papildoma perturbacija, atsiranda sietis, perturbacijos savasis dažnis ω_0 ir nuostolių koeficientas γ_B atitinkamai nurodo osciliatoriaus B charakteristikas. Šios sistemos fizikinė interpretacija tokia - A_0 ir B osciliatorių jungtis imituoja Fabri-Perot terpę, o B tašelis imituoja šviesolaidinį rezonansą. Osciliatorius A_0 periodinėje grandinėje turės atsako funkciją ir pasižymės bangos sklaida, jeigu banga yra paleidžiama sklisti tokios perturbacijos link. Todėl pasirenkami ± 1 osciliatoriai ir banginės funkcijos, kurios tenkina laplasiano lygtį $\frac{\partial^2 A_0}{\partial t^2} = \omega_A(A_{-1} + A_1 - 2A_0)$. Osciliatorius $+1$ nurodo pralaidumo sritį, kas atitiktų padėklą realiai rezonatoriaus sistemai, o -1 nurodo viršutinę terpę, kurioje egzsituoja krentanti ir atspindėta bangos. Galų gale išvedama atsako f-ja $S(\omega)$ ir randama amplitudė A_0, iš kurių atitinkamai randami kompleksiniai atspindžio ir pralaidumo koeficientai r ir t.

Taigi, šis modelis yra pritaikomas p poliarizacijai, kadangi genetinis algoritmas užtikrino didžiausią stiprinimą sub difrakciniam režime. Analitinio modelio parametrai genetinio optimizavimo procedūros dėka rasti tokie, ties kuriais pralaidumo ir atspindžio koeficientai kokybiškai sutampa su skaitiškai modeliuotais. Vienas neatitikimas yra rezonansinio dažnio ω_B nesutapimas su smailės dažniu ω_0. To priežastis yra rezonanso dažnio poslinkis dėl nuostolių ar stiprinimo bei nuo sieties koeficientų, kurie spektriškai paslenka pralaidumo minimumą nuo atspindžio maksimumo. Tai paaiškinama krentančios bangos sąveika tarp diskrečios šviesolaidinės būsenos. Toks pat rezultatas gaunamas ir konservatyviai grandinės sistemai, kuomet sieties koeficientai $\kappa_{AB} = \kappa_{BA} = \kappa$ ir nuostolių/stiprinimo koeficientai $\gamma_{A,B} = 0$.

Vartotojo sąsaja - šeštas skyrius

Šiame darbe pristatoma "ZenScat" vartotojo sąsaja, kurioje yra įtraukti 2D RCWA ir 2D FDFD algoritmai, validacijos ir modalinio metodo konvergavimo tyrimai. Pagrinde RCWA algoritmo sklaidos ir pralaidumo matricų metodai yra kompiliuoti "MatlabCoder" programėlės dėka į C++ kalbą, kuri užtikrina spartesnį difrakcinių efektyvumų skaičiavimą, o 2D FDFD naudojamas vietoje RCWA siekiant paskaičiuoti laukų skirstinius. Vartotojo sąsajos koncepcija iliustruojama 6.12 pav. Sąsaja sudaryta iš naudotojo sąsajos 6.12 pav. a), kurios parinktys - skaičiuoklės ir optimizavimo sąsaja 6.12 pav. b) ir elektromagnetinių laukų skirstinių skaičiuoklės sąsaja, kuri pavaizduota 6.12 pav. c).



6.12 pav. Vartotojo sąsaja "ZenScat" su atidarymo programėle a), difrakcinių efektyvumų skaičiuokle b) ir EM laukų skirstinių skaičiuoklės sąsaja c).

Siekiant įsitikinti, ar algoritmas ir vartotojo sąsaja yra teisingai veikiančios - sąsaja validuojama palyginus jos apskaičiuotus difrakcinius efektyvumus su publikuotomis mokslinėje literatūroje. Validacijos procedūra yra atlikta šviesolaidiniam filtrui su stačiakampės formos moduliacija (rezultatai pavaizduoti 6.2 pav.). Šis įtaisas yra silicio nitrido moduliuotas šviesolaidis ant lydyto kvarco pagrindo. Skaitiniai modeliavimai atlikti su FDTD, kuriuo siekiama charakterizuoti šio įtaiso spektrines charakteristikas keičiantis ir poliarizacijos plokštumos kampui [147]. ZenScat vartotojo sąsaja įvertino spektrinius atsakus su 4 nm poslinkiu TM poliarizacijai (smailė yra ties 742 nm), kas atitinka 0.53%. Tai įtariama dėl šių autorių panaudotos žemos tinklelio diskretizacijos Lumerical terpėje, kuomet ZenScat panaudojo 1024 taškų gardelei pagal x kryptį. Pasak autorių, skaitmeninis modeliavimas atliktas Lumerical komercine pro-

grama, kuriame įterptas 3D FDTD metodas. Kitas nagrinėtas pavyzdys yra harmoninės funkcijos sankirtos, kurios atspindi TE ir TM poliarizacijas statmenu kampu (žr. 6.3 pav.). Du sluoksniai panaudoti siekiant suderinti geometriją ir sulyginti šviesolaidines būsenas, kad nulinės eilės atspindys būtų vienodas tuo pačiu kritimo kampu [148]. Autoriai pateikia Lumerical programa apskaičiuotus rezultatus su rezonansais, kurių smailės bangos ilgis yra 511 nm TE ir TM poliarizacijoms, o ZenScat programa 510.6 nm, kas atitinka 0.4 nm poslinkį. Toliau, validacija atlikta sup-banginės gardelės erdviniam filtrui (žr. 6.4 pav.) ir pastovaus atspindžio optiniam sietuvui (žr. 6.5 pav.). Pusės maksimalaus aukščio kampinis plotis, ties kuriuo pasireiškia filtravimas, yra 0.127°, o rezonanso spektrinis plotis ir smailės bangos ilgis: atitinkamai 0.6 nm ir 852 nm, kaip ir publikacijoje [86].

Tuo tarpu genetinis optimizavimas, kuris yra suderintas su kompiliuotomis algoritmo dalimis, irgi pasižymi sparčia veika. Jis MATLAB terpėje yra naudojamas rasti šviesolaidinių filtrų topologiją, kuri tenkina tikslo funkcijos minimumą. Pati algoritmo koncepcija, kurią naudoja Matlab programinė terpė, yra aprašyta 8 pseudo-algoritme. Naudojantis genetinio optimizavimo procesu, galima rasti geometrinius parametrus grįžtamojo ryšio įtaisams, kurių terpės yra sugeriančios, arba aktyvios. Visais atvejais rastos sugerties ar stiprinimo kreivės yra siaurų juostų ir aitinka aukštos kokybės rezonansus tiek kampiniame, tiek spektriniame diapozonuose. Taigi, tokiu būdu atviros prieigos vartotojo sąsaja yra paruošta optimizavimo uždaviniams vėlesniuose tyrimuose.

Stačiakampės formos gardelių grįžtamojo ryšio struktūroms yra atliktas konvergavimo įvertinimas, t.y., apskaičiuota nulinės eilės difrakcinių efektyvumų priklausomybė nuo erdvinių harmonikų raiškos tiek sub-difrakciniam, tiek sup-difrakciniam veikimo režimams. Įvertinta, jog bent 6 erdvinės harmonikos nuo 0 eilės (pilnai 13 eilių nuo -5 iki 5) reikalingos pilnam konvergavimui tiek silicio, tiek sidabro homogeniniams sluoksniams.

Rezultatai ir išvados

1. Trapecinės formos moduliacija pasižymintys šviesolaidiniai filtrai yra pasiūlyti siekiant užtikrinti plačiajuostį nulinės eilės atspindį, kurio kampinis atsakas yra Reilėjaus anomalijos apribotas, t.y., apribojimo bangos ilgis yra $\lambda_R = \Lambda_x(n_{\text{sub}} \pm \sin\theta)$. Plačiajuostis atspindys yra užtikrinamas bent dviejais rezonansais, o pastovaus atspindžio spektrinis plotis $\Delta\lambda_0 = 46$ nm. Konforminės gardelės gamyba įgyvendinta IBS metodu formuojant Ta_2O_5 dangą ant trapecinė formos padėklo. Dėl didelio sluoksnio storio dangos skersinė moduliacija neatkartoja padėklo formos, bet, palyginus spektrines charakteristikas tarp išmatuoto ir modeliuoto nulinės eilės pralaidumų spektrų, Reilėjaus efektu apribotas atspindys išlieka, kurio spektrinis plotis $\Delta\lambda_0 = 4$ nm.

2. Analitinis Šriodingerio modelis išsprendžia bangos sklaidos nuo potencinės duobės uždavinį *s* poliarizacijai. Šis metodas pritaikytas vieno moduliuoto paviršiaus šviesolaidinių filtrų spektriniam atsakui - nulinės eilės

pralaidumo ir atspindžio koeficientams - charakterizuoti. Potencinė duobė pasižymi dviem veikimo režimais - rezonansiniais atspindžiais, kurių būsenos, priklausomai nuo duobės gylio, yra asimetrinės formos ir šio rezonanso smailė yra tolydi. Pasak analitikos, šio rezonanso pločio ties pusė maksimumo mastelis proporcingas sieties koeficiento γ_0 antrajam laipsniui, o Fabri-Perot sistemos atsako funkcija proporcinga $1/E$. Tuo tarpu kitas rezonansas, esantis ties duobės kraštu, pasižymi netolydžia, aštrios formos smaile ir jos atsako funkcijos mastelis proporcingas $\sqrt{1/\Delta E}$, o rezonanso atspindžio plotis proporcingas koeficiento γ_0 ketvirtam laipsniui. Pagaminti šviesolaidiniai filtrai - Nb_2O_5 ant supergausinės moduliacijos padėklo, ties $4°$ kritimo kampu, pasižymi asimetriniu atspindžiu arti Reilėjaus anomalijos ir plačiajuosčiu, Reilėjaus anomalija apribotu, atspindžiu ties pirmos eilės difrakcinių efektyvumų sankirta.

3. Asimetrinis sugėriklio išdėstymas ant šviesolaidinio filtro pasižymi geresne, padidinta bangų sugertimi s poliarizacijai, palyginus su simetriškai išdėliotu sugėrikliu. Palyginus su analitiniu susietų bangų modeliu, absorbcija yra padidinta per 8/5, RCWA modeliu pasirėmus, sugertis padidėja per 4/3 dalį. Dvigubos moduliacijos plonasluoksnių įtaisų asimetrinė sugertis yra stipriausia ties Reilėjaus bangos ilgiu $\lambda_R = \Lambda_x(n_{\text{sub}} \pm \sin\theta)$ ir šis efektas atlieka sugerties ribojimo vaidmenį tarp pimų difrakcinių eilių. Tai parodo, kad paviršinės bangos, sklindančios per padėklo paviršių, padidina asimetrinę sugertį.

4. Nulinės eilės difrakcinių eilių padidintas stiprinimas yra būdingas šviesolaidiniams rezonansams aukštai rezonansų kokybei, kas atitinka pakankamai mažus rezonansų kreivių pločius. Pasirinkus aukštą stiprinimo spektrinį plotį $\Delta\lambda_0 \approx 30$ nm, šviesolaidiniai filtrų geometriniai parametrai, pasitelkus genetiniu algoritmu, yra randami ir tenkina didžiausią padidintą optinį stiprinimą pirmos eilės šviesolaidiniams rezonansams. Optimizacija svarbi tuo, kad suderintų rezonansą aktyviai terpei, kuri paslenka rezonansą spektre per nanometrų eilę . Sub difrakcinis stiprinimo režimas ($\Lambda_x n_{\text{sub}} < \lambda_0$) pasižymi šviesolaidiniais rezonansais, kurie stiprina nulinės eilės pralaidumo ir atspindžio koeficientus s ir p poliarizacijoms. Tuo tarpu sup-difrakcinis veikimas pasižymi siaurajuosčiu selektyvumu s poliarizacijai, kur $T_{\pm 1,0}$ ir $R_{0,\pm 1}$ eilės egzistuoja.

5. RCWA algoritmo skaitiškai modeliuotų stačiakampių šviesolaidinių filtrų difrakciniai efektyvumai yra palyginti su publikacijų pavyzdžiais, kurie apskaičuoti komercine 3D Lumerical programa. Šių įtaisų skirtumas tarp apskaičiuotų spektrinių smailių bangos ilgių atitinka 0.54%, o harmoninių gardelių filtrams atitinka 0.08%. Tikėtina, kad stačiakampių gardelių atveju Lumerical terpėje buvo panaudota maža resoliucija. Tuo tarpu palyginimas su kita RCWA terpe stačiakampių šviesolaidinių gardelių, veikiančių sup-difrakciniame režime, atveju: bangos ilgių skirtumo tarp smailių nėra. Kompiliuota "ZenScat" vartotojo sąsaja su pralaidumo ir sklaidos matricų algoritmais leidžia pasiekti 10 kart spartesnius difrakcinių

efektyvumų skaičiavimus iki 9 erdvinių harmonikų erdvinės rezoliucijos, o nuo 11 erdvinių harmonikų, skačiavimo sparta siekia 1.5-2 karto, o tai pravartu optimizavimo uždaviniams.

Bibliography

[1] C. Barrera Patiño, J. Vollet-Filho, R. Teixeira-Rosa, H. Quiroz, A. Dussan Cuenca, N. Inada, V. Bagnato, R. Rey-González, Photonic effects in natural nanostructures on Morpho cypris and Greta oto butterfly wings, *Scientific Reports*, **10** (2020).

[2] R. Vaz, M. Frasco, M. G. Sales, Photonics in nature and bioinspired designs: sustainable approaches for a colourful world, *Nanoscale Advances*, **2** (2020).

[3] J. P. Vigneron, J.-F. Colomer, M. Rassart, A. Ingram, V. Lousse, Structural origin of the colored reflections from the black-billed magpie feathers, *Physical review. E, Statistical, nonlinear, and soft matter physics*, **73**, 021914 (2006).

[4] E. Armstrong, C. O'Dwyer, Artificial Opal Photonic Crystals and Inverse Opal Structures – Fundamentals and Applications from Optics to Energy Storage, *Journal of Materials Chemistry*, **3**, 6109–6143 (2015).

[5] R. Cersonsky, J. Antonaglia, B. Dice, S. Glotzer, The diversity of three-dimensional photonic crystals, *Nature Communications*, **12** (2021).

[6] J. Teyssier, S. Saenko, D. Marel, M. Milinkovitch, Photonic crystals cause active color change in chameleons, *Nature communications*, **6**, 6368 (2015).

[7] J. D. Joannopoulos, S. G. Johnson, J. N. Winn, R. D. Meade, *Photonic Crystals: Molding the Flow of Light - Second Edition*, Princeton University Press, rev - revised, 2 ed. (2008).

[8] J. Lou, C. K. M. Fung, K. W. C. Lai, H. Chen, N. Xi, Z. Zhou, Chapter 10 - Design of Photonic Crystal Waveguides, N. Xi, K. W. C. Lai, eds., *Nano Optoelectronic Sensors and Devices*, Micro and Nano Technologies, 163–182, William Andrew Publishing, Oxford (2012).

[9] H. S. Dutta, A. K. Goyal, V. Srivastava, S. Pal, Coupling light in photonic crystal waveguides: A review, *Photonics and Nanostructures - Fundamentals and Applications*, **20**, 41–58 (2016).

[10] B. Momeni, M. Chamanzar, E. S. Hosseini, M. Askari, M. Soltani, A. Adibi, Strong angular dispersion using higher bands of planar silicon photonic crystals, *Opt. Express*, **16**, 14213–14220 (2008).

[11] L. Wu, M. Mazilu, T. Karle, T. Krauss, Superprism phenomena in planar photonic crystals, *IEEE Journal of Quantum Electronics*, **38**, 915–918 (2002).

[12] H. Kosaka, T. Kawashima, A. Tomita, M. Notomi, T. Tamamura, T. Sato, S. Kawakami, Superprism Phenomena in Photonic Crystals, *Physical Review B*, **581** (1998).

[13] E. Semouchkina, R. Duan, N. P. Gandji, S. Jamilan, G. Semouchkin, R. Pandey, Superluminal media formed by photonic crystals for transformation optics-based invisibility cloaks, *Journal of Optics*, **18**, 044007 (2016).

[14] L. Maigyte, K. Staliunas, Spatial filtering with Photonic Crystals, *Applied Physics Reviews*, **2**, 011102 (2015).

[15] K. Staliunas, V. Sánchez-Morcillo, Spatial filtering of light by chirped photonic crystals, *Physical Review A*, **79** (2008).

[16] L. Grinevičiūtė, C. Babayigit, D. Gailevicius, M. Peckus, M. Turduev, T. Tolenis, M. Vengris, H. Kurt, K. Staliunas, Nanostructured Multilayer Coatings for Spatial Filtering, *Advanced Optical Materials* (2021).

[17] D. Gailevicius, V. Purlys, K. Staliunas, Photonic crystal spatial filters fabricated by femtosecond pulsed Bessel beam, *Opt. Lett.*, **44**, 4969–4972 (2019).

[18] R. Rumpf, J. Pazos, C. Garcia, R. Wicker, 3D Printed Lattices with Spatially Variant Self-Collimation, *Progress In Electromagnetics Research*, **139**, 1–14 (2013).

[19] R. Rumpf, J. Pazos, Synthesis of spatially variant lattices, *Optics express*, **20**, 15263–74 (2012).

[20] R. Rumpf, J. Pazos, Optimization of planar self-collimating photonic crystals, *Journal of the Optical Society of America. A, Optics, image science, and vision*, **30**, 1297–304 (2013).

[21] H. Kurt, M. Turduev, Generation of a two-dimensional limited-diffraction beam with self-healing ability by annular-type photonic crystals, *JOSA B*, **29**, 1245–1256 (2012).

[22] D. Vercruysse, N. Sapra, K. Y. Yang, J. Vuckovic, Inverse-Designed Photonic Crystal Circuits for Optical Beam Steering, *ACS Photonics*, **8** (2021).

[23] M. Koshiba, Y. Tsuji, M. Hikari, Time-domain beam propagation method and its application to photonic crystal circuits, *Journal of Lightwave Technology*, **18**, 102–110 (2000).

[24] Q. Hu, J. Zhang, K. Wang, L. Qian, Refractive index sensor with finite dimensions based on a topological guided-mode resonance grating, *Optics & Laser Technology*, **192**, 113487 (2025).

[25] J. Jang, D.-M. Geum, I.-S. Kang, Y.-W. Oh, S. Jung, H. Cho, S. Kim, Guided-Mode Resonance Polarization-Sensitive Narrowband InGaAs Photodetector, *Laser & Photonics Reviews*, **19**, 2401253 (2025).

[26] Y. Ni, C. Chen, S. Wen, *et al.*, Computational spectropolarimetry with a tunable liquid crystal metasurface, *eLight*, **2**, 23 (2022).

[27] K. J. Shayegan, S. Biswas, B. Zhao, *et al.*, Direct observation of the violation of Kirchhoff's law of thermal radiation, *Nature Photonics*, **17**, 891–896 (2023).

[28] H. S. Bark, M.-W. Park, J. E. Bae, K.-H. Jang, Y. U. Jeong, K. Lee, F. Rotermund, T.-I. Jeon, Enhanced Terahertz Characterization of Multilayer Graphene on Guided-Mode Resonance Filter: Boosting Sensitivity and Precision in Electrical and Optical Characteristics, *Advanced Materials Technologies*, **10**, 2400603 (2025).

[29] C. Wu, X. Wei, R. Wu, F. Deng, W. Hong, Strong coupling between high-Q guided mode resonance and excitons in a mirror-coupled WS2 grating structure, *Opt. Lett.*, **50**, 2751–2754 (2025).

[30] S. Bej, N. Tkachenko, R. Fickler, T. Niemi, Ultrafast Modulation of Guided-Mode Resonance in a Nonlinear Silicon Nitride Grating, *Advanced Optical Materials*, **13**, 2402632 (2025).

[31] X. Wang, A. Díaz-Rubio, V. S. Asadchy, G. Ptitcyn, A. A. Generalov, J. Ala-Laurinaho, S. A. Tretyakov, Extreme asymmetry in metasurfaces via evanescent fields engineering: angular-asymmetric absorption, *Physical Review Letters*, **121**, 256802 (2018).

[32] M. Maleki, M. Mehran, Guided-mode resonance sensors: different schemes for different applications, *J. Opt. Soc. Am. B*, **39**, 1634–1643 (2022).

[33] M. Gryga, D. Ciprian, L. Gembalova, P. Hlubina, Sensing based on Bloch surface wave and self-referenced guided mode resonances employing a one-dimensional photonic crystal, *Opt. Express*, **29**, 12996–13010 (2021).

[34] K. Shastri, F. Monticone, Nonlocal flat optics, *Nature Photonics*, **17**, 36–47 (2023).

[35] W. Shi, J. Gu, X. Zhang, Q. Xu, J. Han, Q. Yang, L. Cong, W. Zhang, Terahertz bound states in the continuum with incident angle robustness induced by a dual period metagrating, *Photon. Res.*, **10**, 810–819 (2022).

[36] K. J. Shayegan, B. Zhao, Y. Kim, S. Fan, H. A. Atwater, Nonreciprocal infrared absorption via resonant magneto-optical coupling to InAs, *Science Advances*, **8**, eabm4308 (2022).

[37] J. Zhang, J. Ma, M. Parry, M. Cai, R. Camacho-Morales, L. Xu, D. N. Neshev, A. A. Sukhorukov, Spatially entangled photon pairs from lithium niobate nonlocal metasurfaces, *Science Advances*, **8**, eabq4240 (2022).

[38] T. Lee, J. Kim, I. Koirala, Y. Yang, T. Badloe, J. Jang, J. Rho, Nearly Perfect Transmissive Subtractive Coloration through the Spectral Amplification of Mie Scattering and Lattice Resonance, *ACS Applied Materials & Interfaces*, **13**, 26299–26307, pMID: 34048213 (2021).

[39] M. Li, M. Shi, B. Wang, C. Zhang, S. Yang, Y. Yang, N. Zhou, X. Guo, D. Chen, S. Li, H. Mao, J. Xiong, Quasi-Ordered Nanoforests with Hybrid Plasmon Resonances for Broadband Absorption and Photodetection, *Advanced Functional Materials*, **31**, 2102840 (2021).

[40] Y. Liao, M. Xia, Y. Wang, Y. Chen, X. Zhang, Resonant 2D Wavefront Manipulation via Birefringent Guided-Mode Resonances in Dielectric Phase Gradient Metasurfaces, *Laser & Photonics Reviews*, **19**, e00339 (2025).

[41] E. Klopfer, S. Dagli, D. I. Barton, M. Lawrence, J. A. Dionne, High-Quality-Factor Silicon-on-Lithium Niobate Metasurfaces for Electro-optically Reconfigurable Wavefront Shaping, *Nano Letters*, **22**, 1703–1709, pMID: 35112873 (2022).

[42] S. Tibuleac, R. Magnusson, Reflection and transmission guided-mode resonance filters, *J. Opt. Soc. Am. A*, **14**, 1617–1626 (1997).

[43] R. Amedalor, P. Karvinen, H. Pesonen, J. Turunen, T. Niemi, S. Bej, High-Q guided-mode resonance of a crossed grating with near-flat dispersion, *Applied Physics Letters*, **122**, 161102 (2023).

[44] C. Liu, Y. Bai, J. Zhou, J. Chen, L. Qiao, Refractive index sensing by asymmetric dielectric gratings with both bound states in the continuum and guided mode resonances, *Opt. Express*, **29**, 42978–42988 (2021).

[45] M. J. Uddin, T. Khaleque, R. Magnusson, Guided-mode resonant polarization-controlled tunable color filters, *Opt. Express*, **22**, 12307–12315 (2014).

[46] I. C. Benea-Chelmus, S. Mason, M. L. Meretska, *et al.*, Gigahertz free-space electro-optic modulators based on Mie resonances, *Nature Communications*, **13**, 3170 (2022).

[47] J. Feng, X. Wang, J. Li, *et al.*, Resonant perovskite solar cells with extended band edge, *Nature Communications*, **14**, 5392 (2023).

[48] D. Wang, Z. Liu, H. Wang, M. Li, L. J. Guo, C. Zhang, Structural color generation: from layered thin films to optical metasurfaces, *Nanophotonics*, **12**, 1019–1081 (2023).

[49] R. C. Rumpf, *Design and optimization of nano-optical elements by coupling fabrication to optical behavior*, Ph.D. thesis (2006).

[50] A. Taflove, S. Hagness, *Computational electrodynamics: the finite-difference time-domain method. 2nd ed*, vol. 67–106 (2000).

[51] R. C. Rumpf, *Electromagnetic and Photonic Simulation for the Beginner: Finite Difference Frequency-Domain in MATLAB*, Artech House (2022).

[52] S. Shi, C. Chen, D. Prather, Plane-wave expansion method for calculating band structure of photonic crystal slabs with perfectly matched layers, *Journal of the Optical Society of America. A, Optics, image science, and vision*, **21**, 1769–75 (2004).

[53] M. G. Moharam, D. A. Pommet, E. B. Grann, T. K. Gaylord, Stable implementation of the rigorous coupled-wave analysis for surface-relief gratings: enhanced transmittance matrix approach, *J. Opt. Soc. Am. A*, **12**, 1077–1086 (1995).

[54] L. Li, J. Chandezon, G. Granet, J.-P. Plumey, Rigorous and efficient grating-analysis method made easy for optical engineers, *Appl. Opt.*, **38**, 304–313 (1999).

[55] L. Xie, J. Zhang, Z. Zhang, B. Ma, T. Li, Z. Wang, X. Cheng, Rectangular multilayer dielectric gratings with broadband high diffraction efficiency and enhanced laser damage resistance, *Opt. Express*, **29**, 2669–2678 (2021).

[56] C. Guo, J. Li, M. Xiao, S. Fan, Singular topology of scattering matrices, *Physical Review B*, **108** (2023).

[57] L. Zhu, S. Sandhu, C. Otey, S. Fan, M. Sinclair, T. Luk, Temporal coupled mode theory for thermal emission from a single thermal emitter supporting either a single mode or an orthogonal set of modes, *Applied Physics Letters*, **102** (2013).

[58] Y. Chen, P. Luo, X. Liu, Y. Di, S. Han, X. Cui, L. He, Sensing performance analysis on Fano resonance of metallic double-baffle contained MDM waveguide coupled ring resonator, *Optics & Laser Technology*, **101**, 273–278 (2018).

[59] Y. Fang, K. Wen, Y. Qin, Z. Li, B. Wu, Multiple fano resonances in an end-coupled MIM waveguide system, *Optics Communications*, **452** (2019).

[60] I. Evenor, E. Grinvald, F. Lenz, *et al.*, Analysis of light scattering off photonic crystal slabs in terms of Feshbach resonances, *The European Physical Journal D*, **66** (2012).

[61] X. Yin, J. Jin, M. Soljačić, *et al.*, Observation of topologically enabled unidirectional guided resonances, *Nature*, **580**, 467–471 (2020).

[62] D. Choi, K. Y. Lee, D. J. Shin, *et al.*, Unidirectional guided resonance continuum of Dirac bands in WS_2 bilayer metasurfaces, *Nature Nanotechnology*, **20**, 1026–1033 (2025).

[63] F. Liu, X. Zhang, K. Li, T. Guo, A. Ianoul, J. Albert, Discrimination of Bulk and Surface Refractive Index Change in Plasmonic Sensors with Narrow Bandwidth Resonance Combs, *ACS Sensors*, **6**, 3013–3023, pMID: 34190543 (2021).

[64] S. Cheng, W. Li, H. Zhang, M. N. Akhtar, Z. Yi, Q. Zeng, C. Ma, T. Sun, P. Wu, S. Ahmad, High sensitivity five band tunable metamaterial absorption device based on block like Dirac semimetals, *Optics Communications*, **569**, 130816 (2024).

[65] H. A. Haus, *Waves and fields in optoelectronics..*, Prentice-Hall, Englewood Cliffs (1984).

[66] D. Bykov, L. Doskolovich, V. Soifer, Coupled-mode theory and Fano resonances in guided-mode resonant gratings: the conical diffraction mounting, *Optics Express*, **25**, 1151–1164 (2017).

[67] B. Li, L. Zeng, R. Wen, X. Zhang, Dynamic Regulation of Multiple Fano Resonances Based on Liquid Crystal, *IEEE Photonics Journal*, **15**, 1–6 (2023).

[68] Y. Wang, J. Song, L. Dong, M. Lu, Optical bound states in slotted high-contrast gratings, *J. Opt. Soc. Am. B*, **33**, 2472–2479 (2016).

[69] D. Bykov, E. Bezus, L. Doskolovich, Coupled-wave formalism for bound states in the continuum in guided-mode resonant gratings, *Physical Review A*, **99** (2019).

[70] L. Huang, R. Jin, C. Zhou, *et al.*, Ultrahigh-Q guided mode resonances in an all-dielectric metasurface, *Nature Communications*, **14**, 3433 (2023).

[71] Z. Ai, Y. Yi, H. Yang, M. Liu, Y. Yi, C. Tang, F. Gao, TiN-Ti ultra-broadband solar absorber: Efficient heat absorption and high thermal stability, *Physics Letters A*, **556**, 130827 (2025).

[72] W. Li, Y. Liu, L. Ling, Z. Sheng, S. Cheng, Z. Yi, P. Wu, Q. Zeng, B. Tang, S. Ahmad, The tunable absorber films of grating structure of AlCuFe quasicrystal with high Q and refractive index sensitivity, *Surfaces and Interfaces*, **48**, 104248 (2024).

[73] W. Li, W. Zhao, S. Cheng, H. Zhang, Z. Yi, T. Sun, P. Wu, Q. Zeng, R. Raza, Tunable metamaterial absorption device based on Fabry–Perot resonance as temperature and refractive index sensing, *Optics and Lasers in Engineering*, **181**, 108368 (2024).

[74] E. Yablonovitch, Inhibited Spontaneous Emission in Solid-State Physics and Electronics, *Phys. Rev. Lett.*, **58**, 2059–2062 (1987).

[75] J. Hu, C. R. Menyuk, Understanding leaky modes: slab waveguide revisited, *Adv. Opt. Photon.*, **1**, 58–106 (2009).

[76] R. W. Wood, Anomalous Diffraction Gratings, *Phys. Rev.*, **48**, 928–936 (1935).

[77] J. E. Harvey, R. N. Pfisterer, Understanding diffraction grating behavior: including conical diffraction and Rayleigh anomalies from transmission gratings, *Optical Engineering*, **58**, 087105 (2019).

[78] S. S. Wang, R. Magnusson, Theory and applications of guided-mode resonance filters, *Appl. Opt.*, **32**, 2606–2613 (1993).

[79] R. Rumpf, E. Johnson, Modeling fabrication to accurately place GMR resonances, *Optics express*, **15**, 3452–64 (2007).

[80] W. Suh, Z. Wang, S. Fan, Temporal coupled-mode theory and the presence of non-orthogonal modes in lossless multimode cavities, *IEEE Journal of Quantum Electronics*, **40**, 1511–1518 (2004).

[81] S. Fan, W. Suh, J. D. Joannopoulos, Temporal coupled-mode theory for the Fano resonance in optical resonators, *J. Opt. Soc. Am. A*, **20**, 569–572 (2003).

[82] L. Verslegers, Z. Yu, P. B. Catrysse, S. Fan, Temporal coupled-mode theory for resonant apertures, *J. Opt. Soc. Am. B*, **27**, 1947–1956 (2010).

[83] J.-M. Gerard, B. Gayral, Strong Purcell effect for InAs quantum boxes in three-dimensional solid-state microcavities, *Journal of Lightwave Technology*, **17**, 2089–2095 (1999).

[84] M. V. Rybin, S. F. Mingaleev, M. F. Limonov, Y. S. Kivshar, Purcell effect and Lamb shift as interference phenomena, *Scientific Reports*, **6**, 20599 (2016).

[85] R. C. Rumpf, *Electromagnetic and Photonic Simulation for the Beginner: Finite-Difference Frequency-Domain in MATLAB*, Artech House, Boston, MA USA (2022).

[86] M. Niraula, J. W. Yoon, R. Magnusson, Concurrent spatial and spectral filtering by resonant nanogratings, *Opt. Express*, **23**, 23428–23435 (2015).

[87] L. Grineviciute, S. Melnikas, J. Nikitina, M. Drazdys, A. Selskis, D. Astrauskytė, Optical Coating Deposition on Submicron-Patterned Surfaces, *Coatings*, **15** (2025).

[88] K. Yee, Numerical solution of initial boundary value problems involving maxwell's equations in isotropic media, *IEEE Transactions on Antennas and Propagation*, **14**, 302–307 (1966).

[89] R. Rumpf, Simple implementation of arbitrarily shaped total-field/scattered-field regions in finite-difference frequency-domain, *Progress In Electromagnetics Research B*, **36**, 221–248 (2011).

[90] J.-Y. Wu, D. Kingsland, J.-F. Lee, R. Lee, A comparison of anisotropic PML to Berenger's PML and its application to the finite-element method for EM scattering, *IEEE Transactions on Antennas and Propagation*, **45**, 40–50 (1997).

[91] V. Demir, Graphics Processor Unit (GPU) Acceleration of Finite-Difference Frequency-Domain (FDFD) Method, *Progress In Electromagnetics Research M*, **23**, 29–51 (2012).

[92] R. Rumpf, Improved formulation of scattering matrices for semi-analytical methods that is consistent with convention, *Progress In Electromagnetics Research B*, **35**, 241–261 (2011).

[93] Y. Lan, D. Li, H. Kai, B. Zou, G. Zhang, S. Feng, Inverse design of ultra-compact optical logic gates by genetic algorithm, *Optics Communications*, **569**, 130800 (2024).

[94] F. Reyes, N. Cerpa, A. Candia-Véjar, M. Bardeen, The optimization of success probability for software projects using genetic algorithms, *Journal of Systems and Software*, **84**, 775–785 (2011).

[95] T. Kondo, S. Ura, R. Magnusson, Design of guided-mode resonance mirrors for short laser cavities, *J. Opt. Soc. Am. A*, **32**, 1454–1458 (2015).

[96] S. Zhang, Y. H. Ko, R. Magnusson, Broadband guided-mode resonant reflectors with quasi-equilateral triangle grating profiles, *Opt. Express*, **25**, 28451–28458 (2017).

[97] T. Khaleque, M. J. Uddin, R. Magnusson, Design and fabrication of broadband guided-mode resonant reflectors in TE polarization, *Opt. Express*, **22**, 12349–12358 (2014).

[98] K. Markowski, J. Bojarczuk, P. Araszkiewicz, R. Cybulski, M. Gaska, A. Golaszewski, Analysis of the Performance of WDM-CDM Bragg Grating Interrogation System With High-Contrast Grating VCSEL, *Journal of Lightwave Technology*, **41**, 2892–2903 (2023).

[99] J. Chen, H. Huang, Y. Zhang, X. Chen, X. Li, Reducing electric-field-enhancement in metal-dielectric grating by designing grating with asymmetric ridge, *Scientific Reports*, **8**, 5228 (2018).

[100] M. Rashki, M. R. Rakhshani, F. Kroushawi, O. Takayama, A. V. Lavrinenko, Hybrid trapezoidal grating metasurface supporting guided-mode resonances for biosensing, *J. Opt. Soc. Am. B*, **43**, 841–849 (2026).

[101] H. Hemmati, R. Magnusson, Applicability of Rytov's Full Effective-Medium Formalism to the Physical Description and Design of Resonant Metasurfaces, *ACS Photonics*, **7**, 3177–3187 (2020).

[102] S. Tazawa, S. Matsuo, K. Saito, A general characterization and simulation method for deposition and etching technology, *IEEE Transactions on Semiconductor Manufacturing*, **5**, 27–33 (1992).

[103] M. Subašić, Level Set Methods and Fast Marching Methods:, *Journal of Computing and Information Technology (cit@srce.hr); Vol.11 No.1*, **11** (2003).

[104] M. Shokooh-Saremi, R. Magnusson, Wideband leaky-mode resonance reflectors: Influence of grating profile and sublayers, *Opt. Express*, **16**, 18249–18263 (2008).

[105] Y. Jia, Y. Yan, S. V. Kesava, E. D. Gomez, N. C. Giebink, Passive Parity-Time Symmetry in Organic Thin Film Waveguides, *ACS Photonics*, **2**, 319–325 (2015).

[106] K. Chen, J. He, N. Zheng, S. Wu, H. Zheng, Cutting sinusoidal gratings to enhance light trapping in thin-film silicon solar cells, *Appl. Opt.*, **62**, 688–696 (2023).

[107] Y. Liang, W. Peng, M. Lu, S. Chu, Narrow-band wavelength tunable filter based on asymmetric double layer metallic grating, *Optics Express*, **23**, 14434–14445 (2015).

[108] H. Cao, J. Wiersig, Dielectric microcavities: Model systems for wave chaos and non-Hermitian physics, *Rev. Mod. Phys.*, **87**, 61–111 (2015).

[109] Y. Yan, N. C. Giebink, Passive PT Symmetry in Organic Composite Films via Complex Refractive Index Modulation, *Advanced Optical Materials*, **2**, 423–427 (2014).

[110] Y. Jia, Y. Yan, S. V. Kesava, E. D. Gomez, N. C. Giebink, Passive Parity-Time Symmetry in Organic Thin Film Waveguides, *ACS Photonics*, **2**, 319–325 (2015).

[111] G. Kenanakis, A. Xomalis, A. Selimis, M. Vamvakaki, M. Farsari, M. Kafesaki, C. M. Soukoulis, E. N. Economou, Three-Dimensional Infrared Metamaterial with Asymmetric Transmission, *ACS Photonics*, **2**, 287–294 (2015).

[112] R. Magnusson, M. Shokooh-Saremi, Physical basis for wideband resonant reflectors, *Opt. Express*, **16**, 3456–3462 (2008).

[113] A. Darweesh, S. Bauman, D. T. Debu, J. Herzog, The Role of Rayleigh-Wood Anomalies and Surface Plasmons in Optical Enhancement for Nano-Gratings, *Nanomaterials*, **8**, 809 (2018).

[114] K.-Y. Kim, X. Chong, F. Ren, A. X. Wang, Slow-light effect via Rayleigh anomaly and the effect of finite gratings, *Opt. Lett.*, **40**, 5339–5342 (2015).

[115] L. Grineviciute, I. Lukosiunas, J. Nikitina, A. Selskis, I. Meskelaite, D. Gailevicius, K. Staliunas, Light trapping by non-Hermitian thin films, *Phys. Rev. Appl.*, **23**, 054014 (2025).

[116] O. Aftenieva, J. Brunner, M. Adnan, S. Sarkar, A. Fery, Y. Vaynzof, T. A. F. Konig, Directional Amplified Photoluminescence through Large-Area Perovskite-Based Metasurfaces, *ACS Nano*, **17**, 2399–2410, pMID: 36661409 (2023).

[117] S. Feng, B. Povilus, S. Yang, Color tuning halide perovskites: Optical amplification and lasing, *Materials Today Advances*, **20**, 100431 (2023).

[118] M. Athanasiou, A. Manoli, P. Papagiorgis, K. Georgiou, Y. Berezovska, A. Othonos, M. Bodnarchuk, M. Kovalenko, G. Itskos, Flexible, Free-Standing Polymer Membranes Sensitized by CsPbX3 Nanocrystals as Gain Media for Low Threshold, Multicolor Light Amplification, *ACS Photonics*, **9** (2022).

[119] Q. Dong, X. Fu, D. Seyitliyev, K. Darabi, J. Mendes, L. Lei, Y.-A. Chen, C.-H. Chang, A. Amassian, K. Gundogdu, F. So, Cavity Engineering of Perovskite Distributed Feedback Lasers, *ACS Photonics*, **9**, 3124–3133 (2022).

[120] D. Kim, K. Y. Woo, J. H. Han, T.-W. Lee, H. S. Lee, Y.-H. Cho, K. C. Choi, Nanosinusoidal Surface Zinc Oxide for Optical Out-coupling of Inverted Organic Light-Emitting Diodes, *ACS Photonics*, **5**, 4061–4067 (2018).

[121] N.-V. Hoang, A. Pereira, H. S. Nguyen, E. Drouard, B. Moine, T. Deschamps, R. Orobtchouk, A. Pillonnet, C. Seassal, Giant Enhancement of Luminescence Down-Shifting by a Doubly Resonant Rare-Earth-Doped Photonic Metastructure, *ACS Photonics*, **4**, 1705–1712 (2017).

[122] M. Yoshida, S. Katsuno, T. Inoue, J. Gelleta, K. Izumi, M. Zoysa, K. Ishizaki, S. Noda, High-brightness scalable continuous-wave single-mode photonic-crystal laser, *Nature*, **618**, 1–6 (2023).

[123] S. Katsuno, M. Yoshida, T. Inoue, M. Zoysa, R. Hatsuda, K. Ishizaki, S. Noda, Design and experimental demonstration of photonic-crystal lasers with multijunction active layers, *Applied Physics Express*, **17** (2024).

[124] T. Inoue, M. Yoshida, J. Gelleta, K. Izumi, K. Yoshida, K. Ishizaki, M. Zoysa, S. Noda, General recipe to realize photonic-crystal surface-emitting lasers with 100-W-to-1-kW single-mode operation, *Nature Communications*, **13**, 3262 (2022).

[125] C. Peng, K. Sakai, S. Iwahashi, S. Noda, Three-dimensional coupled-wave analysis for square-lattice photonic crystal surface emitting lasers with transverse-electric polarization: finite-size effects, *Optics Express*, **20**, 15945–15961 (2012).

[126] S. Li, G. Witjaksono, S. Macomber, D. Botez, Analysis of surface-emitting second-order distributed feedback lasers with central grating phaseshift, *IEEE Journal of Selected Topics in Quantum Electronics*, **9**, 1153–1165 (2003).

[127] A. Liu, G. Guan, X. Chai, N. Feng, M. Lu, X. Bai, Y. Zhang, Metal Halide Perovskites toward Electrically Pumped Lasers, *Laser & Photonics Reviews*, **16** (2022).

[128] I. Goldberg, N. Annavarapu, S. Leitner, K. Elkhouly, F. Han, N. Verellen, T. Kuna, W. Qiu, C. Rolin, J. Genoe, R. Gehlhaar, P. Heremans, Multimode Lasing in All-Solution-Processed UV-Nanoimprinted Distributed Feedback MAPbI3 Perovskite Waveguides, *ACS Photonics*, **10**, 1591–1600 (2023).

[129] H. M. Lai, Z. Lu, C. K. K. Choi, W. Zhou, C. Ngo Yau, B. Z. Tang, H. Ko, Direct Room Temperature Synthesis of α-CsPbI3 Perovskite Nanocrystals with High Photoluminescence Quantum Yields: Implications for Lighting and Photovoltaic Applications, *ACS Applied Nano Materials*, **5**, 12366–12373 (2022).

[130] I. Allegro, V. Bonal, E. R. Mamleyev, J. M. Villalvilla, J. A. Quintana, Q. Jin, M. A. Díaz-García, U. Lemmer, Distributed feedback lasers by thermal nanoimprint of perovskites using gelatin gratings, *ACS Applied Materials & Interfaces*, **15**, 8436–8445 (2023).

[131] V. Bonal, J. A. Quintana, J. M. Villalvilla, P. G. Boj, M. A. Díaz-García, Controlling the emission properties of solution-processed organic distributed feedback lasers through resonator design, *Scientific reports*, **9**, 11159 (2019).

[132] P. J. Lestrange, F. Egidi, X. Li, The consequences of improperly describing oscillator strengths beyond the electric dipole approximation, *The Journal of Chemical Physics*, **143**, 234103 (2015).

[133] N. de Gaay Fortman, G.-M. Krause, P. Schall, A. F. Koenderink, Absorption and amplification singularities in metasurface etalons with gain, *Nanophotonics*, **14**, 2317–2329 (2025).

[134] A. Dogariu, A. Kuzmich, L. J. Wang, Transparent anomalous dispersion and superluminal light-pulse propagation at a negative group velocity, *Phys. Rev. A*, **63**, 053806 (2001).

[135] T. Savels, A. P. Mosk, A. Lagendijk, Light scattering from three-level systems: The T matrix of a point dipole with gain, *Phys. Rev. A*, **71**, 043814 (2005).

[136] K. Staliunas, Oscillator Chain: A Simple Model for Universal Description of Excitation of Waveguiding Modes in Thin Films, *Annalen der Physik*, **10**, e00219 (2025).

[137] A. F. Oskooi, D. Roundy, M. Ibanescu, P. Bermel, J. Joannopoulos, S. G. Johnson, Meep: A flexible free-software package for electromagnetic simulations by the FDTD method, *Computer Physics Communications*, **181**, 687–702 (2010).

[138] A. Y. Song, Y. Shi, Q. Lin, S. Fan, Direction-dependent parity-time phase transition and nonreciprocal amplification with dynamic gain-loss modulation, *Physical Review A*, **99**, 013824 (2019).

[139] R. Dharmavarapu, S. H. Ng, F. Eftekhari, S. Juodkazis, S. Bhattacharya, MetaOptics: opensource software for designing metasurface optical element GDSII layouts, *Opt. Express*, **28**, 3505–3516 (2020).

[140] R. Dharmavarapu, S. Bhattacharya, S. Juodkazis, GDOESII: Software for design of diffractive optical elements and phase mask conversion to GDSII lithography files, *SoftwareX*, **9**, 126–131 (2019).

[141] M. Veettikazhy, A. K. Hansen, D. Marti, S. M. Jensen, A. L. Borre, E. R. Andresen, K. Dholakia, P. E. Andersen, BPM-Matlab: an open-source optical propagation simulation tool in MATLAB, *Opt. Express*, **29**, 11819–11832 (2021).

[142] T. E. Magalhães, J. M. Rebordão, PyWolf: A PyOpenCL implementation for simulating the propagation of partially coherent light, *Computer Physics Communications*, **276**, 108336 (2022).

[143] C. Kim, B. Lee, TORCWA: GPU-accelerated Fourier modal method and gradient-based optimization for metasurface design, *Computer Physics Communications*, **282**, 108552 (2022).

[144] M. Minkov, I. Williamson, L. Andreani, D. Gerace, B. Lou, A. Song, T. Hughes, S. Fan, Inverse Design of Photonic Crystals through Automatic Differentiation, *ACS Photonics*, **7** (2020).

[145] B. Lou, S. Fan, RCWA4D: Electromagnetic solver for layered structures with incommensurate periodicities, *Computer Physics Communications*, **306**, 109356 (2025).

[146] V. Liu, S. Fan, S4 : A free electromagnetic solver for layered periodic structures, *Computer Physics Communications*, **183**, 2233–2244 (2012).

[147] S. Sarkar, S. Devinder, P. K. Sahoo, J. Joseph, Exploring tunable single-wavelength detection schemes for guided-mode resonance sensors, *Optics & Laser Technology*, **177**, 111107 (2024).

[148] Y. Y. Li, C. Hu, Y. C. Wu, J. J. Chen, H. H. Feng, Numerical investigation of one-dimensional nonpolarizing guided-mode resonance gratings with conformal dielectric films, *Opt. Express*, **21**, 345–357 (2013).

[149] B. U. N. Lyndin, Modal and C Methods Grating Design and Analysis Software, `https://mcgrating.com/`, accessed: 2022-10-30 (1999).

[150] M. Neviere, R. Petit, M. Cadilhac, About the theory of optical grating coupler-waveguide systems, *Optics Communications*, **8**, 113–117 (1973).

[151] M. Neviere, P. Vincent, R. Petit, M. Cadilhac, Systematic study of resonances of holographic thin film couplers, *Optics Communications*, **9**, 48–53 (1973).

[152] M. Neviere, P. Vincent, R. Petit, M. Cadilhac, Determination of the coupling coefficient of a holographic thin film coupler, *Optics Communications*, **9**, 240–245 (1973).

[153] A. Jacques, D. Ostrowsky, The grating coupler: Comparison of theoretical and experimental results, *Optics Communications*, **13**, 74–77 (1975).

[154] G. Quaranta, G. Basset, O. J. F. Martin, B. Gallinet, Recent Advances in Resonant Waveguide Gratings, *Laser & Photonics Reviews*, **12** (2018).

Curriculum Vitae

Ignas Lukošiūnas

Vilnius, Lithuania

ignas.lukosiunas@ff.vu.lt

Education:

- PhD in Physics, 2022-2026.
- Master Studies, "Lazerių fizika ir optinės technologijos", (Laser Physics and Optical Technologies), 2020-2022.
- Bachelor Studies, "Taikomoji fizika" (Applied Physics), 2016-2020.

Academic work experience:

1. Junior Researcher, Junior Assistant, (Laser Research Center) (from 2022-11 to now).

   As a PhD student, I:

   - Work as a main researcher in the field of nanophotonics, mainly with photonic resonant cavity systems. Worked in projects 1 and 2.
   - Supervise undergraduate students.
   - Teach undergraduate students in Computational Photonics course.

2. Project Specialist, (Laser Research Center).

   As a graduate student, I worked with multilayer thin film optimization for thin film photonic crystal filters in project 2.

3. Laboratory assistant, (Taikomosios elektrodinamikos ir telekomunikaciju institutas), (2018-07 to 2018-12).

   As an undergraduate student, I assisted with Terahertz Laboratory works in TETI institute, under the project of 3.

Courses lectured:
Computational Photonics (2023 - now).

Programming Language level and software

Python (Advanced), Matlab (Advanced), C++ (Intermediate), Blender (Intermediate), Inkscape (Advanced), Origin (Intermediate), Microsoft applications (Advanced).

Projects

1. D. Gailevičius, "ZenScat: waveguide system optimization and applications", from 2024-05-01 to 2025-04-30.

2. K. Staliūnas, "New generation of microchip lasers with integrated photonic microstructures", 09.3.3-LMT-K-712-17-0016, from 2020-04-06 to 2023-08-31.

3. A. Lisauskas, “Directive transistor-based THz detectors // (THzFET)” ESA Contract number: 4000122246/17NL/SC ”Terahertz radiation sources based on nonlinearities of nanometric semiconductor devices” Research Council of Lithuania, contract No. S-LAT-17-3, from 2018-07-02 to 2018-12-31.

Acknowledgments

I acknowledge everyone who shaped, strengthened this work and studies with their kind and honest support.

Ignas Lukošiūnas

Notes

Vilnius University Press
Saulėtekio av. 9, Bld. III , LT-10222 Vilnius
e-mail info@leidykla.vu.lt, www.leidykla.vu.lt
bookshop.vu.lt, journals.vu.lt
Print run copies 20